



Thèse

2020

Open Access

This version of the publication is provided by the author(s) and made available in accordance with the copyright holder(s).

Designed synthesis and surface modification of metal clusters: from
fundamentals to applications

Baghdasaryan, Ani

How to cite

BAGHDASARYAN, Ani. Designed synthesis and surface modification of metal clusters: from fundamentals to applications. Doctoral Thesis, 2020. doi: 10.13097/archive-ouverte/unige:131203

This publication URL: <https://archive-ouverte.unige.ch/unige:131203>

Publication DOI: [10.13097/archive-ouverte/unige:131203](https://doi.org/10.13097/archive-ouverte/unige:131203)

UNIVERSITÉ DE GENÈVE

FACULTÉ DES SCIENCES

Section de chimie et biochimie

Professeur Thomas Bürgi

Département de chimie physique

**Designed Synthesis and Surface Modification of Metal Clusters:
From Fundamentals to Applications**

Thèse

présentée à la Faculté des sciences de l'Université de Genève

pour obtenir le grade de Docteur ès sciences, mention chimie

par

Ani Baghdasaryan

de Sisian, Arménie

Thèse N° 5431

Genève

2020



**UNIVERSITÉ
DE GENÈVE**

FACULTÉ DES SCIENCES

DOCTORAT ÈS SCIENCES, MENTION CHIMIE

Thèse de Madame Ani BAGHDASARYAN

intitulée :

**«Designed Synthesis and Surface Modification of Metal
Clusters: from Fundamentals to Applications»**

La Faculté des sciences, sur le préavis de Monsieur T. BÜRGI, professeur ordinaire et directeur de thèse (Département de chimie physique), Monsieur N. AVARVARI, professeur (MOLTECH-Anjou, Unité Mixte de Recherche 6200, Centre National de la Recherche Scientifique, Université d'Angers, France) et Madame T. LAHTINEN, docteure (Department of Chemistry, Nanoscience Center, University of Jyväskylä, Finland), autorise l'impression de la présente thèse, sans exprimer d'opinion sur les propositions qui y sont énoncées.

Genève, le 27 janvier 2020

Thèse - 5431 -

Le Décanat

N.B. - La thèse doit porter la déclaration précédente et remplir les conditions énumérées dans les "Informations relatives aux thèses de doctorat à l'Université de Genève".

Acknowledgement

Foremost, I would like to express my sincere gratitude to my supervisor Prof. Thomas Bürgi for the provided opportunity to conduct my MSc thesis and later PhD in his research group. I am grateful for his tremendous academic support, his patience, motivation during my masters and especially PhD. His guidance helped me in all the time of research, writing papers and my thesis. He gave me all the freedom to pursue my research, to be able to develop as an individual researcher. I could not have imagined having a better supervisor and mentor for my PhD.

I would like to thank my thesis committee: Prof. Narcis Avarvari and Dr. Tanja Lahtinen for their insightful comments and corrections.

I acknowledge Prof. Jérôme Lacour and Prof. Narcis Avarvari whom I have the chance to collaborate with. I appreciate all the effort and support you have provided me during my scientific journey. It would not have been possible to realize and complete my projects without your support and collaboration. The success that I had is collective and I am grateful for that.

I acknowledge Prof. Massoud Dadras and Prof. Serge Rudaz to access to the laboratory and research facilities for the sake of our research projects.

I acknowledge Dr. Céline Besnard for her help and supervision of the crystallographic measurements of my samples starting from masters until the completion of PhD. I thank Dr. Latevi Max Lawson Daku for the performed calculations and obtained nice results.

I would like to thank Dr. Igor Dolamic for teaching me how to use and employ the HPLC techniques for the separation of clusters. With a special mention to Dr. Elodie Brun, Dr. Yuming Wang, Dr. Manish Sharma, Dr. Kaushik Bhattacharya, Dr. Kévin Martin and Dr. Giovanni Salassa for their help throughout my projects.

Mass Spectrometry Core Facility group, especially Dr. Emmanuel Varesio and Harry Theraulaz are acknowledged for performing endless MALDI-TOF and ESI measurements.

A very special gratitude goes out to all my present and former group members not only for the scientific discussions and briefings we had together, but also for the precious and fond memories outside the science. I will always cherish the memories of our hikes, pizza lunches, going out for dinner and partying.

I am very grateful to Catherine Ludy for her help and patience with never-ending administrative work, Raymond Azoulay for assuring the enjoyable atmosphere in the lab and Patrick Barman for his help with all the technical issues. Dr. Benjamin Doistau and Raymond Azoulay are acknowledged for their help translating my Résumé.

A very special gratitude goes out to all my friends in Geneva, especially Ani Gabrielyan, Tamara and Rafael Moine, Khoren, Narek and their families, Samvel for their support during all these years.

And finally, last but by no means least, my family in Armenia who have provided me through moral and emotional support in my life. I am also grateful to my relatives and friends who have supported me along the way.

Thank you for all your encouragement!

Abstract

Metal nanoclusters (MNCs) with sizes smaller than 2 nm have emerged a massive interest due to their size-tunable photochemical properties, which distinguishes them from their bigger counterparts. The nano-regime generates quantized and discrete electronic levels and molecule-like properties such as HOMO-LUMO transitions, size-dependent photoluminescence, chirality and magnetism. The size-dependent properties can be tuned *in situ* by applying well-established synthetic protocols and by engineering the surface protective ligand shell *ex situ*. This enables the creation of a grand library of fascinating nanoscale materials with editable (*chir*)optical properties and core/shell geometries.

During my Ph.D. I have completed several projects that included the implementation of surface modification strategies to alter the surface composition of atomically precise $\text{Au}_{25}(\text{2-PET})_{18}$ and $\text{Au}_{38}(\text{2-PET})_{24}$ clusters as well as synthesis and characterization of copper clusters.

By carefully choosing the modifying ligand, the surface composition and overall cluster properties can be drastically changed. We have shown that upon performing ligand exchange reactions with helicenes the strong chiral responses of the enantiopure cluster in a wide UV-vis window can be reduced and even shift to higher wavelengths depending on the number of adsorbed ligands. Moreover, an interesting effect has been observed during this process. Not only the CD responses diminish, but also the ligand exchange reaction resulted in the partial racemization of the cluster.

The ligand exchange reaction between thiolated crown ethers (CE) with achiral Au_{25} cluster resulted in the formation of up to five exchanged species in the mixture. The adsorption of the chiral CE ligand on the cluster surface induced chirality and enabled it with fascinating binding properties. The latter was examined using aqueous solutions of multivalent metal cations and non-aqueous solutions of chiral amines by applying ATR-FTIR and ^1H NMR spectroscopic studies. Noticeable IR shifts were observed when the metal cations were trapped inside the crown cavity. Upon binding the chiral amines strong binding affinities and switchable allosteric effect has been detected by NMR.

The synthesis of water-soluble copper clusters protected with GSH ligand resulted in the formation of a crude mixture of clusters with several core-sizes. Advanced spectroscopic and microscopic characterization of the sample indicated the formation of rather isolated and small clusters. The size-separation of the crude sample components was achieved with various analytical techniques. Moreover, the as-synthesized CuNCs showed pronounced antimicrobial effect towards *E. coli* cells.

The synthesis and crystal structure determination of a new sulfur-bridged thiol protected copper cluster has been opened the possibility for engineering new nanoscale materials with fascinating geometrical and optical properties. The synthesized cluster is an important contribution to the library of reported atomically precise copper clusters.

Résumé

Les Nanoclusters métalliques (MNC) de taille inférieure à 2 nm ont suscité un intérêt massif en raison de leurs propriétés photochimiques accordables en fonction de la taille, contrairement à leurs analogues plus grands. Le nano régime génère des niveaux électroniques quantifiés et discrets dans les domaines de la photoluminescence, de la chiralité et du magnétisme dépendant de la taille. Les propriétés dépendant de la taille peuvent être générées *in situ* en appliquant des protocoles synthétiques bien établis et en concevant la coque du ligand de protection de surface *ex situ*. Ceci permet de créer une grande bibliothèque de matériaux nanométriques fascinants avec des propriétés (*chir*)optiques modifiables et des géométries coeur/coquille.

Au cours de mon doctorat, j'ai réalisé plusieurs projets, dont la mise en œuvre de stratégies de modification de surface pour modifier la composition de surface des clusters atomiquement précis $\text{Au}_{25}(\text{2-PET})_{18}$ et $\text{Au}_{38}(\text{2-PET})_{24}$ ainsi que la synthèse et la caractérisation des clusters de cuivre.

En choisissant soigneusement le ligand modificateur, la composition de la surface et les propriétés globales du cluster peuvent être radicalement modifiées. Nous avons montré qu'en effectuant des réactions d'échange de ligands avec des hélicènes, les fortes réponses chirales des clusters énantiopures peuvent être réduites et même passer à des longueurs d'onde supérieures en fonction du nombre de ligands adsorbés, et ce dans une large fenêtre UV-vis. De plus, un effet intéressant a été observé au cours de ce processus. Non seulement les réponses CD diminuent, mais aussi la réaction d'échange de ligands a entraîné la racémisation partielle du cluster.

La réaction d'échange de ligands entre les éthers couronne thiolés (EC) et cluster achiral Au_{25} a entraîné la formation de plus de cinq espèces échangées dans le mélange. L'adsorption du ligand chiral CE sur la surface du cluster a induit la chiralité et lui a permis d'acquérir des propriétés de reconnaissance fascinantes. Ce dernier a été examiné à l'aide de solutions aqueuses de cations métalliques multivalents et de solutions non aqueuses d'amines chirales lors d'études spectroscopiques ATR-FTIR et ^1H NMR. On a observé des décalages IR notables lors de la complexation des cations métalliques par l'éther couronne. Lors de la reconnaissance des amines

chirales, de fortes affinités de liaison et un effet allostérique commutable ont été détectés sur les échelles de temps de la RMN.

La synthèse du cluster de cuivre hydrosolubles protégés par le ligand GSH a donné lieu à la formation d'un mélange brut composé de cluster de taille de coeur différentes. Les caractérisations spectroscopique et microscopique avancées de l'échantillon ont indiqués la formation des clusters plutôt isolés et petits. La séparation par taille des composants bruts de l'échantillon a été réalisée à l'aide de diverses techniques d'analyse. De plus, les CuNCs synthétisés ont montrés un effet antimicrobien prononcé sur les cellules *E. coli*.

La synthèse et la détermination de la structure cristalline d'un nouveau CuNCs protégé par un pont thiol soufré a ouvert la possibilité de concevoir de nouveaux matériaux à l'échelle nanométrique aux propriétés géométriques et optiques fascinantes. Le cluster synthétisé constitué une contribution important à la bibliothèque des clusters de cuivre atomique définie reportés.

Acknowledgement

Abstract

Résumé

Content

A. General introduction

1. Introduction	1
1.1. Nanomaterials and ligand-protected metal nanoclusters.....	1
1.2. Electronic properties and structure.....	2
1.3. Size-dependent properties	5
1.4. Chirality in clusters	7
2. Synthesis of ligand-protected metal nanoclusters (MNCs)	10
2.1. Synthesis of gold nanoclusters (AuNCs)	10
2.1.1. Template mediated synthesis	10
2.1.2. Brust-Schiffrin method	12
2.1.3. Size-focusing synthesis	15
2.2. Synthesis of copper nanoclusters (CuNCs)	17
2.2.1. Template-based synthesis	17
2.2.2. Electrochemical synthesis	23
2.2.3. Water-in-oil (w/o) microemulsion	23
2.2.4. Modified Brust-Schiffrin technique	25
2.2.5. Microwave-assisted polyol synthesis.....	27
3. Characterization of metal nanoclusters	29
3.1. UV-vis spectroscopy	29
3.2. Circular dichroism.....	30
3.3. Transmission electron microscopy.....	32
3.4. X-ray photoelectron spectroscopy	32
3.5. Infrared spectroscopy.....	33
3.6. Mass spectrometry.....	34

3.7. Photoluminescence	35
3.8. Nuclear magnetic resonance (NMR).....	37
3.9. X-ray crystallography	39
4. Size-separation of MNCs	43
4.1. Size-exclusion chromatography (SEC)	43
4.2. Liquid chromatography (HPLC).....	44
4.3. Gel electrophoresis (PAGE).....	45
4.4. Capillary electrophoresis (CE).....	48
References	52

B. Experimental results

5. Post-functionalization of AuNCs	78
5.1. Ligand exchange reactions on chiral Au₃₈ cluster: variations in CD line shapes caused by the modification of ligand shell composition	78
References	92
Supporting information	96
5.2. Combined spectroscopic studies on post-functionalized Au₂₅ cluster as an ATR-FTIR sensor for cations	101
References	117
Supporting information	124
5.3. Induced chirality and cooperativity in post-functionalized Au₂₅	131
References	145
Supporting information	154

6. Synthesis of ligand-protected CuNCs	166
6.1. Facile synthesis, size-separation, characterization, and antimicrobial properties of thiolated copper clusters	166
References	185
Supporting information	192
6.2. Thiolato protected copper sulfide cluster with the tentative composition $\text{Cu}_{74}\text{S}_{15}(\text{2-PET})_{45}$..	198
References	214
Supporting information	222
General conclusions.....	254
Abbreviations	256
List of publications	
Curriculum Vitae	

1. Introduction

1.1. Nanomaterials and ligand-protected metal nanoclusters

“There’s Plenty of Room at the Bottom.

...When we get to the very, very small world-say circuits of seven atoms-we have a lot of new things that would happen that represent completely new opportunities for design. Atoms on a small scale behave like nothing on a large scale, for they satisfy the laws of quantum mechanics...”

Richard Feynman, December 29th, 1959, Caltech

ISO/TS 80004 defines a nanomaterial as a: “material with any external dimension in the nanoscale (size range from approximately 1 – 100 nm) or having internal structure or surface structure in the nanoscale”. In the last decades, a new field, commonly known as a “nanoscience”, has been developing rapidly. It influences various branches of modern science: physics, chemistry, engineering, medicine and technologies. The aim of nanoscience and nanotechnology is to understand kinetic and thermodynamic aspects, and the ability to control and produce objects of a few nanometers in size (ca 1-100nm), **Fig. 1**. These nano objects are classified as an intermediate between single atoms and molecules and bulk matter. However, to even further distinguish different nanomaterials (nanofiber, nanoribbon and [metal]nanoparticles) a general term “nanocluster” has been employed to differentiate a class of nanomaterials composed of less than a few hundred atoms. Within this context, monolayer-protected metal nanoclusters

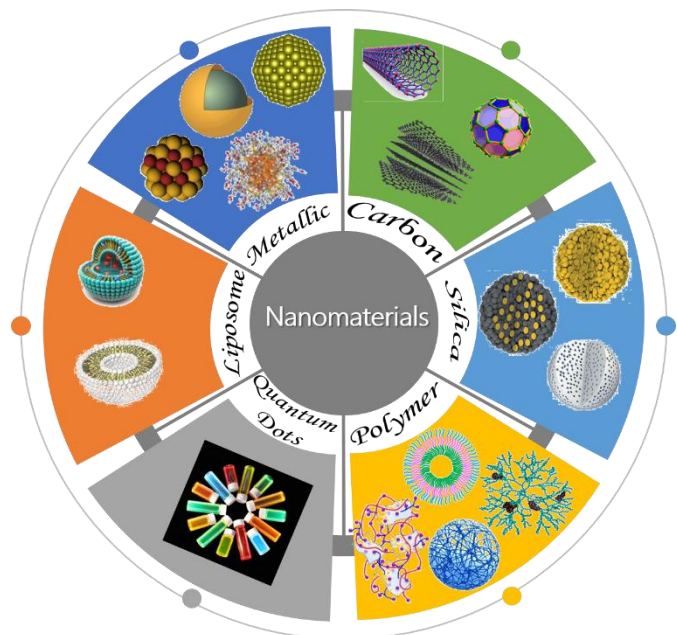


Fig. 1 Schematic illustration of naturally occurring and chemically engineered nanomaterials widely applied in modern nanotechnology.

(MNCs) with a common formula of $M_n(SR)_m$ (where M is Au, Ag and to some extent Cu) have emerged a huge interest in modern scientific communities due to their unique size-dependent properties and the ability to synthesize with atomic precision and in high yields.¹⁻⁵ Over the years “wet chemical” synthesis became a prominent universal method to synthesize highly fluorescent, stable magic size clusters with modifiable ligand shell smaller than 2 nm in size. Thus, depending on the nature of the protective ligand, clusters soluble in aqueous medium or in organic solvents can be prepared. As a capping ligand phosphines, amines and mostly thiols with various backbones structures and valuable functionalities have been incorporated onto a cluster surface.² Besides, the massive progress in analytical platform to perform *in situ* analytical, spectroscopic and microscopic characterization of the as-prepared nanomaterials, drastically improved the understanding of the reaction mechanisms, growth processes and the factors that control the size, shape and morphology of the desired nanomaterial. Moreover, the crystallization of high-quality single crystals revealed tens of fascinating structures with unique metallic core/organometallic shell architectures,^{1-3,6} unusual binding motifs^{2,7,8} that can help to establish structure-chiroptical properties relationship at the nanoscale.

The advantage of nanoclusters with respect to gas phase prepared clusters, quantum dots (QDs) or their bigger counterparts is their strong photoluminescence and biocompatibility,^{1,2,5} that opens a variety of applications in optoelectronics,⁹ catalysis^{6,10-12} and biomedicine.¹³⁻¹⁹ Nanocluster-based biosensors have been extensively applied for the detection of trace amounts of various metal ions, reactive oxygen species (ROS) and toxic chemicals present in water samples or biological environments.^{20,21} It is nonetheless to mention, the development of nanocluster-based machines and carriers for effective and selective drug delivery of pharmaceuticals.^{22,23} Moreover, owing to their excellent biocompatibility and low toxicity, MNCs found important applications in targeted detection and diagnostics of cancerous cells *in vitro* and *in vivo*.²³⁻²⁵

1.2. Electronic properties and structure

Atomically precise and thiolate-protected gold nanoclusters show unique electronic and structural properties, and on top of that are highly stable. In order to understand the origin of

extraordinary stability in these MNCs, several models have been proposed over the years including the “superatom” theory^{26,27} and “jellium model”.²⁸ In a “superatom” theory the valence electrons in MNCs ($6s^1$ electrons in case of gold) are delocalized and continuum energy levels break down into discrete band structures. According to a “jellium model”, which approximates a superatom model, the electron gas is freely floating in a jelly-like medium of averaged ion densities rather than discrete ions (as in superatom model) and can be subjected to an external potential. In this spirit, by solving the Schrödinger equation for a spherical well, an increase of $2(2l+1)$ degeneracies as a function of their angular momentum (l) subshells²⁹ is observed (**Fig. 2**):

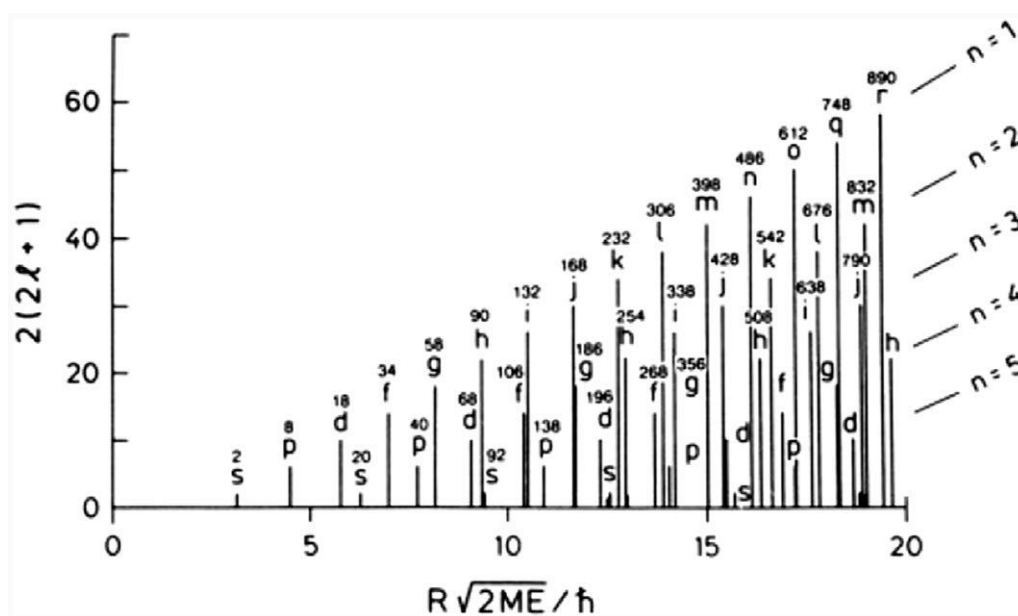



Fig. 2 Shell structure of electrons in each energy level and degeneracies of states for the spherical potential. The degeneracies are presented as a function of an increasing momentum. Reprinted with permission from ref [30]. Copyright (1991) American Chemical Society.

Obviously, the angular momentum subshells filled according to the Aufbau principle, start to group into a single energy shell, where the discrimination of a certain subshell becomes impossible. Going beyond, based on a superatom model a series of electron shell closing numbers^{29,30} also known as “magic” numbers can be derived and considered as a key factor for the clusters’ stability.

Angular momentum shells: $1s^2 1p^6 1d^{10} 2s^2 1f^{14} 2p^6 1g^{18}$

Electron shell closing: $1S^2 | 1P^6 | 1D^{10} | 2S^2 1F^{14} | 2P^6 1G^{18} |$ etc.


Magic numbers: 2, 8, 18, (20), 34, (40), 58, 92 etc.

Thus, ligand passivated clusters fulfilling the electron count of a magic number, would be considered as a superatom, in which gold atoms are donating their $6s^1$ valence electron to sulfur atom (in case of thiolate ligands). The electron count for any cluster with a formula of $Au_n(SR)_m^q$ can be calculated according to the following equation:

$$n_e = N - M - q \quad (1)$$

where N is the number of gold atoms in the cluster, M is the number of thiolate ligands (or any other ligand with one localized electron) and q is the net charge of the cluster. For example, $Au_{25}(SR)_{18}$ cluster can be found in neutral and charged (+1 and -1) states.³¹ In the neutral state, the cluster has a $7e^-$ count ($1S^2 1P^5$) and thus, is an open shell. On contrary, negatively charged one is $8e^-$ system ($1S^2 1P^6$) and thus is considered as a closed shell. These differences in electronic properties result slight changes in their respective UV-vis absorption spectra and explained the extraordinary stability of the negatively charged cluster over others. Surprisingly, when applying the superatom concepts to highly stable and atomically precise $Au_{38}(SR)_{24}$ cluster, the electron counting is 14. Clearly, $14e^-$ system is not a closed shell and it corresponds to the fulfilling of 1D midshell. However, the stability of this cluster can be understood by looking at the crystal structure. Au_{38} does not have a “spherical” core but rather prolate, rod-like geometry. DFT calculations illustrated that strong Jahn-Teller deformations stabilize the HOMO-LUMO gap structure for Au_{38} cluster.³² Much earlier, similar distortions had been observed in $14e^-$ systems of alkaline metal clusters in the gas phase.³³ These observations highlighted the contribution of geometric shells/structures as a key to unusual stability in small clusters.³⁴ The high surface/volume ratio in small nanoclusters is optimized by the geometrical shape they take. In other words, relatively big or bulky structures have lower surface/volume ratio and mostly crystalline fcc-type geometries (highly symmetrical) are adopted. While decreasing the size of the

cluster core (increasing the surface/volume ratio) the more noncrystalline polyhedron geometries such as icosahedron, cuboctahedron and decahedron become prominent among small nanoclusters. Although this trend is largely observed in gold nanoclusters with known structures, lately few exceptions of AuNCs with fcc-based structures have been crystalized (for details see sections 2.1.3 and 3.9).

1.3. Size-dependent properties

The nano regime in ultra-small MNCs breaks down the continuum energy bands into discrete energy levels and the collective oscillations of conduction band electrons typical for plasmonic particles upon interacting with electromagnetic field are no longer dominating (**Fig. 3**). The quantized and discrete state in clusters results in rich molecular-like features in their optical absorption spectrum (*vide infra*).

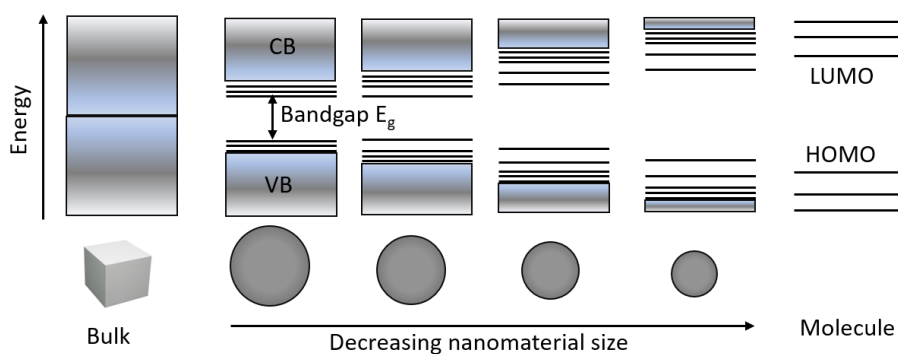


Fig. 3 Quantum confinement effects in nanomaterials and consecutive energy band gap structure. With decreasing the nanomaterial's size, the continuum energies break down into discrete energy levels with an increase of bandgap.

Several questions however remain to be answered: i) what is the typical size of the cluster in order to observe energy quantization in small clusters? and ii) how many atoms or valence electrons they have in their compositions to have strong quantum confinement effects. The Schrödinger's equation for a hydrogen-like atom can be applied for the bigger systems by

considering the first approximation of free-electron model (no electron-electron or electron-ion interactions):³⁵

$$\mathcal{H}\Psi = \left(-\frac{\hbar^2}{2m}\nabla^2 + V\right)\Psi = E\Psi \quad (2)$$

The energies corresponding to principle numbers can be derived by solving equation (2) in Cartesian coordinate system:

$$E_n = \frac{\pi^2\hbar^2}{2ma^2}n^2 \quad (3)$$

The energy is directly proportional to n^2 and the relation can be interpreted as a sphere with radius n , where the number of energy states can be presented as:

$$N' = \frac{1}{8}\left(\frac{4}{3}\pi n^3\right) = \frac{\pi}{6}\left(\frac{2ma^2}{\pi^2\hbar^2}\right)^{\frac{3}{2}}E^{\frac{3}{2}} \quad (4)$$

The density of energy states can be obtained by differentiating the equation (4) with respect to energy E :

$$\frac{dN'}{dE} = \frac{\pi}{4}\left(\frac{2ma^2}{\pi^2\hbar^2}\right)^{\frac{3}{2}}E^{\frac{1}{2}} = \frac{a^3}{4\pi^2}\left(\frac{2m}{\hbar^2}\right)^{\frac{3}{2}}E^{\frac{1}{2}} \quad (5)$$

where a is the volume of particle. The spacing δ between energy levels is a reciprocal of density of energy states:

$$\delta = \frac{4\pi^2}{a^3}\left(\frac{\hbar^2}{2m}\right)^{\frac{3}{2}}E^{-\frac{1}{2}} \quad (6)$$

By applying the equation (6) for the clusters assuming at room temperature the thermal energy ($k_B T$) equals to δ , E is the fermi energy of gold ($E_F=5.5$ eV) the critical size for quantization of energy levels in clusters is approximately 1.7 nm. Since this is a first-order approximation only, it's possible to estimate roughly 2 nm size as a critical size in clusters.³⁶ Moreover, further calculations show that this corresponds to having up to 300 6s valence electrons in the cluster composition. Thus, the critical size of the cluster highly influences its optical properties on a large scale of UV-vis-NIR window. The efficient separation of various clusters differing by only one

metal atom or ligand molecule strongly supports the quantized nature of clusters as a function of their core sizes (Fig. 4).^{37,38}

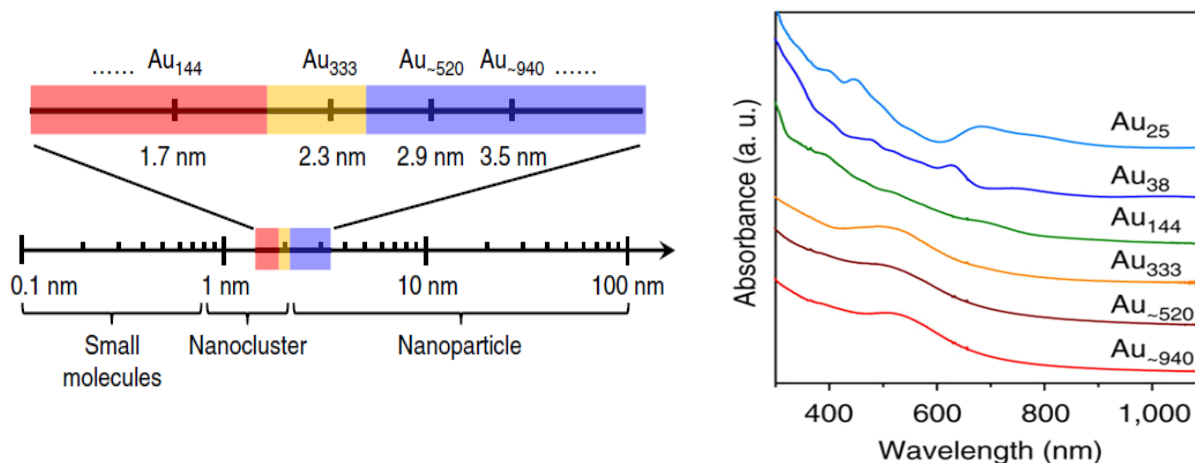


Fig. 4 Size evolution in atomically precise MNCs from metallic nanoparticles (blue zone) to nonmetallic clusters (red zone) (left panel) and typical UV-vis spectra of clusters varying drastically with size (right panel). [37]

The smaller the core size, the more expressed is the absorption features like in the case of $\text{Au}_{25}(\text{SR})_{18}$ and $\text{Au}_{38}(\text{SR})_{24}$. With an increase of the core size (above 2.3 nm), the molecular-like transitions in clusters transform into collective plasmon excitations in nanoparticles and thus, indicating nearly closing the band gap and the overlap of energy levels.

1.4. Chirality in clusters

Chirality is a naturally occurring phenomenon and have been long known in biological and pharmacological platforms. Since the first discovery of chirality in glutathione-protected gold nanoclusters by Whetten group earlier in 2000s,³⁹ a massive progress in theoretical predictions dedicated to understanding the origin of chirality in small nanoclusters having 20-40 atoms was emerged. Several theoretical calculations were conducted to individually analyze the core, the shell and overall structure in order to gain insight into the origin of strong chiral responses in metal-based transitions. To do so, first global structure optimizations using genetic algorithms

with many-body potentials, the most energetically stable cluster sizes were obtained.⁴⁰ Interestingly, chiral configurations of bare and protected clusters came out as low-energy structures. Next, Hausdorff chirality measure (HCM) was used to calculate the degree of chirality in bare and protected Au₂₈ and Au₃₈ clusters.⁴¹ Nonzero values were obtained for both gas phase and protected Au₂₈ cluster, however high symmetry structure of Au₃₈ with zero HCM values were become chiral only after adsorbing thiol ligand on the surface. This leads the conclusion that in case of Au₃₈ cluster, the chirality originates from the distorted metallic core caused by the passivating ligand. First-principle calculations of circular dichroism spectra of Au₃₈(SR)₂₄ cluster showed that indeed, after the passivation the core becomes intrinsically chiral showing Cotton effect in CD line shape (**Fig. 5**).^{42,43} Moreover, the morphology of the cluster played a role in the CD spectrum. The more distorted (low symmetry and chiral) the metallic core is the higher intensity of peaks are observed in CD. In contrast, high symmetry clusters show less intense or no CD.⁴⁴

To the end, several mechanisms have been proposed to explain the origin in various passivated clusters: intrinsically chiral metal core, dissymmetric field model and chiral footprint.^{45,46} The intrinsically chiral metal core or ligand induced chirality in metal nanoclusters including Au₃₈(SR)₂₄^{32,47-49} and Au₁₀₂(SR)₄₄⁵⁰ has been considered as an origin of chirality. Briefly, the passivating ligand (chiral or achiral) induces structural and geometrical distortions in the cluster core due to strong Au-S bond formation and staple motif arrangements on the surface. Although chiral ligands (GSH^{39,51} and penicillamine^{52,53} for instance) possess chiroptical properties in mostly UV

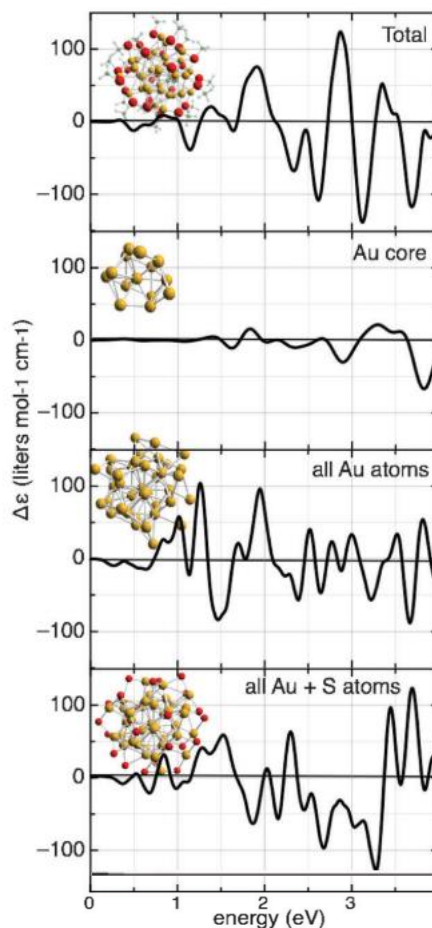


Fig. 5 CD spectra of Au₃₈(SR)₂₄ calculated from first-principles DFT. Reproduced with permission from ref [43]. Copyright © 2009, EDP Sciences, SIF, Springer-Verlag Berlin Heidelberg.

region, the strong CD responses appearing in visible and near IR regions were due to the core structure distortions. A large amount of theoretical efforts supported this mechanism being mostly responsible for strong CD properties.

Dissymmetric field model states that the chirality in metal nanoclusters is due to the adsorption of chiral molecules in a chiral pattern on achiral metallic cores.⁵⁴ In other words, when chiral ligands adsorb on the surface, they transfer chirality to the whole cluster. However, this model could not explain the chirality when achiral ligands were used.

Another model, called “chiral footprint”, implies that when chiral molecules are adsorbed on metallic surfaces, the local environment becomes chiral.⁵⁵ In case of the monolayer-protected clusters, when studying the chirality of N-Isobutyl-cysteine (NIC)-protected nanoclusters by VCD, it was confirmed that carboxylate groups of a chiral ligand additionally bond with the gold by making two-point interactions.⁵⁶ This on the other hand, led to the chiral footprints on the cluster surface, perhaps being the origin of the strong VCD signals.

Although all these models are quite straightforward for certain studied cases, however the intrinsically chiral core model is the main one being vastly utilized for describing the chiroptical properties of monolayer-protected and atomically precise metal clusters.

2. Synthesis of ligand-protected metal nanoclusters (MNCs)

2.1. Synthesis of gold nanoclusters (AuNCs)

The synthetic procedures for preparing nanomaterials are of utmost importance. The large interest in synthesizing nanomaterials comes from their unique and extraordinary applications in different areas of modern science. Therefore, various chemical and physical methods have been developed and applied for large-scale synthesis of gold nanoclusters (AuNCs) with precise atomic compositions.^{13,14,17,57–61}

2.1.1. Template mediated synthesis

Template-based method became a cutting-edge technology for effective synthesis of various nanomaterials with designed structures, morphologies, properties and sizes.^{57,62–64} The main concept of this technique is the formation of the extremely ordered and uniform nanomaterials within the pores, channels or cavities of a nano-matrix. Thus, the target's morphology and the size can be tailored by simply changing the shape of the matrix, i.e. cylinder, rod, sphere. In general, any porous material including naturally occurring minerals and biological substrates can be considered as a template. Hard, i.e. with rigid structure which directly determines the size and shape of target material and soft, i.e. which has more flexible and adjustable structure, template matrices have been extensively used for the synthesis of nanomaterials. Despite the tremendous efforts in synthesizing metals,⁶⁵ semiconductors (CdS, CdSe, ZnSe)^{66,67} and magnetic metal oxides (Fe₃O₄, Co₃O₄)⁶⁸ based on hard template method, soft templates are easier to handle, the reaction requires mild conditions, the template removal process is effortless. Polymer networks, hydrogels, supramolecular assemblies, biomolecules such as DNA, proteins, viruses and other microorganisms can be used as templates. Biological substances are inclusively used for nanostructures synthesis owing their naturally occurring complex structures.

Fluorescent AuNCs with very high quantum yields (QY>35%) can be directly synthesized within polymer pores or embedded inside the biomolecular scaffolds. Moreover, by adjusting the reaction conditions, the precursor ratio as well as protective ligand or bio template, the synthesis can result in blue to red-emissive clusters without losing the characteristic PL properties.⁵⁹ On the account of a very strong Au-S interactions, many proteins, including lysozyme, BSA, human transferrin, lactoferrin, trypsin, pepsin, insulin, horseradish peroxidase, have Cys residues as sulfur-bearing amino acids and have been widely used for the synthesis of fluorescent and biocompatible AuNCs.^{57,60} The process is somewhat like naturally occurring biomineralization, in which bio organisms convert inorganic materials into mineral structures necessary for their proper functioning. Thus, the synthesis of fluorescent inorganic clusters in protein or DNA templates relates to the concept of biomineralization where the initially formed gold-protein complex can be reduced by amino acids and further form self-organized and perfectly arranged nanostructures. Moreover, by altering the pH of the solution, the binding ability of the protein towards metal cations can be increased due to the conformational changes in their secondary structures. It has been shown, that Cys and His residues in proteins (BSA for example) can coordinate with Au³⁺ while the Tyr residues can work as strong reducing agents. Altogether, the reducing-protecting amino acids lead to the formation of stable clusters.⁶⁹ This, on the other hand, is a green process and does not involve the use of aggressive reducing agents or production of toxic by-products, and thus, makes the synthetic method environmentally friendly.

Random or branched structured dendrimers (2nd and 4th generations of OH-terminated PAMAM) and polymers with abundant functional groups have been used for the synthesis of fluorescent AuNCs in the presence of reducing agents such as NaBH₄ or tetrakis(hydroxymethyl)phosphonium chloride (THPC). The resultant clusters with various sizes of Au₅, Au₈, Au₁₃, Au₂₃ and Au₃₁ exhibited bright UV to NIR fluorescence emissions with rather high QYs.^{13,14,57}

Oligonucleotide-derived synthesis of metal nanoclusters emerged an increased attention due to the ease of preparation methods, tunable PL properties, its high photostability. On top of that it serves as an excellent diagnostic tool for biomedical applications towards biosensing, bioimaging and targeting.⁷⁰ Additionally, the synthesis is cost-effective, does not involve the use of expensive

machinery or chemicals and can be directly used for bio applications due to the high viability and nontoxic properties. The atomic compositions of the as-prepared clusters can be controlled by changing the DNA sequences and lengths or designing special targeted sequences for high affinity metals. In general, the synthesis of AuNCs using DNA helices, involves the formation of DNA-Au⁺ (or M⁺ in general) and the reduction with a reducing agent (**Fig. 6**).^{70,71}

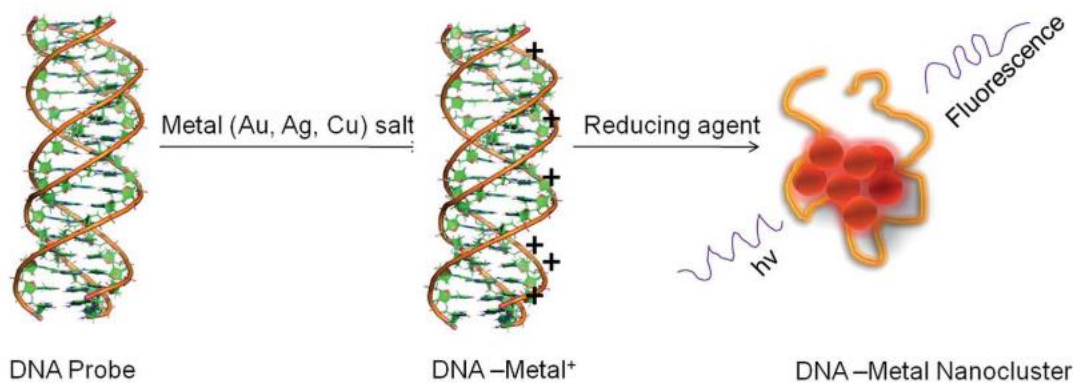


Fig. 6 Schematic diagram of the preparation of DNA-capped metal nanoclusters. Reprinted with permission from ref [70]. Copyright 2016 RSC.

Moreover, while using hairpin (HP)-DNA as a hosting scaffold, the formed clusters showed loop sequence-dependence.⁷¹ The synthesized AuNCs have found an important applications in detection of metal ions, nucleic acids and small biomolecules for pathogen identification, clinical diagnosis, and forensic analysis,^{13,17,57,70} as well as for environmental analysis.¹⁵

2.1.2. Brust-Schiffrin method

The highly accepted and tremendously applied synthetic strategy for the synthesis of ligand-protected metal nanoclusters is the Brust-Schiffrin two-phase method (also one-phase).⁷² The idea is to simultaneously grow metal nanoclusters by protecting their nuclei with a thiol monolayer (**Fig. 7**). This process involves the transfer of AuCl₄⁻ from an aqueous solution to organic phase by using tetraoctylammonium bromide (TOAB) as a phase-transfer reagent. Later gold atoms are reduced with NaBH₄ in the presence of thiol ligand. In contrary, the one-phase

method involves direct mixing of a gold salt and a protective ligand in methanol.⁷³ The mechanistic studies and the analyses of the intermediate species done by NMR and Raman spectroscopic methods revealed the reduction of $[\text{AuX}_4]$ to $[\text{AuX}_2]$ after adding thiol ligand to it (equation 7).^{74,75} Thus, it leads the reduction of Au^{3+} to Au^{1+} in the form of chalcogenate complexes rather than the formation of Au(I)-thiolate polymeric species, which was generally recognized as a precursor for cluster synthesis for a long time. Moreover, Au(I)-thiolate polymeric species are not soluble in most of the solvents and immediate precipitation would have been observed. No Au-S bond has been detected in the Raman spectrum at this stage of reaction.⁷⁵ Furthermore, the successive reduction process of Au (I)-chalcogenate complex by borohydride results in the formation of a polydisperse crude product of several core-sized clusters (equation 8), from which precise compositions can be isolated by various fractionation methods suitable for certain clusters (size exclusion chromatography: SEC, polyacrylamide gel electrophoresis: PAGE, high performance liquid chromatography: HPLC). Several “magic” number clusters with a formula of $\text{Au}_n(\text{SR})_m$ have since been synthesized in high yields and separated efficiently. **Table 1** summarizes all the “magic” clusters that have been reported to date.

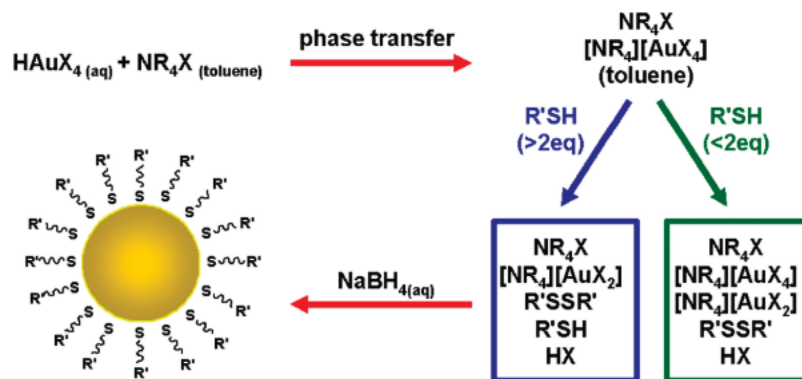


Fig. 7 Schematic representation of Brust-Schiffrin two-phase method. Reprinted with permission from ref [74]. Copyright (2010) American Chemical Society.





Table 1 The complete list of atomically precise gold nanoclusters protected with various thiol ligands: crystal structure and the anatomy. Note, the clusters bigger than Au₁₄₄ already show plasmonic features and are not included in the table.

Formula	Ligand	Crystal structure				Ref.
		Geometry	Monomeric staples Au(SR) ₂	Dimeric staples Au ₂ (SR) ₃	Others	
Au ₁₅ (SR) ₁₃	glutathione (SG)	-	-	-	-	[76–78]
Au ₁₈ (SR) ₁₄	glutathione (SG), S-c-C ₆ H ₁₁	biocuboctahedral	3	1	Au ₄ (SR) ₅	[78–80]
Au ₂₀ (SR) ₁₆	SC ₂ H ₄ Ph, SCH ₂ Ph, SPh- ^t Bu (TBBT)	bitetrahedral	2	-	Au ₈ (SR) ₈ ring and Au ₃ (SR) ₄ trimer	[81–83]
Au ₂₃ (SR) ₁₆ ⁻	S-c-C ₆ H ₁₁ , S- ^t Bu	cuboctahedral	2	-	2x Au ₃ (SR) ₄ and 4x SR	[84,85]
Au ₂₄ (SR) ₁₆	adamantanethiolate (SC ₁₀ H ₁₅)	cuboctahedral	1	1	2x Au ₃ (SR) ₄ and 3x SR	[86]
Au ₂₄ (SR) ₂₀	SC ₂ H ₄ Ph, SCH ₂ Ph, SCH ₂ Ph- ^t Bu	bitetrahedral	-	-	4x Au ₄ (SR) ₅	[82,87,88]
Au ₂₅ (SR) ₁₈ ^q (q = -1, 0, +1)	glutathione (SG), SC ₂ H ₄ Ph, SC _n H _{2n+1} , SPhNH ₂ , captopril (Capt) and others	icosahedral	-	6	-	[31,51,96–104,76,89–95]
Au ₂₈ (SR) ₂₀	SPh- ^t Bu (TBBT), S-c-C ₆ H ₁₁	cuboctahedral	-	4	8x SR	[105,106]
Au ₃₀ (SR) ₁₈	adamantanethiolate (SC ₁₀ H ₁₅)	hcp	-	6	-	[107]
Au ₃₆ (SR) ₂₄	SPh- ^t Bu (TBBT), S-c-C ₅ H ₉ , SPh	fcc	-	4	12x SR	[108–111]
Au ₃₈ (SR) ₂₄	SC ₂ H ₄ Ph, SC _n H _{2n+1}	biicosahedral	3	6	-	[112–116]
Au ₄₀ (SR) ₂₄	SC ₂ H ₄ Ph, SPh- <i>o</i> -CH ₃ (<i>o</i> -MBT)	Au ₂₅ like kernel	6	-	3x Au ₃ (SR) ₄	[117–120]
Au ₄₄ (SR) ₂₈	SPh- ^t Bu (TBBT)	cuboctahedral	-	4	16x SR	[121,122]
Au ₅₂ (SR) ₃₂	SPh- ^t Bu (TBBT)	tetrahedral units	4	8	-	[120]
Au ₅₅ (SR) ₃₁	SC ₂ H ₄ Ph	-	-	-	-	[123–125]
Au ₆₄ (SR) ₃₂	S-c-C ₆ H ₁₁	-	-	-	-	[126]

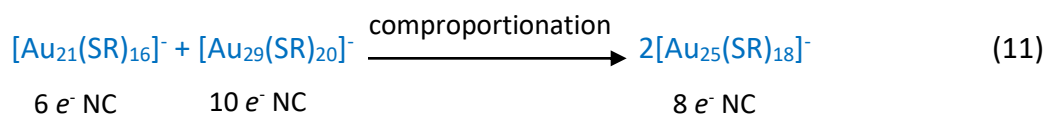
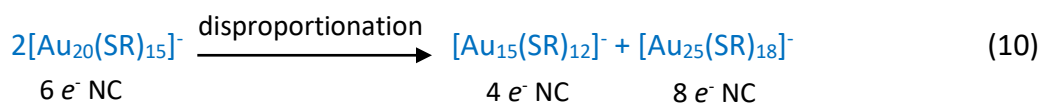
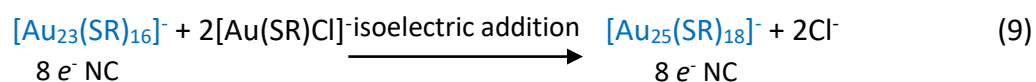
A. GENERAL INTRODUCTION

Au ₆₇ (SR) ₃₅	SC ₂ H ₄ Ph	-	-	-	-	[127]
Au ₉₉ (SR) ₄₂	SPh, SPh- <i>p</i> -CH ₃	-	-	-	-	[128]
Au ₁₀₂ (SR) ₄₄	SPh- <i>p</i> -COOH	icosahedral	19	2	-	[129,130]
Au ₁₀₄ (SR) ₄₁	SPh- <i>m</i> -CH ₃	-	-	-	-	[117]
Au ₁₃₀ (SR) ₅₀	SPh- <i>p</i> -CH ₃ (p-MBT), SC _n H _{2n+1} , SC ₂ H ₄ Ph, dithioldurene/SC ₂ H ₄ Ph	Ino-decahedral	25	-	-	[117,131– 133]
Au ₁₃₃ (SR) ₅₂	SPh- ^t Bu (TBBT)	icosahedral	26	-	-	[134,135]
Au ₁₃₇ (SR) ₅₆	SC ₂ H ₄ Ph	-	-	-	-	[136]
Au ₁₄₄ (SR) ₆₀	SC ₂ H ₄ Ph, SC _n H _{2n+1}	hcp	30	-	-	[113,137– 139]

2.1.3. Size-focusing synthesis

Although Brust-Schiffrin method is widely accepted and universal synthetic method for the preparation of atomically precise gold nanoclusters with various sizes in a controlled manner,^{72,73} certain magic size clusters could not be synthesized in a typical Brust-Schiffrin method. Recently, a new synthetic strategy known as “size-focusing” has been realized to solve above-mentioned problem by selectively producing certain cluster sizes under harsh heating conditions of a cluster solution with the addition of a thiol ligand (same kind or different one). Earlier it has been shown, that GSH-and 2-PET-protected AuNCs under heating conditions transform into Au₂₅(SR)₁₈ cluster.^{140,141} Thus, the latter being more resistance to thiol etching, becomes the most stable cluster size amongst others and the core-etching of other bigger clusters leads to the population increase of Au₂₅. Upon heating of the dodecanethiol-protected ~14 kDa clusters (equivalent of around 75 gold atoms in the composition) in neat thiol showed the gradual appearance of a 8 kDa cluster’s peak in mass spectrometry.¹⁴² More interestingly, the spacing between peaks corresponded to the combined mass of Au-S, which was the clear indication of sulfur cleavage from the ligand and incorporation into the cluster composition. The growth mechanisms and driving forces behind intercluster transformations were long been a debated

topic in the scientific community. However, the detailed time-tracking of the intermediate species of intercluster conversion showed that the pre-formed Au(I)-thiolate complexes or Au(I)-chalcogenate complexes during reduction in the presence of excess thiol result in the formation of small nanoclusters (I stage).^{143,144} Moreover, stage I is a kinetically controlled growth process which results in the formation of small narrow size distribution of clusters. However, in the second stage (equation 10) the formed clusters coalesce into bigger clusters that are back transformed into more stable ones (thermodynamically controlled size-focusing). Overall, the size-focusing process evolves three distinct modes of cluster growth: isoelectronic addition (equation 9), disproportionation (equation 10) and comproportionation (equation 11) for the formation of Au₂₅ cluster (**Scheme 1**).¹⁴³



Scheme 1 Thermodynamically controlled size-focusing modes observed in Au₂₅ cluster. Reprinted with permission from ref [143]. Copyright (2014) American Chemical Society.

Although, this growth mechanism has not been applied for the size-focusing synthesis of chiral Au₃₈(SR)₂₄ cluster,^{113–116} however one cannot exclude the possibility of similar phenomenon in the synthesis of Au₃₈. Interestingly, while using another thiol ligand for etching/ligand exchange purposes, unusual and unexpected structural conversions can lead to the formation of new clusters with unique geometries. For example, the etching of Au₃₈ with the excess of SPh^tBu (TBBT),^{108,109} S-C-C₅H₉¹¹⁰ and SPh¹¹¹ resulted in the formation of Au₃₆ cluster. Note, Au₃₆(SR)₂₄ cluster crystallizes in fcc-form. It was a debating question whether the fcc-structures can be obtained under nanoscale regime. Because the fcc-structures are typical for bigger counterparts of nanomaterials (plasmonic) and of course bulk, initially it was accepted that the geometrical

variations like hcp, bcp, icosahedron etc. are more energetically favored over fcc. However, the crystal structure of Au₃₆ revealed the first ever fcc-structure in monolayer-protected clusters. Thus, all these results once again proved the uniqueness and universality of size-focusing method for the formation of most stable cluster sizes and to push the limit of typical Brust-Schiffrin method to synthesize unique MNCs with unusual core-geometries.

2.2. Synthesis of copper nanoclusters (CuNCs)

The breakthrough in the field of nanomaterials science starting in early 90s, made possible the synthesis of nanomaterials down to sub-nanometer sizes. Over the last few decades, a massive progress has been registered for mainly noble metals Au and Ag, both in gas phase and in solution, protected by organic and water-soluble ligands. The absolute structure determination made possible the understanding of the formation mechanisms and develop new efficient and effective synthetic protocols for the synthesis of unique functional building blocks. However, despite the extensive research progress in the field of gold and silver nanoclusters, the studies focusing on the preparation and functionalization of other metals like earth abundant copper is still in its infancy.¹⁴⁵ The problem lies in the difficulty of preparing extremely tiny and stable copper nanoparticles and nanoclusters. Copper being in the same group with gold and silver, shares similar properties and can be taken as a viable alternative to expensive and rare metals. Therefore, the synthetic procedures applied for the preparation of gold and silver clusters, were directly applied for the synthesis of copper nanoclusters. Moreover, the modifications and slight changes made in the synthetic methods and reaction conditions helped to successfully overcome the difficulty of preparing and characterizing the atomically precise and stable CuNCs.^{3,5,146}

2.2.1. Template-based synthesis

As mentioned in 2.1.1. the template assisted method later has been also applied for the synthesis of copper nanomaterials.¹⁶

Polymers: Several polymers with various structures as applicable templates were used for the synthesis of CuNCs. However, the first report dates back almost two decades ago with poly(amidoamine), PAMAM polymer templates.¹⁴⁷ The synthesis of the CuNCs consisting of 4 to 64 atoms was performed using fourth generation (G4) PAMAM dendrimers with ethylenediamine core (G4-OH). The reaction was followed by UV-vis, which showed the shift in Cu^{2+} characteristic *d-d* transition in the presence of a template, which on the other hand suggested the incorporation and ligation of copper atoms into the interior of dendrimer. In addition, upon reduction of the pre-formed copper complex, the characteristic UV-vis features disappeared and instead, smooth increase in the absorbance was detected. The exponential-like shape of the spectrum indicated the formation of band-like electronic structure and that the copper atoms are not present in isolated form but rather are clustered inside the polymer with an average diameter less than 1.8 nm based on TEM micrographs.

Polyethyleneimine (PEI) as a template has been used in the synthesis of copper nanoclusters.^{148–152} The group of Hong Qun Luo has established the synthesis method for the preparation of stable and highly fluorescent (QY of 3.8 % in ethanol) clusters with a diameter of 1.8 nm.¹⁴⁸ The synthetic procedure involved the reduction of the aqueous solutions of CuSO_4 and PEI with hydrazine hydrate upon heating at 95 °C for 19 h. The final reaction product had a color of cyan and exhibited blue emission (emission peak maximum at 480 nm) while exciting at 355 nm. Taking the advantage of the unique fluorescent properties of PEI-capped CuNCs, the authors tested its capabilities as a sensor to detect glucose, hydrogen peroxide¹⁴⁸ and Sudan I-IV dyes¹⁴⁹ based on fluorescence quenching. It is well known that the level of glucose, as a key energy source for living organisms, is controlled by insulin-mediated signaling and any perturbation in insulin secretion may result in high levels of blood glucose. The latter can cause type-2 diabetes, metabolic syndrome, hypertension and cardiovascular risk. Moreover, glucose can be oxidized to hydrogen peroxide and gluconic acid catalyzed by Glucose Oxidase (GOx) enzyme. On the other hand, H_2O_2 as a reactive oxygen species (ROS) is crucial for oxidative cellular signaling transductions, it induces intracellular stress and accelerates aging. Hence, the early diagnosis of H_2O_2 can prevent the development of certain diseases. It was shown, that in PEI-capped CuNCs quenching of PL is due to the oxidation of CuNCs by H_2O_2 . Moreover, CuNCs showed selectivity

towards glucose among other carbohydrates. Later, PEI-capped CuNCs were applied for the detection of Sudan I-IV dyes,¹⁴⁹ which are artificial azo dyes that are used in industry and food market for coloring purposes. The interaction mechanism of the CuNCs and Sudan dyes and the quenching effect of emission was explained by Förster resonance energy transfer (FRET).

Another simple synthetic strategy was proposed for the synthesis of water-soluble and biocompatible CuNCs. When functionalized lipoic acid (LA) attached to a tunable length of polyethylene glycol (PEG) segment was used as a template, the reduction with NaBH₄ resulted in the formation of good-quality and highly fluorescent CuNCs (QY of 3.6% in water) with an average size of 2.5 nm.¹⁵³ The examination of CuNCs stability proved that the formed clusters show long-term stability when exposed to daylight and UV irradiation. However, when similar reaction was carried out using both dihydrolipoic acid (DHLLA) and poly(vinylpyrrolidone) (PVP)²³ or just PVP alone¹⁵⁴ as capping agents and ascorbic acid as a reductant, CuNCs with an average size of 1.9 nm were formed.

The synthesis of red fluorescence CuNCs was achieved by using polystyrene sulfonate (PSS)¹⁵⁵ and other multidentate polymers¹⁵⁶ as templating scaffolds.

Proteins: Proteins as structural biomolecules were widely used for the synthesis of versatile and biocompatible CuNCs.^{25,157,166–175,158,176,177,159–165} Among a huge number of accessible proteins, bovine serum albumin (BSA) gained much more attention due to its high-water solubility and an ability to bind various organic and inorganic substances in a noncovalent fashion. Due to the well-defined structure, containing charged amino acids and 35 thiol groups from Cys residues, BSA offers perfect albumin-binding sites for nanocluster formation. The synthesis of CuNCs involves three steps till completion.¹⁷¹ In the first step, upon mixing the reactants, at neutral pH, -COOH carboxylate groups of the protein become partially dissociated and immediately form a complex with Cu²⁺. The coordination complex results in a formation of viscous paste. To enhance the solubility and further reduction with BSA, in the second step of reaction, the pH of the medium needs to be increased up to 12 by adding 1M NaOH under heating at 55 °C. However, as a reducing agent, BSA is relatively weak and to completely reduce Cu²⁺ to metallic copper, long reaction times might be required. Different reducing agents such as hydrogen peroxide,^{164,171,178}

hydrazine hydrate ($\text{N}_2\text{H}_4 \cdot 2\text{H}_2\text{O}$)^{159,160,175} have been proposed to facilitate the last step of the reduction process. For example, the addition of trace amount of hydrogen peroxide not only reduces α -helix of the protein and increases the number of random and δ -structures, but also produces $\bullet\text{OH}$ radicals which can break peptide bonds in BSA and reduce the ordered α -helix structures. Altogether, it will enhance the reduction ability of the protein towards Cu^{2+} and lead to faster cluster formation.¹⁷¹ On the other hand, while using hydrazine hydrate, with decreasing the pH, the α -helix can be transformed to δ -sheets and random coil structures, which are more dominant and produce more functional groups ($-\text{OH}$, $-\text{NH}$ and $-\text{COOH}$) and consequently, became more accessible for the interaction with cluster.¹⁶⁰ As a result, red emissive CuNCs with an average size of 2.4 nm were successfully synthesized.

Other proteins such as trypsin,¹⁵⁸ human serum albumin (HSA),¹⁶⁷ transferrin,¹⁶⁸ papain,¹⁶⁹ cellulase¹⁷⁰ and lysozyme^{159,177} were also reported as an effective capping agent for the preparation of fluorescent copper nanoclusters.

Another blue-emitting CuNCs containing 12 copper atoms were synthesized using human serum albumin (HSA).¹⁶⁷ Several reports proposed the use of CuNCs as a Förster Resonance Energy Transfer (FRET) assay.^{165,167,174} FRET as a nonradiative energy transfer process, is used for analyzing the structural and dynamic changes between two fluorophores, when one of them is being an energy acceptor and the other one acts as a donor. However, FRET is distance dependent ($1/r^6$) and in order to observe such a transfer, the interacting molecules must be in proximity (normally 1-10 nm). In order to study its applicability as a FRET assay, the interaction between donor CuNCs and coumarin 153 (C 153),¹⁶⁷ 2,4,6-trinitrophenol (TNT, picric acid)¹⁶⁵ and cobalt complex¹⁷⁴ as an acceptor has been studied. The PL emission peak of CuNCs was decreased with increasing the concentration of dye indicating the Förster energy transfer in CuNCs protected with HSA/BSA template.

DNA: DNA as a naturally occurring biostructure with variable lengths and sequences have been used for the synthesis of CuNCs.^{179,180,189–191,181–188} Double-stranded DNA (dsDNA) with adjustable sequences and lengths has been considered as a template for the synthesis of fluorescent copper nanoparticles/nanoclusters. It has been shown that the reaction between the dsDNA and copper

salt is completed within few minutes in the presence of ascorbic acid. However, a high metal cation to base ratios were required for the formation of fluorescent nanoclusters. The reason is that at lower concentrations of metal precursor, Cu^{2+} first binds to backbone phosphate groups of DNA via a nonspecific interaction. However, with increasing the concentration, the metallization of high affinity bases is favored. Consequently, the reduction of the pre-formed complex with ascorbic acid leads to the formation of fluorescent CuNCs.¹⁸² Moreover, the order of mixing reagents was found to be crucial for the synthesis. Generally, the copper salt is mixed with the ligand/template in the first step and then later being reduced by the reducing agent. However, in the case of dsDNA, the yield is much higher when first copper salt is reduced with ascorbic acid and then templated inside of DNA.¹⁸⁰ The oxygen atoms (as hard Lewis bases) of phosphodiester groups and nitrogen atoms (relatively strong Lewis bases) of the nucleobases bind to Cu^{2+} and therefore, stabilization of a metal cation inhibits metallization of the template. However, when the salt is first reduced to Cu^+ , it can undergo disproportionation and the formed Cu^0 can occupy and cluster inside the grooves of dsDNA. Consequently, the size of the nanoparticle/nanocluster can be tuned by changing the number of DNA base pairs, i.e. much longer DNA templates resulted in the formation of nanoparticles rather than clusters. However, shorter DNA templates lead to the formation of CuNCS with very low fluorescence intensity. In contrast, the PL properties were improved by increasing the length of DNA strands to some extent.^{183,186} Initially it has been shown that the mismatches in nucleotides in duplex do not lead nanocluster formation whereas complete matches result in the formation of fluorescent nanoclusters.¹⁸⁰ A new research suggested that DNA sequences with certain mutations can successfully template CuNCs and be used as labels for mutation detection¹⁸² and even observe the deletion of entire coding regions (exons) in some genes.¹⁸⁸ PL properties of prepared CuNCs is mismatch dependent and can be used for hot-spot mutation detection. The emission spectra of CuNCs templated with probe DNA and several sequences with mutations in one base pair revealed strong variations in emission intensity. Moreover, not only the length, but also the position of the mutation in the strand played an important role in the PL properties of CuNCs. Thus, CuNCs with fully matched duplex of dsDNA as a fluorescent probe can be used as a label to detect mutations and mismatch discrimination in base pairs in DNA sequences (**Fig. 8**).

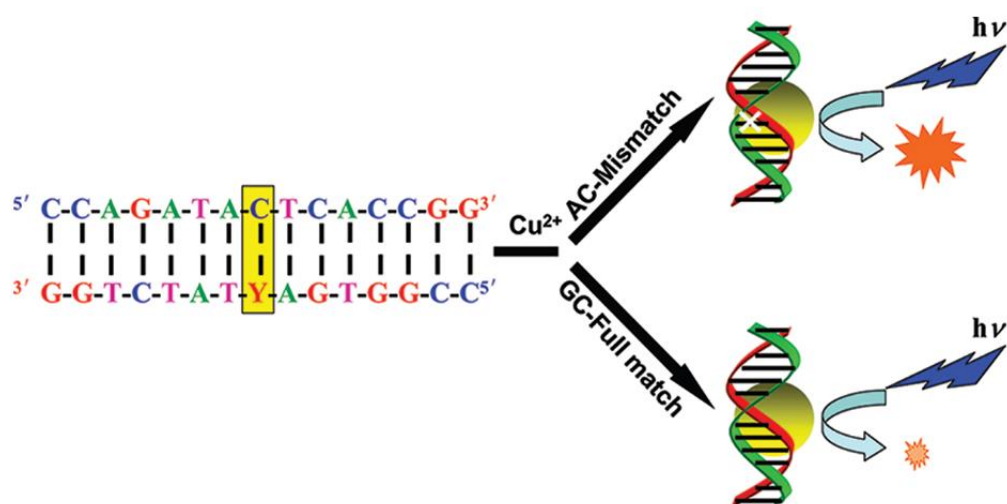


Fig. 8 Schematic representation of detection strategy (Y: SNP site). Reprinted with permission from ref [182]. Copyright (2012) American Chemical Society.

The discrimination of the mismatches or mutations in DNA sequences is especially important for the diagnosis of cancer at earlier stages in patients. Therefore, efficient and biocompatible probes are very much requested.

The absence of grooves and base pairs in single-stranded DNA (ssDNA) excluded the formation of stable CuNCs, however the extensive research in the field showed that highly thymine-dependent sequences of ssDNA can lead to the formation of CuNCs and the red-emissive PL properties can be improved by increasing the number of repeating thymine bases in the sequence.¹⁸⁴ Moreover, specific selections of single-stranded DNA (ssDNA) including random ssDNA, poly(adenine) (polyA), poly(thymine) (polyT), poly(cytosine) (polyC) and poly(guanine) (polyG) have been used for the synthesis of fluorescent copper nanoparticles (CuNPs).¹⁹² It was shown that only polyT-templated CuNPs emitted fluorescence signal at 615 nm under excitation at 340 nm. Moreover, the size of the obtained CuNPs and enhanced fluorescence can be tuned by increasing the length of polyT under the same reaction conditions. Thus, the fluorescent probe based on polyT-templated CuNPs have been used as a practical and applicable oxidase-based biosensor for sensing hydrogen peroxide and glucose,¹⁹³ melamine¹⁹⁴ and alkaline phosphatase

(ALP),¹⁹⁵ the level of which in human serum is associated with several diseases such as hepatitis, prostatic and bone cancer.

2.2.2. Electrochemical synthesis

The electrochemical synthesis method has been widely used for the synthesis of nanomaterials with different sizes and morphologies.¹⁹⁶ The method is based on the electrochemical reduction of copper salt and the deposition on the cathode in a typical electrochemical cell. The size, structure and the morphologies of the nanoparticles can be controlled by changing the applied currents^{197–199} and using different templates within electrolyte solutions.¹⁹⁸ For instance, copper nanorods with the mean transverse diameter of 30 nm and the mean longitudinal length of 400 nm can be synthesized in a two-electrode cell, in which a copper plate as an anode was complemented to platinum cathode.¹⁹⁸

However, the first report on the synthesis of copper nanoclusters using electrochemical method came out in 2010.²⁰⁰ The synthesis of a very small CuNCs was done in a three-electrode conventional electrochemical cell; a copper plate as an anode, a platinum sheet as a cathode and Ag/AgCl as a reference electrode. Cu ions produced from soluble copper anode were reduced and spontaneously formed clusters. Tetrabutylammonium nitrate (TBAN) was used as an electrolyte and protective environment from aggregation and oxidation. Blue emissive CuNCs (QY of 13%) with an average size of 0.61 nm showed molecular-like transitions on the UV-vis spectrum with a large band gap (3.7 eV). The composition of the cluster was confirmed by laser desorption/ionization (LDI)-TOF mass analysis, in which several species of Cu_n with $n \leq 14$ were detected. Recently, a new electrochemical method for the synthesis of CuNCs using TBAN as a scaffold resulted in the selected formation of Cu_{13} clusters²⁰¹ later used for the detection of Pb^{2+} .

2.2.3. Water-in-oil (w/o) microemulsion

Microemulsions, as heterogeneous systems, consisting of two immiscible liquids, where one (dispersed phase) is scattered inside the second phase (dispersing phase), are used as

microreactors for the realization of various chemical processes. Depending of the nature of two liquid phases, mainly two types of emulsions can be described: water-in-oil (*w/o*, reverse micelles) and oil-in-water (*o/w*).²⁰² In *w/o*-type microemulsions the precursor for the nanomaterial to be synthesized is dispersed inside the water droplet where the chemical reduction is taking place. The surfactant molecules tend to form micellar assemblies at *w/o* boundary. Consequently, the size of the water droplets can be varied from few to hundreds of nanometers by changing the surfactants used. Depending on the nature and the structure of surfactant, different types and sizes of micelles can be formed. By controlling the micellar formation, the size and the shape of targeted nanomaterial can be directly regulated. In 1993 French researchers reported the first synthesis of CuNPs in *w/o* microemulsion using NaBH₄ or hydrazine as reducing agents.²⁰³ The effect of the surfactant content inside the microemulsion on the size evolution has been shown^{203,204} and the appearance of a plasmon peak of the formed nanoparticles has been observed.^{203,205} The size of the particles can be tuned from 2-10 nm by increasing the water content. On the other hand, this leads to the pronounced appearance of plasmon peak at 570 nm. The opposite effect has been observed with the change of surfactant content. Also, CuNPs with an average size of 5-15 nm were formed from the reduction of copper salt inside the water droplet surrounded by nonionic surfactants.²⁰⁶ The effect of the amount of reducing agent appeared to drastically influence the formation of the metallic nanoparticles.^{205,207} The size evolution of CuNCs was studied in terms of α parameter, which is defined by the number of reducing agent moles used for the reaction with respect to the stoichiometric amount needed for the reduction of copper cations (**Fig. 9**).²⁰⁷

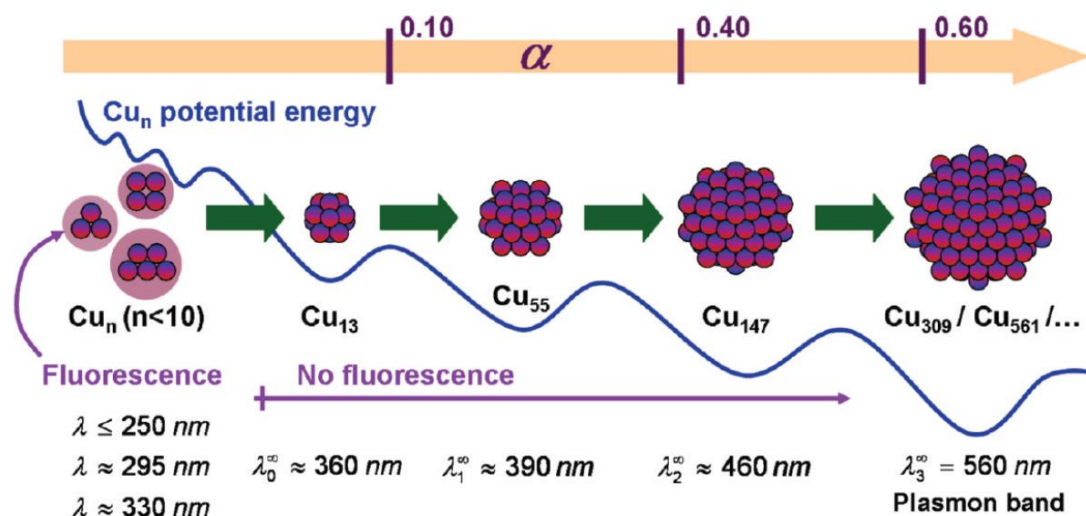


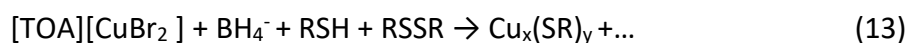
Fig. 9 Schematic representation of copper nanocluster size evolution with increasing the molar percentage (α) of NaBH_4 . The clusters with $n \leq 13$ are fluorescent whereas big particles with $n \geq 309$ show characteristic plasmon resonance band. Reprinted with permission from ref [207]. Copyright (2009) American Chemical Society.

With an increase of NaBH_4 concentration, bigger clusters and finally particles were obtained. The fluorescence studies showed that only the small clusters showed strong PL properties whereas big clusters and nanoparticles showed no emission. Based on the results, several closed shell clusters can be estimated. The first 6 geometric closed shells are 13, 55, 147, 309, 561 and 923 and the formation of clusters with these sizes are directly linked to the concentration of reducing agent. Small Cu_n clusters with $n \leq 13$ atoms, are strongly fluorescent and formed at lower α values, whereas big sizes and nanoparticles form by increasing the α .

2.2.4. Modified Brust-Schiffrin technique

As discussed above in section 2.1.2, Brust-Schiffrin method was extensively used for the preparation of atomically precise gold nanoclusters in large quantities and narrow size distributions. However, the method is not limited to gold nanocluster, and since then has been applied for the synthesis of other metal clusters, in particular copper. The reduction process of the metal solution containing protective ligand as well as the structure and composition of

intermediate species has been described in detail in section 2.1.2. Similarly, [TOA][CuBr₂] complex was formed as an intermediate product in the synthesis of copper nanocluster (equation 12), the reduction of which in the presence of 2-mercapto-5-n-propylpyrimidine (MMP) resulted in the formation of CuNCs:^{74,146,208}



In this case, clusters with $x \leq 8$ compositions were formed and their presence was confirmed by ESI mass spectrometry. Interestingly, it was shown that in the synthesis of dihydrolipoic acid (DHLA) protected stable clusters the choice of a reducing agent is of great importance.²⁰⁹ Cu⁰ species are highly susceptible to oxidation in aqueous solution and thus, NaBH₄ as a strong reducing agent, immediately decomposes in a medium and consequently, does not inhibit the oxidation of the metal. Moreover, hydrazine (N₂H₄) being weaker reducing agent than NaBH₄, decomposes slowly but does not improve the stability of the clusters significantly. While using tetrakis(hydroxymethyl)phosphonium chloride (THPC) as a reducing agent, not only the stability of the DHLA-stabilized cluster increases due to additional interaction with copper core, but also the PL can be tuned from red²⁰⁹ to bright orange emission²¹⁰ depending on the applied reaction conditions. In another case, (3-mercaptopropyl)trimethoxysilane protected copper nanoclusters showed strong red emission in the presence of trace amount of water.²¹¹ The phenomenon known as water triggered bonding induced emission (BIE) has been applied for the detection of water traces in organic solvents due to the polymerization of the silicic acid on the cluster surface. Tannic acid (TA) protected CuNCs have found applications as an on-off-on fluorescent probes for the detection of ascorbic acid in the solutions,²¹² for the determination of phosphate²¹³ and ferric ions²¹⁴ in water solutions. Reductant-free synthesis of D-penicillamine protected CuNCs made possible their important applications as a turn-on fluorescent probe for the detection of hydrogen sulfide²¹⁵ and hydrogen peroxide²¹⁶ in the water as well as for trace amount of Cu²⁺ in polluted water samples.²¹⁷ Other ligands such as cysteine,^{10,218–220} histidine,²²¹ bile acid

derivatives,²²² mercaptobenzoic acid²²³ and dopamine²²⁴ were successfully applied as capping agents for the synthesis of luminescent clusters in a typical Brust-Schiffrin method.

2.2.5. Microwave-assisted polyol synthesis

Recently, a newly developed method known as microwave (MW)-assisted synthesis has been applied for the synthesis of copper nanomaterials.²²⁵⁻²²⁷ The proposed method is based on the use of microwaves as an energy source. The electromagnetic energy is converted into heat which allows the heating of reaction mixture to high temperatures. The advantage of the MW synthesis is based on the homogeneous heating of the sample in a very short period of time.

The first preparation of CuNPs using microwave irradiation was described in 2004.²²⁵ The authors reported the MW-assisted synthesis of CuNCs with an average size of 10 nm in ethylene glycol while NaH₂PO₂*H₂O was used as a reducing agent. The size of the particles could be tuned by changing the molar ratio between copper salt and the reducing agent. The reduction of copper was slower at lower reductant concentrations, leading to the formation of agglomerates. The increase of the molar ratio enhanced the reduction rate, more nuclei were formed and thus, smaller particles. However, the further increase did not affect the size of the particles anymore. A few years later, the synthesis of fluorescent CuNCs with an average size of 2 nm has been successfully performed in an ethylene glycol solution containing metal salt and NaOH.²²⁶ The synthesis of clusters at high temperatures and inert atmosphere lead to the immediate change in solution color from blue to brown indicating the formation of clusters. The successful formation of Cu₉ species was confirmed by MALDI mass spectrometry. It was also shown that high temperatures and a use of a base were essential for the cluster formation. Precisely, the high concentrations of NaOH were necessary to form [Cu(OH)₄]²⁻, [Cu(OCH₂CH₂O)₂]²⁻ and aldehyde from the dehydration of ethylene glycol. Furthermore, the resultant aldehyde can reduce copper ions at higher temperatures. Moreover, during the reduction of copper, ethylene glycol undergoes ethoxylation and forms poly(ethylene)glycol (PEG), which later adsorbs on the surface of CuNCs. The surface passivation restricts the further agglomeration and oxidation of formed clusters.

A. GENERAL INTRODUCTION

Lately, tannic acid protected CuNCs were synthesized under MW irradiation.²²⁷ The mixture of copper salt and tannic acid as both reducing agent and a protective ligand, changed the color from blue to pale yellow upon exposure to MW radiation. Note the longer irradiation times and higher powers resulted in the agglomeration of CuNCs and in the decrease of fluorescence intensity. The prepared cluster was used as a turn-on fluorescence probe for dopamine detection. The addition of Fe (III) quenched the emission, however, 95% of it was recovered after adding the dopamine. Recently BSA-protected CuNCs synthesis has been completed using microwave radiation.¹⁷⁸ The as-prepared clusters have been later applied for the detection of dopamine in serum samples.

3. Characterization of metal nanoclusters

3.1. UV-vis spectroscopy

UV-vis spectroscopy is ubiquitous among modern spectroscopic methods. It has become a method of choice for identification and quantification of inorganic and organic compounds with a wide variety of chromophore structures. Needless to say, UV-vis absorption spectrum is a characteristic optical fingerprint for both qualitative (identification) and quantitative (concentration) analysis for a cluster of interest. Due to the quantum confinement effects, the continuum conduction and valence bands break down into discrete energy levels in clusters (with the sizes smaller than 2 nm). Thus, depending on the size of the cluster core, gold nanoclusters with well-defined compositions can possess characteristic electronic transitions in UV-vis spectrum.²²⁸ Among other characterization methods available in modern labs, the UV-vis spectroscopy is a first aid in clusters' identification process after separation of each individual fraction on size-exclusion column. Combined with theoretical calculations, each electronic transition in UV-vis spectrum can be assigned accordingly. The conversion of the wavelength scale into photon energy, enables the determination of HOMO-LUMO energy gap by extrapolating the absorbance to zero value. Normally, the optical gap gets bigger by decreasing the size of the cluster. For instance, the optical gap for very well-known $\text{Au}_{25}(\text{SR})_{24}$ ^{92,229–232} and $\text{Au}_{38}(\text{SR})_{24}$ ^{113,114,116,229,233,234} is ≈ 1.3 eV and ≈ 0.9 eV, respectively. Moreover, various oxidation states for the same cluster can be distinguished from UV-vis spectrum. For example, Au_{25} can be neutral and charged (both negatively and positively). Although, the charge state of the cluster does not actually change the HOMO-LUMO gap, the intensity of the bands for neutral and charged cluster at lower wavelengths, in particular at 400 nm and 460 nm, varies with obvious color differences in their solutions. Note the solution of neutral Au_{25} is green, whereas charged one is orange reddish. In general, the DFT calculations performed for $\text{Au}_{25}(\text{SR})_{18}^-$ revealed the origin of each electronic transition in UV-vis spectrum.^{35,89} Precisely, the first transition appearing at 1.52 eV corresponds to the intraband sp-sp HOMO-LUMO transition. Second peak at 2.63 eV

is correlated to the mixed intraband ($sp \rightarrow sp$) and interband ($d \rightarrow sp$) transitions. Besides, the last peak at 2.91 eV is purely interband ($d \rightarrow sp$) transition. The contributions from the protective ligand can be seen at higher energies.

Unlike gold nanoclusters, copper nanoclusters do not possess rich absorption features in visible region of the spectrum. The distinct electronic transitions are mostly in UV region governed by the absorption of the protective ligand. Moreover, in CuNCs the high energy absorption at ca. 260–275 nm was assigned as an intraligand (IL) $n(S) \rightarrow \pi^*$ transition.^{235–237} Additionally, CuNCs show moderate absorption in 300–500 nm and strong absorption below 260 nm. This transition arises from ligand- to-metal charge transfer (LMCT).²³⁸

Thus, the UV-vis spectroscopy is an elegant technique to probe the electronic properties of the clusters as a function of their core size and to perform quantitative analysis.

3.2. Circular dichroism

Chirality, as a naturally occurring phenomenon, is described as a geometric property of molecules. Nanomaterials and especially nanoclusters are no exceptions. Some of the atomically precise gold clusters possess chiral properties such as $Au_{28}(TBBT)_{20}$,¹⁰⁵ $Au_{38}(2-PET)_{24}$,^{48,49} $Au_{40}(2-PET)_{24}$,²³⁹ $Au_{102}(2-PET)_{44}$ ¹²⁹ etc. Since different enantiomers of the same chiral compound interact differently with the polarized light, then this phenomenon can be taken as a physical basis to distinguish enantiomers and to determine their absolute configurations. The difference in absorbance between left and right circularly polarized light when passing through the chiral environment is known as a circular dichroism (CD). Moreover, when the UV-vis region of the spectrum is considered, the CD measurements are related to the electronic transitions (ECD). While using the IR light, the vibrational modes of the enantiopure molecules are studied (VCD measurements).

The advances of the analytical separation methods of clusters massively improved their precise and trustworthy physical characterization. Incidentally, the chiroptical measurements of water-soluble clusters protected with biologically active chiral molecules, i.e. GSH,^{47,240} penicillamine,^{52,53} captopril⁹⁴ and other ligands,^{56,241–244} gave rise to strong CD signals. Note that

strong chiroptical features in the large optical window from UV to near IR, have not been observed in the case of big particles and their crude samples. As described in section 1.4 several mechanisms have been proposed for understanding the origin of such a strong CD response such as chiral metal core, chiral footprint and dissymmetrical field.⁴⁵ According to the chiral footprint mechanism, the chirality was originating from the adsorbed chiral ligands,^{245–248} whereas the chiral metal core mechanism considers the origin of chirality in the clusters protected with achiral ligands to be due to the arrangements of achiral ligands in a chiral fashion on a cluster surface.^{48,239} For instance, Au₃₈(2-PET)₂₄ cluster is chiral while achiral 2-PET ligands are passivating the surface of the metallic core. The left-handed cluster (A- Au₃₈(2-PET)₂₄; A: anticlockwise) and the right-handed cluster (C- Au₃₈(2-PET)₂₄; C: counter-anticlockwise) give rise to strong ECD⁴⁸ and VCD signals⁴⁹ in UV-vis (300-800 nm) and IR regions (1200-1700 cm⁻¹), respectively. The signals are perfect mirror images of each other and the calculated anisotropy factors ($\Delta A/A$) at different wavelengths were the highest amongst other chiral clusters.⁴⁷ When comparing the CD signals of Au₃₈ protected with naturally chiral molecules such as GSH and captopril,⁴⁷ it becomes clear, that the CD pattern varies with the ligand although the absorption spectrum did not change much. The cluster core and geometrical structure stayed intact and the differences in their CD responses are due to the combined effect of both intrinsically chiral core and chiral ligand. Moreover, the intensity and the shape of the ECD signals is dependent on the cluster size whereas VCD is mostly a local characteristic and only depends on the conformation of the adsorbed ligand.²⁴⁹ Thus, the VCD signals can be considered as a molecule's own identification fingerprints. However, the total structure information and assignments of the peaks to different vibrational modes cannot be obtained without comparing the experimental and calculated VCD spectra. Since the VCD spectrum is strongly dependent on the conformation of the adsorbed ligand, typical VCD spectrum of the cluster of interest can be changed by changing the nature and the structure of the ligand.

The above-mentioned works show the capacity of the CD techniques as a unique and powerful tool to measure the chiroptical properties and perform conformational studies on the clusters with various protective ligands.

3.3. Transmission electron microscopy

A relatively simple way to obtain the size distribution and the morphology of the nanoscale objects, is to perform microscopic imaging, e.g. TEM. The basic concept relies on the use of electron beam passing through the thin layer of deposited sample on a coated grid. However, the imaging of the small nanoclusters of few nanometers in size, is very challenging. Because of an intense electron beam, the decomposition or even the aggregation of the sample is a challenge. That is why, sometimes the size distribution observed from TEM is not in agreement with the actual size of the cluster. However, this does not throw shade on the importance of the TEM as a microscopic technique. In the beginning of the thiolate-protected gold nanoclusters' era, highly pure and monodisperse clusters were separated from their crude mixtures and detailed spectroscopic characterization revealed the evolution of their properties as a function of the cluster core size. Among other characterization techniques, TEM analysis came in handy to have a clue of their size distribution.^{52,76,123,130,242,250} Although it is impossible to “see” the organic layer around the cluster core in TEM, it gives a hint about the overall core size.

For copper nanocluster, it was even more difficult and challenging to image and obtain the exact size-distribution histograms due to their yet unestablished and sophisticated synthetic protocols towards the preparation of stable clusters.^{171,182,209,214,251–255} In many reported cases the discrepancy of the observed size from TEM microscopic imaging and alternative methods (dynamic light scattering,²³ DOSY^{256,257} etc.) were of a major concern. Nonetheless, it is still a powerful technique to estimate the approximate size of a monodisperse sample and the size distribution of a polydisperse mixtures of clusters.

3.4. X-ray photoelectron spectroscopy

X-ray photoelectron spectroscopy is a surface sensitive analytical technique to analyze the composition, oxidation state and empirical formula of the material being analyzed. The concept is based on the interaction of the core electrons of the sample with an incident X-ray beam. The ejected electrons have characteristic energies for each energy level for every element present in

the sample. Thus, by measuring a survey XPS spectrum of the analyte, a complete picture of the composition and oxidation state can be extracted.²⁵⁸ For AuNCs, the main attention needs to be paid on 4f region of XPS spectrum. Au 4f_{7/2} and 4f_{5/2} have characteristic binding energies at 83.8 and 87.5 eV corresponding to Au⁰.⁷² Any shift from this value is a sign of change in metal's oxidation state. More information on the AuNCs can be obtained by using higher energy X-ray based techniques such as X-ray absorption-edge structure (XANES) and X-ray absorption fine structure (XAFES) in synchrotron facilities.^{258–261}

XPS is extensively used for the CuNCs characterization. Due to the difficulties in preparing and crystallizing stable copper nanoclusters, XPS became a paramount analytical tool to determine the oxidation state of the metal inside the cluster composition. The binding energies of characteristic Cu 2p_{1/2} and Cu 2p_{3/2} appear at 952.3 and 932.3 eV, respectively, which belong to Cu⁰.^{23,154,253,262} However, the binding energy of Cu 2p_{3/2} of Cu⁺¹ is only 0.1 eV apart. Thus, copper appears in a mixed oxidation state (Cu⁺¹ and/or Cu⁰) in the cluster. Moreover, Cu²⁺, typical to all the species having a d⁹ configuration, will show a satellite peak at around 942 eV, and hence, the absence of this signal in survey spectrum will indicate the successful reduction of the copper ion. Depending on the ligand protecting the metallic core, specific elements can also be analyzed. In S 2p spectrum, the presence of a strong peak at 165.7 eV indicates the chemisorption of sulfur on the cluster surface. The peaks at the 284.6, 399.4, 530.9 eV can be assigned to C 1s, N 1s and O 1s, respectively.^{208,214,252,263}

Thus, the composition and the chemical environment of the analyte can be directly checked and analyzed by XPS spectroscopy.

3.5. Infrared spectroscopy

Infrared (IR) spectroscopy is one of the most common and widely employed spectroscopic techniques to determine structures and identify functional groups present in organic and hybrid inorganic materials. It becomes especially handy in characterizing the MNCs. The first indication of the successful anchoring of thiol group on the cluster surface can be inferred by the absence

of characteristic S-H stretching vibrational mode at 2559 cm^{-1} . Other functional groups such as carboxylate and amine can be directly tested and identified. However, IR characterization is not limited to basic spectroscopic analysis, but extends to more sophisticated and complicated *in situ* measurements.²⁴⁹ Although the NIR and mid-IR regions of the spectrum are mostly considered for daily characterization, far-IR can be used to further study metal-S interactions at the interface. For instance, for a series of well-defined gold clusters (Au_{144} , Au_{40} , Au_{38} , Au_{25}) all protected with the same type of ligand (in this case 2-PET), share similar far-IR profiles associated with Au-S vibrations.²⁶⁴ However, depending on the size of the cluster as well as the type of staple motif, Au-S vibrations having characteristic tangential Au(staple)-S(staple) and radial Au(core)-S(staple) modes vary drastically. Not only the intensities are affected but also some shift to lower wavelengths. Thus, with the help of DFT calculations, each vibration of Au-S at the interface can be carefully assigned.

Unlike far-IR region, the mid-infrared region is highly associated with the protective ligand and shows the typical vibrations of the organic chains and indicates the attained ligand conformation on the surface. Moreover, a consistent trend showed that while increasing the length of the alkyl chains (above C_6), the ligand adopts more ordered (anti) conformations, whereas short ligands are more prone to disordering (gauche conformation).²⁶⁵ More importantly, the studies indicated the presence of critical length of the ligand, at which the transformation from trans to gauche takes place.

In general, infrared spectroscopy is a powerful technique to be employed for the better understanding of the structure and interactions at the interface in thiolate-protected clusters.

3.6. Mass spectrometry

Mass spectrometry (MS) is a critical analytical technique not only for the determination of the chemical composition and to check the molecular purity of the cluster but also it opens a large platform to monitor the ligand exchange reactions *in situ* and analyze the intermediate products of such processes at any time. Thus, it gives an insight into reaction mechanisms at nanoscale. Several mass spectrometry techniques based on soft and hard ionization modes, have been used

for the determination of the clusters' composition.^{118,240,266,267} However, most of such analyses were conducted using matrix-assisted laser desorption/ionization (MALDI) and electrospray ionization (ESI). Although MALDI mass spectrometry performed with various organic matrices ([3-(4-tert-butylphenyl)-2-methyl-2-propenylidene]malononitrile as DCTB, 2,5-dihydroxy benzoic acid as DHB and α -Cyano-4-hydroxycinnamic acid as CHCA), is utterly the first choice among others,²⁶⁸ it results in massive fragmentation of the cluster and leads to complicated m/z profile (hard ionization technique). On the contrary, ESI as a soft ionization technique allows analyzing multiply charged clusters and gives clearer mass profiles. Both techniques are well suited for the needs in the cluster field. By choosing a proper MALDI matrix and ionization conditions in ESI, a mass detection of atomically precise AuNCs became a blueprint to assign their compositions and follow reaction dynamics. So far, it was possible to analyze and determine the compositions of clusters having up to several kDa masses.^{47,48,274,76,101,240,269–273} More interestingly, the analysis of mass spectrum at lower mass ranges (meaning the fragmentation peaks) revealed the ionization of high abundance cyclic $\text{Au}_4(\text{SR})_4$ species in all magic-numbered clusters.^{115,118,144,240,266,268,274} The formed tetrameric fragment is believed to be released from staple motifs via intramolecular mechanism.²⁶⁶ Analysis of this cyclic species is especially useful for studying the ligand exchange products of the clusters with mixed ligand shells.²⁶⁸ Other fragments corresponding to the loss of AuSR units are also evident from MALDI. The release of cyclic $\text{Au}_4(\text{SR})_4$ species has also been observed in $\text{Au}_{38}(\text{2-PET})_{24}$ cluster, where additional peak at m/z 9341 was assigned to $\text{Au}_{34}(\text{2-PET})_{19}\text{S}$.¹¹⁸

3.7. Photoluminescence

Photoluminescence (PL) as a molecular property to absorb light of a particular energy and to emit it at much longer wavelengths, is an intriguing phenomenon being a basis of fluorescent microscopy techniques. It is nonetheless to mention the importance of these techniques in modern spectroscopy and biology labs to study the light-matter interactions under biological environments. For that purpose, intrinsic (naturally occurring, e.g. porphyrins) and extrinsic (synthesized, such as organic molecules and quantum dots) fluorophores with high quantum

yields (QYs) have been applied as a dye to detect and label biological specimens and various metal ions/small molecules in contaminated environments.^{14,57,60} However, in the demanding nanotechnology, highly fluorescent but biocompatible and nontoxic dyes are highly requested. After the discovery of monolayer-protected clusters, massive research efforts have been devoted in synthesizing nanomaterial-based fluorophores. Recent progress in that field resulted in the synthesis of various clusters-based fluorophores with high QYs, which are, more importantly, biocompatible.^{13,15,16,20} With respect to gold, copper nanoclusters are more preferred due to stronger PL properties and higher QYs. Moreover, a new phenomenon known as “aggregation induced emission”²⁷⁵ was linked to be responsible of such a strong fluorescence in majority of MNCs.^{4,150,151,163,216,263,276,277} However, a great deal of computational simulations is necessary to understand the origin and the basis of such transitions in the clusters. Perhaps, the situation is relatively “easier” in case of the gold clusters due to the known compositions with atomic precisions. However, it becomes much complicated for CuNCs due to the unresolved structural information. Several attempts were carried out to obtain in-depth understanding of PL fundamentals and mechanisms. TD-DFT calculations on negatively charged $\text{Au}_{25}(\text{SR})_{18}$ cluster showed that several excited state transitions are involved in PL of the cluster.²⁷⁸ Moreover, the transitions are metal core-based and do not involve charge transfer from the ligands. The fluorescence of $\text{Au}_{38}(\text{SR})_{24}$ was predominantly assigned to core-based HOMO-LUMO transition.²⁷⁹ In case of PVP-protected CuNCs the low-energy excitation was associated with ligand-to-metal charge transfer (LMCT), whereas the high-energy excitation could be metal-perturbed intraligand transition. The emission peak was attributed to the metal perturbed intraligand phosphorescence (0.8 μs radiative lifetime).²³ Occasionally, dual-emission was also observed in AuNCs^{280,281} and in CuNCs.^{208,282} The low-energy emission was assigned to the intraband HOMO-LUMO transitions within the sp-band whereas the high-energy emission was attributed to the interband transition from excited states in the sp-band to d-band.

Thus, in-depth understanding of PL mechanisms and corresponding photo physics can be achieved only by having a complete understanding of size-structure-composition-property relationship in MNCs.

3.8. Nuclear magnetic resonance (NMR)

Nuclear magnetic resonance (NMR) spectroscopy is a powerful technique to identify and determine the structures of organic molecules. However, last couple of years it has been frequently used for the analysis of thiolate-protected gold nanoclusters. Although the use of NMR active nuclei (^{13}C , ^1H , ^{19}F , ^{31}P) gives the information of the surrounding ligand, the protons close to the metallic core of the cluster are very much affected and the signals get broader or even lost with increasing the size of the cluster. Nevertheless, this does not interdict the further use of the technique as an important characterization tool in the cluster field. As such, several papers reported the use of 1D and 2D NMR techniques to study the structure and the dynamics of the ligand shell on the cluster surface as well as the reactivity and kinetics of the ligand exchange processes.²⁸³ Multidimensional NMR techniques including total correlation spectroscopy (TOCSY), heteronuclear single-quantum correlation spectroscopy (HSQC) combined with theoretical calculations allowed to fully assign all 22 symmetry unique proton signals in 2D NMR spectrum of $\text{Au}_{102}(\text{p-MBA})_{44}$ cluster.²⁸⁴ The size of the clusters protected with both organic and water-soluble ligands can be directly measured from diffusion ordered NMR spectroscopy (DOSY). The diffusion coefficient of a given cluster dissolved in an appropriate NMR solvent can be obtained and later be used to determine the hydrodynamic radius of the cluster based on Stokes-Einstein equation:

$$r = \frac{k_B T}{6\pi\eta D} \quad (14)$$

where k_B is Boltzmann constant, T is temperature, η is the solvent viscosity and D is the measured diffusion coefficient. The equation implies, that the bigger the size of the cluster is, the slower it will diffuse in the medium. Thus, the hydrodynamic radius should increase with the increase of the cluster size. For example, the measured hydrodynamic radii of $\text{Au}_{25}(\text{2-PET})_{18}$, $\text{Au}_{38}(\text{2-PET})_{24}$ and $\text{Au}_{144}(\text{2-PET})_{60}$ are 1.7, 2.2, and 3.1 nm, respectively.²⁵⁶ The obtained values were close to the actual sizes based on the X-ray structure. On the contrary, for water-soluble $\text{Au}_{102}(\text{2-PET})_{44}$ the hydrodynamic radius was strongly influenced by the counterion present in the aqueous solution.²⁵⁷ The uniqueness of the NMR techniques in cluster research relies on the ability to

distinguish different oxidation states of the same cluster. For instance, $\text{Au}_{25}(\text{2-PET})_{18}^q$ ($q=-1, 0, +1$)^{91,92,232} can be found in oxidized (paramagnetic) and reduced (diamagnetic) forms, and thus have different electron counts. This, on the other hand, will change the resonance structures and properties of the adjacent protons attached to the metal core. In fact, it was shown that the α - CH_2 protons of neutral Au_{25} are shifted ~ 2 ppm down field with respect to negatively charged Au_{25} (3.13 ppm for reduced and 5.17 ppm for oxidized cluster).^{285,286} Careful inspection of the NMR spectrum of Au_{25} cluster allows to differentiate α - and β - CH_2 protons for each binding site of the dimeric staples, marked as “in” and “out”^{286,287} positions in **Fig. 10**.

In total there are 6 “out” positions and 12 “in” binding positions and the proton resonances corresponding to each binding position are different for every oxidation state of the cluster. The performed DFT calculations strongly supported the interpretation and the origin of the proton resonances in terms of the different binding positions. Moreover, based on this concept, the kinetics of the ligand exchange reactions can be *in situ* analyzed by monitoring the integrals of the “out” and “in”

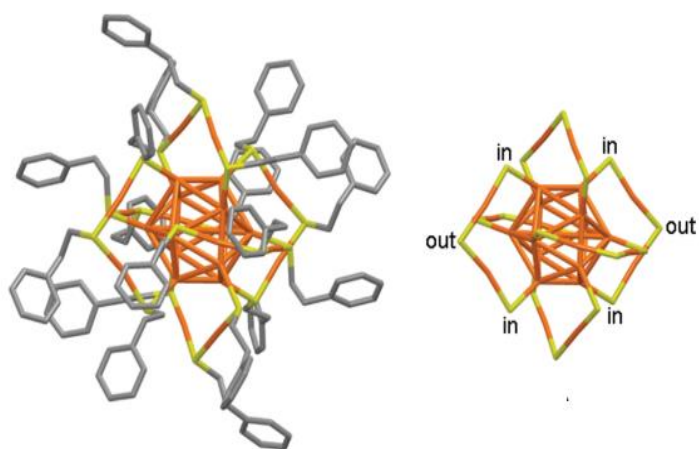


Fig. 10 The structure and the “in” and “out” binding sites of $\text{Au}_{25}(\text{2-PET})_{18}$ clusters. Gold and sulfur atoms are shown in orange and green, respectively. Reprinted with permission from ref [286]. Copyright (2011) American Chemical Society.

positions.^{288,289} The information gained from the kinetic profiles can be further used for the understanding of the ligand exchange reaction mechanisms and the dynamic nature of the protected shell of the cluster on NMR timescales.²⁸⁹ Moving further, combining 2D NMR techniques with excessive calculations showed once again the possible chirality transfer from intrinsically chiral gold core to the protective and yet achiral ligand.^{290,291}

Thus, above-mentioned examples prove the importance of NMR techniques as a sophisticated tool to gain insight into the structure and properties of atomically precise and thiolate-protected metal nanocluster.

3.9. X-ray crystallography

X-ray crystallography is thus far the utmost important and informational technique for the total structure determination of ligand-protected metal clusters. The X-ray structure of the cluster is of paramount importance because it is a key for understanding the stability of the cluster, the construction and the arrangement of the ligands and the origin of unique chiroptical properties. However, the main challenge is to be able to grow high quality crystals from solutions. Technically, the issue is often the small sample quantities due to cost-related problems. Nevertheless, during the last decade, a huge number of crystal structures mostly for gold nanoclusters and relatively less for copper became available. The structure determination of these clusters revealed for the first time the unique binding and the specific arrangement of the ligands on the cluster surface via formation of different staple motifs and bridging of sulfurs (**Fig. 11**).² The first reported crystal structure of a thiolate-protected gold nanocluster was $\text{Au}_{102}(\text{p-MBA})_{44}$ with decahedral structure in early 2007.¹²⁹ The total structure of the cluster can be dissected as a truncated Au_{49} kernel (Marks decahedron). The addition of 15-atom unit to the bottom and top of the Au_{49} kernel, constructs the next Au_{79} kernel. The latter is considered as an outer core level and is protected by five monomeric staples (presented as $\text{Au}(\text{SR})_2$) on each top and bottom sides, nine monomers and two dimers (presented as $\text{Au}_2(\text{SR})_3$) at the waist (**Fig. 12a**). The next reported structure which is to date one of the most studied cluster, is $\text{Au}_{25}(\text{SR})_{18}$ ^{89–91} (**Fig. 12b**). The cluster possesses icosahedral Au_{13} kernel. Total of six dimeric staple motifs are surrounding the icosahedral core along three perpendicular C_2 axes. In case of $\text{Au}_{38}(\text{SR})_{24}$ cluster, the core consists of an Au_{23} kernel, which is formed from the fusion of two icosahedral Au_{13} cores having a common Au_3 face (**Fig. 13**).²⁹²

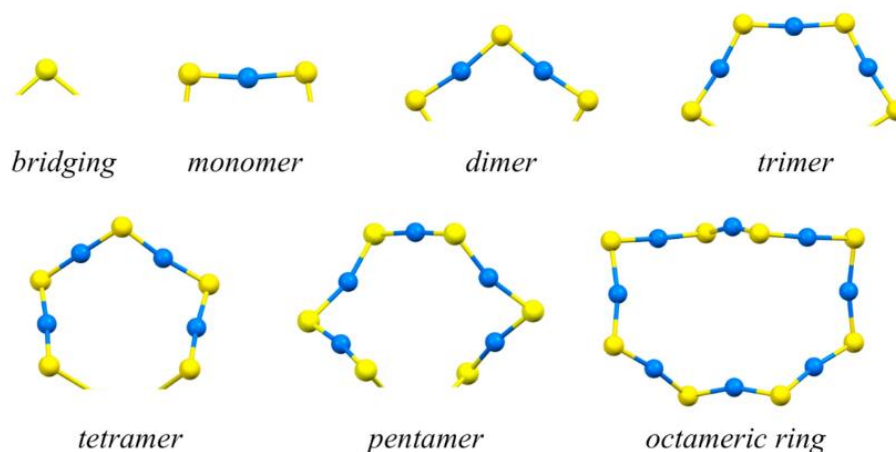


Fig. 11 The structure of all known staple motifs found in $Au_n(SR)_m$ clusters. Sulfur atoms are presented in yellow, the gold atoms on the staple are presented in blue. For clarity the functional R group is omitted. Reprinted with permission from ref [2]. Copyright (2016) American Chemical Society.

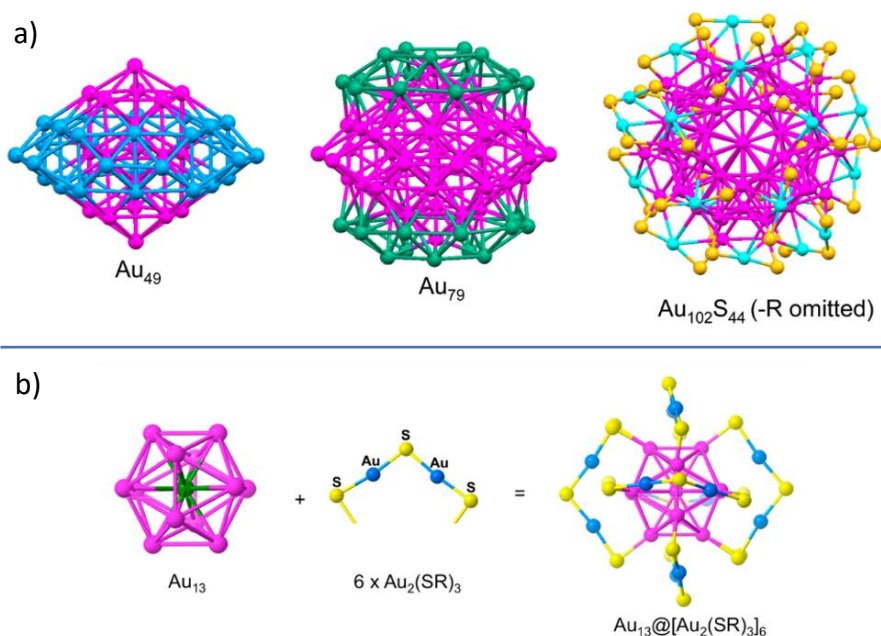


Fig. 12 X-ray structure of a) $Au_{102}(p\text{-MBA})_{44}$ constructed from the kernels and the sulfur atoms of the thiol ligands. Reprinted with permission from ref [129]. Copyright (2007) American Association for the Advancement of Science. b) $Au_{25}(SR)_{18}$ constructed from the Au_{13} kernel and surrounded by six dimeric staple motifs. Reprinted with permission from ref [2]. Copyright (2016) American Chemical Society.

Both the top and the bottom icosahedrons are protected by three dimeric staples whereas three monomeric staples are arranged around the waist. Moreover, the dimeric staples are arranged in a chiral fashion thus making the whole cluster chiral. Two enantiomers of the clusters were found within a single unit cell.

Other geometrical structures of $Au_n(SR)_m$ clusters such as face-centered cubic (fcc), body-centered cubic (bcc) and hexagonal close-packed (hcp) were also reported. For example, the first ever reported fcc-structured cluster of gold was $Au_{36}(SPh-tBu)_{24}$.^{108,111} The cluster consists of a fcc Au_{28} kernel protected by four dimeric staples and twelve simple bridging thiolates. Another example of the fcc-structure is $Au_{28}(SR)_{20}$ cluster.¹⁰⁵ Bcc and hcp structures include $Au_{38}S_2(S-Adm)_{20}$ ²⁹³ and $Au_{18}(SC_6H_{11})_{14}$ ^{79,80} clusters, respectively.

The establishment of synthetic protocols for preparing highly stable and atomically precise copper nanoclusters has not yet been very successful and it became far more challenging to grow high quality crystals. Not surprisingly, there are only finite number of reported crystal structures for atomically precise CuNCs (**Fig. 14**).⁶ The reported spherical and polyhedral crystal structures of copper were retained by performing the synthesis in the presence of phosphine, selenide and to some extent thiol ligands.²⁹⁴ Moreover, all these structures can be classified into several groups based on the constructive

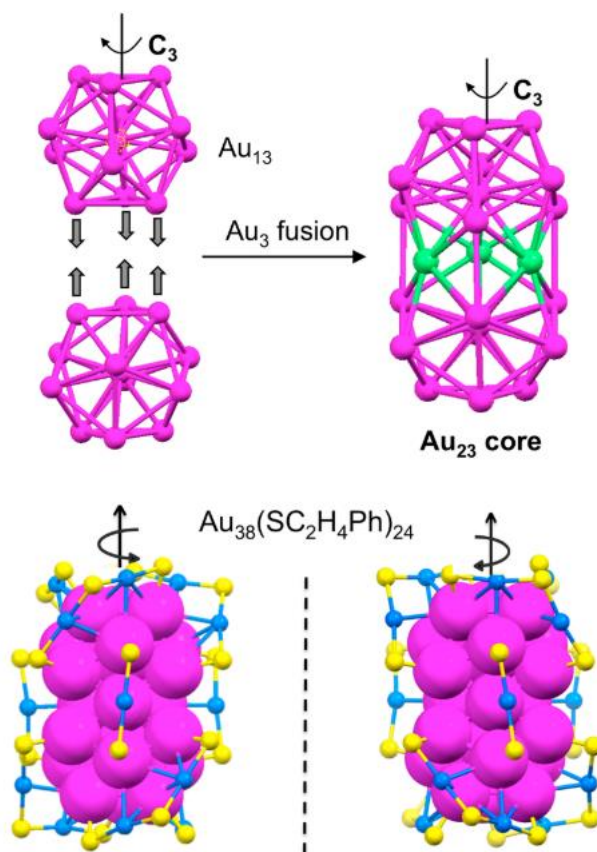


Fig. 13 X-ray structure of $Au_{38}(SR)_{24}$ cluster. The fusion of two Au_{13} icosahedral kernels results in biicosahedral Au_{23} kernel. The arrangement of the dimeric staples on the cluster surface introduces chirality. Sulfur atoms are presented in yellow, the gold atoms on the staple are presented in blue, whereas the ones in the core are colored in magenta. For clarity the functional R group is omitted. Reprinted with permission from ref [292]. Copyright (2010) American Chemical Society.

building block's architecture. For example, $[\text{Cu}_{13}\{\text{S}_2\text{CN}^n\text{Bu}_2\}_6(\text{acetylide})_4]\text{PF}_6$ and $[\text{Cu}_{25}\text{H}_{22}(\text{PPh}_3)_{12}]\text{Cl}$, $[\text{Cu}_{29}\text{Cl}_4\text{H}_{22}(\text{Ph}_2\text{phen})_{12}]\text{Cl}$ clusters consist of Cu_{13} centered-cuboctahedral and icosahedral cores, respectively.^{295–297} $[\text{Cu}_{28}(\text{H})_{15}(\text{S}_2\text{CNR})_{12}]\text{PF}_6$ and $[\text{Cu}_{14}\text{H}_{12}(\text{phen})_6(\text{PPh}_3)_4][\text{Cl}]_2$ consist of tetrahedron Cu_4 core encapsulated inside the copper cage.^{298,299} Hexacapped pseudo-rhombohedral Cu_{14} core, trigonal-bipyramidal $[\text{Cu}_2\text{H}_5]^{3-}$ core as well as Cu_6^{4+} core within the interior of the structure have been reported too.^{294,300–306}

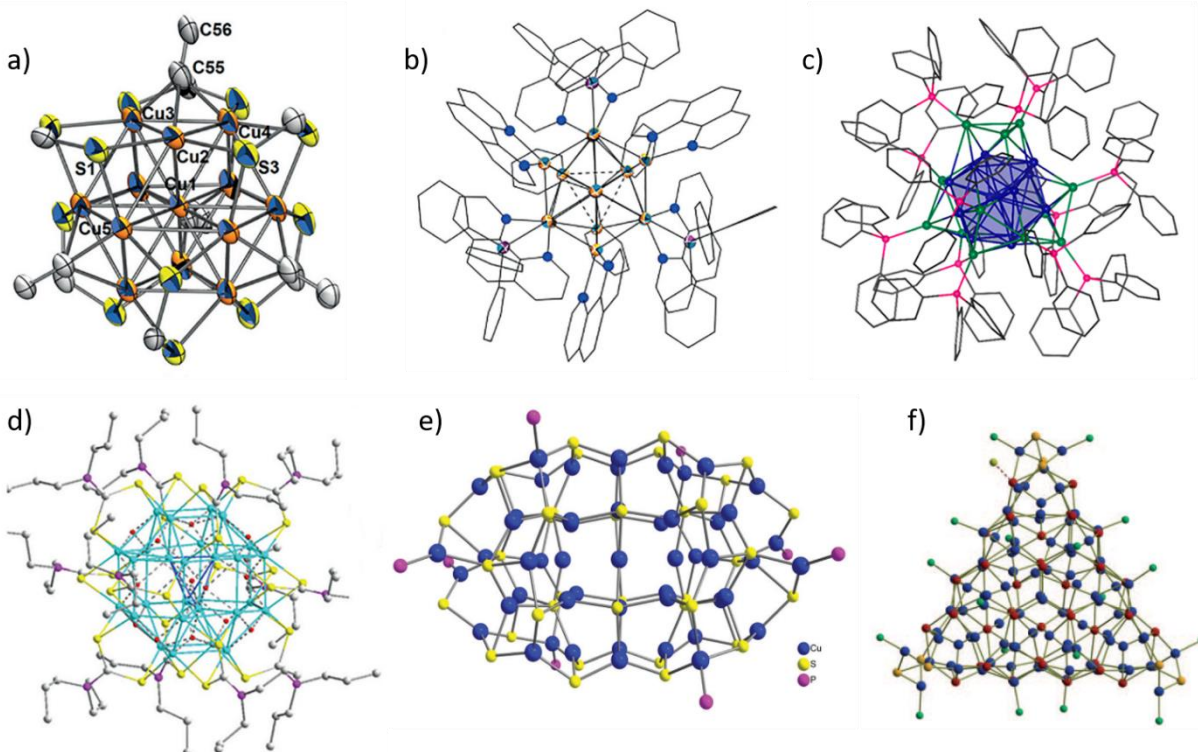


Fig. 14 X-ray structure of a) $[\text{Cu}_{13}\{\text{S}_2\text{CN}^n\text{Bu}_2\}_6(\text{acetylide})_4]\text{PF}_6$ cluster cation constructed from Cu_{13} central cuboctahedron framework. Reproduced with permission from ref [295]. © 2016 Wiley-VCH Verlag GmbH & Co. KGaA, Weinheim. b) $[\text{Cu}_{14}\text{H}_{12}(\text{phen})_6(\text{PPh}_3)_4][\text{Cl}]_2$ constructed from $[\text{Cu}_4]^{4+}$ core. Reproduced with permission from ref [299]. © 2015 WILEY-VCH Verlag GmbH & Co. KGaA, Weinheim. c) $[\text{Cu}_{25}\text{H}_{22}(\text{PPh}_3)_{12}]\text{Cl}$ cluster which has partially $\text{Cu}(0)$ character. Cu_{13} centered-icosahedral core is protected with four $[\text{Cu}(\text{PPh}_3)]_3$ motifs. Reprinted with permission from ref [307]. Copyright (2015) American Chemical Society. d) $[\text{Cu}_{28}(\text{H})_{15}\{\text{S}_2\text{CNPr}_2\}_{12}]$ cluster with a rhombicuboctahedral Cu_{24} core, which is protected with 24 sulfur ligands. Reproduced with permission from ref [298]. © 2014 WILEY-VCH Verlag GmbH & Co. KGaA, Weinheim. e) $[\text{Cu}_{52}\text{S}_{12}(\text{SCH}_2\text{C}_6\text{H}_4^t\text{Bu})_{28}(\text{PPh}_3)_8]$ cluster, for simplicity only the core is shown. Reprinted with permission from ref [304]. Copyright 2016 RSC. f) $[\text{Cu}_{93}\text{Se}_{42}(\text{Se}-\text{C}_6\text{H}_4-\text{SMe})_9(\text{PPh}_3)_{18}]$ cluster. Reproduced with permission from ref [303]. Copyright © 2010 WILEY-VCH Verlag GmbH & Co. KGaA, Weinheim.

4. Size-separation of MNCs

4.1. Size-exclusion chromatography (SEC)

Size-exclusion chromatography was amongst the first analytical methods to apply for obtaining narrow size (shape) distribution of nanomaterials when passing through the compact gel medium with various pore sizes. The SEC separation mechanism of nanomaterials is directly related to their sizes. The bigger particles/clusters elute faster in early fractions since they cannot penetrate the small pores and thus, their progress through the gel is not hindered. In contrary, smaller clusters take longer eluting times, because they can penetrate all the pores of the gel that are bigger than their sizes (**Fig. 15**). Thus, depending on the nature and properties of the nanomaterial, various gels and beads compatible with organic and aqueous solvents can be applied for the SEC separation.³⁰⁸ For example, thiolate-protected noble metal nanoclusters are separated using polystyrene-divinyl-benzene beads (BioRad BioBeads SX series) suspended in organic solvents (THF, DCM and toluene)^{123,242} and silica based gels with water as a flushing eluent.²⁵⁰ The beads normally operate at 400-14000 Da limits with cross linkages from 1-12%. Pore dimensions and exclusion limits are also influenced by the eluant and the maximal expansion of the matrix can be achieved with relatively nonpolar aromatic solvents. This allows the separation of the crude polydisperse sample into distinct bands in the column according to their elution order of decreasing size. Later, each separated band is characterized with UV-vis

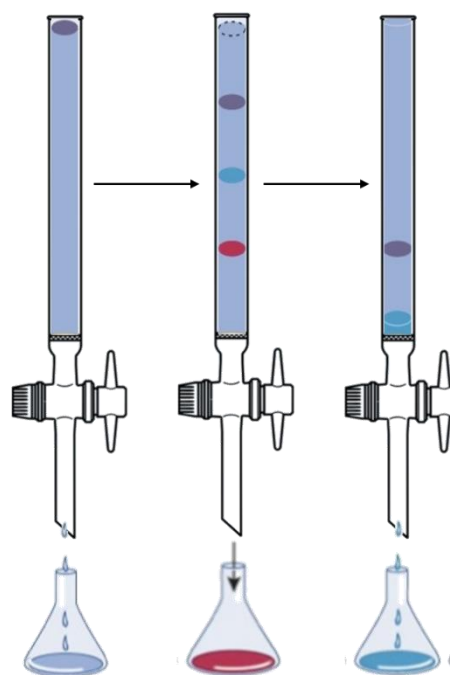


Fig. 15 Schematic representation of SEC separation. Different particles migrate through the gel at different rates.

spectroscopy for example to further compare and establish their sizes and monodispersity of the cluster.

SEC method proved to be an excellent analytical method for the successful separation of atomically precise clusters of gold at a large scale of sample quantities.^{119,309}

4.2. Liquid chromatography (HPLC)

High performance liquid chromatography (HPLC) is considered as one of the most useful and applicable analytical method for the (chiral) separation of clusters with various core sizes.^{48,105,132,271,310–312} The massive progress in analytical platform with the development of advanced HPLC machines and columns (C8, C18, Phenomenex Cellulose 1-5, Phenomenex Amylose 1-3, CHIRALPAK® IA, IB, IC, ID, IE and IF from Daicel Corporation) operating in reverse and normal phases compatible with organic solvents and aqueous medium, readily became available for the separations of gold nanoclusters.^{266,313,314} The first enantio-separation of atomically precise and intrinsically chiral Au₃₈(2-PET)₂₄ cluster has been reported in 2012.⁴⁸ The high-resolution separation of clockwise and anticlockwise enantiomers of the cluster was achieved using chiral Phenomenex Lux-Cellulose-1 column with hexane/IPA (80:20) solvent system as a mobile phase. The online UV-vis detection of the separated enantiomers in the chromatogram showed excellent monodispersity and purity of the clusters for the first time. Moreover, the use of the HPLC technique for the separation of the cluster enantiomers helped afterwards to experimentally prove the origin of strong CD signals in the clusters supported by theoretical calculations. Later, the same separation method has been applied for the separation of Au₄₀(2-PET)₂₄ enantiomers and understanding of the racemization mechanisms and kinetics at relatively higher temperatures with respect to Au₃₈(2-PET)₂₄.²³⁹

Meanwhile, Negishi and co-workers established and introduced the linear and step-gradient methods for the efficient separation of clusters of the same size with mixed ligand shells,^{101,312,315} their corresponding coordination isomers^{312,316–318} and doped species.^{269,270,312,317,319,320} For example, high-resolution separations of Au₂₅(SR₁)_{18-x}(SR₂)_x, Au₂₄Pd(SR₁)_{18-x}(S/SeR₂)_x clusters were

achieved with linear gradient mode.³¹⁵ In this case the separation was due to the differences in polarities of the functional groups in the mixed ligand shell clusters even though the mass difference of the ligands was negligible. When the polarities were not drastically different, the linear gradient mode was not so effective, instead the step-gradient was more efficient. Thus, two different mechanisms play a role in separations of different clusters. In case of linear gradient, upon the continuous change of the mobile phase composition, the clusters are separated according to the order of their surface polarity. In step-gradient mode of separation, the mobile phase is immediately transferred to the composition of the solvent, where the clusters are very much soluble. Thus, the retention of the clusters inside the column is controlled by the partition coefficient.

4.3. Gel electrophoresis (PAGE)

Electrophoresis is a migration of charged molecules/particles under applied electric field.^{321,322} The velocity of the movement is determined by the following equation:

$$v = \mu_e E \quad (15)$$

where v is an ion velocity, μ_e is an electrophoretic mobility and E is an electric field. Each migrating particle under given media has a characteristic constant mobility, which is defined by the electric force and is balanced by its frictional force:

$$F_e = qE, \quad F_f = -fv = -6\pi\eta rv \quad (16)$$

where q is an ion charge, f is the friction coefficient and η is solution viscosity, r is an ion radius and v is an ion velocity. At equilibrium state these two forces are equal in magnitude and the mobility can be directly derived as follows:

$$\mu_e = \frac{q}{6\pi\eta r}, \quad (17)$$

where q is a net charge, r is the Stokes radius of a charged particle (considered as the size of it) and η is the viscosity. Thus, based on equation 17 small, highly charged species have higher

mobility. The electrophoretic mobility depends on buffer viscosity and if the electrophoresis is taking place in the gel, then it also depends on the porosity of the gel. To obtain better separations, electrophoresis is carried out in an anticonvective medium such as a gel matrix. The gel networks constructed from agarose and polyacrylamide are widely used as matrices for horizontal/vertical electrophoresis in slab gels. These matrices act as molecular sieves for separation of molecules based on their size-to-charge ratio. Unlike agarose, the acrylamide-based gels show higher mechanical stability and are chemically inert.

Polymerization and casting of the gel: Polyacrylamide gels are obtained from the polymerization of acrylamide and *N,N'*-methylenebisacrylamide (shortly Bis-acrylamide). Bis-acrylamide serves as a cross-linker agent for the gel. The polymerization is initiated by the addition of *N,N,N',N'*-tetraethylmethylenediamine (TEMED) as a catalyst along with freshly prepared ammonium persulfate (APS) as an initiator (**Fig. 16**). The foremost advantage of polyacrylamide gel matrix is the control of the gel porosity and hardness by changing the mass-volume percentage (*T*) and proportion of crosslinker (*C*) of acrylamide and Bis-acrylamide (equation 18).

$$T = \frac{m(\text{acrylamide}) + m(\text{Bis - acrylamide})}{\text{Total volume}} \times 100\% \quad (18)$$

$$C = \frac{m(\text{Bis - acrylamide})}{m(\text{acrylamide}) + m(\text{Bis - acrylamide})} \times 100\%$$

The amount of crosslinking of a gel determines the size of the pores in the matrix, which in turn, controls the size of the molecules that can pass through the gel. So, as the concentration of acrylamide (*T*, %) in the gel increases, the pore size in the gel gets smaller and larger molecules are excluded from migrating through the gel. Thus, by adjusting the *T* and *C* parameters, polydisperse nanoparticles and nanoclusters can be separated successfully in a single run. Moreover, the external conditions for polymerization need to be taken into consideration as well. For example, the temperature control is critical for the reproducibility of gel. The polymerization reaction on the other hand is exothermic and combined with the external temperature, drives the onward reaction faster.

A. GENERAL INTRODUCTION

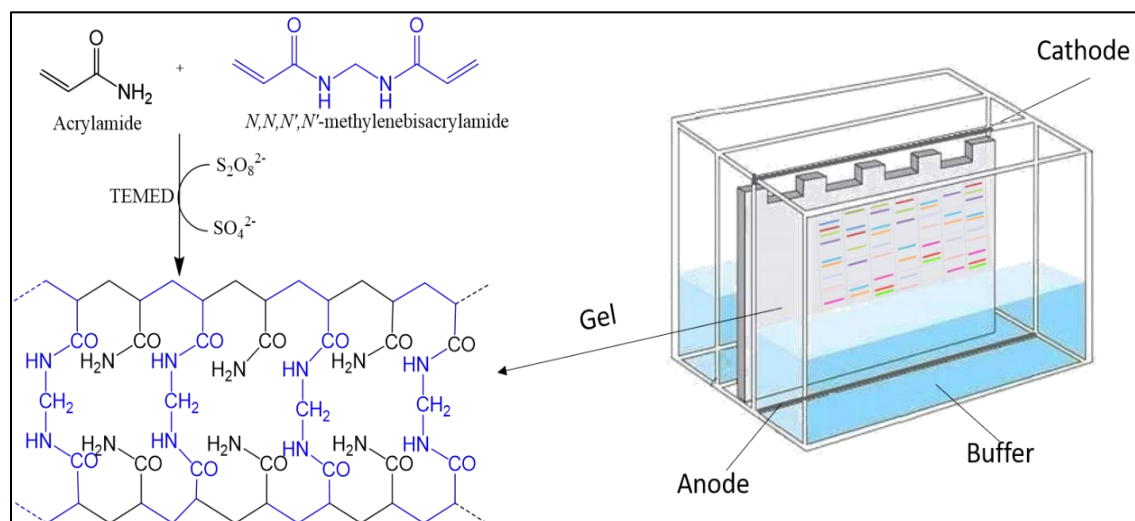


Fig. 16 Schematic representation of the PAGE-separation of the charged particles.

The mechanical properties of the gel depend drastically on temperature. If the polymerization is carried out at low temperature (0-4 °C), then it results in turbid and inelastic gel. Quite contrary, gels prepared at 25 °C are less porous, more transparent and more elastic. Other experimental parameters such as the applied voltage, the pH and the concentration of the running buffer must be taken into account. Note that although higher voltages will reduce the running and separation time drastically, it will increase the amount of generated heat and will reduce the resolution of the separated peaks. The pH of the buffer should be considerably neutral or basic in order to avoid the hydrolysis of the charged sample (in case of negatively charged sample). The buffer is the main supply for ions to carry the current and to maintain the variation of pH minimal. If the loaded charged sample is subjected to changing pH it will not be separated properly. Thus, depending on the chemical properties of the sample, different buffers can be used for PAGE, such as Tris/Acetate/EDTA (TAE), Tris/Borate/EDTA (TBE), Tris/glycine etc.

Almost two decades ago the first report on the separation of glutathione-capped gold cluster came out showing the significance and importance of PAGE as an analytical separation technique not only for biological molecules but also for relatively new and unique noble clusters. The slight modifications in the experimental conditions for gel casting including the concentrations of monomers (acrylamide/bis-acrylamide) changing from low-density gels (20% T and 7.5% C) to high-density gels (24% T and 7% C), Au-GSH clusters with well-defined compositions can be

separated according to their mass-to-charge ratios.^{76,240,272,274} More importantly, it was shown that the high-resolution PAGE separations resulted in the instant separation of the compounds with the same core sizes differing only in one or few GSH ligands adsorbed on the surface. Using enantiopure *D/L* penicillamine,^{52,53} *N*-Isobutyryl-cysteine,⁵⁶ the synthesis and further separations were succeeded with PAGE of total contents of the acrylamide monomers of 3% (acrylamide/Bis, 94:6) and 25% (acrylamide/Bis, 93:7) for the stacking and resolving gels, respectively. Much bigger Au₁₀₂(*p*-MBA)₄₄ conjugated with DNA was separated from the crude mixture using SDS-PAGE method in TBE buffers.²⁷³

4.4. Capillary electrophoresis (CE)

As discussed above, the electrophoresis is a differential movement of charged species. In case of CE, the ionized species move across the anti-convective gel-free narrow capillaries (normally made of fused silica, FS).^{323,324} However, unlike PAGE, additional forces and physical effects contribute to the basic expression of electrophoresis equation. The main difference between CE with PAGE is that the driving force for CE is electroosmotic flow (EOF) which arises on the walls of capillary tube due to the applied electric field (equation 19). It also determines the time ions migrate from the start point until they reach to the detector window.

$$\mu_{EOF} = \frac{\varepsilon\xi}{4\pi\eta} \quad (19)$$

where μ_{eEOF} is the EOF mobility, ξ is the zeta potential, ε is the solution dielectric constant. The migration time and experimental parameters can be used to calculate the mobility of the injected analyte:

$$\mu_a = \mu_{eff} + \mu_{EOF} = \frac{I}{t_a E} = \frac{IL}{t_a V} \quad (20)$$

$$\mu_{eff} = \alpha_i \mu_e$$

where V is the applied voltage, l is the effective capillary length (until the detector), L is the total capillary length, t_a is the analyte's migration time, E is the electric field and μ_a is the analyte's mobility. Under applied experimental conditions, mostly all capillary walls possess electric charge and in case of FS capillaries, the EOF is strongly controlled by silanol groups. Since the charge is strongly pH-dependent, the magnitude of EOF is also strongly pH-dependent. At basic conditions the silanol groups are deprotonated and EOF is significantly greater. In contrast, at low pH silanol groups become protonated and thus EOF is reduced. One advantage of EOF is the flat flow profile throughout the capillary. The flow profile is uniformly distributed along the capillary length and the flow rate is constant at most. Thus, no peak broadening is expected. This is in contrast to HPLC-based separations, where the flow profile is pressure-driven and yields in laminar flow. Another benefit of EOF is that all charged species and even neutrals are migrating in the same direction (Fig. 17).

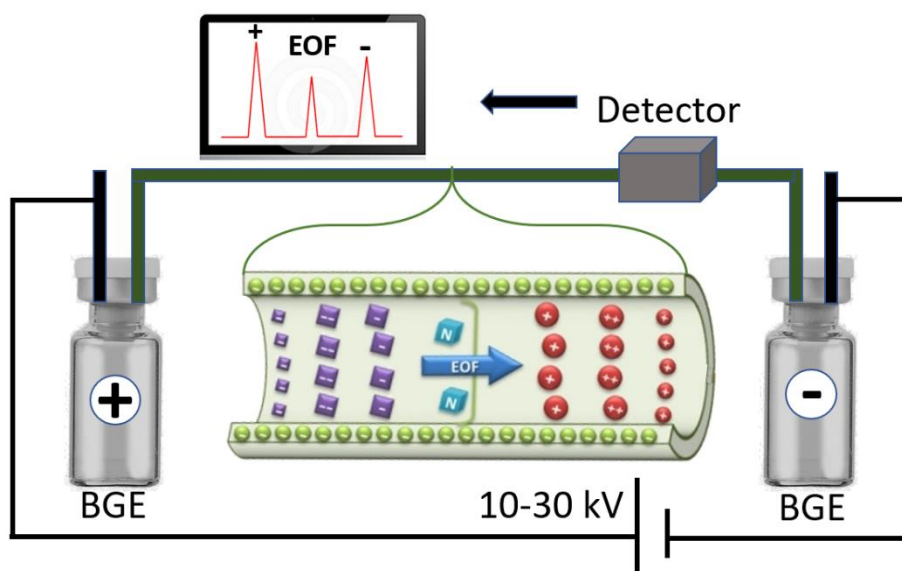


Fig. 17 Schematic representation of CE separation technique.

When the capillary surface is negatively charged, the flow is from anode to cathode (positive detection mode). Anions are attracted towards anode; however, they will be pushed towards the cathode since the magnitude of EOF is much greater than their effective electrophoretic mobility. Cations migrate faster since they have the same migration directionality as the EOF. Neutral species cannot be separated but they are still carried with EOF. Thus, the order of detected

species in electropherogram will be positively charged, neutrals (associated with EOF) and negatively charged species. High quality separation profiles can be observed after carefully considering several CE aspects. Basically, the rate of EOF can be modified by changing the electric field or pH. Firstly, by lowering the applied electric field, the EOF will be decreased and as a result, the analysis time, separation efficiency and the resolution of peaks will be affected accordingly. Secondly, low pH buffers or high pH buffers are avoided to use, since they will lead protonation/deprotonation of both capillary surface and possibly solute. Additionally, the concentration and ionic strength of the buffer can be very crucial for CE separations, since high concentration of buffer generates Joule heat within capillaries. Lastly, EOF can be controlled by modification of capillary walls. The change of capillary wall charge can decrease or even reverse EOF, thus anions and cations can migrate in opposite directions.

The detection (UV-vis, fluorescence) of the separated eluents is achieved through the transparent “window” obtained by burning or scraping off the coating on the capillary tube. CE technique has several separation modes depending on the physical-chemical properties of the injected sample, such as capillary zone electrophoresis (CZE), micellar electrokinetic chromatography (MEKC), capillary electrochromatography (CEC), capillary isoelectric focusing (CIEF), capillary gel electrophoresis (CGE) and capillary isotachopheresis (CITP). However, the most applicable operational mode is CZE, where the charged species are separated under high electric field inside the capillary filled with buffer called background electrolyte (BGE).

Capillary electrophoresis (CE) provides a great analytical platform for the separation of MNCs based on their size, shape and charge. CE technique coupled with mass spectrometry and Taylor Dispersion Analysis (TDA), was extensively used for the separation and size determination of various nanoparticles including gold and silver.³²⁵ MEKS and CZE modes were utilized for the CE-separation of spherical hydrophilic gold nanoparticles in 70 mM surfactant SDS with 10 mM CAPS buffer at pH 10³²⁶ and 6 mM sodium acetate with acetic acid adjusted to pH 5,³²⁷ respectively. It allowed the separation of spherical AuNPs with the sizes varying by two orders of magnitude. The electrophoretic mobility of the migrating particle was directly proportional to its size. Not only the particles were separated according to their sizes, but also the separation of different shaped particles in a single run could be achieved.

As such, several experimental parameters have been adjusted prior to the separation of polydisperse AuNCs.^{328–331} Firstly, the study of the concentration of buffer from 10 mM to 50 mM showed a strong effect on the magnitude of EOF. As mentioned above, the increase of buffer concentration reduces the thickness of the double layer, which on the other hand reduces the zeta potential and thus reduces EOF. Depending on the size of AuNCs, under these circumstances, a longer migration times are observed. However, the longer it takes for the clusters to migrate through the capillary, the better is the resolution of the separated AuNCs peaks.³²⁸ Unfortunately, depending on the chemical properties of the protective ligand and the balance between protonated/deprotonated species within BGEs, in some cases certain high concentrations lead to the aggregation of the AuNCs.

Secondly, since the zeta potential is determined by the charge accumulated on the capillary wall, and the charge is strongly pH-dependent, the highly resolved separations of negatively charged AuNCs can be achieved by optimizing the basic pH value.^{328,330} For example, at $\text{pH} < 10$ the dissociation of Si-OH groups on the capillary surface drastically increases the zeta potential and thus the EOF. Nevertheless, at $\text{pH} > 10$ the dissociation of silanol groups becomes saturated and does not control the magnitude of EOF anymore. The repulsion of the huge amount of negative charge accumulated on the capillary wall and the negative charge carried by the clusters pushes them towards the anode and thus increasing the migration time.

Lastly, the high-performance separations of AuNCs in CE have been achieved by varying the amount of the organic solvent loaded.³²⁸ In fact, this is due to the change in viscosity and dielectric constant of the medium that can control the speed of EOF according to the equation 19. The increase of organic solvent in the buffer causes the diffusion layer to become compressed and therefore, the zeta potential and EOF decrease drastically.

Thus, as an effective and reliable analytical separation technique, capillary electrophoresis provides an alternative fast and cost-effective separation and online characterization of nanomaterials of varying size, shape and compositions.

References

- (1) Chakraborty, I.; Pradeep, T. Atomically Precise Clusters of Noble Metals: Emerging Link between Atoms and Nanoparticles. *Chem. Rev.* **2017**, *117* (12), 8208–8271.
- (2) Jin, R.; Zeng, C.; Zhou, M.; Chen, Y. Atomically Precise Colloidal Metal Nanoclusters and Nanoparticles: Fundamentals and Opportunities. *Chem. Rev.* **2016**, *116* (18), 10346–10413.
- (3) Sharma, S.; Chakrahari, K. K.; Saillard, J.-Y.; Liu, C. W. Structurally Precise Dichalcogenolate-Protected Copper and Silver Superatomic Nanoclusters and Their Alloys. *Acc. Chem. Res.* **2018**, *51* (10), 2475–2483.
- (4) Maity, S.; Bain, D.; Patra, A. Engineering Atomically Precise Copper Nanoclusters with Aggregation Induced Emission. *J. Phys. Chem. C* **2019**, *123* (4), 2506–2515.
- (5) Das, N. K.; Mukherjee, S. Size-Controlled Atomically Precise Copper Nanoclusters: Synthetic Protocols, Spectroscopic Properties and Applications. *Phys. Sci. Rev.* **2018**, *3* (11), 1–22.
- (6) Liu, X.; Astruc, D. Atomically Precise Copper Nanoclusters and Their Applications. *Coord. Chem. Rev.* **2018**, *359*, 112–126.
- (7) Nishigaki, J.; Tsunoyama, R.; Tsunoyama, H.; Ichikuni, N.; Yamazoe, S.; Negishi, Y.; Ito, M.; Matsuo, T.; Tamao, K.; Tsukuda, T. A New Binding Motif of Sterically Demanding Thiolates on a Gold Cluster. *J. Am. Chem. Soc.* **2012**, *134* (35), 14295–14297.
- (8) Maity, P.; Takano, S.; Yamazoe, S.; Wakabayashi, T.; Tsukuda, T. Binding Motif of Terminal Alkynes on Gold Clusters. *J. Am. Chem. Soc.* **2013**, *135* (25), 9450–9457.
- (9) Galchenko, M.; Black, A.; Heymann, L.; Klinke, C. Field Effect and Photoconduction in Au₂₅ Nanoclusters Films. *Adv. Mater.* **2019**, *31* (18), 1900684.
- (10) Basu, K.; Paul, S.; Jana, R.; Datta, A.; Banerjee, A. Red-Emitting Copper Nanoclusters: From Bulk-Scale Synthesis to Catalytic Reduction. *ACS Sustain. Chem. Eng.* **2019**, *7* (2), 1998–2007.
- (11) Fang, J.; Zhang, B.; Yao, Q.; Yang, Y.; Xie, J.; Yan, N. Recent Advances in the Synthesis and Catalytic Applications of Ligand-Protected, Atomically Precise Metal Nanoclusters. *Coordination Chemistry Reviews*. Elsevier B.V. September 2016, pp 1–29.
- (12) Li, G.; Jin, R. Atomically Precise Gold Nanoclusters as New Model Catalysts. *Acc. Chem. Res.* **2013**, *46* (8), 1749–1758.
- (13) Zheng, Y.; Lai, L.; Liu, W.; Jiang, H.; Wang, X. Recent Advances in Biomedical Applications of Fluorescent Gold Nanoclusters. *Adv. Colloid Interface Sci.* **2017**, *242*, 1–16.

- (14) Chen, L.-Y.; Wang, C.-W.; Yuan, Z.; Chang, H.-T. Fluorescent Gold Nanoclusters: Recent Advances in Sensing and Imaging. *Anal. Chem.* **2015**, *87* (1), 216–229.
- (15) Liu, M.; Tang, F.; Yang, Z.; Xu, J.; Yang, X. Recent Progress on Gold-Nanocluster-Based Fluorescent Probe for Environmental Analysis and Biological Sensing. *J. Anal. Methods Chem.* **2019**, *2019*, 1–10.
- (16) Wang, Z.; Chen, B.; Rogach, A. L. Synthesis, Optical Properties and Applications of Light-Emitting Copper Nanoclusters. *Nanoscale Horizons* **2017**, *2* (3), 135–146.
- (17) Kaur, N.; Aditya, R. N.; Singh, A.; Kuo, T.-R. Biomedical Applications for Gold Nanoclusters: Recent Developments and Future Perspectives. *Nanoscale Res. Lett.* **2018**, *13* (1), 302.
- (18) Mathew, A.; Pradeep, T. Noble Metal Clusters: Applications in Energy, Environment, and Biology. *Part. Part. Syst. Charact.* **2014**, *31* (10), 1017–1053.
- (19) Goswami, N.; Zheng, K.; Xie, J. Bio-NCs – the Marriage of Ultrasmall Metal Nanoclusters with Biomolecules. *Nanoscale* **2014**, *6* (22), 13328–13347.
- (20) Guo, Y.; Cao, F.; Lei, X.; Mang, L.; Cheng, S.; Song, J. Fluorescent Copper Nanoparticles: Recent Advances in Synthesis and Applications for Sensing Metal Ions. *Nanoscale* **2016**, *8* (9), 4852–4863.
- (21) Hu, X.; Liu, T.; Zhuang, Y.; Wang, W.; Li, Y.; Fan, W.; Huang, Y. Recent Advances in the Analytical Applications of Copper Nanoclusters. *TrAC Trends Anal. Chem.* **2016**, *77*, 66–75.
- (22) Li, Q.; Pan, Y.; Chen, T.; Du, Y.; Ge, H.; Zhang, B.; Xie, J.; Yu, H.; Zhu, M. Design and Mechanistic Study of a Novel Gold Nanocluster-Based Drug Delivery System. *Nanoscale* **2018**, *10* (21), 10166–10172.
- (23) Ghosh, R.; Goswami, U.; Ghosh, S. S.; Paul, A.; Chattopadhyay, A. Synergistic Anticancer Activity of Fluorescent Copper Nanoclusters and Cisplatin Delivered through a Hydrogel Nanocarrier. *ACS Appl. Mater. Interfaces* **2015**, *7* (1), 209–222.
- (24) Dutta, A.; Goswami, U.; Chattopadhyay, A. Probing Cancer Cells through Intracellular Aggregation-Induced Emission Kinetic Rate of Copper Nanoclusters. *ACS Appl. Mater. Interfaces* **2018**, *10* (23), 19459–19472.
- (25) Gao, F.; Cai, P.; Yang, W.; Xue, J.; Gao, L.; Liu, R.; Wang, Y.; Zhao, Y.; He, X.; Zhao, L.; et al. Ultrasmall [⁶⁴Cu]Cu Nanoclusters for Targeting Orthotopic Lung Tumors Using Accurate Positron Emission Tomography Imaging. *ACS Nano* **2015**, *9* (5), 4976–4986.
- (26) Walter, M.; Akola, J.; Lopez-Acevedo, O.; Jadzinsky, P. D.; Calero, G.; Ackerson, C. J.; Whetten, R. L.; Gronbeck, H.; Hakkinen, H. A Unified View of Ligand-Protected Gold Clusters as Superatom Complexes. *Proc. Natl. Acad. Sci.* **2008**, *105* (27), 9157–9162.
- (27) Häkkinen, H. Ligand-Protected Gold Nanoclusters as Superatoms—Insights from Theory and Computations. In *Frontiers of Nanoscience*; Elsevier Ltd, 2012; Vol. 3, pp 129–157.

- (28) Lin, Z.; Slee, T.; Mingos, D. M. P. A Structural Jellium Model of Cluster Electronic Structure. *Chem. Phys.* **1990**, *142* (2), 321–334.
- (29) Martin, T. P.; Bergmann, T.; Goehlich, H.; Lange, T. Shell Structure of Clusters. *J. Phys. Chem.* **1991**, *95* (17), 6421–6429.
- (30) Häkkinen, H. Electronic Shell Structures in Bare and Protected Metal Nanoclusters. *Adv. Phys. X* **2016**, *1* (3), 467–491.
- (31) Tofanelli, M. A.; Salorinne, K.; Ni, T. W.; Malola, S.; Newell, B.; Phillips, B.; Häkkinen, H.; Ackerson, C. J. Jahn–Teller Effects in Au₂₅(SR)₁₈. *Chem. Sci.* **2016**, *7* (3), 1882–1890.
- (32) Lopez-Acevedo, O.; Tsunoyama, H.; Tsukuda, T.; Häkkinen, H.; Aikens, C. M. Chirality and Electronic Structure of the Thiolate-Protected Au₃₈ Nanocluster. *J. Am. Chem. Soc.* **2010**, *132* (23), 8210–8218.
- (33) De Heer, W. A. The Physics of Simple Metal Clusters: Experimental Aspects and Simple Models. *Rev. Mod. Phys.* **1993**, *65* (3), 611–676.
- (34) Baletto, F.; Ferrando, R. Structural Properties of Nanoclusters: Energetic, Thermodynamic, and Kinetic Effects. *Rev. Mod. Phys.* **2005**, *77* (1), 371–423.
- (35) Jin, R. Quantum Sized, Thiolate-Protected Gold Nanoclusters. *Nanoscale* **2010**, *2* (3), 343–362.
- (36) Varnavski, O.; Ramakrishna, G.; Kim, J.; Lee, D.; Goodson, T. Critical Size for the Observation of Quantum Confinement in Optically Excited Gold Clusters. *J. Am. Chem. Soc.* **2010**, *132* (1), 16–17.
- (37) Zhou, M.; Zeng, C.; Chen, Y.; Zhao, S.; Sfeir, M. Y.; Zhu, M.; Jin, R. Evolution from the Plasmon to Exciton State in Ligand-Protected Atomically Precise Gold Nanoparticles. *Nat. Commun.* **2016**, *7* (1), 13240.
- (38) Kothalawala, N.; Lee West IV, J.; Dass, A. Size-Dependent Molecule-like to Plasmonic Transition in Water-Soluble Glutathione Stabilized Gold Nanomolecules. *Nanoscale* **2014**, *6* (2), 683–687.
- (39) Schaaff, T. G.; Whetten, R. L. Giant Gold–Glutathione Cluster Compounds: Intense Optical Activity in Metal-Based Transitions. *J. Phys. Chem. B* **2000**, *104* (12), 2630–2641.
- (40) Garzón, I. L.; Reyes-Nava, J. A.; Rodríguez-Hernández, J. I.; Sigal, I.; Beltrán, M. R.; Michaelian, K. Chirality in Bare and Passivated Gold Nanoclusters. *Phys. Rev. B* **2002**, *66* (7), 073403.
- (41) Garzón, I. L.; A; Beltrán, M. R.; González, G.; Gutiérrez-González, I.; Michaelian, K.; Reyes-Nava, J. A.; Rodríguez-Hernández, and J. I. Chirality, Defects, and Disorder in Gold Clusters. *Eur. Phys. J. D - At. Mol. Opt. Phys.* **2003**, *24* (1–3), 105–109.
- (42) Román-Velázquez, C. E.; Noguez, C.; Garzón, I. L. Circular Dichroism Simulated Spectra of

- Chiral Gold Nanoclusters: A Dipole Approximation. *J. Phys. Chem. B* **2003**, *107* (44), 12035–12038.
- (43) Hidalgo, F.; Sánchez-Castillo, A.; Garzón, I. L.; Noguez, C. First-Principles Calculations of Circular Dichroism of Ligand-Protected Gold Nanoparticles. *Eur. Phys. J. D* **2009**, *52* (1–3), 179–182.
- (44) Noguez, C.; Sánchez-Castillo, A.; Hidalgo, F. Role of Morphology in the Enhanced Optical Activity of Ligand-Protected Metal Nanoparticles. *J. Phys. Chem. Lett.* **2011**, *2* (9), 1038–1044.
- (45) Noguez, C.; Garzón, I. L. Optically Active Metal Nanoparticles. *Chem. Soc. Rev.* **2009**, *38* (3), 757.
- (46) Knoppe, S.; Bürgi, T. Chirality in Thiolate-Protected Gold Clusters. *Acc. Chem. Res.* **2014**, *47* (4), 1318–1326.
- (47) Xu, Q.; Kumar, S.; Jin, S.; Qian, H.; Zhu, M.; Jin, R. Chiral 38-Gold-Atom Nanoclusters: Synthesis and Chiroptical Properties. *Small* **2014**, *10* (5), 1008–1014.
- (48) Dolamic, I.; Knoppe, S.; Dass, A.; Bürgi, T. First Enantioseparation and Circular Dichroism Spectra of Au₃₈ Clusters Protected by Achiral Ligands. *Nat. Commun.* **2012**, *3* (1), 798.
- (49) Dolamic, I.; Varnholt, B.; Bürgi, T. Chirality Transfer from Gold Nanocluster to Adsorbate Evidenced by Vibrational Circular Dichroism. *Nat. Commun.* **2015**, *6* (1), 7117.
- (50) Knoppe, S.; Wong, O. A.; Malola, S.; Häkkinen, H.; Bürgi, T.; Verbiest, T.; Ackerson, C. J. Chiral Phase Transfer and Enantioenrichment of Thiolate-Protected Au₁₀₂ Clusters. *J. Am. Chem. Soc.* **2014**, *136* (11), 4129–4132.
- (51) Wu, Z.; Gayathri, C.; Gil, R. R.; Jin, R. Probing the Structure and Charge State of Glutathione-Capped Au₂₅(SG)₁₈ Clusters by NMR and Mass Spectrometry. *J. Am. Chem. Soc.* **2009**, *131* (18), 6535–6542.
- (52) Yao, H.; Miki, K.; Nishida, N.; Sasaki, A.; Kimura, K. Large Optical Activity of Gold Nanocluster Enantiomers Induced by a Pair of Optically Active Penicillamines. *J. Am. Chem. Soc.* **2005**, *127* (44), 15536–15543.
- (53) Yao, H.; Fukui, T.; Kimura, K. Chiroptical Responses of D-/L -Penicillamine-Capped Gold Clusters under Perturbations of Temperature Change and Phase Transfer. *J. Phys. Chem. C* **2007**, *111* (41), 14968–14976.
- (54) Goldsmith, M.-R.; George, C. B.; Zuber, G.; Naaman, R.; Waldeck, D. H.; Wipf, P.; Beratan, D. N. The Chiroptical Signature of Achiral Metal Clusters Induced by Dissymmetric Adsorbates. *Phys. Chem. Chem. Phys.* **2006**, *8* (1), 63–67.
- (55) Humblot, V.; Haq, S.; Muryn, C.; Hofer, W. A.; Raval, R. From Local Adsorption Stresses to Chiral Surfaces: (R, R)-Tartaric Acid on Ni(110). *J. Am. Chem. Soc.* **2002**, *124* (3), 503–510.

- (56) Gautier, C.; Bürgi, T. Chiral N-Isobutyryl-Cysteine Protected Gold Nanoparticles: Preparation, Size Selection, and Optical Activity in the UV-vis and Infrared. *J. Am. Chem. Soc.* **2006**, *128* (34), 11079–11087.
- (57) Cui, M.; Zhao, Y.; Song, Q. Synthesis, Optical Properties and Applications of Ultra-Small Luminescent Gold Nanoclusters. *TrAC Trends Anal. Chem.* **2014**, *57*, 73–82.
- (58) Shang, L.; Dong, S.; Nienhaus, G. U. Ultra-Small Fluorescent Metal Nanoclusters: Synthesis and Biological Applications. *Nano Today* **2011**, *6* (4), 401–418.
- (59) Lin, C. J.; Li, J. K.; Lee, C.; Hsieh, J.; Wang, H.; Chang, W. H.; Shen, J.; Chan, W.; Yeh, H. Synthesis of Fluorescent Metallic Nanoclusters toward Biomedical Application: Recent Progress and Present Challenges. *J. Med. Biol. Eng.* **2009**, *29* (6), 276–283.
- (60) Chevrier, D. M. Properties and Applications of Protein-Stabilized Fluorescent Gold Nanoclusters: Short Review. *J. Nanophotonics* **2012**, *6* (1), 064504.
- (61) Ma, Z.; Wang, P.; Xiong, L.; Pei, Y. Thiolate-Protected Gold Nanoclusters: Structural Prediction and the Understandings of Electronic Stability from First Principles Simulations. *Wiley Interdiscip. Rev. Comput. Mol. Sci.* **2017**, *7* (4), e1315.
- (62) Huczko, A. Template-Based Synthesis of Nanomaterials. *Appl. Phys. A Mater. Sci. Process.* **2000**, *70* (4), 365–376.
- (63) Liu, Y.; Goebel, J.; Yin, Y. Templated Synthesis of Nanostructured Materials. *Chem. Soc. Rev.* **2013**, *42* (7), 2610–2653.
- (64) Xie, Y.; Kocaefe, D.; Chen, C.; Kocaefe, Y. Review of Research on Template Methods in Preparation of Nanomaterials. *J. Nanomater.* **2016**, *2016*, 1–10.
- (65) Mody, V.; Siwale, R.; Singh, A.; Mody, H. Introduction to Metallic Nanoparticles. *J. Pharm. Bioallied Sci.* **2010**, *2* (4), 282.
- (66) Smith, A. M.; Nie, S. Semiconductor Nanocrystals: Structure, Properties, and Band Gap Engineering. *Acc. Chem. Res.* **2010**, *43* (2), 190–200.
- (67) Suresh, S. Semiconductor Nanomaterials, Methods and Applications: A Review. *Nanosci. Nanotechnol.* **2013**, *3* (3), 62–74.
- (68) Coey, J. M. D.; Venkatesan, M.; Xu, H. Introduction to Magnetic Oxides. In *Functional Metal Oxides*; Wiley-VCH Verlag GmbH & Co. KGaA: Weinheim, Germany, 2013; pp 1–49.
- (69) Tan, Y. N.; Lee, J. Y.; Wang, D. I. C. Uncovering the Design Rules for Peptide Synthesis of Metal Nanoparticles. *J. Am. Chem. Soc.* **2010**, *132* (16), 5677–5686.
- (70) Pandya, A.; Lad, A. N.; Singh, S. P.; Shanker, R. DNA Assembled Metal Nanoclusters: Synthesis to Novel Applications. *RSC Adv.* **2016**, *6* (114), 113095–113114.
- (71) Liu, G.; Shao, Y.; Wu, F.; Xu, S.; Peng, J.; Liu, L. DNA-Hosted Fluorescent Gold Nanoclusters:

- Sequence-Dependent Formation. *Nanotechnology* **2013**, *24* (1), 015503.
- (72) Brust, M.; Walker, M.; Bethell, D.; Schiffrin, D. J.; Whyman, R. Synthesis of Thiol-Derivatized Gold Nanoparticles in a Two-Phase Liquid–Liquid System. *J. Chem. Soc., Chem. Commun.* **1994**, No. 7, 801–802.
- (73) Brust, M.; Fink, J.; Bethell, D.; Schiffrin, D. J.; Kiely, C. Synthesis and Reactions of Functionalised Gold Nanoparticles. *J. Chem. Soc. Chem. Commun.* **1995**, No. 16, 1655.
- (74) Goulet, P. J. G.; Lennox, R. B. New Insights into Brust–Schiffrin Metal Nanoparticle Synthesis. *J. Am. Chem. Soc.* **2010**, *132* (28), 9582–9584.
- (75) Li, Y.; Zaluzhna, O.; Xu, B.; Gao, Y.; Modest, J. M.; Tong, Y. J. Mechanistic Insights into the Brust–Schiffrin Two-Phase Synthesis of Organo-Chalcogenate-Protected Metal Nanoparticles. *J. Am. Chem. Soc.* **2011**, *133* (7), 2092–2095.
- (76) Negishi, Y.; Nobusada, K.; Tsukuda, T. Glutathione-Protected Gold Clusters Revisited: Bridging the Gap between Gold(I)–Thiolate Complexes and Thiolate-Protected Gold Nanocrystals. *J. Am. Chem. Soc.* **2005**, *127* (14), 5261–5270.
- (77) Yu, Y.; Chen, X.; Yao, Q.; Yu, Y.; Yan, N.; Xie, J. Scalable and Precise Synthesis of Thiolated Au_{10–12}, Au₁₅, Au₁₈, and Au₂₅ Nanoclusters via PH Controlled CO Reduction. *Chem. Mater.* **2013**, *25* (6), 946–952.
- (78) Yao, Q.; Yu, Y.; Yuan, X.; Yu, Y.; Xie, J.; Lee, J. Y. Two-Phase Synthesis of Small Thiolate-Protected Au₁₅ and Au₁₈ Nanoclusters. *Small* **2013**, *9* (16), 2696–2701.
- (79) Chen, S.; Wang, S.; Zhong, J.; Song, Y.; Zhang, J.; Sheng, H.; Pei, Y.; Zhu, M. The Structure and Optical Properties of the [Au₁₈(SR)₁₄] Nanocluster. *Angew. Chemie Int. Ed.* **2015**, *54* (10), 3145–3149.
- (80) Das, A.; Liu, C.; Byun, H. Y.; Nobusada, K.; Zhao, S.; Rosi, N.; Jin, R. Structure Determination of [Au₁₈(SR)₁₄]. *Angew. Chemie Int. Ed.* **2015**, *54* (10), 3140–3144.
- (81) Zeng, C.; Liu, C.; Chen, Y.; Rosi, N. L.; Jin, R. Gold–Thiolate Ring as a Protecting Motif in the Au₂₀(SR)₁₆ Nanocluster and Implications. *J. Am. Chem. Soc.* **2014**, *136* (34), 11922–11925.
- (82) Zhu, X.; Jin, S.; Wang, S.; Meng, X.; Zhu, C.; Zhu, M.; Jin, R. One-Pot Synthesis of Phenylmethanethiolate-Protected Au₂₀(SR)₁₆ and Au₂₄(SR)₂₀ Nanoclusters and Insight into the Kinetic Control. *Chem. - An Asian J.* **2013**, *8* (11), 2739–2745.
- (83) Zhu, M.; Qian, H.; Jin, R. Thiolate-Protected Au₂₀ Clusters with a Large Energy Gap of 2.1 eV. *J. Am. Chem. Soc.* **2009**, *131* (21), 7220–7221.
- (84) Das, A.; Li, T.; Nobusada, K.; Zeng, C.; Rosi, N. L.; Jin, R. Nonsuperatomic [Au₂₃(SC₆H₁₁)₁₆] – Nanocluster Featuring Bipyramidal Au₁₅ Kernel and Trimeric Au₃(SR)₄ Motif. *J. Am. Chem. Soc.* **2013**, *135* (49), 18264–18267.
- (85) Hesari, M.; Workentin, M. S. Facile Synthesis of Au₂₃(SC(CH₃)₃)₁₆ Clusters. *J. Mater. Chem.*

- C **2014**, 2 (18), 3631–3638.
- (86) Crasto, D.; Barcaro, G.; Stener, M.; Sementa, L.; Fortunelli, A.; Dass, A. Au₂₄(SAdm)₁₆ Nanomolecules: X-Ray Crystal Structure, Theoretical Analysis, Adaptability of Adamantane Ligands to Form Au₂₃(SAdm)₁₆ and Au₂₅(SAdm)₁₆, and Its Relation to Au₂₅(SR)₁₈. *J. Am. Chem. Soc.* **2014**, 136 (42), 14933–14940.
- (87) Das, A.; Li, T.; Li, G.; Nobusada, K.; Zeng, C.; Rosi, N. L.; Jin, R. Crystal Structure and Electronic Properties of a Thiolate-Protected Au₂₄ Nanocluster. *Nanoscale* **2014**, 6 (12), 6458.
- (88) Zhu, M.; Qian, H.; Jin, R. Thiolate-Protected Au₂₄(SC₂H₄Ph)₂₀ Nanoclusters: Superatoms or Not? *J. Phys. Chem. Lett.* **2010**, 1 (6), 1003–1007.
- (89) Zhu, M.; Aikens, C. M.; Hollander, F. J.; Schatz, G. C.; Jin, R. Correlating the Crystal Structure of A Thiol-Protected Au₂₅ Cluster and Optical Properties. *J. Am. Chem. Soc.* **2008**, 130 (18), 5883–5885.
- (90) Heaven, M. W.; Dass, A.; White, P. S.; Holt, K. M.; Murray, R. W. Crystal Structure of the Gold Nanoparticle [N(C₈H₁₇)₄][Au₂₅(SCH₂CH₂Ph)₁₈]. *J. Am. Chem. Soc.* **2008**, 130 (12), 3754–3755.
- (91) Dainese, T.; Antonello, S.; Gascón, J. A.; Pan, F.; Perera, N. V.; Ruzzi, M.; Venzo, A.; Zoleo, A.; Rissanen, K.; Maran, F. Au₂₅(SEt)₁₈, a Nearly Naked Thiolate-Protected Au₂₅ Cluster: Structural Analysis by Single Crystal X-Ray Crystallography and Electron Nuclear Double Resonance. *ACS Nano* **2014**, 8 (4), 3904–3912.
- (92) Zhu, M.; Lanni, E.; Garg, N.; Bier, M. E.; Jin, R. Kinetically Controlled, High-Yield Synthesis of Au₂₅ Clusters. *J. Am. Chem. Soc.* **2008**, 130 (4), 1138–1139.
- (93) Wu, Z.; Suhan, J.; Jin, R. One-Pot Synthesis of Atomically Monodisperse, Thiol-Functionalized Au₂₅ Nanoclusters. *J. Mater. Chem.* **2009**, 19 (5), 622–626.
- (94) Kumar, S.; Jin, R. Water-Soluble Au₂₅(Capt)₁₈ Nanoclusters: Synthesis, Thermal Stability, and Optical Properties. *Nanoscale* **2012**, 4 (14), 4222.
- (95) Yuan, X.; Zhang, B.; Luo, Z.; Yao, Q.; Leong, D. T.; Yan, N.; Xie, J. Balancing the Rate of Cluster Growth and Etching for Gram-Scale Synthesis of Thiolate-Protected Au₂₅ Nanoclusters with Atomic Precision. *Angew. Chemie Int. Ed.* **2014**, 53 (18), 4623–4627.
- (96) Shichibu, Y.; Negishi, Y.; Tsukuda, T.; Teranishi, T. Large-Scale Synthesis of Thiolated Au₂₅ Clusters via Ligand Exchange Reactions of Phosphine-Stabilized Au₁₁ Clusters. *J. Am. Chem. Soc.* **2005**, 127 (39), 13464–13465.
- (97) Shibu, E. S.; Muhammed, M. A. H.; Tsukuda, T.; Pradeep, T. Ligand Exchange of Au₂₅SG₁₈ Leading to Functionalized Gold Clusters: Spectroscopy, Kinetics, and Luminescence. *J. Phys. Chem. C* **2008**, 112 (32), 12168–12176.

- (98) Zhu, M.; Eckenhoff, W. T.; Pintauer, T.; Jin, R. Conversion of Anionic $[\text{Au}_{25}(\text{SCH}_2\text{CH}_2\text{Ph})_{18}]^-$ Cluster to Charge Neutral Cluster via Air Oxidation. *J. Phys. Chem. C* **2008**, *112* (37), 14221–14224.
- (99) Resch-Genger, U.; Rurack, K. Determination of the Photoluminescence Quantum Yield of Dilute Dye Solutions (IUPAC Technical Report). *Pure Appl. Chem.* **2013**, *85* (10), 2005–2013.
- (100) Lavenn, C.; Albrieux, F.; Bergeret, G.; Chiriach, R.; Delichère, P.; Tuel, A.; Demessence, A. Functionalized Gold Magic Clusters: $\text{Au}_{25}(\text{SPhNH}_2)_{17}$. *Nanoscale* **2012**, *4* (23), 7334.
- (101) Niihori, Y.; Matsuzaki, M.; Pradeep, T.; Negishi, Y. Separation of Precise Compositions of Noble Metal Clusters Protected with Mixed Ligands. *J. Am. Chem. Soc.* **2013**, *135* (13), 4946–4949.
- (102) Antonello, S.; Arrigoni, G.; Dainese, T.; De Nardi, M.; Parisio, G.; Perotti, L.; René, A.; Venzo, A.; Maran, F. Electron Transfer through 3D Monolayers on Au_{25} Clusters. *ACS Nano* **2014**, *8* (3), 2788–2795.
- (103) De Nardi, M.; Antonello, S.; Jiang, D.; Pan, F.; Rissanen, K.; Ruzzi, M.; Venzo, A.; Zoleo, A.; Maran, F. Gold Nanowired: A Linear $(\text{Au}_{25})_n$ Polymer from Au_{25} Molecular Clusters. *ACS Nano* **2014**, *8* (8), 8505–8512.
- (104) Katla, S. K.; Zhang, J.; Castro, E.; Bernal, R. A.; Li, X. Atomically Precise $\text{Au}_{25}(\text{SG})_{18}$ Nanoclusters: Rapid Single-Step Synthesis and Application in Photothermal Therapy. *ACS Appl. Mater. Interfaces* **2018**, *10* (1), 75–82.
- (105) Zeng, C.; Li, T.; Das, A.; Rosi, N. L.; Jin, R. Chiral Structure of Thiolate-Protected 28-Gold-Atom Nanocluster Determined by X-Ray Crystallography. *J. Am. Chem. Soc.* **2013**, *135* (27), 10011–10013.
- (106) Chen, Y.; Liu, C.; Tang, Q.; Zeng, C.; Higaki, T.; Das, A.; Jiang, D.; Rosi, N. L.; Jin, R. Isomerism in $\text{Au}_{28}(\text{SR})_{20}$ Nanocluster and Stable Structures. *J. Am. Chem. Soc.* **2016**, *138* (5), 1482–1485.
- (107) Higaki, T.; Liu, C.; Zeng, C.; Jin, R.; Chen, Y.; Rosi, N. L.; Jin, R. Controlling the Atomic Structure of Au_{30} Nanoclusters by a Ligand-Based Strategy. *Angew. Chemie Int. Ed.* **2016**, *55* (23), 6694–6697.
- (108) Zeng, C.; Qian, H.; Li, T.; Li, G.; Rosi, N. L.; Yoon, B.; Barnett, R. N.; Whetten, R. L.; Landman, U.; Jin, R. Total Structure and Electronic Properties of the Gold Nanocrystal $\text{Au}_{36}(\text{SR})_{24}$. *Angew. Chemie Int. Ed.* **2012**, *51* (52), 13114–13118.
- (109) Zeng, C.; Liu, C.; Pei, Y.; Jin, R. Thiol Ligand-Induced Transformation of $\text{Au}_{38}(\text{SC}_2\text{H}_4\text{Ph})_{24}$ to $\text{Au}_{36}(\text{SPh-}t\text{-Bu})_{24}$. *ACS Nano* **2013**, *7* (7), 6138–6145.
- (110) Das, A.; Liu, C.; Zeng, C.; Li, G.; Li, T.; Rosi, N. L.; Jin, R. Cyclopentanethiolato-Protected $\text{Au}_{36}(\text{SC}_5\text{H}_9)_{24}$ Nanocluster: Crystal Structure and Implications for the Steric and Electronic Effects of Ligand. *J. Phys. Chem. A* **2014**, *118* (37), 8264–8269.

- (111) Nimmala, P. R.; Knoppe, S.; Jupally, V. R.; Delcamp, J. H.; Aikens, C. M.; Dass, A. Au₃₆(SPh)₂₄ Nanomolecules: X-Ray Crystal Structure, Optical Spectroscopy, Electrochemistry, and Theoretical Analysis. *J. Phys. Chem. B* **2014**, *118* (49), 14157–14167.
- (112) Qian, H.; Eckenhoff, W. T.; Zhu, Y.; Pintauer, T.; Jin, R. Total Structure Determination of Thiolate-Protected Au₃₈ Nanoparticles. *J. Am. Chem. Soc.* **2010**, *132* (24), 8280–8281.
- (113) Chaki, N. K.; Negishi, Y.; Tsunoyama, H.; Shichibu, Y.; Tsukuda, T. Ubiquitous 8 and 29 KDa Gold:Alkanethiolate Cluster Compounds: Mass-Spectrometric Determination of Molecular Formulas and Structural Implications. *J. Am. Chem. Soc.* **2008**, *130* (27), 8608–8610.
- (114) Qian, H.; Zhu, M.; Andersen, U. N.; Jin, R. Facile, Large-Scale Synthesis of Dodecanethiol-Stabilized Au₃₈ Clusters. *J. Phys. Chem. A* **2009**, *113* (16), 4281–4284.
- (115) Qian, H.; Zhu, Y.; Jin, R. Size-Focusing Synthesis, Optical and Electrochemical Properties of Monodisperse Au₃₈(SC₂H₄Ph)₂₄ Nanoclusters. *ACS Nano* **2009**, *3* (11), 3795–3803.
- (116) Stellwagen, D.; Weber, A.; Bovenkamp, G. L.; Jin, R.; Bitter, J. H.; Kumar, C. S. S. R. Ligand Control in Thiol Stabilized Au₃₈ Clusters. *RSC Adv.* **2012**, *2* (6), 2276.
- (117) Chen, Y.; Zeng, C.; Kauffman, D. R.; Jin, R. Tuning the Magic Size of Atomically Precise Gold Nanoclusters via Isomeric Methylbenzenethiols. *Nano Lett.* **2015**, *15* (5), 3603–3609.
- (118) Qian, H.; Zhu, Y.; Jin, R. Isolation of Ubiquitous Au₄₀(SR)₂₄ Clusters from the 8 KDa Gold Clusters. *J. Am. Chem. Soc.* **2010**, *132* (13), 4583–4585.
- (119) Knoppe, S.; Boudon, J.; Dolamic, I.; Dass, A.; Bürgi, T. Size Exclusion Chromatography for Semipreparative Scale Separation of Au₃₈(SR)₂₄ and Au₄₀(SR)₂₄ and Larger Clusters. *Anal. Chem.* **2011**, *83* (13), 5056–5061.
- (120) Zeng, C.; Chen, Y.; Liu, C.; Nobusada, K.; Rosi, N. L.; Jin, R. Gold Tetrahedra Coil up: Kekulé-like and Double Helical Superstructures. *Sci. Adv.* **2015**, *1* (9), e1500425.
- (121) Zeng, C.; Chen, Y.; Li, G.; Jin, R. Synthesis of a Au₄₄(SR)₂₈ Nanocluster: Structure Prediction and Evolution from Au₂₈(SR)₂₀, Au₃₆(SR)₂₄ to Au₄₄(SR)₂₈. *Chem. Commun.* **2014**, *50* (1), 55–57.
- (122) Zeng, C.; Chen, Y.; Iida, K.; Nobusada, K.; Kirschbaum, K.; Lambright, K. J.; Jin, R. Gold Quantum Boxes: On the Periodicities and the Quantum Confinement in the Au₂₈, Au₃₆, Au₄₄, and Au₅₂ Magic Series. *J. Am. Chem. Soc.* **2016**, *138* (12), 3950–3953.
- (123) Tsunoyama, H.; Negishi, Y.; Tsukuda, T. Chromatographic Isolation of “Missing” Au₅₅ Clusters Protected by Alkanethiolates. *J. Am. Chem. Soc.* **2006**, *128* (18), 6036–6037.
- (124) Tsunoyama, R.; Tsunoyama, H.; Pannopard, P.; Limtrakul, J.; Tsukuda, T. MALDI Mass Analysis of 11 KDa Gold Clusters Protected by Octadecanethiolate Ligands. *J. Phys. Chem. C* **2010**, *114* (38), 16004–16009.
- (125) Qian, H.; Jin, R. Synthesis and Electrospray Mass Spectrometry Determination of Thiolate-

- Protected Au₅₅(SR)₃₁ Nanoclusters. *Chem. Commun.* **2011**, 47 (41), 11462.
- (126) Zeng, C.; Chen, Y.; Li, G.; Jin, R. Magic Size Au₆₄(S-c-C₆H₁₁)₃₂ Nanocluster Protected by Cyclohexanethiolate. *Chem. Mater.* **2014**, 26 (8), 2635–2641.
- (127) Nimmala, P. R.; Yoon, B.; Whetten, R. L.; Landman, U.; Dass, A. Au₆₇(SR)₃₅ Nanomolecules: Characteristic Size-Specific Optical, Electrochemical, Structural Properties and First-Principles Theoretical Analysis. *J. Phys. Chem. A* **2013**, 117 (2), 504–517.
- (128) Li, G.; Zeng, C.; Jin, R. Thermally Robust Au₉₉(SPh)₄₂ Nanoclusters for Chemoselective Hydrogenation of Nitrobenzaldehyde Derivatives in Water. *J. Am. Chem. Soc.* **2014**, 136 (9), 3673–3679.
- (129) Jadzinsky, P. D.; Calero, G.; Ackerson, C. J.; Bushnell, D. A.; Kornberg, R. D. Structure of a Thiol Monolayer-Protected Gold Nanoparticle at 1.1 Å Resolution. *Science*. **2007**, 318 (5849), 430–433.
- (130) Levi-Kalisman, Y.; Jadzinsky, P. D.; Kalisman, N.; Tsunoyama, H.; Tsukuda, T.; Bushnell, D. A.; Kornberg, R. D. Synthesis and Characterization of Au₁₀₂(p-MBA)₄₄ Nanoparticles. *J. Am. Chem. Soc.* **2011**, 133 (9), 2976–2982.
- (131) Chen, Y.; Zeng, C.; Liu, C.; Kirschbaum, K.; Gayathri, C.; Gil, R. R.; Rosi, N. L.; Jin, R. Crystal Structure of Barrel-Shaped Chiral Au₁₃₀(p-MBT)₅₀ Nanocluster. *J. Am. Chem. Soc.* **2015**, 137 (32), 10076–10079.
- (132) Negishi, Y.; Sakamoto, C.; Ohyama, T.; Tsukuda, T. Synthesis and the Origin of the Stability of Thiolate-Protected Au₁₃₀ and Au₁₈₇ Clusters. *J. Phys. Chem. Lett.* **2012**, 3 (12), 1624–1628.
- (133) Tang, Z.; Robinson, D. A.; Bokossa, N.; Xu, B.; Wang, S.; Wang, G. Mixed Dithiolate Durene-DT and Monothiolate Phenylethanethiolate Protected Au₁₃₀ Nanoparticles with Discrete Core and Core-Ligand Energy States. *J. Am. Chem. Soc.* **2011**, 133 (40), 16037–16044.
- (134) Dass, A.; Theivendran, S.; Nimmala, P. R.; Kumara, C.; Jupally, V. R.; Fortunelli, A.; Sementa, L.; Barcaro, G.; Zuo, X.; Noll, B. C. Au₁₃₃(SPh-^tBu)₅₂ Nanomolecules: X-Ray Crystallography, Optical, Electrochemical, and Theoretical Analysis. *J. Am. Chem. Soc.* **2015**, 137 (14), 4610–4613.
- (135) Zeng, C.; Chen, Y.; Kirschbaum, K.; Appavoo, K.; Sfeir, M. Y.; Jin, R. Structural Patterns at All Scales in a Nonmetallic Chiral Au₁₃₃(SR)₅₂ Nanoparticle. *Sci. Adv.* **2015**, 1 (2), e1500045.
- (136) Jupally, V. R.; Dharmaratne, A. C.; Crasto, D.; Huckaba, A. J.; Kumara, C.; Nimmala, P. R.; Kothalawala, N.; Delcamp, J. H.; Dass, A. Au₁₃₇(SR)₅₆ Nanomolecules: Composition, Optical Spectroscopy, Electrochemistry and Electrocatalytic Reduction of CO₂. *Chem. Commun.* **2014**, 50 (69), 9895.
- (137) Qian, H.; Jin, R. Controlling Nanoparticles with Atomic Precision: The Case of Au₁₄₄(SCH₂CH₂Ph)₆₀. *Nano Lett.* **2009**, 9 (12), 4083–4087.

- (138) Qian, H.; Jin, R. Ambient Synthesis of Au₁₄₄(SR)₆₀ Nanoclusters in Methanol. *Chem. Mater.* **2011**, *23* (8), 2209–2217.
- (139) Yan, N.; Xia, N.; Liao, L.; Zhu, M.; Jin, F.; Jin, R.; Wu, Z. Unraveling the Long-Pursued Au₁₄₄ Structure by X-Ray Crystallography. *Sci. Adv.* **2018**, *4* (10), eaat7259.
- (140) Shichibu, Y.; Negishi, Y.; Tsunoyama, H.; Kanehara, M.; Teranishi, T.; Tsukuda, T. Extremely High Stability of Glutathionate-Protected Au₂₅ Clusters Against Core Etching. *Small* **2007**, *3* (5), 835–839.
- (141) Dharmaratne, A. C.; Krick, T.; Dass, A. Nanocluster Size Evolution Studied by Mass Spectrometry in Room Temperature Au₂₅(SR)₁₈ Synthesis. *J. Am. Chem. Soc.* **2009**, *131* (38), 13604–13605.
- (142) Schaaff, T. G.; Whetten, R. L. Controlled Etching of Au:SR Cluster Compounds. *J. Phys. Chem. B* **1999**, *103* (44), 9394–9396.
- (143) Luo, Z.; Nachammai, V.; Zhang, B.; Yan, N.; Leong, D. T.; Jiang, D.; Xie, J. Toward Understanding the Growth Mechanism: Tracing All Stable Intermediate Species from Reduction of Au(I)–Thiolate Complexes to Evolution of Au₂₅ Nanoclusters. *J. Am. Chem. Soc.* **2014**, *136* (30), 10577–10580.
- (144) Liu, C.; Li, G.; Pang, G.; Jin, R. Toward Understanding the Growth Mechanism of Au_n(SR)_m Nanoclusters: Effect of Solvent on Cluster Size. *RSC Adv.* **2013**, *3* (25), 9778.
- (145) Shahsavari, S.; Hadian-Ghazvini, S.; Hooriabad Saboor, F.; Menbari Oskouie, I.; Hasany, M.; Simchi, A.; Rogach, A. L. Ligand Functionalized Copper Nanoclusters for Versatile Applications in Catalysis, Sensing, Bioimaging, and Optoelectronics. *Mater. Chem. Front.* **2019**, No. Scheme 1.
- (146) Lu, Y.; Wei, W.; Chen, W. Copper Nanoclusters: Synthesis, Characterization and Properties. *Chinese Sci. Bull.* **2012**, *57* (1), 41–47.
- (147) Zhao, M.; Sun, L.; Crooks, R. M. Preparation of Cu Nanoclusters within Dendrimer Templates. *J. Am. Chem. Soc.* **1998**, *120* (19), 4877–4878.
- (148) Ling, Y.; Zhang, N.; Qu, F.; Wen, T.; Gao, Z. F.; Li, N. B.; Luo, H. Q. Fluorescent Detection of Hydrogen Peroxide and Glucose with Polyethyleneimine-Templated Cu Nanoclusters. *Spectrochim. Acta Part A Mol. Biomol. Spectrosc.* **2014**, *118*, 315–320.
- (149) Ling, Y.; Li, J. X.; Qu, F.; Li, N. B.; Luo, H. Q. Rapid Fluorescence Assay for Sudan Dyes Using Polyethyleneimine-Coated Copper Nanoclusters. *Microchim. Acta* **2014**, *181* (9–10), 1069–1075.
- (150) Ling, Y.; Wu, J. J.; Gao, Z. F.; Li, N. B.; Luo, H. Q. Enhanced Emission of Polyethyleneimine-Coated Copper Nanoclusters and Their Solvent Effect. *J. Phys. Chem. C* **2015**, *119* (48), 27173–27177.

- (151) Zhong, Y.; Wang, Q.; He, Y.; Ge, Y.; Song, G. A Novel Fluorescence and Naked Eye Sensor for Iodide in Urine Based on the Iodide Induced Oxidative Etching and Aggregation of Cu Nanoclusters. *Sensors Actuators B Chem.* **2015**, *209*, 147–153.
- (152) Feng, J.; Ju, Y.; Liu, J.; Zhang, H.; Chen, X. Polyethyleneimine-Templated Copper Nanoclusters via Ascorbic Acid Reduction Approach as Ferric Ion Sensor. *Anal. Chim. Acta* **2015**, *854*, 153–160.
- (153) Fernández-Ujados, M.; Trapiella-Alfonso, L.; Costa-Fernández, J. M.; Pereiro, R.; Sanz-Medel, A. One-Step Aqueous Synthesis of Fluorescent Copper Nanoclusters by Direct Metal Reduction. *Nanotechnology* **2013**, *24* (49), 495601.
- (154) Tang, Q.; Yang, T.; Huang, Y. Copper Nanocluster-Based Fluorescent Probe for Hypochlorite. *Microchim. Acta* **2015**, *182* (13–14), 2337–2343.
- (155) Chen, P.-C.; Li, Y.-C.; Ma, J.-Y.; Huang, J.-Y.; Chen, C.-F.; Chang, H.-T. Size-Tunable Copper Nanocluster Aggregates and Their Application in Hydrogen Sulfide Sensing on Paper-Based Devices. *Sci. Rep.* **2016**, *6* (1), 24882.
- (156) Gui, R.; Sun, J.; Cao, X.; Wang, Y.; Jin, H. Multidentate Polymers Stabilized Water-Dispersed Copper Nanoclusters: Facile Photoreduction Synthesis and Selective Fluorescence Turn-on Response. *RSC Adv.* **2014**, *4* (55), 29083.
- (157) Xu, S.; Chen, F.; Deng, M.; Sui, Y. Luminol Chemiluminescence Enhanced by Copper Nanoclusters and Its Analytical Application. *RSC Adv.* **2014**, *4* (30), 15664–15670.
- (158) Wang, W.; Leng, F.; Zhan, L.; Chang, Y.; Yang, X. X.; Lan, J.; Huang, C. Z. One-Step Prepared Fluorescent Copper Nanoclusters for Reversible PH-Sensing. *Analyst* **2014**, *139* (12), 2990–2993.
- (159) Ghosh, R.; Sahoo, A. K.; Ghosh, S. S.; Paul, A.; Chattopadhyay, A. Blue-Emitting Copper Nanoclusters Synthesized in the Presence of Lysozyme as Candidates for Cell Labeling. *ACS Appl. Mater. Interfaces* **2014**, *6* (6), 3822–3828.
- (160) Wang, C.; Wang, C.; Xu, L.; Cheng, H.; Lin, Q.; Zhang, C. Protein-Directed Synthesis of PH-Responsive Red Fluorescent Copper Nanoclusters and Their Applications in Cellular Imaging and Catalysis. *Nanoscale* **2014**, *6* (3), 1775–1781.
- (161) Xu, S.; Deng, M.; Sui, Y.; Zhang, Y.; Chen, F. Ultrasensitive Determination of Bisphenol A in Water by Inhibition of Copper Nanoclusters-Enhanced Chemiluminescence from the Luminol–KMnO₄ System. *RSC Adv.* **2014**, *4* (84), 44644–44649.
- (162) Gao, Z.; Su, R.; Qi, W.; Wang, L.; He, Z. Copper Nanocluster-Based Fluorescent Sensors for Sensitive and Selective Detection of Kojic Acid in Food Stuff. *Sensors Actuators B Chem.* **2014**, *195*, 359–364.
- (163) Chen, H.; Lin, L.; Li, H.; Li, J.; Lin, J.-M. Aggregation-Induced Structure Transition of Protein-Stabilized Zinc/Copper Nanoclusters for Amplified Chemiluminescence. *ACS Nano* **2015**, *9*

- (2), 2173–2183.
- (164) Xiaoqing, L.; Ruiyi, L.; Xiaohuan, L.; Zaijun, L. Ultra Sensitive and Wide-Range PH Sensor Based on the BSA-Capped Cu Nanoclusters Fabricated by Fast Synthesis through the Use of Hydrogen Peroxide Additive. *RSC Adv.* **2015**, 5 (60), 48835–48841.
- (165) Deng, X.; Huang, X.; Wu, D. Förster Resonance-Energy-Transfer Detection of 2,4,6-Trinitrophenol Using Copper Nanoclusters. *Anal. Bioanal. Chem.* **2015**, 407 (16), 4607–4613.
- (166) Zhong, Y.; Zhu, J.; Wang, Q.; He, Y.; Ge, Y.; Song, C. Copper Nanoclusters Coated with Bovine Serum Albumin as a Regenerable Fluorescent Probe for Copper(II) Ion. *Microchim. Acta* **2015**, 182 (5–6), 909–915.
- (167) Ghosh, S.; Das, N. K.; Anand, U.; Mukherjee, S. Photostable Copper Nanoclusters: Compatible Förster Resonance Energy-Transfer Assays and a Nanothermometer. *J. Phys. Chem. Lett.* **2015**, 6 (7), 1293–1298.
- (168) Zhao, T.; He, X.-W.; Li, W.-Y.; Zhang, Y.-K. Transferrin-Directed Preparation of Red-Emitting Copper Nanoclusters for Targeted Imaging of Transferrin Receptor over-Expressed Cancer Cells. *J. Mater. Chem. B* **2015**, 3 (11), 2388–2394.
- (169) Miao, H.; Zhong, D.; Zhou, Z.; Yang, X. Papain-Templated Cu Nanoclusters: Assaying and Exhibiting Dramatic Antibacterial Activity Cooperating with H₂O₂. *Nanoscale* **2015**, 7 (45), 19066–19072.
- (170) Singh, A.; Rai, T.; Panda, D. Photoluminescence Dynamics of Copper Nanoclusters Synthesized by Cellulase: Role of the Random-Coil Structure. *RSC Adv.* **2016**, 6 (60), 55539–55545.
- (171) Xiaoqing, L.; Ruiyi, L.; Zaijun, L.; Xiulan, S.; Zhouping, W.; Junkang, L. Fast Synthesis of Copper Nanoclusters through the Use of Hydrogen Peroxide Additive and Their Application for the Fluorescence Detection of Hg²⁺ in Water Samples. *New J. Chem.* **2015**, 39 (7), 5240–5248.
- (172) Goswami, N.; Giri, A.; Bootharaju, M. S.; Xavier, P. L.; Pradeep, T.; Pal, S. K. Copper Quantum Clusters in Protein Matrix: Potential Sensor of Pb²⁺ Ion. *Anal. Chem.* **2011**, 83 (24), 9676–9680.
- (173) Hu, L.; Yuan, Y.; Zhang, L.; Zhao, J.; Majeed, S.; Xu, G. Copper Nanoclusters as Peroxidase Mimetics and Their Applications to H₂O₂ and Glucose Detection. *Anal. Chim. Acta* **2013**, 762, 83–86.
- (174) Patel, A. S.; Sahoo, H.; Mohanty, T. Probing the Förster Resonance Energy Transfer between Fluorescent Copper Nanoclusters and Cobalt Complex. *Appl. Phys. Lett.* **2014**, 105 (6), 063112.
- (175) Wang, B.; Gui, R.; Jin, H.; He, W.; Wang, Z. Red-Emitting BSA-Stabilized Copper

- Nanoclusters Acted as a Sensitive Probe for Fluorescence Sensing and Visual Imaging Detection of Rutin. *Talanta* **2018**, *178* (August 2017), 1006–1010.
- (176) Zhao, M.; Chen, A.-Y.; Huang, D.; Zhuo, Y.; Chai, Y.-Q.; Yuan, R. Cu Nanoclusters: Novel Electrochemiluminescence Emitters for Bioanalysis. *Anal. Chem.* **2016**, *88* (23), 11527–11532.
- (177) Wang, C.; Shu, S.; Yao, Y.; Song, Q. A Fluorescent Biosensor of Lysozyme-Stabilized Copper Nanoclusters for the Selective Detection of Glucose. *RSC Adv.* **2015**, *5* (123), 101599–101606.
- (178) Aparna, R. S.; Devi, J. S. A.; Nebu, J.; Syamchand, S. S.; George, S. Rapid Response of Dopamine towards Insitu Synthesised Copper Nanocluster in Presence of H₂O₂. *J. Photochem. Photobiol. A Chem.* **2019**, *379* (March), 63–71.
- (179) Monson, C. F.; Woolley, A. T. DNA-Templated Construction of Copper Nanowires. *Nano Lett.* **2003**, *3* (3), 359–363.
- (180) Rotaru, A.; Dutta, S.; Jentzsch, E.; Gothelf, K.; Mokhir, A. Selective DsDNA-Templated Formation of Copper Nanoparticles in Solution. *Angew. Chemie Int. Ed.* **2010**, *49* (33), 5665–5667.
- (181) Zhou, Z.; Du, Y.; Dong, S. Double-Strand DNA-Templated Formation of Copper Nanoparticles as Fluorescent Probe for Label-Free Aptamer Sensor. *Anal. Chem.* **2011**, *83* (13), 5122–5127.
- (182) Jia, X.; Li, J.; Han, L.; Ren, J.; Yang, X.; Wang, E. DNA-Hosted Copper Nanoclusters for Fluorescent Identification of Single Nucleotide Polymorphisms. *ACS Nano* **2012**, *6* (4), 3311–3317.
- (183) Chen, J.; Liu, J.; Fang, Z.; Zeng, L. Random DsDNA-Templated Formation of Copper Nanoparticles as Novel Fluorescence Probes for Label-Free Lead Ions Detection. *Chem. Commun.* **2012**, *48* (7), 1057–1059.
- (184) Liu, G.; Shao, Y.; Peng, J.; Dai, W.; Liu, L.; Xu, S.; Wu, F.; Wu, X. Highly Thymine-Dependent Formation of Fluorescent Copper Nanoparticles Templated by ss-DNA. *Nanotechnology* **2013**, *24* (34), 345502.
- (185) Zhang, L.; Zhao, J.; Duan, M.; Zhang, H.; Jiang, J.; Yu, R. Inhibition of dsDNA-Templated Copper Nanoparticles by Pyrophosphate as a Label-Free Fluorescent Strategy for Alkaline Phosphatase Assay. *Anal. Chem.* **2013**, *85* (8), 3797–3801.
- (186) Wang, X.-P.; Yin, B.-C.; Ye, B.-C. A Novel Fluorescence Probe of dsDNA-Templated Copper Nanoclusters for Quantitative Detection of MicroRNAs. *RSC Adv.* **2013**, *3* (23), 8633.
- (187) Xu, F.; Shi, H.; He, X.; Wang, K.; He, D.; Guo, Q.; Qing, Z.; Yan, L.; Ye, X.; Li, D.; et al. Concatemeric dsDNA-Templated Copper Nanoparticles Strategy with Improved Sensitivity and Stability Based on Rolling Circle Replication and Its Application in MicroRNA Detection.

- Anal. Chem.* **2014**, *86* (14), 6976–6982.
- (188) Chen, C.-A.; Wang, C.-C.; Jong, Y.-J.; Wu, S.-M. Label-Free Fluorescent Copper Nanoclusters for Genotyping of Deletion and Duplication of Duchenne Muscular Dystrophy. *Anal. Chem.* **2015**, *87* (12), 6228–6232.
- (189) Zhang, H.; Lin, Z.; Su, X. Label-Free Detection of Exonuclease III by Using dsDNA-Templated Copper Nanoparticles as Fluorescent Probe. *Talanta* **2015**, *131*, 59–63.
- (190) Zhu, X.; Shi, H.; Shen, Y.; Zhang, B.; Zhao, J.; Li, G. A Green Method of Staining DNA in Polyacrylamide Gel Electrophoresis Based on Fluorescent Copper Nanoclusters Synthesized in Situ. *Nano Res.* **2015**, *8* (8), 2714–2720.
- (191) Borghei, Y.-S.; Hosseini, M.; Ganjali, M. R.; Hosseinkhani, S. Label-Free Fluorescent Detection of MicroRNA-155 Based on Synthesis of Hairpin DNA-Templated Copper Nanoclusters by Etching (Top-down Approach). *Sensors Actuators B Chem.* **2017**, *248* (2), 133–139.
- (192) Qing, Z.; He, X.; He, D.; Wang, K.; Xu, F.; Qing, T.; Yang, X. Poly(Thymine)-Templated Selective Formation of Fluorescent Copper Nanoparticles. *Angew. Chemie Int. Ed.* **2013**, *52* (37), 9719–9722.
- (193) Mao, Z.; Qing, Z.; Qing, T.; Xu, F.; Wen, L.; He, X.; He, D.; Shi, H.; Wang, K. Poly(Thymine)-Templated Copper Nanoparticles as a Fluorescent Indicator for Hydrogen Peroxide and Oxidase-Based Biosensing. *Anal. Chem.* **2015**, *87* (14), 7454–7460.
- (194) Zhu, H.-W.; Dai, W.-X.; Yu, X.-D.; Xu, J.-J.; Chen, H.-Y. Poly Thymine Stabilized Copper Nanoclusters as a Fluorescence Probe for Melamine Sensing. *Talanta* **2015**, *144*, 642–647.
- (195) Yang, D.; Guo, Z.; Tang, Y.; Miao, P. Poly(Thymine)-Templated Selective Formation of Copper Nanoparticles for Alkaline Phosphatase Analysis Aided by Alkyne–Azide Cycloaddition “Click” Reaction. *ACS Appl. Nano Mater.* **2018**, *1* (1), 168–174.
- (196) Li, G.-R.; Xu, H.; Lu, X.-F.; Feng, J.-X.; Tong, Y.-X.; Su, C.-Y. Electrochemical Synthesis of Nanostructured Materials for Electrochemical Energy Conversion and Storage. *Nanoscale* **2013**, *5* (10), 4056.
- (197) Raja, M.; Subha, J.; Ali, F. B.; Ryu, S. H. Synthesis of Copper Nanoparticles by Electroreduction Process. *Mater. Manuf. Process.* **2008**, *23* (8), 782–785.
- (198) Yang, X.; Chen, S.; Zhao, S.; Li, D.; Ma, H. Synthesis of Copper Nanorods Using Electrochemical Methods. *J. Serbian Chem. Soc.* **2003**, *68* (11), 843–847.
- (199) Zhang, Q. B.; Hua, Y. X. Electrochemical Synthesis of Copper Nanoparticles Using Cuprous Oxide as a Precursor in Choline Chloride–Urea Deep Eutectic Solvent: Nucleation and Growth Mechanism. *Phys. Chem. Chem. Phys.* **2014**, *16* (48), 27088–27095.
- (200) Vilar-Vidal, N.; Blanco, M. C.; López-Quintela, M. A.; Rivas, J.; Serra, C. Electrochemical

- Synthesis of Very Stable Photoluminescent Copper Clusters. *J. Phys. Chem. C* **2010**, *114* (38), 15924–15930.
- (201) Vilar-Vidal, N.; Rivas, J.; López-Quintela, M. A. Copper Clusters as Novel Fluorescent Probes for the Detection and Photocatalytic Elimination of Lead Ions. *Phys. Chem. Chem. Phys.* **2014**, *16* (48), 26427–26430.
- (202) Georgieva, A.; Panayotova, K.; Bogdanov, B.; Stefanov, Z. Microemulsions – Properties, Application and Perspectives. *Sci. Technol.* **2012**, *4* (1), 207–231.
- (203) Lisiecki, I.; Pileni, M. P. Synthesis of Copper Metallic Clusters Using Reverse Micelles as Microreactors. *J. Am. Chem. Soc.* **1993**, *115* (10), 3887–3896.
- (204) Solanki, J. N.; Sengupta, R.; Murthy, Z. V. P. Synthesis of Copper Sulphide and Copper Nanoparticles with Microemulsion Method. *Solid State Sci.* **2010**, *12* (9), 1560–1566.
- (205) Lisiecki, I.; Pileni, M. P. Copper Metallic Particles Synthesized “in Situ” in Reverse Micelles: Influence of Various Parameters on the Size of the Particles. *J. Phys. Chem.* **1995**, *99* (14), 5077–5082.
- (206) Qi, L.; Ma, J.; Shen, J. Synthesis of Copper Nanoparticles in Nonionic Water-in-Oil Microemulsions. *J. Colloid Interface Sci.* **1997**, *186* (2), 498–500.
- (207) Vázquez-Vázquez, C.; Bañobre-López, M.; Mitra, A.; López-Quintela, M. A.; Rivas, J. Synthesis of Small Atomic Copper Clusters in Microemulsions. *Langmuir* **2009**, *25* (14), 8208–8216.
- (208) Wei, W.; Lu, Y.; Chen, W.; Chen, S. One-Pot Synthesis, Photoluminescence, and Electrocatalytic Properties of Subnanometer-Sized Copper Clusters. *J. Am. Chem. Soc.* **2011**, *133* (7), 2060–2063.
- (209) Li, D.; Chen, Z.; Wan, Z.; Yang, T.; Wang, H.; Mei, X. One-Pot Development of Water Soluble Copper Nanoclusters with Red Emission and Aggregation Induced Fluorescence Enhancement. *RSC Adv.* **2016**, *6* (41), 34090–34095.
- (210) Zhou, T.; Yao, Q.; Zhao, T.; Chen, X. One-Pot Synthesis of Fluorescent DHLA-Stabilized Cu Nanoclusters for the Determination of H₂O₂. *Talanta* **2015**, *141*, 80–85.
- (211) Zhao, M.; Feng, H.; Zhang, X.; Ao, H.; Qian, Z. Bonding-Induced Emission of Silyl-Protected Copper Nanoclusters for Luminescence Turn-on Detection of Trace Water in Organic Solvents. *Analyst* **2017**, *142* (24), 4613–4617.
- (212) Rao, H.; Ge, H.; Lu, Z.; Liu, W.; Chen, Z.; Zhang, Z.; Wang, X.; Zou, P.; Wang, Y.; He, H.; et al. Copper Nanoclusters as an On-off-on Fluorescent Probe for Ascorbic Acid. *Microchim. Acta* **2016**, *183* (5), 1651–1657.
- (213) Cao, H.; Chen, Z.; Huang, Y. Copper Nanocluster Coupling Europium as an Off-to-on Fluorescence Probe for the Determination of Phosphate Ion in Water Samples. *Talanta*

- 2015, 143, 450–456.
- (214) Cao, H.; Chen, Z.; Zheng, H.; Huang, Y. Copper Nanoclusters as a Highly Sensitive and Selective Fluorescence Sensor for Ferric Ions in Serum and Living Cells by Imaging. *Biosens. Bioelectron.* **2014**, 62, 189–195.
- (215) Ma, J.; Chen, P.; Chang, H. Detection of Hydrogen Sulfide through Photoluminescence Quenching of Penicillamine-Copper Nanocluster Aggregates. *Nanotechnology* **2014**, 25 (19), 195502.
- (216) Jia, X.; Yang, X.; Li, J.; Li, D.; Wang, E. Stable Cu Nanoclusters: From an Aggregation-Induced Emission Mechanism to Biosensing and Catalytic Applications. *Chem. Commun.* **2014**, 50 (2), 237–239.
- (217) Li, D.; Li, B.; Yang, S. I. A Selective Fluorescence Turn-on Sensing System for Evaluation of Cu²⁺ Polluted Water Based on Ultra-Fast Formation of Fluorescent Copper Nanoclusters. *Anal. Methods* **2015**, 7 (6), 2278–2282.
- (218) Cui, M.; Song, G.; Wang, C.; Song, Q. Synthesis of Cysteine-Functionalized Water-Soluble Luminescent Copper Nanoclusters and Their Application to the Determination of Chromium(VI). *Microchim. Acta* **2015**, 182 (7–8), 1371–1377.
- (219) Li, Z.; Guo, S.; Lu, C. A Highly Selective Fluorescent Probe for Sulfide Ions Based on Aggregation of Cu Nanocluster Induced Emission Enhancement. *Analyst* **2015**, 140 (8), 2719–2725.
- (220) Bhunia, S.; Kumar, S.; Purkayastha, P. Application of Photoinduced Electron Transfer with Copper Nanoclusters toward Finding Characteristics of Protein Pockets. *ACS Omega* **2019**, 4 (2), 2523–2532.
- (221) Zhao, X. J.; Huang, C. Z. Water-Soluble Luminescent Copper Nanoclusters Reduced and Protected by Histidine for Sensing of Guanosine 5'-Triphosphate. *New J. Chem.* **2014**, 38 (8), 3673.
- (222) Shen, J.-S.; Chen, Y.-L.; Wang, Q.-P.; Yu, T.; Huang, X.-Y.; Yang, Y.; Zhang, H.-W. In Situ Synthesis of Red Emissive Copper Nanoclusters in Supramolecular Hydrogels. *J. Mater. Chem. C* **2013**, 1 (11), 2092.
- (223) Lin, Y.-J.; Chen, P.-C.; Yuan, Z.; Ma, J.-Y.; Chang, H.-T. The Isomeric Effect of Mercaptobenzoic Acids on the Preparation and Fluorescence Properties of Copper Nanoclusters. *Chem. Commun.* **2015**, 51 (60), 11983–11986.
- (224) Zou, H. Y.; Lan, J.; Huang, C. Z. Dopamine Derived Copper Nanocrystals Used as an Efficient Sensing, Catalysis and Antibacterial Agent. *RSC Adv.* **2015**, 5 (69), 55832–55838.
- (225) Zhu, H.; Zhang, C.; Yin, Y. Rapid Synthesis of Copper Nanoparticles by Sodium Hypophosphite Reduction in Ethylene Glycol under Microwave Irradiation. *J. Cryst. Growth* **2004**, 270 (3–4), 722–728.

- (226) Kawasaki, H.; Kosaka, Y.; Myoujin, Y.; Narushima, T.; Yonezawa, T.; Arakawa, R. Microwave-Assisted Polyol Synthesis of Copper Nanocrystals without Using Additional Protective Agents. *Chem. Commun.* **2011**, 47 (27), 7740.
- (227) Aparna, R. S.; Syamchand, S. S.; George, S. Tannic Acid Stabilised Copper Nanocluster Developed Through Microwave Mediated Synthesis as a Fluorescent Probe for the Turn on Detection of Dopamine. *J. Clust. Sci.* **2017**, 28 (4), 2223–2238.
- (228) Jin, R. Atomically Precise Metal Nanoclusters: Stable Sizes and Optical Properties. *Nanoscale* **2015**, 7 (5), 1549–1565.
- (229) Qian, H.; Liu, C.; Jin, R. Controlled Growth of Molecularly Pure Au₂₅(SR)₁₈ and Au₃₈(SR)₂₄ Nanoclusters from the Same Polydispersed Crude Product. *Sci. China Chem.* **2012**, 55 (11), 2359–2365.
- (230) Li, G.; Abroshan, H.; Chen, Y.; Jin, R.; Kim, H. J. Experimental and Mechanistic Understanding of Aldehyde Hydrogenation Using Au₂₅ Nanoclusters with Lewis Acids: Unique Sites for Catalytic Reactions. *J. Am. Chem. Soc.* **2015**, 137 (45), 14295–14304.
- (231) Yuan, X.; Yu, Y.; Yao, Q.; Zhang, Q.; Xie, J. Fast Synthesis of Thiolated Au₂₅ Nanoclusters via Protection–Deprotection Method. *J. Phys. Chem. Lett.* **2012**, 3 (17), 2310–2314.
- (232) Lu, Y.; Jiang, Y.; Gao, X.; Chen, W. Charge State-Dependent Catalytic Activity of [Au₂₅(SC₁₂H₂₅)₁₈] Nanoclusters for the Two-Electron Reduction of Dioxygen to Hydrogen Peroxide. *Chem. Commun.* **2014**, 50 (62), 8464–8467.
- (233) Qian, H.; Zhu, Y.; Jin, R. Size-Focusing Synthesis, Optical and Electrochemical Properties of Monodisperse Au₃₈(SC₂H₄Ph)₂₄ Nanoclusters. *ACS Nano* **2009**, 3 (11), 3795–3803.
- (234) Toikkanen, O.; Ruiz, V.; Rönholm, G.; Kalkkinen, N.; Liljeroth, P.; Quinn, B. M. Synthesis and Stability of Monolayer-Protected Au₃₈ Clusters. *J. Am. Chem. Soc.* **2008**, 130 (33), 11049–11055.
- (235) Yam, V. W.-W.; Lam, C.-H.; Fung, W. K.-M.; Cheung, K.-K. Syntheses, Photophysics, and Photochemistry of Trinuclear Copper(I) Thiolate and Hexanuclear Copper(I) Selenolate Complexes: X-Ray Crystal Structures of [Cu₆(μ-Dppm)₄(μ₃-SePh)₄](BF₄)₂ and [Cu₆{μ-(Ph₂P)₂NH}₄(μ₃-SePh)₄](BF₄)₂. *Inorg. Chem.* **2001**, 40 (14), 3435–3442.
- (236) Leung, W.-P.; Chan, Y.-C.; Mak, T. C. W. Synthesis and Characterization of an Octanuclear Copper(I) Methanediide Cluster. *Dalt. Trans.* **2014**, 43 (1), 63–66.
- (237) Ford, P. C.; Vogler, A. Photochemical and Photophysical Properties of Tetranuclear and Hexanuclear Clusters of Metals with d¹⁰ and s² Electronic Configurations. *Acc. Chem. Res.* **1993**, 26 (4), 220–226.
- (238) Xu, H.; Yip, J. H. K. Novel Luminescent Tetranuclear and Pentanuclear Copper(I)–Dithiolates. *Inorg. Chem.* **2003**, 42 (15), 4492–4494.

- (239) Varnholt, B.; Dolamic, I.; Knoppe, S.; Bürgi, T. On the Flexibility of the Gold–Thiolate Interface: Racemization of the Au₄₀(SR)₂₄ Cluster. *Nanoscale* **2013**, *5* (20), 9568.
- (240) Schaaff, T. G.; Whetten, R. L. Giant Gold–Glutathione Cluster Compounds: Intense Optical Activity in Metal-Based Transitions. *J. Phys. Chem. B* **2000**, *104* (12), 2630–2641.
- (241) Gautier, C.; Bürgi, T. Chiral Inversion of Gold Nanoparticles. *J. Am. Chem. Soc.* **2008**, *130* (22), 7077–7084.
- (242) Gautier, C.; Taras, R.; Gladiali, S.; Bürgi, T. Chiral 1,1'-Binaphthyl-2,2'-Dithiol-Stabilized Gold Clusters: Size Separation and Optical Activity in the UV–Vis. *Chirality* **2008**, *20* (3–4), 486–493.
- (243) Gautier, C.; Bürgi, T. Chiral Gold Nanoparticles. *ChemPhysChem* **2009**, *10* (3), 483–492.
- (244) Gautier, C.; Bürgi, T. Vibrational Circular Dichroism of Adsorbed Molecules: BINAS on Gold Nanoparticles. *J. Phys. Chem. C* **2010**, *114* (38), 15897–15902.
- (245) Molina, B.; Sánchez-Castillo, A.; Knoppe, S.; Garzón, I. L.; Bürgi, T.; Tlahuice-Flores, A. Structures and Chiroptical Properties of the BINAS-Monosubstituted Au₃₈(SCH₃)₂₄ Cluster. *Nanoscale* **2013**, *5* (22), 10956.
- (246) Si, S.; Gautier, C.; Boudon, J.; Taras, R.; Gladiali, S.; Bürgi, T. Ligand Exchange on Au₂₅ Cluster with Chiral Thiols. *J. Phys. Chem. C* **2009**, *113* (30), 12966–12969.
- (247) Knoppe, S.; Azoulay, R.; Dass, A.; Bürgi, T. In Situ Reaction Monitoring Reveals a Diastereoselective Ligand Exchange Reaction between the Intrinsically Chiral Au₃₈(SR)₂₄ and Chiral Thiols. *J. Am. Chem. Soc.* **2012**, *134* (50), 20302–20305.
- (248) Knoppe, S.; Bürgi, T. The Fate of Au₂₅(SR)₁₈ Clusters upon Ligand Exchange with Binaphthyl-Dithiol: Interstaple Binding vs. Decomposition. *Phys. Chem. Chem. Phys.* **2013**, *15* (38), 15816.
- (249) Nieto-Ortega, B.; Bürgi, T. Vibrational Properties of Thiolate-Protected Gold Nanoclusters. *Acc. Chem. Res.* **2018**, *51* (11), 2811–2819.
- (250) Siebrands, T.; Giersig, M.; Mulvaney, P.; Fischer, C. H. Steric Exclusion Chromatography of Nanometer-Sized Gold Particles. *Langmuir* **1993**, *9* (9), 2297–2300.
- (251) Wang, C.; Cheng, H.; Sun, Y.; Lin, Q.; Zhang, C. Rapid Sonochemical Synthesis of Luminescent and Paramagnetic Copper Nanoclusters for Bimodal Bioimaging. *ChemNanoMat* **2015**, *1* (1), 27–31.
- (252) Wang, C.; Ling, L.; Yao, Y.; Song, Q. One-Step Synthesis of Fluorescent Smart Thermo-Responsive Copper Clusters: A Potential Nanothermometer in Living Cells. *Nano Res.* **2015**, *8* (6), 1975–1986.
- (253) Huang, H.; Li, H.; Wang, A.-J.; Zhong, S.-X.; Fang, K.-M.; Feng, J.-J. Green Synthesis of Peptide-Templated Fluorescent Copper Nanoclusters for Temperature Sensing and

- Cellular Imaging. *Analyst* **2014**, *139* (24), 6536–6541.
- (254) Das, N. K.; Ghosh, S.; Priya, A.; Datta, S.; Mukherjee, S. Luminescent Copper Nanoclusters as a Specific Cell-Imaging Probe and a Selective Metal Ion Sensor. *J. Phys. Chem. C* **2015**, *119* (43), 24657–24664.
- (255) Zhou, T.; Xu, W.; Yao, Q.; Zhao, T.; Chen, X. Highly Fluorescent Copper Nanoclusters as a Probe for the Determination of PH. *Methods Appl. Fluoresc.* **2015**, *3* (4), 044002.
- (256) Salorinne, K.; Lahtinen, T.; Koivisto, J.; Kalenius, E.; Nissinen, M.; Pettersson, M.; Häkkinen, H. Nondestructive Size Determination of Thiol-Stabilized Gold Nanoclusters in Solution by Diffusion Ordered NMR Spectroscopy. *Anal. Chem.* **2013**, *85* (7), 3489–3492.
- (257) Salorinne, K.; Lahtinen, T.; Malola, S.; Koivisto, J.; Häkkinen, H. Solvation Chemistry of Water-Soluble Thiol-Protected Gold Nanocluster Au₁₀₂ from DOSY NMR Spectroscopy and DFT Calculations. *Nanoscale* **2014**, *6* (14), 7823–7826.
- (258) Zhang, P. X-Ray Spectroscopy of Gold–Thiolate Nanoclusters. *J. Phys. Chem. C* **2014**, *118* (44), 25291–25299.
- (259) Zhang, P.; Sham, T. K. X-Ray Studies of the Structure and Electronic Behavior of Alkanethiolate-Capped Gold Nanoparticles: The Interplay of Size and Surface Effects. *Phys. Rev. Lett.* **2003**, *90* (24), 245502.
- (260) MacDonald, M. A.; Zhang, P.; Qian, H.; Jin, R. Site-Specific and Size-Dependent Bonding of Compositionally Precise Gold–Thiolate Nanoparticles from X-Ray Spectroscopy. *J. Phys. Chem. Lett.* **2010**, *1* (12), 1821–1825.
- (261) Sels, A.; Salassa, G.; Pollitt, S.; Guglieri, C.; Rupprechter, G.; Barrabés, N.; Bürgi, T. Structural Investigation of the Ligand Exchange Reaction with Rigid Dithiol on Doped (Pt, Pd) Au₂₅ Clusters. *J. Phys. Chem. C* **2017**, *121* (20), 10919–10926.
- (262) Yang, X.; Feng, Y.; Zhu, S.; Luo, Y.; Zhuo, Y.; Dou, Y. One-Step Synthesis and Applications of Fluorescent Cu Nanoclusters Stabilized by L-Cysteine in Aqueous Solution. *Anal. Chim. Acta* **2014**, *847*, 49–54.
- (263) Jia, X.; Li, J.; Wang, E. Cu Nanoclusters with Aggregation Induced Emission Enhancement. *Small* **2013**, *9* (22), 3873–3879.
- (264) Dolamic, I.; Varnholt, B.; Bürgi, T. Far-Infrared Spectra of Well-Defined Thiolate-Protected Gold Clusters. *Phys. Chem. Chem. Phys.* **2013**, *15* (45), 19561.
- (265) Tero, T. R.; Malola, S.; Koncz, B.; Pohjolainen, E.; Lautala, S.; Mustalahti, S.; Permi, P.; Groenhof, G.; Pettersson, M.; Häkkinen, H. Dynamic Stabilization of the Ligand-Metal Interface in Atomically Precise Gold Nanoclusters Au₆₈ and Au₁₄₄ Protected by Meta-Mercaptobenzoic Acid. *ACS Nano* **2017**, *11* (12), 11872–11879.
- (266) Zhang, Y.; Shuang, S.; Dong, C.; Lo, C. K.; Paa, M. C.; Choi, M. M. F. Application of HPLC

- and MALDI-TOF MS for Studying As-Synthesized Ligand-Protected Gold Nanoclusters Products. *Anal. Chem.* **2009**, *81* (4), 1676–1685.
- (267) Chakraborty, P.; Pradeep, T. The Emerging Interface of Mass Spectrometry with Materials. *NPG Asia Mater.* **2019**, *11* (1), 48.
- (268) Dass, A.; Stevenson, A.; Dubay, G. R.; Tracy, J. B.; Murray, R. W. Nanoparticle MALDI-TOF Mass Spectrometry without Fragmentation: Au₂₅(SCH₂CH₂Ph)₁₈ and Mixed Monolayer Au₂₅(SCH₂CH₂Ph)_{18-x}(L)_x. *J. Am. Chem. Soc.* **2008**, *130* (18), 5940–5946.
- (269) Niihori, Y.; Shima, D.; Yoshida, K.; Hamada, K.; Nair, L. V.; Hossain, S.; Kurashige, W.; Negishi, Y. High-Performance Liquid Chromatography Mass Spectrometry of Gold and Alloy Clusters Protected by Hydrophilic Thiolates. *Nanoscale* **2018**, *10* (4), 1641–1649.
- (270) Negishi, Y.; Kurashige, W.; Niihori, Y.; Iwasa, T.; Nobusada, K. Isolation, Structure, and Stability of a Dodecanethiolate-Protected Pd₁Au₂₄ Cluster. *Phys. Chem. Chem. Phys.* **2010**, *12* (23), 6219.
- (271) Negishi, Y.; Nakazaki, T.; Malola, S.; Takano, S.; Niihori, Y.; Kurashige, W.; Yamazoe, S.; Tsukuda, T.; Häkkinen, H. A Critical Size for Emergence of Nonbulk Electronic and Geometric Structures in Dodecanethiolate-Protected Au Clusters. *J. Am. Chem. Soc.* **2015**, *137* (3), 1206–1212.
- (272) Schaaff, T. G.; Knight, G.; Shafiqullin, M. N.; Borkman, R. F.; Whetten, R. L. Isolation and Selected Properties of a 10.4 KDa Gold:Glutathione Cluster Compound. *J. Phys. Chem. B* **1998**, *102* (52), 10643–10646.
- (273) Levi-Kalisman, Y.; Jadzinsky, P. D.; Kalisman, N.; Tsunoyama, H.; Tsukuda, T.; Bushnell, D. A.; Kornberg, R. D. Synthesis and Characterization of Au₁₀₂(*p*-MBA)₄₄ Nanoparticles. *J. Am. Chem. Soc.* **2011**, *133* (9), 2976–2982.
- (274) Negishi, Y.; Takasugi, Y.; Sato, S.; Yao, H.; Kimura, K.; Tsukuda, T. Magic-Numbered Au *n* Clusters Protected by Glutathione Monolayers (*n* = 18, 21, 25, 28, 32, 39): Isolation and Spectroscopic Characterization. *J. Am. Chem. Soc.* **2004**, *126* (21), 6518–6519.
- (275) Hong, Y.; Lam, J. W. Y.; Tang, B. Z. Aggregation-Induced Emission. *Chem. Soc. Rev.* **2011**, *40* (11), 5361.
- (276) Goswami, N.; Yao, Q.; Luo, Z.; Li, J.; Chen, T.; Xie, J. Luminescent Metal Nanoclusters with Aggregation-Induced Emission. *J. Phys. Chem. Lett.* **2016**, *7* (6), 962–975.
- (277) Li, Z.; Guo, S.; Lu, C. A Highly Selective Fluorescent Probe for Sulfide Ions Based on Aggregation of Cu Nanocluster Induced Emission Enhancement. *Analyst* **2015**, *140* (8), 2719–2725.
- (278) Weerawardene, K. L. D. M.; Aikens, C. M. Theoretical Insights into the Origin of Photoluminescence of Au₂₅(SR)₁₈⁻ Nanoparticles. *J. Am. Chem. Soc.* **2016**, *138* (35), 11202–11210.

- (279) Weerawardene, K. L. D. M.; Guidez, E. B.; Aikens, C. M. Photoluminescence Origin of Au₃₈(SR)₂₄ and Au₂₂(SR)₁₈ Nanoparticles: A Theoretical Perspective. *J. Phys. Chem. C* **2017**, *121* (28), 15416–15423.
- (280) Link, S.; Beeby, A.; FitzGerald, S.; El-Sayed, M. A.; Schaaff, T. G.; Whetten, R. L. Visible to Infrared Luminescence from a 28-Atom Gold Cluster. *J. Phys. Chem. B* **2002**, *106* (13), 3410–3415.
- (281) Shu, T.; Wang, J.; Lin, X.; Zhou, Z.; Liang, F.; Su, L.; Zhang, X. Dual-Emissive Gold Nanoclusters for Label-Free and Separation-Free Ratiometric Fluorescence Sensing of 4-Nitrophenol Based on the Inner Filter Effect. *J. Mater. Chem. C* **2018**, *6* (18), 5033–5038.
- (282) Yang, J.; Li, Z.; Jia, Q. Design of Dual-Emission Fluorescence Sensor Based on Cu Nanoclusters with Solvent-Dependent Effects: Visual Detection of Water via a Smartphone. *Sensors Actuators B Chem.* **2019**, *297* (July), 126807.
- (283) Salassa, G.; Bürgi, T. NMR Spectroscopy: A Potent Tool for Studying Monolayer-Protected Metal Nanoclusters. *Nanoscale Horizons* **2018**, *3* (5), 457–463.
- (284) Salorinne, K.; Malola, S.; Wong, O. A.; Rithner, C. D.; Chen, X.; Ackerson, C. J.; Häkkinen, H. Conformation and Dynamics of the Ligand Shell of a Water-Soluble Au₁₀₂ Nanoparticle. *Nat. Commun.* **2016**, *7* (1), 10401.
- (285) Parker, J. F.; Choi, J. P.; Wang, W.; Murray, R. W. Electron Self-Exchange Dynamics of the Nanoparticle Couple [Au₂₅(SC₂Ph)₁₈]^{0/1-} by Nuclear Magnetic Resonance Line-Broadening. *J. Phys. Chem. C* **2008**, *112* (36), 13976–13981.
- (286) Venzo, A.; Antonello, S.; Gascón, J. A.; Guryanov, I.; Leapman, R. D.; Perera, N. V.; Sousa, A.; Zamuner, M.; Zanella, A.; Maran, F. Effect of the Charge State ($z = -1, 0, +1$) on the Nuclear Magnetic Resonance of Monodisperse Au₂₅[S(CH₂)₂Ph]₁₈^z Clusters. *Anal. Chem.* **2011**, *83* (16), 6355–6362.
- (287) Agrachev, M.; Antonello, S.; Dainese, T.; Gascón, J. A.; Pan, F.; Rissanen, K.; Ruzzi, M.; Venzo, A.; Zoleo, A.; Maran, F. A Magnetic Look into the Protecting Layer of Au₂₅ Clusters. *Chem. Sci.* **2016**, *7* (12), 6910–6918.
- (288) Pengo, P.; Bazzo, C.; Boccalon, M.; Pasquato, L. Differential Reactivity of the Inner and Outer Positions of Au₂₅(SCH₂CH₂Ph)₁₈ Dimeric Staples under Place Exchange Conditions. *Chem. Commun.* **2015**, *51* (15), 3204–3207.
- (289) Salassa, G.; Sels, A.; Mancin, F.; Bürgi, T. Dynamic Nature of Thiolate Monolayer in Au₂₅(SR)₁₈ Nanoclusters. *ACS Nano* **2017**, *11* (12), 12609–12614.
- (290) Qian, H.; Zhu, M.; Gayathri, C.; Gil, R. R.; Jin, R. Chirality in Gold Nanoclusters Probed by NMR Spectroscopy. *ACS Nano* **2011**, *5* (11), 8935–8942.
- (291) Riccardi, L.; De Biasi, F.; De Vivo, M.; Bürgi, T.; Rastrelli, F.; Salassa, G. Dynamic Origin of Chirality Transfer between Chiral Surface and Achiral Ligand in Au₃₈ Clusters. *ACS Nano*

- 2019, 13 (6), 7127–7134.
- (292) Qian, H.; Eckenhoff, W. T.; Zhu, Y.; Pintauer, T.; Jin, R. Total Structure Determination of Thiolate-Protected Au₃₈ Nanoparticles. *J. Am. Chem. Soc.* **2010**, 132 (24), 8280–8281.
- (293) Liu, C.; Li, T.; Li, G.; Nobusada, K.; Zeng, C.; Pang, G.; Rosi, N. L.; Jin, R. Observation of Body-Centered Cubic Gold Nanocluster. *Angew. Chemie Int. Ed.* **2015**, 54 (34), 9826–9829.
- (294) Dehnen, S.; Eichhöfer, A.; Fenske, D. Chalcogen-Bridged Copper Clusters. *Eur. J. Inorg. Chem.* **2002**, 2002 (2), 279.
- (295) Chakrahari, K. K.; Liao, J. H.; Kahlal, S.; Liu, Y. C.; Chiang, M. H.; Saillard, J. Y.; Liu, C. W. [Cu₁₃{S₂CNⁿBu₂}₆(Acetylide)₄]⁺: A Two-Electron Superatom. *Angew. Chemie - Int. Ed.* **2016**, 55 (47), 14704–14708.
- (296) Nguyen, T.-A. D.; Jones, Z. R.; Goldsmith, B. R.; Buratto, W. R.; Wu, G.; Scott, S. L.; Hayton, T. W. A Cu₂₅ Nanocluster with Partial Cu(0) Character. *J. Am. Chem. Soc.* **2015**, 137 (41), 13319–13324.
- (297) Nguyen, T. A. D.; Jones, Z. R.; Leto, D. F.; Wu, G.; Scott, S. L.; Hayton, T. W. Ligand-Exchange-Induced Growth of an Atomically Precise Cu₂₉ Nanocluster from a Smaller Cluster. *Chem. Mater.* **2016**, 28 (22), 8385–8390.
- (298) Edwards, A. J.; Dhayal, R. S.; Liao, P. K.; Liao, J. H.; Chiang, M. H.; Piltz, R. O.; Kahlal, S.; Saillard, J. Y.; Liu, C. W. Chinese Puzzle Molecule: A 15 hydride, 28 copper Atom Nanoball. *Angew. Chemie - Int. Ed.* **2014**, 53 (28), 7214–7218.
- (299) Nguyen, T. A. D.; Goldsmith, B. R.; Zaman, H. T.; Wu, G.; Peters, B.; Hayton, T. W. Synthesis and Characterization of a Cu₁₄ Hydride Cluster Supported by Neutral Donor Ligands. *Chem. - A Eur. J.* **2015**, 21 (14), 5341–5344.
- (300) Dhayal, R. S.; Liao, J.-H.; Lin, Y.-R.; Liao, P.-K.; Kahlal, S.; Saillard, J.-Y.; Liu, C. W. A Nanospheric Polyhydrido Copper Cluster of Elongated Triangular Orthobicupola Array: Liberation of H₂ from Solar Energy. *J. Am. Chem. Soc.* **2013**, 135 (12), 4704–4707.
- (301) Dhayal, R. S.; Liao, J. H.; Kahlal, S.; Wang, X.; Liu, Y. C.; Chiang, M. H.; Van Zyl, W. E.; Saillard, J. Y.; Liu, C. W. [Cu₃₂(H)₂₀{S₂P(O*i*Pr)₂]₁₂]: The Largest Number of Hydrides Recorded in a Molecular Nanocluster by Neutron Diffraction. *Chem. - A Eur. J.* **2015**, 21 (23), 8369–8374.
- (302) Huertos, M. A.; Cano, I.; Bandeira, N. A. G.; Benet-Buchholz, J.; Bo, C.; van Leeuwen, P. W. N. M. Phosphinothiolates as Ligands for Polyhydrido Copper Nanoclusters. *Chem. - A Eur. J.* **2014**, 20 (49), 16121–16127.
- (303) Fu, M.-L.; Issac, I.; Fenske, D.; Fuhr, O. Metal-Rich Copper Chalcogenide Clusters at the Border Between Molecule and Bulk Phase: The Structures of [Cu₉₃Se₄₂(SeC₆H₄SMe)₉(PPh₃)₁₈], [Cu₉₆Se₄₅(SeC₆H₄SMe)₆(PPh₃)₁₈], and [Cu₁₃₆S₅₆(SCH₂C₄H₃O)₂₄(Dpppt)₁₀]. *Angew. Chemie Int. Ed.* **2010**, 49 (38), 6899–6903.

- (304) Bestgen, S.; Fuhr, O.; Roesky, P. W.; Fenske, D. Synthesis and Molecular Structure of a Spheroidal Binary Nanoscale Copper Sulfide Cluster. *Dalt. Trans.* **2016**, 45 (38), 14907–14910.
- (305) Duan, T.; Zhang, X.-Z.; Zhang, Q. Synthesis and Crystal Structure of a Polynuclear Copper-Selenide Cluster $[\text{Cu}'_{36}(\text{Cu}^{\text{II}}\text{Cl})_2\text{Se}_{13}(\text{SePh})_{12}(\text{Dppe})_6] \cdot 3\text{EtOH}$. *Zeitschrift für Naturforsch. B* **2008**, 63 (8), 941–944.
- (306) Li, Y.; Wang, J.; Luo, P.; Ma, X.; Dong, X.; Wang, Z.; Du, C.; Zang, S.; Mak, T. C. W. Cu_{14} Cluster with Partial Cu(0) Character: Difference in Electronic Structure from Isostructural Silver Analog. *Adv. Sci.* **2019**, 1900833 (0), 1900833.
- (307) Nguyen, T.-A. D.; Jones, Z. R.; Goldsmith, B. R.; Buratto, W. R.; Wu, G.; Scott, S. L.; Hayton, T. W. A Cu_{25} Nanocluster with Partial Cu(0) Character. *J. Am. Chem. Soc.* **2015**, 137 (41), 13319–13324.
- (308) Pitkänen, L.; Striegel, A. M. Size-Exclusion Chromatography of Metal Nanoparticles and Quantum Dots. *TrAC Trends Anal. Chem.* **2016**, 80, 311–320.
- (309) Al-Somali, A. M.; Krueger, K. M.; Falkner, J. C.; Colvin, V. L. Recycling Size Exclusion Chromatography for the Analysis and Separation of Nanocrystalline Gold. *Anal. Chem.* **2004**, 76 (19), 5903–5910.
- (310) Niihori, Y.; Uchida, C.; Kurashige, W.; Negishi, Y. High-Resolution Separation of Thiolate-Protected Gold Clusters by Reversed-Phase High-Performance Liquid Chromatography. *Phys. Chem. Chem. Phys.* **2016**, 18 (6), 4251–4265.
- (311) Niihori, Y.; Kikuchi, Y.; Shima, D.; Uchida, C.; Sharma, S.; Hossain, S.; Kurashige, W.; Negishi, Y. Separation of Glutathionate-Protected Gold Clusters by Reversed-Phase Ion-Pair High-Performance Liquid Chromatography. *Ind. Eng. Chem. Res.* **2017**, 56 (4), 1029–1035.
- (312) Niihori, Y.; Yoshida, K.; Hossain, S.; Kurashige, W.; Negishi, Y. Deepening the Understanding of Thiolate-Protected Metal Clusters Using High-Performance Liquid Chromatography. *Bull. Chem. Soc. Jpn.* **2019**, 92 (3), 664–695.
- (313) Song, Y.; Jimenez, V.; McKinney, C.; Donkers, R.; Murray, R. W. Estimation of Size for 1–2 nm Nanoparticles Using an HPLC Electrochemical Detector of Double Layer Charging. *Anal. Chem.* **2003**, 75 (19), 5088–5096.
- (314) Jimenez, V. L.; Leopold, M. C.; Mazzitelli, C.; Jorgenson, J. W.; Murray, R. W. HPLC of Monolayer-Protected Gold Nanoclusters. *Anal. Chem.* **2003**, 75 (2), 199–206.
- (315) Niihori, Y.; Matsuzaki, M.; Uchida, C.; Negishi, Y. Advanced Use of High-Performance Liquid Chromatography for Synthesis of Controlled Metal Clusters. *Nanoscale* **2014**, 6 (14), 7889–7896.
- (316) Sels, A.; Barrabés, N.; Knoppe, S.; Bürgi, T. Isolation of Atomically Precise Mixed Ligand Shell PdAu_{24} Clusters. *Nanoscale* **2016**, 8 (21), 11130–11135.

- (317) Niihori, Y.; Koyama, Y.; Watanabe, S.; Hashimoto, S.; Hossain, S.; Nair, L. V.; Kumar, B.; Kurashige, W.; Negishi, Y. Atomic and Isomeric Separation of Thiolate-Protected Alloy Clusters. *J. Phys. Chem. Lett.* **2018**, *9* (17), 4930–4934.
- (318) Niihori, Y.; Kikuchi, Y.; Kato, A.; Matsuzaki, M.; Negishi, Y. Understanding Ligand-Exchange Reactions on Thiolate-Protected Gold Clusters by Probing Isomer Distributions Using Reversed-Phase High-Performance Liquid Chromatography. *ACS Nano* **2015**, *9* (9), 9347–9356.
- (319) Barrabés, N.; Zhang, B.; Bürgi, T. Racemization of Chiral Pd₂Au₃₆(SC₂H₄Ph)₂₄: Doping Increases the Flexibility of the Cluster Surface. *J. Am. Chem. Soc.* **2014**, *136* (41), 14361–14364.
- (320) Zhang, B.; Bürgi, T. Doping Silver Increases the Au₃₈(SR)₂₄ Cluster Surface Flexibility. *J. Phys. Chem. C* **2016**, *120* (8), 4660–4666.
- (321) Adamson, N. J.; Reynolds, E. C. Rules Relating Electrophoretic Mobility, Charge and Molecular Size of Peptides and Proteins. *J. Chromatogr. B Biomed. Sci. Appl.* **1997**, *699* (1–2), 133–147.
- (322) Westermeier, R. Gel Electrophoresis. In *eLS*; John Wiley & Sons, Ltd: Chichester, UK, 2005; pp 165–167.
- (323) Deshmane, S. L.; Mukerjee, R.; Fan, S.; Sawaya, B. E. High-Performance Capillary Electrophoresis for Determining HIV-1 Tat Protein in Neurons. *PLoS One* **2011**, *6* (1), e16148.
- (324) Tagliaro, F.; Manetto, G.; Crivellente, F.; Smith, F. . A Brief Introduction to Capillary Electrophoresis. *Forensic Sci. Int.* **1998**, *92* (2–3), 75–88.
- (325) Chetwynd, A.; Guggenheim, E.; Briffa, S.; Thorn, J.; Lynch, I.; Valsami-Jones, E. Current Application of Capillary Electrophoresis in Nanomaterial Characterisation and Its Potential to Characterise the Protein and Small Molecule Corona. *Nanomaterials* **2018**, *8* (2), 99.
- (326) Franze, B.; Strenge, I.; Engelhard, C. Separation and Detection of Gold Nanoparticles with Capillary Electrophoresis and ICP-MS in Single Particle Mode (CE-SP-ICP-MS). *J. Anal. At. Spectrom.* **2017**, *32* (8), 1481–1489.
- (327) Schnabel, U.; Fischer, C.-H.; Kenndler, E. Characterization of Colloidal Gold Nanoparticles According to Size by Capillary Zone Electrophoresis. *J. Microcolumn Sep.* **1997**, *9* (7), 529–534.
- (328) Wan, T.; Tang, F.; Yin, Y.; Zhang, M.; Choi, M. M. F.; Yang, X. Size-dependent Electrophoretic Migration and Separation of Water-soluble Gold Nanoclusters by Capillary Electrophoresis. *Electrophoresis* **2019**, *40* (9), 1345–1352.
- (329) Lo, C. K.; Paa, M. C.; Xiao, D.; Choi, M. M. F. Capillary Electrophoresis, Mass Spectrometry, and UV-Visible Absorption Studies on Electrolyte-Induced Fractionation of Gold

Nanoclusters. *Anal. Chem.* **2008**, *80* (7), 2439–2446.

- (330) Bouri, M.; Salghi, R.; Algarra, M.; Zougagh, M.; Ríos, A. A Novel Approach to Size Separation of Gold Nanoparticles by Capillary Electrophoresis–Evaporative Light Scattering Detection. *RSC Adv.* **2015**, *5* (22), 16672–16677.
- (331) Dziomba, S.; Ciura, K.; Kociałkowska, P.; Prahl, A.; Wielgomas, B. Gold Nanoparticles Dispersion Stability under Dynamic Coating Conditions in Capillary Zone Electrophoresis. *J. Chromatogr. A* **2018**, *1550* (September 2017), 63–67.

Post-functionalization of AuNCs

5.1. Ligand exchange reactions on chiral Au₃₈ cluster: variations in CD line shapes caused by the modification of ligand shell composition

Ligand exchange reactions have become a highly accomplishable post-synthetic strategy to precisely engineer the ligand shell of atomically precise noble metal nanoclusters. By modifying the chemical structure of the exchanging ligand with chromophore substituents or adding chiral centers allows direct functionalization of the cluster with desired properties. As such, post-functionalized gold nanoclusters with unique physical-chemical properties found applications in optoelectronics, catalysis and biomedicine. Herein, we successfully performed ligand exchange reactions with chiral Au₃₈(2-PET)₂₄ cluster (both racemic and enantiopure forms) and chiral [4]-helicene-2-thiol ligand (MT4). The reaction products with a composition of Au₃₈(2-PET)_{24-x}(MT4)_x were analyzed using UV-vis spectroscopy and MALDI mass spectrometry. It was found that up to ten 2-PET ligands can be replaced with a chiral ligand on the cluster surface according to MALDI analysis. Consequently, the UV-vis and CD spectra of the cluster have been strongly affected by the ligand exchange reaction. The intensity of CD signals of Au₃₈(2-PET)_{24-x}(MT4)_x were drastically reduced and red shifted with respect to reference Au₃₈(2-PET)₂₄ cluster. Moreover, the appearance of the other enantiomer in the HPLC chromatogram revealed the partial racemization of the cluster. Altogether, we envisioned the possible mechanism of the ligand exchange reaction and partial racemization of the enantiomers caused by the adsorption of chiral MT4 ligand.

1. Introduction

Recently, ultra-small thiolate-protected gold nanoclusters of the formula of $Au_n(SR)_m$ (< 2 nm core diameter) have gained tremendous interest in research due to their unique size-dependent chiroptical properties.^{1,2} Due to the nano-size regime, the distinctive quantum confinement effects result in discrete electronic energy band gap structure and molecular-like properties, such as HOMO-LUMO electronic transition, enhanced photoluminescence and intrinsic magnetism.^{3,4} These unique properties are drastically different from their larger counterparts (nanoparticles) and provide opportunities for developing new applications.⁵⁻¹⁰ Thus, a detailed characterization of size-dependent electronic properties such as optical absorption spectra,¹¹ circular dichroism (ECD and VCD),¹²⁻¹⁵ nonlinear optical properties^{16,17} and photoluminescence,^{18,19} is a prerequisite to further assess their applications. However, among several clusters that have been successfully synthesized and characterized with various physical-chemical methods,^{20,21} an atomically precise $Au_{38}(SR)_{24}$ cluster attracts much interest due to its intrinsic metal-based chiral features in a large optical window. Briefly, the structure of an Au_{38} cluster consists of an Au_{23} kernel, which is formed by the fusion of two icosahedral Au_{13} cores having a common Au_3 face.²² Moreover, the Au_{23} core is surrounded by three monomeric (Au-S-Au) and six dimeric (Au-S-Au-S-Au) staples. More importantly, the long staples are organized in a chiral fashion, thus giving rise to strong chiroptical responses.

Although atomically precise gold nanoclusters emerge pronounced chiroptical properties, high stability and catalytic activity, it can further be altered by applying post-synthetic functionalization strategies: metal doping and ligand exchange.²³ Among this, ligand exchange reactions are especially useful for modifying the protective ligand shell and surface composition in a controlled manner.²³ The choice of the exchanging ligand plays a crucial role on chiroptical properties, stability and solubility of the resulting reaction products. Furthermore, it can lead to dramatic changes in clusters' native properties. In this context, structural distortions upon attaching a new ligand to the cluster surface are highly plausible and even the transformations of clusters have been observed.^{24,25}

Several examples of the ligand exchange reaction between Au₃₈ cluster and chiral 1,1'-binaphthyl-2,2'-dithiol (BINAS),²⁶ [2,2] paracyclophane-4-thiol (PCP-4-SH)²⁷ and achiral thiophenol²⁸ ligands have already been reported. Herein, the reactions arose obvious changes in the UV-vis spectrum associated with the formation of various species. In addition, the modification of the ligand shell composition sometimes induced instability and initiated the decomposition of the cluster in the solution. However, recent studies showed, that depending on the structure of the incoming ligand, the ligand exchange reaction is not only limited to structural and geometrical distortions leading to the formation of mixed ligand shell species in solution, but also causes substantial core-size transformations and thus resulting in the appearance of different clusters in the solution. For example, a novel Au₃₆ cluster with an unusual fcc-core structure has been synthesized as a result of a harsh etching process in the presence of a new thiol ligand.^{24,25,29}

Based on the above-mentioned works, we aimed to study the ligand exchange reaction between chiral, but kinetically labile [4]-helicene-2-thiol ligand and Au₃₈(2-PET)₂₄ cluster. The choice and an interest in helicenes are justified for several reasons.

First, helicenes, as polycyclic aromatic compounds, resemble a screw-type molecular system and are analogues to biologically relevant compounds.³⁰ Second, as helical structures, they are intrinsically chiral and possess strong chiroptical properties. The properties and the structures can be varied by modifying its backbone, attaching functional groups or increasing the number of fused aromatic rings in the structure, i.e. increasing the degree of helicity. The separation of *M* and *P* enantiomers of higher helicenes (pentahelicene and bigger) has already been achieved and they possess perfect mirror images of one another in their corresponding electronic CD spectra (ECD).³¹ However, unlike the other helicenes, the enantiomeric separation of [4]-helicene has not been achieved due to the low racemization barrier (< 16 kJ/mol)^{32,33} and only the calculated CD spectrum is available.³¹

Thus, initially, our keen interest was to examine whether the attachment of the [4]-helicene-2-thiol ligand to the intrinsically chiral and enantiopure cluster would stabilize the chiral configuration of the ligand and whether one configuration would be preferred over the other depending on the cluster's absolute configuration.

2. Experimental Section

2.1. Materials. Hydrogen tetrachloroaurate (III) trihydrate (ACS, Alfa Aesar, 99.99%), L-glutathione reduced (Carl Roth AG, ≥98%), sodium borohydride (Aldrich, ≥96%) acetone (Fisher, 99.7%), toluene (Fisher, 99.9%), ethanol (Sigma-Aldrich, >99.8%), methanol (Fisher, 99.9%), 2-phenylethanethiol (Sigma-Aldrich-Fluka, 99+%), dichloromethane (Merck, 99.7+%), nanopure water (>18 MΩ), [4]-helicene-2-thiol ligand (MT4 shortly, was received in collaboration with Prof. Narcis Avarvari, University of Angers, France).

2.2. Synthesis of chiral Au₃₈(2-PET)₂₄ cluster and ligand exchange reaction with MT4 ligand.

Au₃₈(2-PET)₂₄ cluster was synthesized according to the previously established protocol.³⁴ Briefly, 1 g of tetrachloroauric acid trihydrate (HAuCl₄*3H₂O) dissolved in 50 mL acetone was mixed with 3.12 g L-glutathione (GSH) suspension in acetone and vigorously stirred for 30 min in an ice bath. Afterwards, freshly prepared and ice-cooled solution of sodium borohydride (960 mg NaBH₄ in 30 mL H₂O) was added all at once. Immediately, the reaction mixture changed its color to dark brown corresponding to the formation of Au_n(GS)_m precipitate. The reaction mixture was left to stir at room temperature for 20 min. After that, the acetone was decanted, and the crude mixture was washed with methanol several times. Next, the GSH-protected clusters were dissolved in 30 mL of water. 1.6 mL of ethanol as a phase transfer agent together with 10 mL of toluene were also added. After all, 10 mL of 2-phenylethylthiol (2-PET shortly) ligand was added and the crude mixture was left for etching at 80 °C for 4 h. After reaction, the black precipitant was filtrated through PTFE syringe filter (0.2 μm), extensively washed with methanol to remove excess thiol and other by-products and finally, dried in vacuum rotary evaporator at room temperature.

Note that the above described synthesis leads to the formation of polydisperse mixture of various particles and clusters. The separation of Au₃₈ clusters was completed with size-exclusion chromatography (SEC) using BioBeads SX-1 suspended in toluene.

Ligand exchange reaction between chiral Au₃₈(2-PET)₂₄ cluster and MT4 ligand was carried out under mild reactions conditions (1:20, 1:50 and 1:100 cluster/ligand molar ratios, room temperature or elevated heating, toluene solution, 24 h). The number of exchanged ligands on

the cluster surface was controlled by altering the cluster/ligand molar ratios as well as heating the solution up to 50 °C.

2.3. Characterization methods. UV-vis spectra were recorded on the Varian Cary 50 spectrophotometer, using a quartz cuvette of 1 cm path length. Spectra were measured in toluene and normalized at 400 nm.

CD spectra were recorded on a JASCO J-815 CD-spectrometer using a quartz cuvette of 2 mm path length. The spectra were recorded in diluted solutions of DCM and the signal of the solvent was subtracted. For each spectrum, three scans at a scanning speed of 100 nm/min at a data pitch of 0.1 nm were averaged. The spectra were recorded at 20 °C; for temperature control, a JASCO PFD-350S Peltier element was used. Anisotropy factors ($\Delta A/A$) $g = \theta$ [mdeg]/ (32980 \times A) were calculated using the ultraviolet-visible spectrum provided by the CD spectrometer.

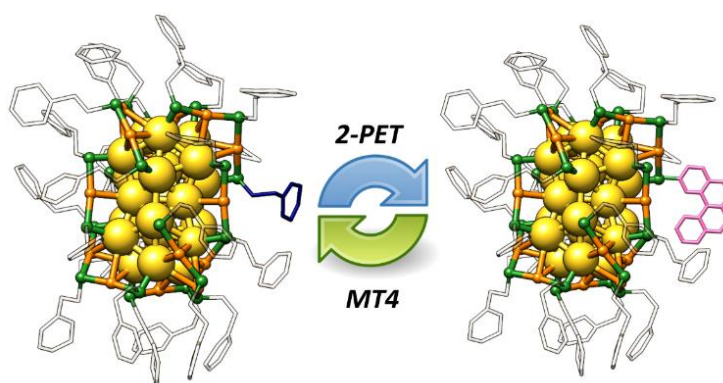
MALDI-TOF mass spectra were obtained using a Bruker Autoflex mass spectrometer equipped with a nitrogen laser at near threshold laser fluence in positive linear mode. [3-(4-tert-butylphenyl)-2-methyl-2-propenylidene]malononitrile was used as the matrix with a 1:1000 analyte : matrix ratio. A volume of 2 μ l of the analyte/matrix mixture was applied to the target and air-dried.

Chromatographic HPLC separation of the chiral Au₃₈(2-PET)₂₄ and exchange samples were successfully achieved on a JASCO 20XX HPLC system equipped with a semipreparative Phenomenex Lux-Cellulose-1 column (5 μ m, 250 mm \times 10 mm) using n-hexane:isopropanol (80:20) mobile phase at the flow rate of 3 mL/min. The analytes were detected with a JASCO 2077 plus UV detector operated at 300 nm.

3. Results and Discussion

In general, the concept of ligand exchange reaction relies on tuning the chiroptical properties of the native cluster and introducing new functionalities by carefully choosing appropriate, functional ligands. Since the thiolated MT4 ligand is intrinsically chiral, one would expect a change or enhancement of the CD signals of Au₃₈ cluster after ligand exchange reaction. However, as we

have already mentioned about the impracticability of obtaining enantiomers of the MT4 ligand, only the racemic mixture of the helicine ligand has been considered for further ligand exchange process with both racemic and enantiopure cluster. For this purpose, the ligand exchange reaction between intrinsically chiral $\text{Au}_{38}(\text{2-PET})_{24}$ cluster (racemic mixture) and MT4 ligand was carried out at 50 °C by using different cluster/ligand molar ratios (1:20, 1:50 and 1:100). Note, that one incoming MT4 ligand would exchange with one 2-PET ligand leading to the formation of clusters with an $\text{Au}_{38}(\text{2-PET})_{24-x}(\text{MT4})_x$ composition as shown in **Scheme 1**.



Scheme 1 Schematic representation of the ligand exchange reaction between Au_{38} cluster and MT4 ligand. The gold atoms on the staples are colored in orange, sulfur atoms are in green. The leaving 2-PET ligand is highlighted in blue and the incoming MT4 in magenta.

First, two initial cluster/ligand ratios (1:50 and 1:100) were used to study the effect of the ligand concentration on the total number of exchange product on the cluster surface. Preliminary analyses showed (not shown), that high concentrations of helical ligand (above 10 equivalents of ligand) are necessary to drive the ligand exchange reaction forward and thus, two concentrations as mentioned above were used. The UV-vis spectrum of the $\text{Au}_{38}(\text{2-PET})_{24}$ before the reaction was recorded to be further used as a reference. According to the UV-vis results in **Fig. 1**, the spectrum of 1:50 cluster/ligand molar ratio perfectly matches with the reference. No obvious changes are evident on the absorption spectrum upon ligand exchange reaction between leaving 2-PET ligand and incoming MT4 ligand. Yet several exchanged species were formed in the solution according to the MALDI analysis (to be discussed later). However, with increasing the

concentration of ligand (100 equivalents with respect to cluster), the characteristic absorption fingerprints of the cluster become less expressed at higher wavelengths. Additionally, at lower wavelengths, i.e. below 400 nm, a strong increase in absorbance on the UV-vis spectrum is mostly ascribed to the MT4 ligand (**Fig. S1**).

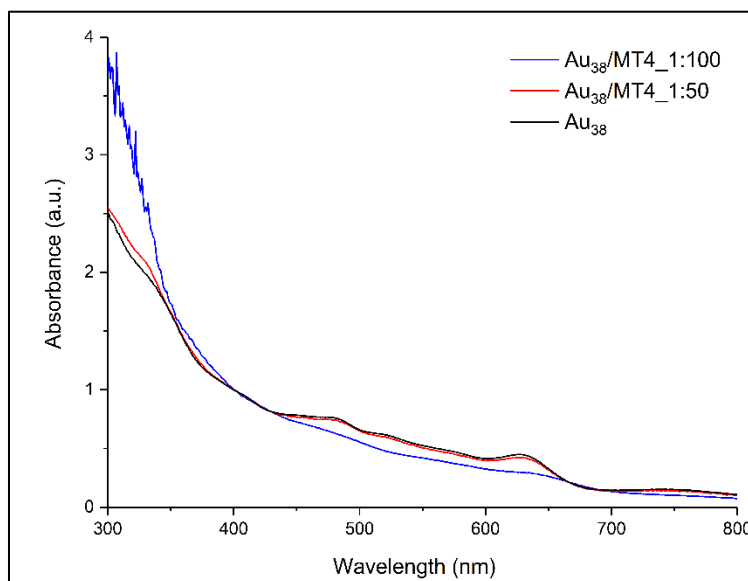


Fig. 1 UV-vis spectra of exchange samples using 1:50 and 1:100 cluster/ligand molar ratios. The UV-vis spectrum of $\text{Au}_{38}(\text{2-PET})_{24}$ is used as a reference. The spectra were measured in toluene and are normalized at 400 nm for comparison.

According to MALDI analyses (**Fig. 2**), up to three MT4 ligands were successfully exchanged on the cluster surface. The mass difference between incoming and the leaving ligand is about m/z 123 thus giving rise to a mass spectrum with equally spaced ($\Delta m=123$) peaks corresponding to the addition of MT4 ligands to the parent cluster. From the mass spectra the average exchange number can be calculated. By doing so, $\bar{x}=0.87$ and $\bar{x}=0.93$ were calculated for 1:50 and 1:100 cluster/ligand molar ratios respectively (**Table S1**). We noted that depending on the ionization (laser) power in the mass spectrometer, the relative intensities of most abundant species in the sample varied, however, the maximal exchange number of MT4 ligand has not been much affected. Besides our efforts to minimize in-source fragmentation of the sample, under applied ionization power different fragments reached to the detector and were carefully examined.

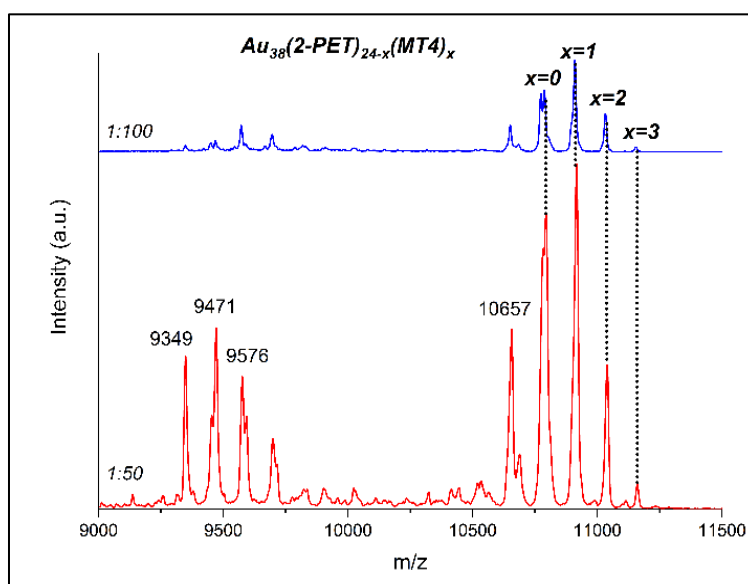


Fig. 2 MALDI analyses of the samples after ligand exchange reactions using 1:50 and 1:100 cluster/ligand molar ratios. The exchanged species are presented by the symbol “x”.

As such, the mass difference between m/z 9458 and the parent peak at m/z 10778 is +1336 which corresponds to the very well-known cyclic $\text{Au}_4(2\text{-PET})_4$ fragment typical for all magic-numbered gold clusters.³⁵ It is believed that the tetrameric fragment unit is formed from the staple motifs³⁶ and thus provides a valuable information about the surface composition. It is especially very useful for the analysis of mixed ligand shell cluster. Hence, the presence of this fragment with incorporated MT4 ligand in their composition such as $\text{Au}_4(2\text{-PET})_3\text{MT}_4$, $\text{Au}_4(2\text{-PET})_2(\text{MT}_4)_2$, $\text{Au}_4(2\text{-PET})(\text{MT}_4)_3$ and $\text{Au}_4(\text{MT}_4)_4$ was highly anticipated in the mass spectrum. Careful inspection of the mass spectrum at very low m/z range (1200-1900) for the sample containing up to 3 exchanged species (1/100 cluster/ligand ratio, top panel in **Fig. 2**) shows the formation of $\text{Au}_4(2\text{-PET})_{4-x}(\text{MT}_4)_x$ substituted cyclic species with $x=0-2$ (**Fig. S2**). Note that higher substituted fragments ($x=3,4$) were also detected for the samples containing more MT4 ligands on the surface (not shown).

Furthermore, up to nine MT4 ligands ($\bar{x}=4.3$) were exchanged with 2-PET ligand on Au_{38} cluster when leaving the reaction to proceed for longer times, on a large scale of starting reactants (**Fig. S3**). In general, maximum ten MT4 ligand can be adsorbed on the cluster (to be discussed later). Further changes in the reaction conditions did not lead to further exchange, in particular it was

not possible to prepare a cluster with 24 MT4 ligands. Possibly, the limitation in having more MT4 ligands contributing to the final composition of the mixed ligand shell can be explained considering the rigidity and bulkiness of the MT4 ligand. In fact, the more MT4 ligands adsorb on the cluster surface, the more the sterically hindered the neighboring ligands become. This on the other hand vastly decreases the spatial distances between adjacent ligands and the repulsion between them at some point becomes unavoidable. As a matter of fact, the decomposition of the cluster due to the induced instability on the surface can take place. Indeed, we have noticed the formation of thin plasmonic layer and insoluble by-products around the flask after ligand exchange reaction when bigger amount of MT4 ligand was introduced to the reaction mixture.

Moreover, the increase of the number of helical ligands on the cluster surface, has a direct influence on its UV-vis spectrum. Precisely, the absorption bands between 400 to 600 nm flatten and the well-pronounced peak at around 630 nm is even slightly red shifted (with respect to the reference spectrum of Au₃₈) (**Fig. S4**). Previously, similar phenomenon has also been observed for the ligand exchange reaction with dithiol BINAS ligand.²⁸ Even though the characteristic optical fingerprints of the Au₃₈ have been diminished, the core size of the cluster has been preserved during the ligand exchange process.

Next, since the optical properties of the cluster are strongly affected by attaching the helical ligand to the cluster, we anticipated changes in chiroptical properties of the cluster. To test our hypothesis, first, the enantiomers of the chiral Au₃₈(2-PET)₂₄ cluster were separated on HPLC according to the previously described protocol.³⁷ Afterwards, similar ligand exchange procedure as mentioned above has been carried out. Except, the heating of the reaction mixture was excluded and the reacting species were stirred at room temperature to avoid the racemization of the cluster.³⁸ Moreover, the initial concentration of the MT4 ligand was reduced to 20 equivalents in order to inhibit the ligand exchange rate and have less exchanged MT4 on the cluster surface. Besides, we aimed to see the effect of a single helicene on optical and chiral properties of the cluster. To start with, the reaction products were first characterized by UV-vis spectroscopy and MALDI mass spectrometry. UV-vis analyses (**Fig. S5**) do not show any changes on the optical fingerprints of the cluster (similar to what we have observed when using 50 equivalents of MT4 ligand) whereas MALDI showed the appearance of up to 3 exchanged species

in the mass spectra at higher m/z for both enantiomers of the cluster (**Fig. S6**). The exchanged species $Au_{38}(2-PET)_{24-x}(MT4)_x$ (where $x=3$) were separated from the unreacted parent Au_{38} cluster on HPLC system using the same separation protocol and conditions as reported for the enantioseparation of Au_{38} (**Fig. 3**).³⁷ After passing the crude mixture in SEC column to purify from free ligand, a small volume of the reaction mixture (20 μ L) was injected into the chiral column operating at normal isocratic elution mode. In the chromatograms, the first peaks associated with enantiopure cluster were labelled as P1 (25-33 min and 54-70 min for E1 and E2, respectively) whereas the exchanged products of both enantiomers were named P2 (35-52 min and 72-85 min for exchanged species) (**Fig. 3**). Note, P1 peaks of unreacted enantiomers have sharp and symmetric shapes and elute earlier (short retention times) whereas P2 exchanged species retain longer inside the column and thus have more asymmetric shape with a larger peak width.

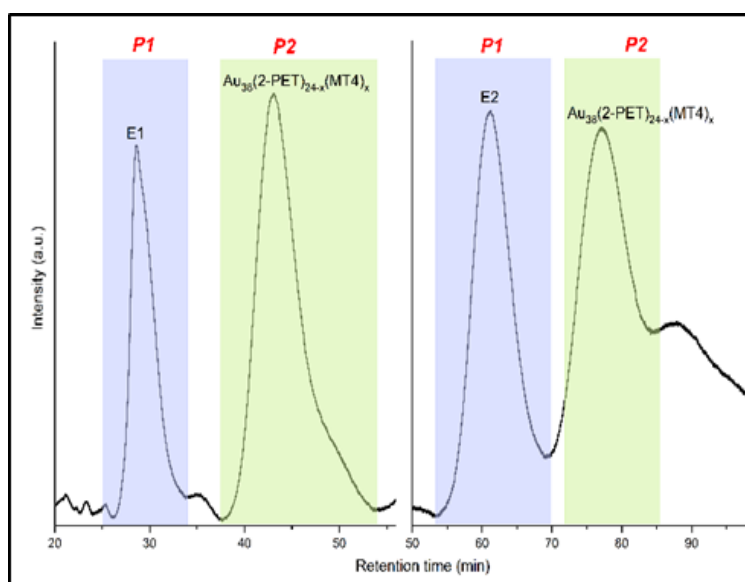


Fig. 3 HPLC chromatograms of E1/E2+MT4. The eluting peaks were detected at 300 nm. The peak of exchanged products is highlighted in green, whereas the parent cluster is marked in purple.

This means that several exchange products are contributing to it and since they are not well resolved, they all come out as a single peak at higher retention times. A small broad peak after P2 of the second enantiomer of cluster has also been observed, unfortunately further analysis of this peak was not successful. Moreover, new peaks matching well with the HPLC retention

profiles of pure enantiomers of the cluster, also elute in the chromatogram. Note, the peak of the opposite enantiomer was not present before the reaction (**Fig. S7**). Since only enantiopure Au₃₈ was used for each ligand exchange reaction, the appearance of the other enantiomer in the chromatogram indicates the partial racemization of the cluster. It was previously shown,³⁸ that the racemization of enantiopure Au₃₈(2-PET)₂₄ cluster takes place at relatively high temperatures, i.e. above 50 °C. When following the evolution of CD responses as a function of temperature, the intensity of peaks of the enantiomers slowly approaches zero, thereby indicating the total racemization of the cluster. On the other hand, since the MT4 ligand is kinetically labile, it can tilt frequently and perhaps, upon adsorbing on the cluster surface, it causes a local distortion and hence, accelerates the cluster's racemization even at room temperature.

However, we cannot draw a definitive conclusion about that, since no systematic studies on racemization of the cluster after ligand exchange reaction have been performed. Recently, *Malola et al* theoretically predicted that the chiral inversion of Au₃₈ cluster is sensitive to the size, structure and core composition and involves the reconstruction of the metallic core without breaking a Au-S bond.³⁹ In this case, it is possible that the adsorption of the MT4 ligand onto the cluster surface accelerates the rotation of the three Au atoms at the pole of the cluster resulting in the rearrangement of long staple motifs into the opposite enantiomer.

If our hypothesis is correct, one would expect to see changes and variations in CD spectrum. For that, P2 peaks were collected repeatedly after each injection step and analyzed by the CD spectroscopy (**Fig. 4 left panel**). The calculated CD spectrum of a non-functionalized *M*-[4]-helicene has several negative and positive bands all positioned below 330 nm.³¹ Since the cluster itself has a strong absorption below 300 nm, the contribution of exchanged MT4 ligand to the chiral signals of the cluster are obscure. Nonetheless, the metal-based CD responses in the visible region of the spectrum are drastically decreased when comparing with the reference cluster. However, the intensity does not reach to zero value meaning that both spectra are still mirror images to each other and the characteristic transitions at around 350, 400, 450, 570 and 630 nm are still recognizable. Since the intensity of CD signals is concentration dependent, to make the comparison more trustworthy, the concentration factor was excluded by calculating the anisotropy factor *g* for each enantiopure sample (**Fig. 4 right panel**). Paying close attention to

anisotropy factors g , the signal profile corresponding to the exchange species of the first enantiomer is hugely affected and became almost flat. As it has been shown in **Fig. S6**, the MALDI analyses show more exchanged species with higher intensities for the first enantiomer. Thus, we can draw a conclusion that the more helicene is attached to the cluster surface the more it causes changes to its electronic properties.

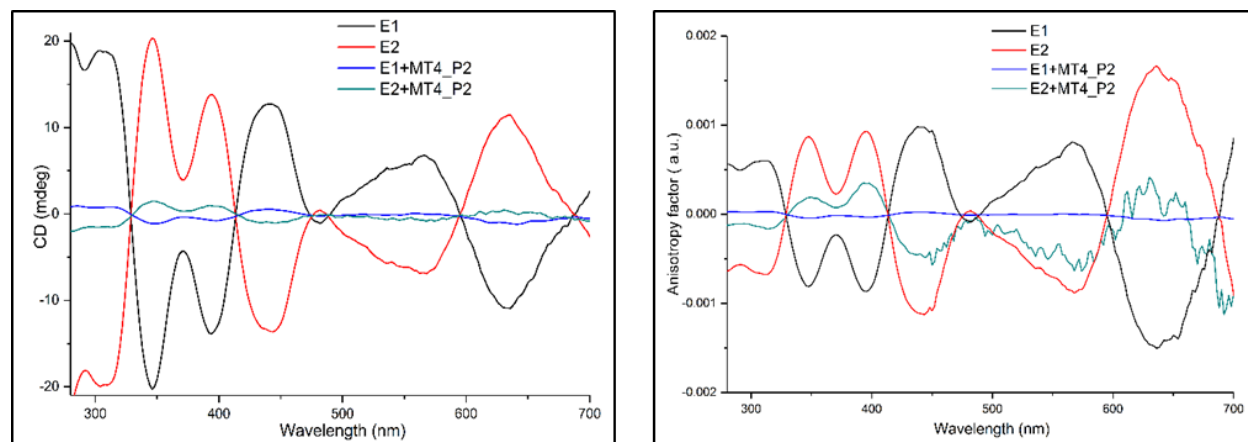


Fig. 4 CD responses (left) and anisotropy factors g (right) of samples and their references. Both the samples and the reference were measured in DCM and the solvent background was subtracted afterwards.

To further prove this, another ligand exchange reaction was carried out under slightly modified reaction conditions. Specifically, a higher ligand to cluster ratio was used (100:1) and the reaction mixture was left to stir for 24 h at room temperature. As we have seen before, the UV-vis spectra for each enantiomeric sample showed less expressed features in the visible region (not shown). MALDI mass spectrum shows maximum ten exchanged species ($\bar{x}=3$ and $\bar{x}=2.4$ for the first and the second enantiomers respectively) in both samples (**Fig. S8**). When comparing the anisotropy factors g of the exchanged products with the reference enantiopure cluster, not only the intensity of the peaks drops down by the factor of 11, but surprisingly mostly all the peaks red shift (**Fig. 5 and Table 1**).

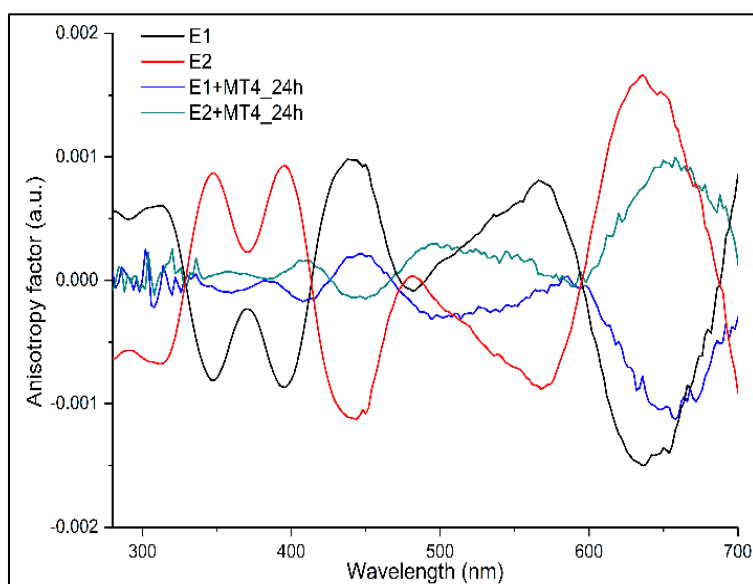


Fig. 5 Anisotropy factors g of exchanged samples and their references measured in DCM. The solvent background has been subtracted afterwards.

Table 1 Wavelengths and anisotropy factors g for enantiomer 2 and corresponding exchange sample.

Enantiomer 2		E2+MT4	
Wavelength (nm)	g factor (a.u.)	Wavelength (nm)	g factor (a.u.)
348	8.6×10^{-4}	359	6.51×10^{-5}
395	9.12×10^{-4}	408	1.64×10^{-4}
444	-1.1×10^{-3}	445	-1.4×10^{-4}
568	-8.7×10^{-4}	495	2.86×10^{-4}
636	1.6×10^{-3}	655	9.48×10^{-4}

Besides, the peak at around 570 nm for E2 enantiomer is now blue shifted about 73 nm and even switched its sign with respect to the parent cluster. Previously *O. Lopez-Acevedo et al* have studied the electronic and optical properties of Au_{38} cluster by DFT computations.¹² The computational model satisfactorily reproduced the experimental CD spectrum and made the assignments of peaks at low energy possible. As such it has been shown that the peaks between 0.9-1.4 eV arise from the combination of several metal-based HOMO-LUMO transitions. The high energy transitions at 1.6-2.2 eV include contributions from the ligand shell. Possibly the changes

of the intensity and the sign especially for the peak at 568 nm is affected because of the MT4 ligand and includes the excitations out of the lower energy ligand orbitals.

Thus, based on the results we had so far, we can conclude that the ligand exchange reaction between 2-PET and MT4 ligands leads to the partial racemization of the enantiopure cluster as well as causes some electronic changes. We assume that the cluster and the aromatic ring from the helicene ligand communicate electronically. However, at this stage we cannot draw definitive conclusions unless additional calculations are performed. Moreover, the CD signals become strongly affected and at some point, an inversion of the CD line shapes and a change in sign takes place.

4. Conclusions

We have shown, that the ligand exchange reaction between intrinsically chiral $\text{Au}_{38}(\text{2-PET})_{24}$ and chiral MT4 ligand resulted in the formation of up to ten exchanged species with a composition of $\text{Au}_{38}(\text{2-PET})_{24-x}(\text{MT4})_x$. The adsorption of the helical ligand resulted in obvious changes on the optical spectrum of the cluster. The diminishing of the UV-vis bands intensity and even the red shift of some electronic transitions at higher ligand concentrations indicated the electronic changes upon ligand exchange although the core size of the cluster has been preserved. HPLC monitoring of the reaction and separation of the enantiopure exchange products from their native cluster showed the appearance of the other enantiomer of the cluster in the solution. Thus, the ligand exchange reaction leads to the partial racemization of the cluster. On the other hand, the adsorption of the MT4 ligand significantly changes the CD line shapes and even causes the inversion of the sign of some peaks.

References

- (1) Jin, R.; Zeng, C.; Zhou, M.; Chen, Y. Atomically Precise Colloidal Metal Nanoclusters and Nanoparticles: Fundamentals and Opportunities. *Chem. Rev.* **2016**, *116* (18), 10346–10413.
- (2) Chakraborty, I.; Pradeep, T. Atomically Precise Clusters of Noble Metals: Emerging Link between Atoms and Nanoparticles. *Chem. Rev.* **2017**, *117* (12), 8208–8271.
- (3) Varnavski, O.; Ramakrishna, G.; Kim, J.; Lee, D.; Goodson, T. Critical Size for the Observation of Quantum Confinement in Optically Excited Gold Clusters. *J. Am. Chem. Soc.* **2010**, *132* (1), 16–17.
- (4) Daniel, M. C. M.; Astruc, D. Gold Nanoparticles: Assembly, Supramolecular Chemistry, Quantum-Size Related Properties and Applications toward Biology, Catalysis and Nanotechnology. *Chem. Rev.* **2004**, *104* (1), 293–346.
- (5) Rosi, N. L.; Giljohann, D. A.; Thaxton, C. S.; Lytton-Jean, A. K. R.; Han, M. S.; Mirkin, C. A. Oligonucleotide-Modified Gold Nanoparticles for Intracellular Gene Regulation. *Science*. **2006**, *312* (5776), 1027–1030.
- (6) Kim Thanh, N. T.; Rosenzweig, Z. Development of an Aggregation-Based Immunoassay for Anti-Protein A Using Gold Nanoparticles. *Anal. Chem.* **2002**, *74* (7), 1624–1628.
- (7) Niemeyer, C. M. Nanoparticles, Proteins, and Nucleic Acids: Biotechnology Meets Materials Science. *Angew. Chemie Int. Ed.* **2001**, *40* (22), 4128–4158.
- (8) Wohltjen, H.; Snow, A. W. Colloidal Metal–Insulator–Metal Ensemble Chemiresistor Sensor. *Anal. Chem.* **1998**, *70* (14), 2856–2859.
- (9) Zheng, N.; Stucky, G. D. A General Synthetic Strategy for Oxide-Supported Metal Nanoparticle Catalysts. *J. Am. Chem. Soc.* **2006**, *128* (44), 14278–14280.
- (10) Pumera, M.; Wang, J.; Grushka, E.; Polsky, R. Gold Nanoparticle-Enhanced Microchip Capillary Electrophoresis. *Anal. Chem.* **2001**, *73* (22), 5625–5628.

- (11) Jin, R. Atomically Precise Metal Nanoclusters: Stable Sizes and Optical Properties. *Nanoscale* **2015**, 7 (5), 1549–1565.
- (12) Lopez-Acevedo, O.; Tsunoyama, H.; Tsukuda, T.; Häkkinen, H.; Aikens, C. M. Chirality and Electronic Structure of the Thiolate-Protected Au₃₈ Nanocluster. *J. Am. Chem. Soc.* **2010**, 132 (23), 8210–8218.
- (13) Dolamic, I.; Varnholt, B.; Bürgi, T. Chirality Transfer from Gold Nanocluster to Adsorbate Evidenced by Vibrational Circular Dichroism. *Nat. Commun.* **2015**, 6 (1), 7117.
- (14) Nieto-Ortega, B.; Bürgi, T. Vibrational Properties of Thiolate-Protected Gold Nanoclusters. *Acc. Chem. Res.* **2018**, 51 (11), 2811–2819.
- (15) Knoppe, S.; Bürgi, T. Chirality in Thiolate-Protected Gold Clusters. *Acc. Chem. Res.* **2014**, 47 (4), 1318–1326.
- (16) Philip, R.; Chantharasupawong, P.; Qian, H.; Jin, R.; Thomas, J. Evolution of Nonlinear Optical Properties: From Gold Atomic Clusters to Plasmonic Nanocrystals. *Nano Lett.* **2012**, 12 (9), 4661–4667.
- (17) Inouye, H.; Tanaka, K.; Tanahashi, I.; Hirao, K. Ultrafast Dynamics of Nonequilibrium Electrons in a Gold Nanoparticle System. *Phys. Rev. B* **1998**, 57 (18), 11334–11340.
- (18) Cui, M.; Zhao, Y.; Song, Q. Synthesis, Optical Properties and Applications of Ultra-Small Luminescent Gold Nanoclusters. *TrAC Trends Anal. Chem.* **2014**, 57, 73–82.
- (19) Qu, X.; Li, Y.; Li, L.; Wang, Y.; Liang, J.; Liang, J. Fluorescent Gold Nanoclusters: Synthesis and Recent Biological Application. *J. Nanomater.* **2015**, 1–23.
- (20) Häkkinen, H.; Walter, M.; Grönbeck, H. Divide and Protect: Capping Gold Nanoclusters with Molecular Gold–Thiolate Rings. *J. Phys. Chem. B* **2006**, 110 (20), 9927–9931.
- (21) Qian, H.; Zhu, Y.; Jin, R. Size-Focusing Synthesis, Optical and Electrochemical Properties of Monodisperse Au₃₈(SC₂H₄Ph)₂₄ Nanoclusters. *ACS Nano* **2009**, 3 (11), 3795–3803.

- (22) Qian, H.; Eckenhoff, W. T.; Zhu, Y.; Pintauer, T.; Jin, R. Total Structure Determination of Thiolate-Protected Au₃₈ Nanoparticles. *J. Am. Chem. Soc.* **2010**, *132* (24), 8280–8281.
- (23) Niihori, Y.; Hossain, S.; Kumar, B.; Nair, L. V.; Kurashige, W.; Negishi, Y. Perspective: Exchange Reactions in Thiolate-Protected Metal Clusters. *APL Mater.* **2017**, *5* (5).
- (24) Zeng, C.; Liu, C.; Pei, Y.; Jin, R. Thiol Ligand-Induced Transformation of Au₃₈(SC₂H₄Ph)₂₄ to Au₃₆(SPh-*t*-Bu)₂₄. *ACS Nano* **2013**, *7* (7), 6138–6145.
- (25) Das, A.; Liu, C.; Zeng, C.; Li, G.; Li, T.; Rosi, N. L.; Jin, R. Cyclopentanethiolato-Protected Au₃₆(SC₅H₉)₂₄ Nanocluster: Crystal Structure and Implications for the Steric and Electronic Effects of Ligand. *J. Phys. Chem. A* **2014**, *118* (37), 8264–8269.
- (26) Knoppe, S.; Azoulay, R.; Dass, A.; Bürgi, T. In Situ Reaction Monitoring Reveals a Diastereoselective Ligand Exchange Reaction between the Intrinsically Chiral Au₃₈(SR)₂₄ and Chiral Thiols. *J. Am. Chem. Soc.* **2012**, *134* (50), 20302–20305.
- (27) Beqa, L.; Deschamps, D.; Perrio, S.; Gaumont, A. C.; Knoppe, S.; Bürgi, T. Ligand Exchange Reaction on Au₃₈(SR)₂₄, Separation of Au₃₈(SR)₂₃(SR')₁ Regioisomers, and Migration of Thiolates. *J. Phys. Chem. C* **2013**, *117* (41), 21619–21625.
- (28) Knoppe, S.; Dharmaratne, A. C.; Schreiner, E.; Dass, A.; Bürgi, T. Ligand Exchange Reactions on Au₃₈ and Au₄₀ Clusters: A Combined Circular Dichroism and Mass Spectrometry Study. *J. Am. Chem. Soc.* **2010**, *132* (47), 16783–16789.
- (29) Zeng, C.; Qian, H.; Li, T.; Li, G.; Rosi, N. L.; Yoon, B.; Barnett, R. N.; Whetten, R. L.; Landman, U.; Jin, R. Total Structure and Electronic Properties of the Gold Nanocrystal Au₃₆(SR)₂₄. *Angew. Chemie Int. Ed.* **2012**, *51* (52), 13114–13118.
- (30) Shen, Y.; Chen, C. F. Helicenes: Synthesis and Applications. *Chem. Rev.* **2012**, *112* (3), 1463–1535.

- (31) Furche, F.; Ahlrichs, R.; Wachsmann, C.; Weber, E.; Sobanski, A.; Vögtle, F.; Grimme, S. Circular Dichroism of Helicenes Investigated by Time-Dependent Density Functional Theory. *J. Am. Chem. Soc.* **2000**, *122* (8), 1717–1724.
- (32) Grimme, S.; Peyerimhoff, S. D. Theoretical Study of the Structures and Racemization Barriers of [n]Helicenes (n = 3-6, 8). *Chem. Phys.* **1996**, *204* (2-3 SPEC. ISS.), 411–417.
- (33) Barroso, J.; Cabellos, J. L.; Pan, S.; Murillo, F.; Zarate, X.; Fernandez-Herrera, M. A.; Merino, G. Revisiting the Racemization Mechanism of Helicenes. *Chem. Commun.* **2017**, *54* (2), 188–191.
- (34) Knoppe, S.; Boudon, J.; Dolamic, I.; Dass, A.; Bürgi, T. Size Exclusion Chromatography for Semipreparative Scale Separation of Au₃₈(SR)₂₄ and Au₄₀(SR)₂₄ and Larger Clusters. *Anal. Chem.* **2011**, *83* (13), 5056–5061.
- (35) Dass, A.; Stevenson, A.; Dubay, G. R.; Tracy, J. B.; Murray, R. W. Nanoparticle MALDI-TOF Mass Spectrometry without Fragmentation: Au₂₅(SCH₂CH₂Ph)₁₈ and Mixed Monolayer Au₂₅(SCH₂CH₂Ph)_{18-x}(L)_x. *J. Am. Chem. Soc.* **2008**, *130* (18), 5940–5946.
- (36) Zhang, Y.; Shuang, S.; Dong, C.; Lo, C. K.; Paa, M. C.; Choi, M. M. F. Application of HPLC and MALDI-TOF MS for Studying As-Synthesized Ligand-Protected Gold Nanoclusters Products. *Anal. Chem.* **2009**, *81* (4), 1676–1685.
- (37) Dolamic, I.; Knoppe, S.; Dass, A.; Bürgi, T. First Enantioseparation and Circular Dichroism Spectra of Au₃₈ Clusters Protected by Achiral Ligands. *Nat. Commun.* **2012**, *3* (1), 798.
- (38) Knoppe, S.; Dolamic, I.; Bürgi, T. Racemization of a Chiral Nanoparticle Evidences the Flexibility of the Gold–Thiolate Interface. *J. Am. Chem. Soc.* **2012**, *134* (31), 13114–13120.
- (39) Malola, S.; Häkkinen, H. Chiral Inversion of Thiolate-Protected Gold Nanoclusters via Core Reconstruction without Breaking a Au-S Bond. *J. Am. Chem. Soc.* **2019**, *141* (14), 6006–6012.

Supporting information

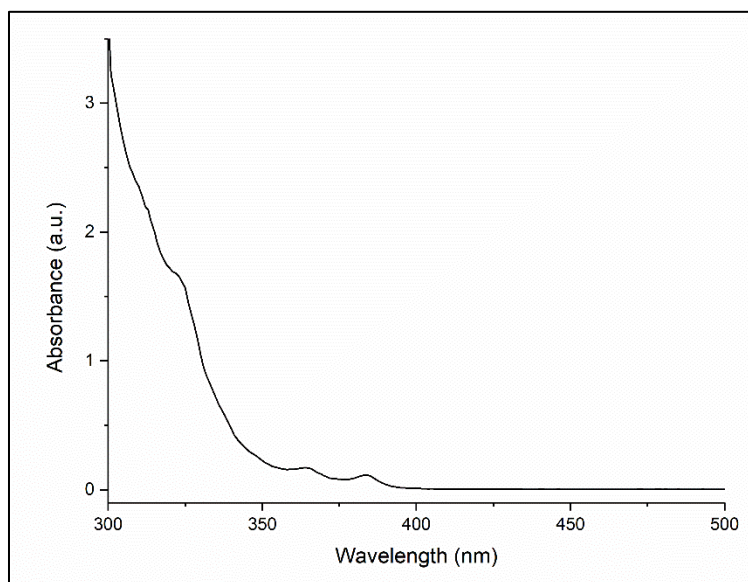


Fig. S1 UV-vis spectrum of MT4 ligand in toluene.

Table S1 Calculated masses for each exchange product in the mass spectrum.

Au ₃₈ (2-PET) _{24-x} (MT4) _x		
Number of exchanges	Formula	Theoretical masses/ Da
x=1	Au ₃₈ (2-PET) ₂₃ (MT4)	10901
x=2	Au ₃₈ (2-PET) ₂₂ (MT4) ₂	11024
x=3	Au ₃₈ (2-PET) ₂₁ (MT4) ₃	11147
x=4	Au ₂₅ (2-PET) ₂₀ (MT4) ₄	11270
x=5	Au ₃₈ (2-PET) ₁₉ (MT4) ₅	11393
x=6	Au ₃₈ (2-PET) ₁₈ (MT4) ₆	11520
x=7	Au ₃₈ (2-PET) ₁₇ (MT4) ₇	11643
x=8	Au ₃₈ (2-PET) ₁₆ (MT4) ₈	11766
x=9	Au ₃₈ (2-PET) ₁₅ (MT4) ₉	11889

$$\bar{x} = \frac{\sum I_x * x}{\sum I_x}$$

where \bar{x} is an average exchange, I_x is an intensity of the peak and x is an exchange number.

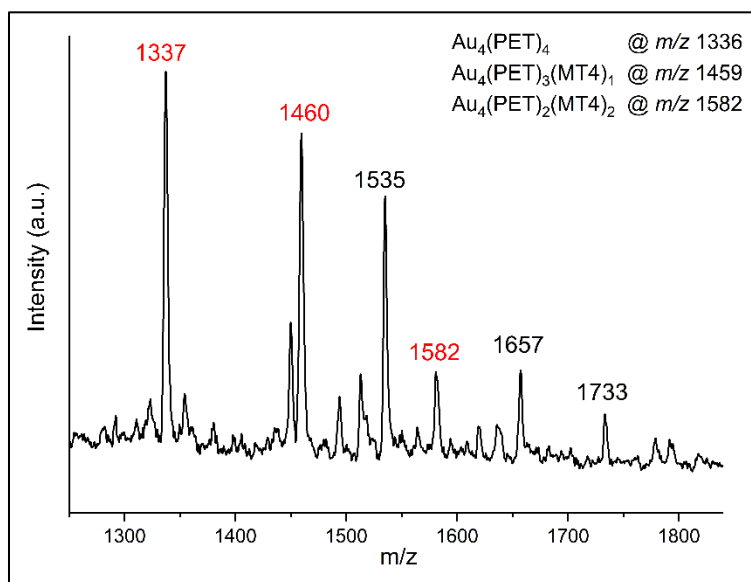


Fig. S2 MALDI analysis of the fragmentation pattern at lower m/z range when 1:100 cluster/ligand ratios were used for the reaction. The substituted $Au_4(2-PET)_{4-x}(MT4)_x$ cyclic species are marked in red.

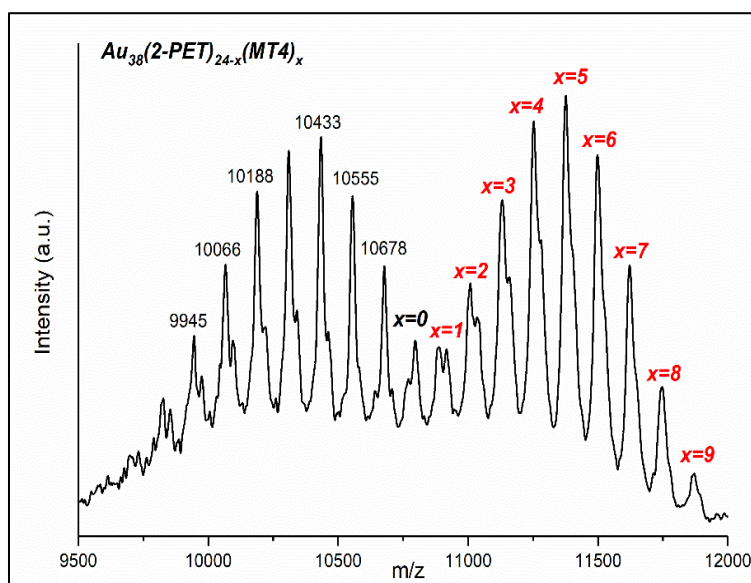


Fig. S3 MALDI analysis of the sample after ligand exchange reaction. The number of exchange species are marked in red.

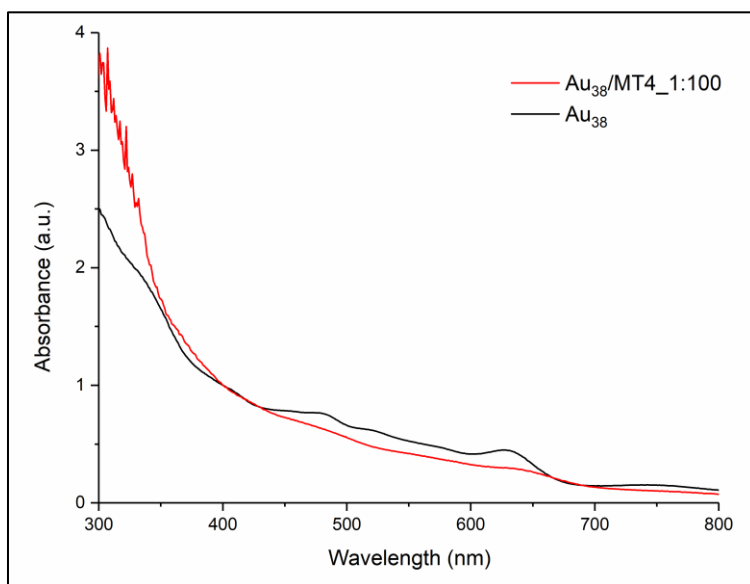


Fig. S4 UV-vis spectra of sample after ligand exchange reaction using 1:100 cluster/ligand ratio on a large-scale synthesis (5 mg of Au₃₈). The spectra are normalized and compared with Au₃₈ before reaction.

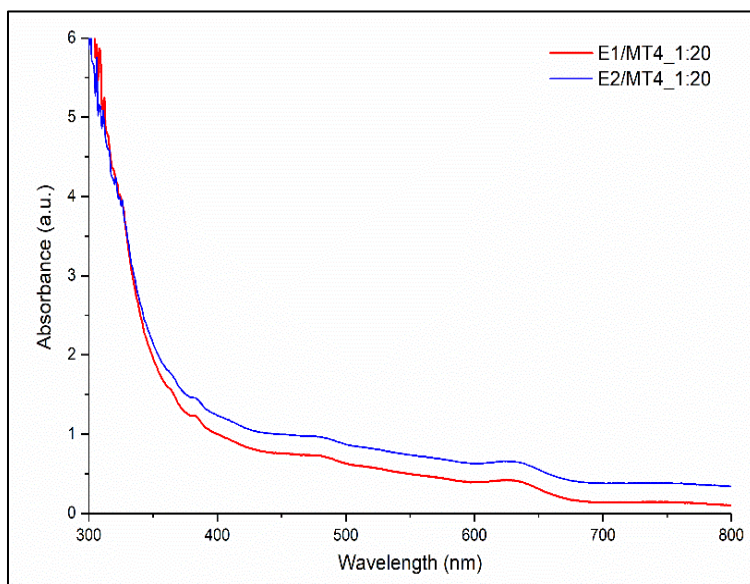


Fig. S5 UV-vis spectra of E1/ E2+MT4 using 1:20 cluster/ligand molar ratios. The spectra are normalized at 400 nm for better comparison.

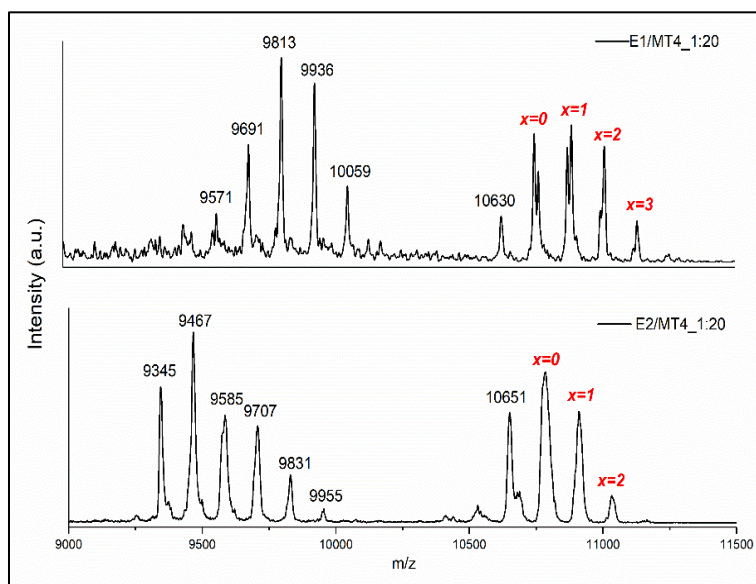


Fig. S6 MALDI mass spectra of E1/ E2+MT4 after ligand exchange reaction.

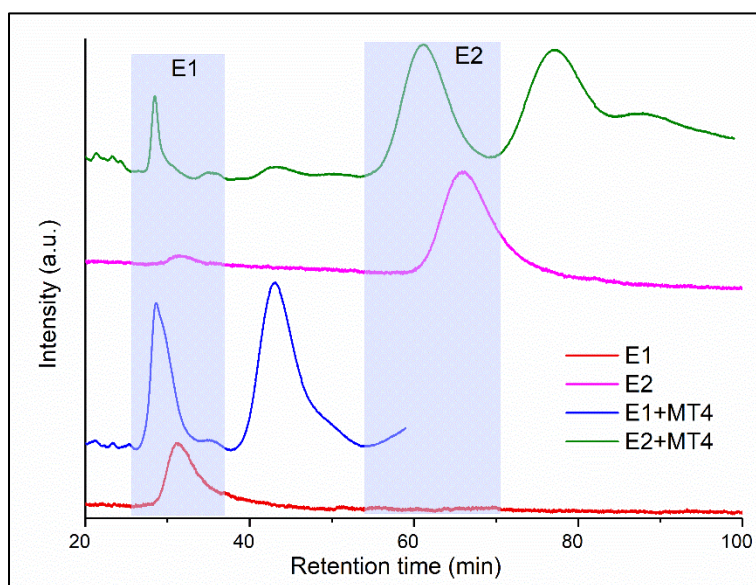


Fig. S7 HPLC separations of the exchanged species after ligand exchange reaction with enantiopure cluster. The chromatograms are compared with reference chromatogram of enantiopure cluster.

B. EXPERIMENTAL PART

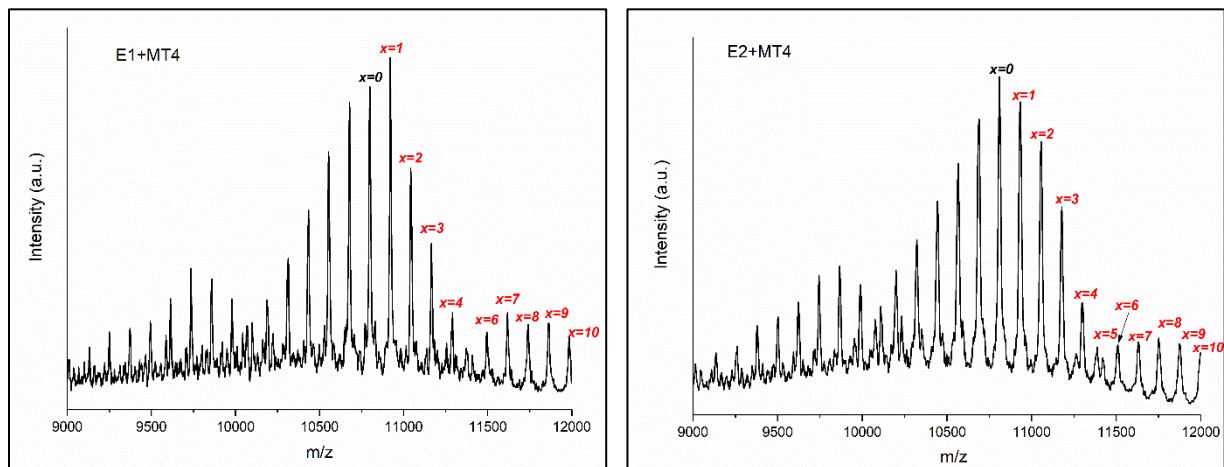


Fig. S8 MALDI mass spectra of E1/ E2+MT4 after ligand exchange reaction.

5.2. Combined spectroscopic studies on post-functionalized Au₂₅ cluster as an ATR-FTIR sensor for cations

Recently, significant research activity has been devoted to thiolate-protected gold clusters due to their attractive optical and electronic properties. These properties as well as solubility and stability can be controlled by post-synthetic modification strategies. Herein, the ligand exchange reaction between Au₂₅(2-PET)₁₈ cluster (where 2-PET is 2-phenylethanethiol) and a di-thiolated crown ether (*t*-CE) ligands bearing two chromophores was studied. The post-functionalization aimed to endow the cluster with ion binding properties. The reaction was followed *in situ* by UV-vis, ¹H NMR and HPLC. MALDI mass analysis revealed the incorporation of 5 *t*-CE ligands into the ligand shell. Once functionalized MALDI furthermore showed complexation of sodium ions to the cluster. ATR-FTIR spectroscopic studies using aqueous solutions of K⁺, Ba²⁺, Gd³⁺ and Eu³⁺ showed noticeable spectral shifts of the C-O stretching band around 1100 cm⁻¹ upon complexation. Further spectral changes point towards a conformational change of the two chromophores that are attached to the crown ether. Density functional theory calculations indicate that the di-thiol ligand bridges two staple units on the cluster. The calculations furthermore reproduce the spectral shift of the C-O stretching vibrations upon complex formation and reveal a conformational change that involves the two chromophores attached to the crown ether. The functionalized clusters have therefore attractive ion sensing properties due to the combination of binding properties, mainly due to the crown ether, and the possibility for signal transduction via an induced conformational change involving chromophore units.

1. Introduction

In recent years, the interest in thiolate-protected gold clusters has grown and a substantial number of atomically precise clusters with distinct physical-chemical properties were synthesized and characterized.^{1,2} Furthermore, post-synthetic modification strategies such as ligand-exchange reaction,³⁻⁹ metal doping and alloying^{10,11} were applied to tune cluster properties and/or to integrate new type of functionalities. Such reactions exert a profound influence on the optical, electronic, catalytic and biomedical properties of the clusters.^{3,12,13} For instance, mixed ligand shell clusters can drastically change or even lose their distinct native cluster optical fingerprints despite the preservation of their core size.^{3,14,15} Functionalized thiols with various backbone structures can be used for ligand exchange reactions.^{16,17}

Crown ethers have been applied as complexing agents for primary and secondary alkylammonium ions,¹⁸⁻²⁰ some transition metal ions,²¹ lanthanides and actinides²² and for small molecules such as urea, thiourea, acetonitrile and nitro compounds.^{23,24} These neutral synthetic heterocyclic compounds are of interest due to their powerful cation binding properties in areas such as host-guest chemistry and in the construction of well-defined supramolecular assemblies. Crown-based sensors designed for cation recognition with high selectivity and a variety of responses can be developed by the attachment of a chromophore, fluorophore or luminophore into the crown framework.²⁵ The combination of synthetic versatility and well-tailored design opens the door for diverse applications related to molecular recognition, chirality and catalysis. Combined experimental and theoretical studies reveal the ion selectivity in terms of their size matching with the guest ions. For example, 12-crown-4 (**12C4**) has higher binding affinity towards Li^+ ,²⁶ whereas 15-crown-5 (**15C5**) and 18-crown-6 (**18C6**) show stronger encapsulation efficiencies towards Na^+ and K^+ , respectively.²⁷⁻²⁹ The binding properties of these ligands with cations on Au surfaces have been studied previously.^{28,29} Several examples of gold clusters, although not atomically well defined, being used in sensing applications of heavy metals and toxic anions in environment and biota, have also been reported.³⁰⁻³⁶ Metal sensing properties of freestanding composite films of Au_{15} has been reported, too.³⁷ However, to the best of our knowledge this is the first report on ion sensing capability of an atomically precise functionalized

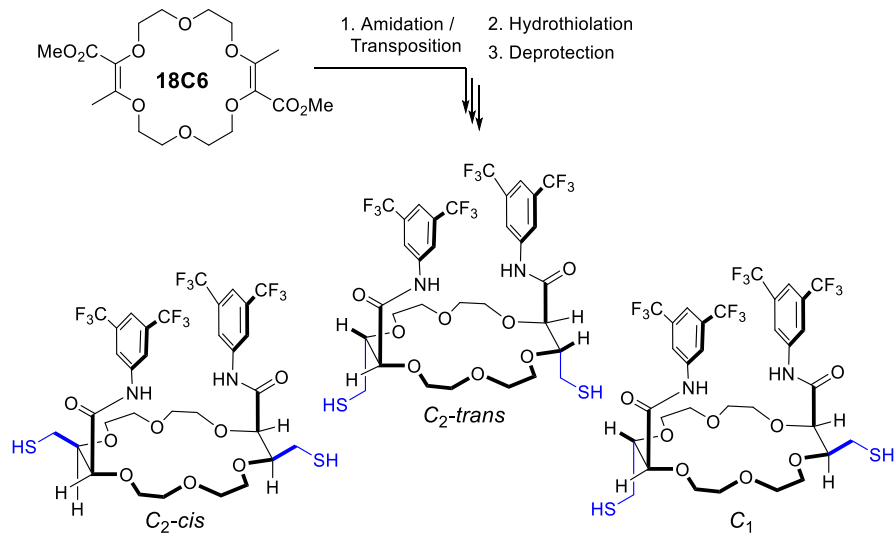
monolayer-protected gold cluster. The functionalization of atomically precise $\text{Au}_{25}(\text{2-PET})_{18}$ cluster (where 2-PET is 2-phenylethanethiol) with di-thiolated crown ether ligand, bearing two chromophores, leads to new compounds with ion binding properties. In the following we describe the preparation of mixed ligand shell Au_{25} clusters and demonstrate their ability to bind metal ions. Furthermore, we show that complexation leads to conformational changes of the ligand involving the attached chromophores, which could potentially be used for signal transduction.

2. Experimental

2.1. Materials. Hydrogen tetrachloroaurate (III) tridhydrate (ACS, Alfa Aesar, 99.99%), tetraoctylammonium bromide (Sigma-Aldrich, 98%), 2-phenylethanethiol (Sigma-Aldrich-Fluka, 99+%), sodium borohydride (Aldrich, $\geq 96\%$), KBr (Merck, for spectroscopy), Gadolinium (III) chloride hydrate (Sigma-Aldrich-Fluka, 99.99%), Europium (III) chloride hexahydrate (Strem, 99.9%), acetone (Fisher, 99.7%), toluene (Fisher, 99.9%), ethanol (Sigma-Aldrich, $>99.8\%$), methanol (Fisher, 99.9%), dichloromethane (Merck, 99.7+%) were used as received. Milli-Q water was used (18.2 M Ω .cm), {N2,N11-bis(3,5-bis(trifluoromethyl)phenyl)-3,12-bis(mercaptomethyl)-1,4,7,10,13,16-hexaoxacyclooctadecane-2,11-dicarboxamide} ligand (thiolated crown ether, abbreviated *t*-CE).

2.2. Synthesis of $\text{Au}_{25}(\text{2-PET})_{18}$ cluster and ligand exchange reaction with *t*-CE ligand. $\text{Au}_{25}(\text{2-PET})_{18}$ cluster was synthesized based on reported protocols.^{38,39} Briefly, 1g of $\text{HAuCl}_4 \cdot 3\text{H}_2\text{O}$ mixed with tetraoctylammonium bromide (abbreviated TOAB) was dissolved in THF and stirred for 15 min. Then 10 mL of 2-PET ligand was added until the solution gradually changed color from red to yellow and eventually turned colorless. At this point, 900 mg NaBH_4 dissolved in 50 mL ice-cold water was added at once and the reaction mixture was allowed to stir for 3 h. Furthermore, the reaction solution was filtered with paper to remove the insoluble Au(I)-SR complexes. The filtered solution was evaporated, and the crude sample was washed with Milli-Q water and MeOH several times to remove unreacted precursors. The purified sample was dried in a vacuum rotary evaporator at room temperature. Note that during this synthesis mainly negatively

charged cluster was obtained as evidenced by UV-vis spectra.⁴⁰ Upon silica-gel column chromatography under aerobic conditions the cluster was oxidized to its uncharged form. The synthesis of the *t*-CE ligand, presented in **Scheme 1**, was performed as recently reported.⁴¹ We made use of the [3+6+3+6] condensation of methyl α -diazo- β -ketoester with 1,4-dioxane to yield unsaturated macrocycle **18C6** (**Scheme 1**, up to 20 gram scale, 0.01-0.001 mol% of dirhodium catalyst).⁴²⁻⁴⁵ Then, stereoselective deconjugation in presence of 3,5-bis(trifluoromethyl)aniline and *t*-BuOK,⁴⁶⁻⁵⁴ followed by double hydrothiolation of the bis enol ether adduct with thioacetic acid led, under photo-mediated conditions and after saponification, to three separated *t*-CE macrocycles containing four defined stereocenters in only three steps from 1,4-dioxane. By NMR spectroscopy, the two C_2 -symmetric derivatives can be readily differentiated from the single C_1 isomer. The assignment of the relative *cis* and *trans* configurations was unambiguously determined by X-ray crystallography.⁴¹



Scheme 1 Synthesis of the three stereoisomers of the *t*-CE ligand.

Ligand exchange reaction between neutral $Au_{25}(2\text{-PET})_{18}$ and selected *t*-CE ligand were carried out under mild conditions (1:3 and 1:10 cluster/ligand molar ratios, room temperature, DCM solution, 16 h). The number of exchanged ligands was controlled by altering the reaction conditions (**Fig. 1**). Note that the *t*-CE ligands are chiral, and they were only used in racemic form for the experiments described herein.

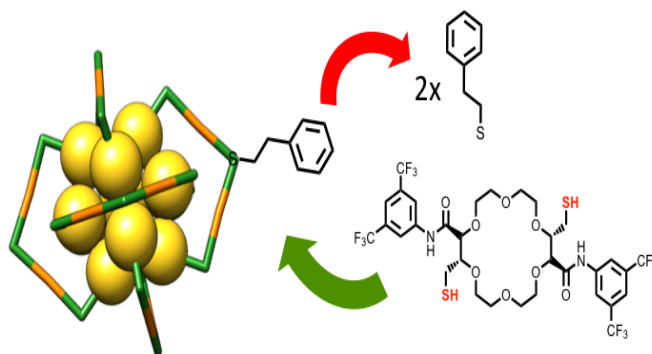


Fig. 1 Schematic representation of the ligand exchange reaction with Au₂₅ cluster and C₂-*trans* t-CE ligand.

2.3. Characterization methods. UV-vis spectra were recorded on a Varian Cary 50 spectrophotometer, using a quartz cuvette of 1 cm path length. Spectra were measured in the range of 200-1000 nm in DCM with a scanning speed of 200 nm/min (UV-vis bandwidth 2 nm and NIR bandwidth 2 nm).

NMR spectra were recorded on a Bruker Avance 400 MHz spectrometer. ¹H NMR chemical shifts are given in ppm relative to SiMe₄, with the solvent resonance used as internal reference. NMR-monitored thiol exchange reaction was performed in a screw-cup NMR tube in which t-CE ligand and Au₂₅(2-PET)₁₈ were dissolved in DCM-*d*₂. Proton spectra were acquired every hour for 14 hours. Delay time between the thiol addition and the end of the first NMR-spectrum was measured. The evolution in time (*t*) of the peak integrals (*y*) of free thiol were fitted with a three parameters exponential function included in the MestReNova 11.0.1:

$$y = B + F \exp(-tG)$$

In which *B* is the value of the peak integral at infinite time.

Ligand exchange was studied by chromatography (HPLC) on a JASCO 20XX HPLC system equipped with an analytical CHIRALPAK[®] IA column (5 μm, 4 mm x 10 mm) using n-hexane/ethanol (90:10) mobile phase at a flow rate of 1 mL/min. The analytes were detected with a JASCO 2077 plus UV detector operated at 300 nm.

MALDI-TOF mass analysis was performed on an AXIMA-CFR⁺ MALDI-TOF-MS (Shimadzu, Duisburg, Germany) mass spectrometer equipped with a nitrogen laser in positive mode. [3-(4-tert-butylphenyl)-2-methyl-2-propenylidene]malononitrile (DCTB) was used as a matrix with a 1:1000 analyte : matrix ratio. A volume of 2 μl of the analyte/matrix mixture was applied to the target and air-dried.

Ion binding properties were examined by attenuated total reflection-Fourier transform infrared spectroscopy (ATR-FTIR) on a Bruker V80 FTIR spectrometer equipped with a narrow-band MTC detector. ATR spectra were recorded at room temperature with a resolution of 4 cm^{-1} . Cluster solution in DCM with a total concentration of 0.5 mg/mL was drop cast onto a Ge internal reflection element (IRE) (52 \times 20 \times 1 mm, KOMLAS). After solvent evaporation, loose cluster particles were removed by flowing water over the IRE. After air-drying, the film was ready for use. A dedicated flow-through cell was used composed of a Teflon piece and a fused silica plate (45 \times 35 \times 3 mm) and the flow-rate was controlled by a peristaltic pump (Ismatec, Reglo 100) located before the cell.⁵⁵ A viton-ring seal (1 mm) defined the thickness of the fluid compartment, which had a volume of 0.5 mL. The cell was mounted on an attachment for ATR measurements (Wilks Scientific) within the sample compartment. *In situ* spectroscopic studies were performed using KBr, BaCl₂, GdCl₃·H₂O and EuCl₃·6H₂O aqueous solutions, changing concentrations from 50 ppm to 5000 ppm. Milli-Q water was flowing at a flow rate of 3 mL/min to remove loose clusters and afterward background was recorded. The water was switched to metal salt solution and spectra were measured for 3 h continuously at a flow rate of 1.2 mL/min.

2.4. Computational methods

Structure optimizations energy calculations and the calculation of IR spectra were performed using Gaussian software package.⁵⁶ The calculations were performed using the B3PW91 functional and a 6-31G** basis set for H, C, O, N, F, S and K, a Lanl2MB for Au and a Lanl2DZ for Ba. Prior to the calculation of the spectra all degrees of freedom were completely relaxed in order to reach equilibrium geometries. IR spectra were constructed from calculated dipole strengths assuming a Gaussian band shape with a half-width at half-maximum of 5 cm^{-1} . All calculations

were performed for the gas phase species. For the calculations involving the cluster the 2-PET ligands were replaced with S-H groups. Note that the neutral cluster is an open shell system. The calculations were performed on the anion cluster, which has a closed $1S^21P^6$ superatom electronic shell.

3. Results and discussion

The ligand exchange reaction between $Au_{25}(2\text{-PET})_{18}$ cluster and *t*-CE ligands was followed *in situ* by UV-vis and ^1H NMR spectroscopy over the time course of about a day. As mentioned earlier, di-thiolated *t*-CE ligand exists in three possible stereoisomeric forms, *i.e.* the $C_2\text{-cis}$, $C_2\text{-trans}$ and C_1 (**Scheme 1**). All three separated isomers were used in independent ligand exchange reactions. With the $C_2\text{-cis}$ and C_1 isomers, the ligand exchange processes resulted in marked precipitation. In these cases, the bidentate/bisthiolated stereoisomers most probably act as linkers between clusters and, as a result, multimers or cluster chains are formed, which eventually precipitate as they grow larger. These structures, which may have interesting properties, were not studied as their investigation is out of the scope of this paper. Finally, interactions of the $C_2\text{-trans}$ stereoisomer were performed and resulted in successful ligand exchanges without any precipitation; this moiety was selected for the remainder of the study.

During the exchange reaction, the color of the solution gradually changed from green (characteristic for neutral $Au_{25}(2\text{-PET})_{18}$ cluster) to reddish in agreement with obvious changes in the UV-vis spectra (**Fig. 2**). Characteristic optical fingerprints of the Au_{25} cluster were still recognizable but less pronounced in the visible region (**Fig. 2**). Furthermore, in size exclusion chromatography (SEC, Bio-Beads™ S-X1 Support gel) two distinguishable fractions marked as F1 (reddish) and F2 (greenish) corresponding to the exchanged species and non-reacted cluster were successfully separated. MALDI analysis (**Fig. 3**) revealed the formation of several exchanged clusters in fraction F1. $Au_{25}(2\text{-PET})_{18-2x}(t\text{-CE})_x$ species with up to 4 exchanged *t*-CE ligands were detected with an average exchange number of $\bar{x}=2$ (**Table S1**).

B. EXPERIMENTAL PART

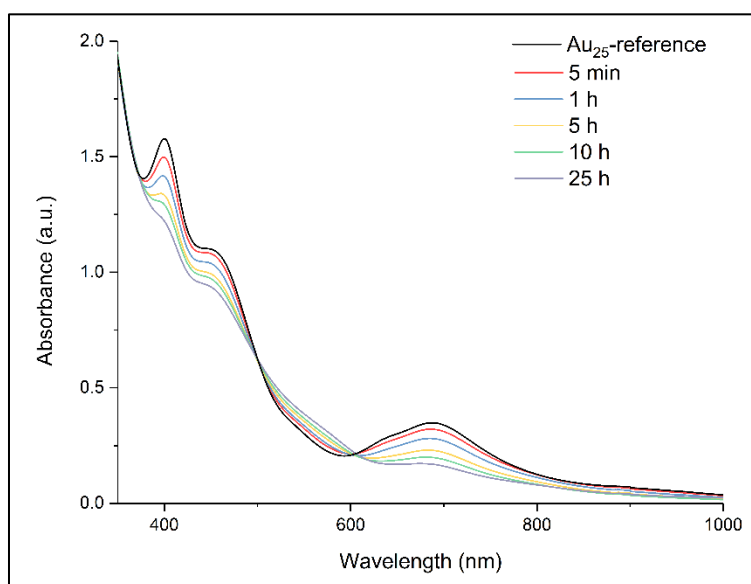


Fig. 2 *In situ* UV-vis study of ligand exchange reaction. 1:10 cluster/ *t*-CE ratio was used for *in situ* reaction monitoring. The spectra are scaled for better comparison. The spectrum of Au₂₅ cluster before ligand addition was recorded as a reference.

Fraction F2 contained pure Au₂₅ cluster (**Fig. 3**). Mass spectra showed that one incoming *t*-CE ligand exchanges with two 2-PET ligands, leading to clusters of composition Au₂₅(2-PET)_{18-2x}(*t*-CE)_x. No sign of partially exchanged ligand (one *t*-CE for one 2-PET) could be found in the mass spectra. Not assigned peaks in **Fig. 3** are the fragments of the exchanged species.

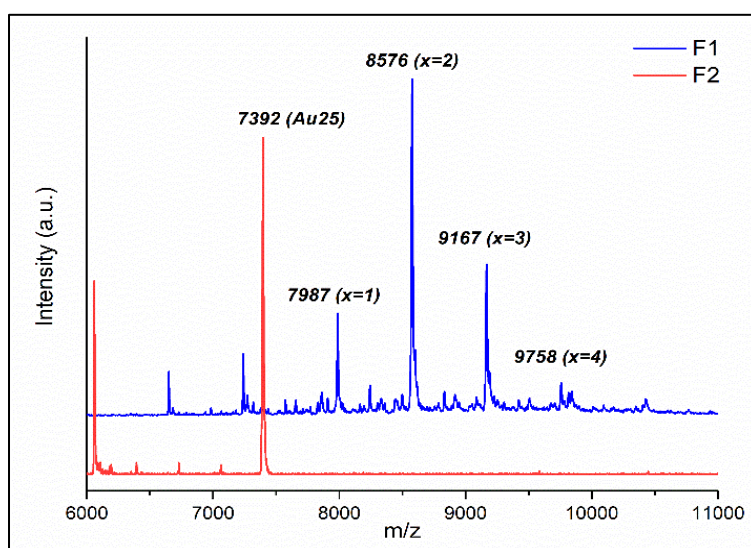


Fig. 3 MALDI analysis of the two separated fractions (F1 and F2) on SEC column.

MALDI showed that no more than five *t*-CE ligands can be adsorbed on the cluster (see supporting information **Fig. S1**), even when further increasing the cluster/ligand ratio (up to 1:20) as well as reaction time. Probably the large size of *t*-CE does not allow the adsorption of more than five *t*-CE ligands on the cluster. Careful inspection of the MALDI mass spectra revealed an interesting feature. For the ligand exchanged clusters additional peaks at higher mass $m/z + 23$ were detected (**Fig. 4**). The mass difference corresponds to Na^+ ions. Note, that the additional peak was not observed for parent $\text{Au}_{25}(\text{2-PET})_{18}$. This observation indicates the trapping of Na^+ in the crown ether cavity of the *t*-CE ligand and provides first evidence for the affinity of adsorbed ligand for metal ions.

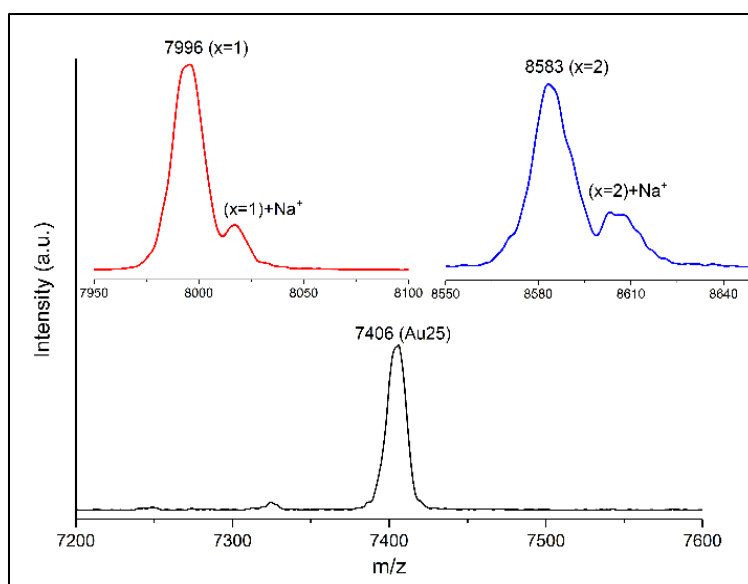


Fig. 4 MALDI mass spectra of $\text{Au}_{25}(\text{2-PET})_{18-2x}(\text{t-CE})_x$ exchanged species with Na^+ adducts. The mass spectrum of $\text{Au}_{25}(\text{2-PET})_{18}$ is also shown for comparison.

^1H NMR spectroscopic analyses showed the change in the signals' intensity of incoming *t*-CE ligand and exchanged 2-PET thiol (Au_{25} : *t*-CE ratio of 1:3, **Fig. 5**). Over time the intensity of free *t*-CE ligand (4.4, 7.6 and 9.2 ppm) decreased due to anchoring onto the cluster. Similarly, the intensity of signals due to 2-PET ligand (2.9 ppm) increased. Analysis of the kinetics showed that at equilibrium 62% of the *t*-CE ligand has exchanged with 2-PET on the cluster surface. Moreover, the NMR spectrum of exchanged sample showed clear differences with respect to reference Au_{25} .

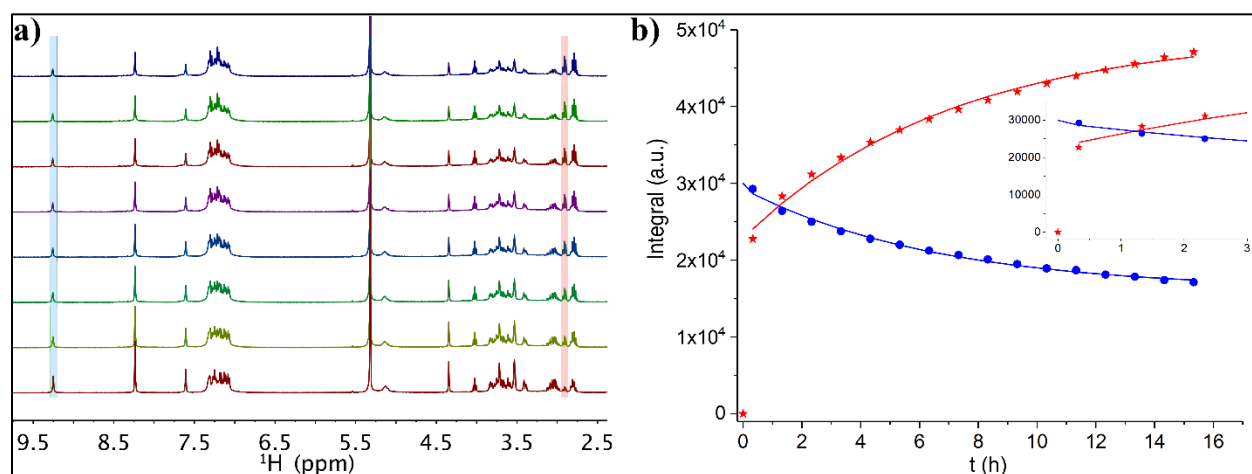
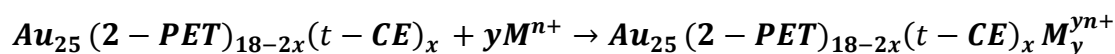


Fig. 5 a) Thiol exchange reaction between $\text{Au}_{25}(\text{2-PET})_{18}$ and 3 equivalents of *t*-CE followed by NMR. ^1H -NMR was recorded every hour in DCM-2d for 14 h (herein, from bottom to top each spectrum corresponds to the increase of reaction time of 2 h). b) Exponential fitting of the integral of the leaving 2-PET (red crosses, 2.95 ppm) and entering *t*-CE (blue circles, 9.25 ppm).

HPLC analyses were performed to monitor the ligand exchange reaction (**Fig. S2**). In a control experiment $\text{Au}_{25}(\text{2-PET})_{18}$ cluster eluted at 13.5 min. Immediately after adding the ligand a new peak at 12.6 min retention time was observed indicating ligand exchange reaction. It is worth mentioning that the first exchange between the cluster and the *t*-CE ligand happens very fast resulting in a new peak in the chromatogram immediately after starting the ligand exchange reaction (**Fig. S2**). This confirms the NMR results, which show a high level of released 2-PET after short time (**Fig. 5b**). Moreover, MALDI analysis (not shown) of the sample after NMR studies shows an average exchange number \bar{x} of 2.4. Hence, considering that this number corresponds to the last point of the NMR fitting curve one can estimate the composition (\bar{x}) at which the change from very fast to moderate exchange rate is taking place. In fact, this estimation yields $\bar{x}=1.1$, indicating that the first exchange is much faster than the subsequent exchanges. This is in line with previous observations that rigid dithiol like BINAS (1,1'-binaphthyl-2,2'-dithiol) undergo first ligand exchange considerably faster than subsequent ones.⁴ Possibly the ligand shell becomes more rigid due to the incorporated ligand, which slows down further exchange.

For *in situ* ATR-IR experiments $\text{Au}_{25}(\text{2-PET})_{18-2x}(\textit{t}\text{-CE})_x$ sample containing up to 4 exchanged species ($\bar{x}=2.3$, separated from precursor Au_{25} cluster on SEC column), were used. First, the

cluster was deposited on Ge crystal by drop casting. After air drying, a reference IR spectrum of the solid film was measured and later used for comparison. Afterwards, the whole system was flushed with water for 30 min until the signal was stable. At this point, a background was recorded, and the aqueous solution of the salts were flowed through the cell. Several concentrations of salts of interest were used for an ion sensing. The ion incorporation onto the crown ether cavity can be expressed by the following equation:



where M^{n+} is K^+ , Ba^{2+} , Gd^{3+} and Eu^{3+} .

The following experimental data refer to the salt concentration of 5000 ppm. Note that the reported ATR-IR spectra reveal the spectral changes that are induced by the interaction of the ions with the cluster film, since the reference was recorded in pure water just before admitting the salt solution. In all IR spectra, noticeable changes in intensity and frequency were observed at around 1034 cm^{-1} . This frequency corresponds to the C-O stretching vibration of the crown ether unit.^{28,29} The insertion of metal cations leads to the spectral changes of **18C6** moiety. The spectral features in IR spectra depend on the nature of the encapsulated ions. **Fig. 6** displays IR difference spectra after encapsulation of K^+ and Ba^{2+} . The vibrational spectra show that the band at around 1034 cm^{-1} shifts towards lower frequencies. Such a shift was attributed to the conformational changes of the crown ether upon complex formation with cations and fluctuation of the guest position inside the cavity.²⁹ A maximum shift $\delta=7\text{ cm}^{-1}$ was observed during K^+ encapsulation as well as an increase in intensity. The peak positions of other bands (e.g. C-H bending of the aromatic rings at 1276 cm^{-1} , C-H bending at $1379\text{-}1467\text{ cm}^{-1}$, amide bands at $1541\text{-}1660\text{ cm}^{-1}$) were less affected although their relative intensities change during host-guest complex formation. Note that the introduction of salts changes the water spectrum, which is reflected in broad signals in the spectra above 1600 cm^{-1} .

It has been shown that some earth alkaline metals have binding affinities towards crown cavities, and that derived from 18C6 macrocycles in particular.^{50,51,54,57} We therefore tested aqueous

B. EXPERIMENTAL PART

solutions of Ba^{2+} salt. The ionic radius of barium of 135 pm, compares well with the ionic radius of K^+ (138 pm).

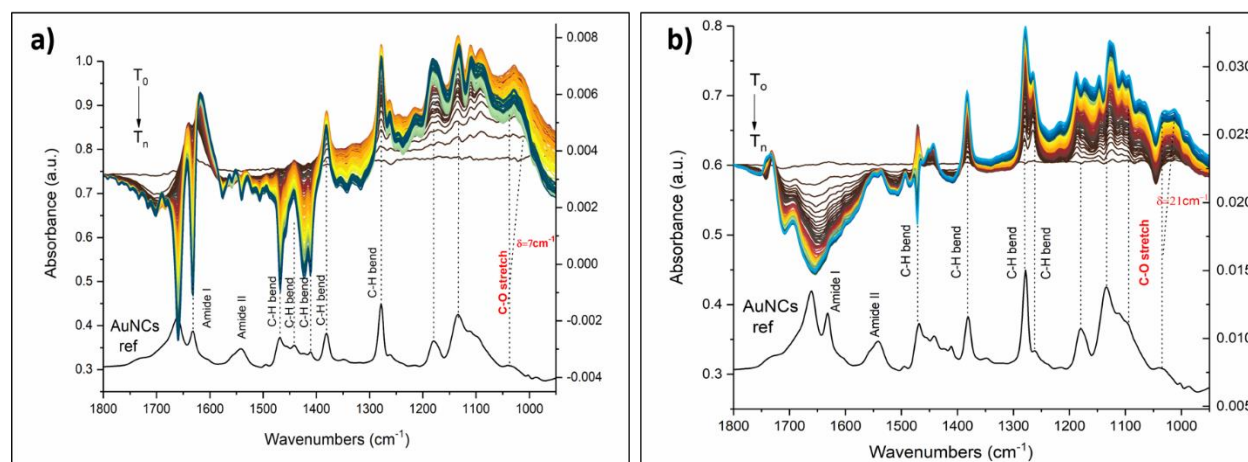


Fig. 6 *In situ* ATR-FTIR spectra of M^{n+} -cluster complexes using 5000 ppm aqueous solutions of a) KBr and b) BaCl_2 . The spectra are scaled for better comparison. Left axis refers to the cluster reference spectrum shown at the bottom. Right axis refers to the *in situ* spectra shown at the top.

It is therefore likely to see enhanced binding possibilities for barium as well. Indeed ATR-FTIR spectra revealed changes upon flowing Ba^{2+} salt (**Fig. 6b**). As expected, Ba^{2+} showed strong affinity towards crown moieties with a shift of 21 cm^{-1} of the C-O band. Other spectral changes were also seen. For example, the dominant band at around 1276 cm^{-1} appeared as a single band in the reference film spectrum but when the film interacted with the Ba^{2+} salt a second peak at slightly lower wavenumber appeared. A similar observation has been observed in the case of K^+ (**Fig. 6a**) although less prominent. The differences in the spectra and the correlation between binding and the nature of the ions can be explained by considering the electrostatic *Born* factor z^2/R .⁵⁰ Although the ionic radii of K^+ and Ba^{2+} are quite similar, the difference in charge state drastically affects the *Born* factor (0.724 and $2.96 \text{ eu}\cdot\text{\AA}^{-1}$ for K^+ and Ba^{2+} , respectively) and the observed vibrational shifts as a result of metal recognition and binding increases accordingly. Hence, these results are in line with the general trends of electrostatic *Born* factors. Interestingly, similar spectral changes and red shifts of the C-O band were observed using aqueous solutions of lanthanides, i.e. gadolinium (Gd^{3+}) and europium (Eu^{3+}) (**Fig. 7**).⁵⁸ The ionic radius of these ions (94 pm Gd^{3+} , 95 pm Eu^{3+}) are quite different compared to the one of K^+ (138 pm). On the other

hand, not only the size and nature of an ion but also its charge state could have an impact on the complex formation chemistry.

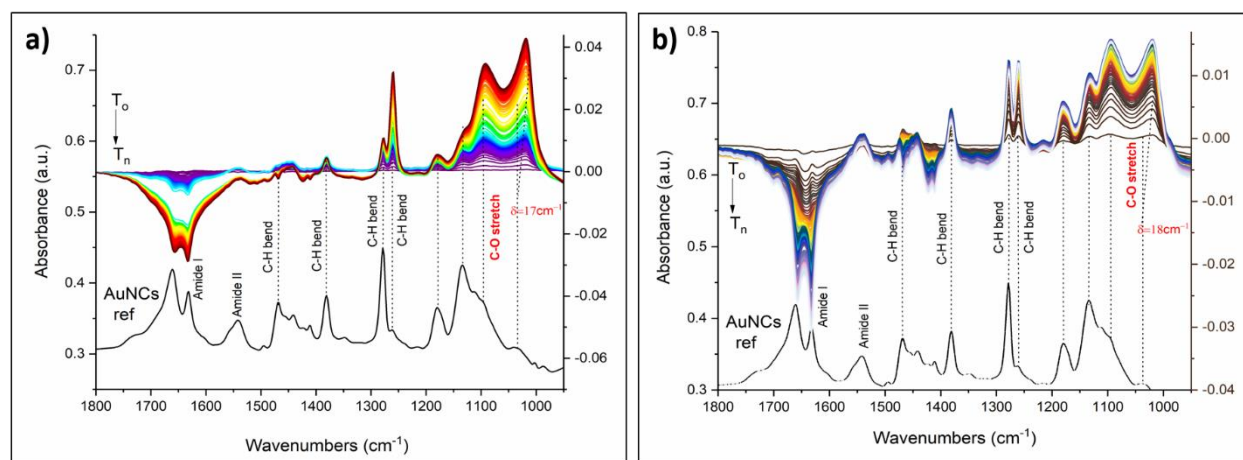


Fig. 7 *In situ* ATR-FTIR spectra of M^{3+} -cluster complexes using 5000 ppm aqueous solutions of a) $\text{EuCl}_3 \cdot 6\text{H}_2\text{O}$ and b) $\text{GdCl}_3 \cdot \text{H}_2\text{O}$. The spectra are scaled for better comparison. Left axis refers to the cluster reference spectrum shown at the bottom. Right axis refers to the *in situ* spectra shown at the top.

Compared to K^+ quite large red shifts were observed in case of lanthanides ($\delta=18 \text{ cm}^{-1}$ and $\delta=17 \text{ cm}^{-1}$). When comparing the electrostatic *Born* factors of lanthanides (9.57 and $9.47 \text{ eu} \cdot \text{\AA}^{-1}$ for Gd^{3+} and Eu^{3+} , respectively) with K^+ , the observed vibrational shifts are increased as expected, however, it is less pronounced with respect to Ba^{2+} . Note that this observation is also anticipated based on the general electrostatic *Born* factor trends.

Note, that after flowing water through the ATR-IR cell for an hour, no blue shifts of the C-O-C vibrations were observed (**Fig. S3**). This means, that the incorporated metal cations are strongly complexed to the crown ether.

The kinetics of ion incorporation can be studied quantitatively by fitting the absorbance of the C-O stretching vibration as a function of time (**Fig. S4**). Herein, the reaction was assumed to be pseudo-first-order considering the concentration of salt was constant with respect to the cluster. Therefore, the rate constant (k) for each case was determined using first order rate equation. Apparent rate constants for K^+ ($0.79 \pm 0.05 \text{ min}^{-1}$), Ba^{2+} ($0.32 \pm 0.04 \text{ min}^{-1}$), Eu^{3+} ($0.76 \pm 0.07 \text{ min}^{-1}$)

and Gd^{3+} ($0.48 \pm 0.03 \text{ min}^{-1}$) for supramolecular complex formation with the functionalized Au_{25} cluster were found to be quite similar.

4. DFT calculations

Density functional theory (DFT) calculations were performed for several reasons. First of all, we wanted to study where the *t*-CE ligand could bind on the cluster and if the binding would affect its structure (conformation). Second, we wanted to clarify if binding of cations in the crown cavity would induce structural changes on the ligand and if these are affected by the ligand binding to the cluster. Furthermore, we wanted to see how the binding of cations affects the vibrational spectra.

In the crystal structure the *t*-CE ligand is rather distorted with the two phenyl rings twisted and quite far from each other. Starting from the crystal structure a complete geometry optimization resulted in the structure shown in **Fig. S5a**. This is not the only stable conformation of the free molecule, however, a more symmetric structure, with the phenyl ring closer together was considerably less stable (see structure b in **Fig. S5**). Interestingly, when binding K^+ to the distorted structure a rather drastic conformational change took place during geometry optimization towards the more symmetric structure (**Fig. S6a**). The structure furthermore changed when replacing K^+ by Ba^{2+} (**Fig. S6b**). In both cases one of the two N-H groups was found to be closer to the cation than the other. However, in the Ba^{2+} case the proton of the amide group is further oriented away from the cation, possibly due to increased charge repulsion, which leads to a further tilt of the two phenyl groups, which are not parallel to each other anymore.

Based on DFT calculations, we found two binding positions on the cluster. In one the ligand binds on one staple, i.e. the sulfur groups of the *t*-CE ligand are part of one single staple (**Fig. S7**). In the other binding mode, the *t*-CE ligand bridges two staples (**Fig. 8a**), similar to what has been found for BINAS.^{59,60} The latter binding mode is considerably more stable, and we therefore focus on this binding mode in the following (**Fig. 8a**).

We now focus on the calculated IR spectra, first of the unbound ligand (**Fig. S8**). It became evident that the conformation has an effect on the IR spectra, especially also in the region around 1100 cm^{-1} , where the C-O vibrations are calculated.

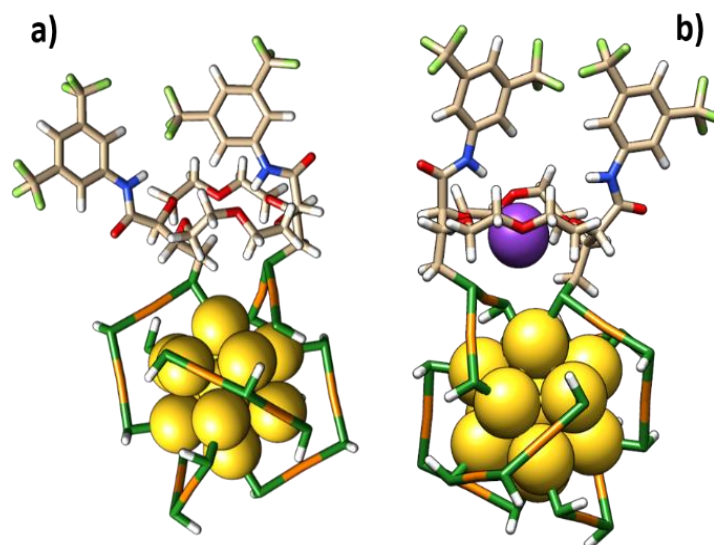


Fig. 8 a) The possible exchange site of the ligand on the cluster surface and b) conformational changes upon complexation with K^+ based on DFT calculations.

Binding of K^+ changed the IR spectrum, in particular the prominent C-O vibrational band shifted down in frequency (as observed in the experiments). When K^+ was replaced by Ba^{2+} the spectrum changed again quite drastically (**Fig. S8**).

The vibrational spectrum of the free *t*-CE ligand and of the one adsorbed on the cluster surface were found to be quite similar, as a comparison shows (**Fig. S9**). The most prominent change is the weakening of the C-O vibrations upon adsorption. Upon complexation with K^+ the spectral region around 1200 cm^{-1} and below exhibited changes and the C-O vibrations shifted to lower frequency, in agreement with experiment. Moreover, the calculated IR spectra of free ligand compared to the spectra of the cluster and the complex with the metal cations showed that the conformational changes led to changes in amide II (N-H bending) region below 1600 cm^{-1} (frequency shifts and intensity changes), in accordance with structural changes as discussed above. The experimental spectra revealed quite a drastic change of the aromatic C-H in plane

bending around 1276 cm^{-1} (emergence of a second band at lower frequency). The calculations do not quite reproduce that although it is noted that the corresponding band shifted slightly to lower wavenumbers upon complexation. To sum up, the calculations predict a shift to lower wavenumbers of the C-O stretching band of the crown ether unit upon complexation, in agreement with experiment. Furthermore, in agreement with experiment the calculations disclose spectral changes associated with a conformational change of the *t*-CE ligand due to complex formation.

5. Conclusions

In summary, ligand exchange reaction between $\text{Au}_{25}(\text{2-PET})_{24}$ cluster and *t*-CE ligand was studied *in situ* with several methods including UV-vis, ^1H NMR and HPLC. The smoothing of the optical fingerprint bands in the UV-vis spectra correlated with the change in solution color as well as changes in NMR signals indicate the success of the ligand-for-ligand reaction. Moreover, MALDI-TOF mass analysis showed the formation of up to $x=5$ $\text{Au}_{25}(\text{2-PET})_{18-2x}(\textit{t}\text{-CE})_x$ exchange species. The reaction monitoring with HPLC showed immediate changes in the chromatogram after ligand injection, in agreement with NMR, which showed a fast first ligand exchange. MALDI mass spectra revealed complexation of Na^+ by the exchanged cluster. The ATR-FTIR studies of ion binding ability of the $\text{Au}_{25}(\text{2-PET})_{18-2x}(\textit{t}\text{-CE})_x$ sample with aqueous solutions of M^{n+} salts (where M^{n+} is K^+ , Ba^{2+} , Gd^{3+} and Eu^{3+}) revealed significant red shifts of C-O stretching vibrations due to an ion encapsulation into a crown cavity. Further spectral changes pointed towards a conformational change of the ligand upon complex formation. Calculations highlighted the most probable and energetically favorable interstaple binding site for the *t*-CE ligand. Calculated vibrational spectra showed pronounced C-O frequency shifts during host-guest complex formation in agreement with experimental data. The complexation leads to some conformational changes of the ligand, which is also reflected in the calculated vibrational spectra. The formed supramolecular complexes exhibit very good stability. The used ligand combines ion binding possibilities, through the crown ether unit, with the possibility to transduce the binding event through a conformational change which may affect the optical properties of the chromophores

attached to it. This makes the post-functionalized Au₂₅ cluster a promising candidate for ion sensing applications. The insight gained in this study will guide the further development of the composite nanoscale material towards this goal.

References

- (1) Jin, R.; Zeng, C.; Zhou, M.; Chen, Y. Atomically Precise Colloidal Metal Nanoclusters and Nanoparticles: Fundamentals and Opportunities. *Chem. Rev.* **2016**, *116* (18), 10346–10413.
- (2) Chakraborty, I.; Pradeep, T. Atomically Precise Clusters of Noble Metals: Emerging Link between Atoms and Nanoparticles. *Chem. Rev.* **2017**, *117* (12), 8208–8271.
- (3) Knoppe, S., Dharmaratne, A. C., Schreiner, E., Dass, A. & Bürgi, T. Ligand Exchange Reactions on Au₃₈ and Au₄₀ Clusters: A Combined Circular Dichroism and Mass Spectrometry Study. *J. Am. Chem. Soc.* **2010**, *132*, 16783–16789.
- (4) Knoppe, S., Azoulay, R., Dass, A. & Bürgi, T. In situ reaction monitoring reveals a diastereoselective ligand exchange reaction between the intrinsically chiral Au₃₈(SR)₂₄ and chiral thiols. *J. Am. Chem. Soc.* **2012**, *134*, 20302–20305.
- (5) Heinecke, C. L.; Ni, T. W.; Malola, S.; Mäkinen, V.; Wong, O. A.; Häkkinen, H.; Ackerson, C. J. Structural and Theoretical Basis for Ligand Exchange on Thiolate Monolayer Protected Gold Nanoclusters. *J. Am. Chem. Soc.* **2012**, *134* (32), 13316–13322.
- (6) Beqa, L.; Deschamps, D.; Perrio, S.; Gaumont, A.-C.; Knoppe, S.; Bürgi, T. Ligand Exchange Reaction on Au₃₈(SR)₂₄, Separation of Au₃₈(SR)₂₃(SR')₁ Regioisomers, and Migration of Thiolates. *J. Phys. Chem. C* **2013**, *117* (41), 21619–21625.
- (7) Ni, T. W., Tofanelli, M. A., Phillips, B. D. & Ackerson, C. J. Structural basis for ligand exchange on Au₂₅(SR)₁₈. *Inorg. Chem.* **2014**, *53*, 6500–6502.
- (8) Fernando, A. & Aikens, C. M. Ligand Exchange Mechanism on Thiolate Monolayer Protected Au₂₅(SR)₁₈ Nanoclusters. *J. Phys. Chem. C* **2015**, *119*, 20179–20187.

- (9) Sels, A., Salassa, G., Pollitt, S., Guglieri, C., Rupprechter, G., Barrabés, N., Bürgi, T. Structural Investigation of the Ligand Exchange Reaction with Rigid Dithiol on Doped (Pt, Pd) Au₂₅ Clusters. *J. Phys. Chem. C* **2017**, *121*, 20, 10919-10926.
- (10) Sels, A., Barrabés, N., Knoppe, S. & Bürgi, T. Isolation of atomically precise mixed ligand shell PdAu₂₄ clusters. *Nanoscale* **2016**, *8*, 11130–11135.
- (11) Kazan, R., Zhang, B. & Bürgi, T. Au₃₈Cu₁(2-PET)₂₄ nanocluster: synthesis, enantioseparation and luminescence. *Dalt. Trans.* **2017**, *46*, 7708–7713.
- (12) Shichibu, Y., Negishi, Y., Tsukuda, T. & Teranishi, T. Large-scale synthesis of thiolated Au₂₅ clusters via ligand exchange reactions of phosphine-stabilized Au₁₁ clusters. *J. Am. Chem. Soc.* **2005**, *127*, 13464–13465.
- (13) Shibu, E. S., Muhammed, M. a. H., Tsukuda, T. & Pradeep, T. Ligand Exchange of Au₂₅SG₁₈ Leading to Functionalized Gold Clusters: Spectroscopy, Kinetics, and Luminescence. *J. Phys. Chem. C* **2008**, *112*, 12168–12176.
- (14) Jupally, V. R. et al. Interstaple dithiol cross-linking in Au₂₅(SR)₁₈ nanomolecules: A combined mass spectrometric and computational study. *J. Am. Chem. Soc.* **2011**, *133*, 20258–20266.
- (15) Li, M.-B., Tian, S.-K., Wu, Z. & Jin, R. Peeling the Core–Shell Au₂₅ Nanocluster by Reverse Ligand-Exchange. *Chem. Mater.* **2016**, *28*, 1022–1025.
- (16) Si, S. et al. Ligand Exchange on Au₂₅ Cluster with Chiral Thiols. *J. Phys. Chem. C* **2009**, *113*, 12966–12969.
- (17) Reyes, E., Madueño, R., Blázquez, M. & Pineda, T. Facile Exchange of Ligands on the 6-Mercaptopurine-Monolayer Protected Gold Clusters Surface. *J. Phys. Chem. C* **2010**, *114*, 15955–15962.

- (18) Dapporto, P., Paoli, P., Matijašić, I. & Tušek-Božić, L. Crystal structures of complexes of ammonium and potassium hexafluorophosphate with dibenzo-18-crown-6. Molecular mechanics studies on the uncomplexed macrocycle. *Inorganica Chim. Acta* **1996**, *252*, 383–389.
- (19) Cantrill, S. J.; Fulton, D. A.; Heiss, A. M.; Pease, A. R.; Stoddart, J. F.; White, A. J. P.; Williams, D. J. The Influence of Macrocyclic Polyether Constitution upon Ammonium Ion/Crown Ether Recognition Processes. *Chem. - A Eur. J.* **2000**, *6* (12), 2274–2287.
- (20) Gokel, G. W., Leevy, W. M. & Weber, M. E. Crown ethers: Sensors for ions and molecular scaffolds for materials and biological models. *Chem. Rev.* **2004**, *104*, 2723–2750.
- (21) van Veggel, F. C. J. M., Verboom, W. & Reinhoudt, D. N. Metallomacrocycles: Supramolecular Chemistry with Hard and Soft Metal Cations in Action. *Chem. Rev.* **1994**, *94*, 279–299.
- (22) Gorden, A. E. V, Xu, J., Raymond, K. N. & Durbin, P. Rational design of sequestering agents for plutonium and other actinides. *Chem. Rev.* **2003**, *103*, 4207–4282.
- (23) Uiterwijk, J. W. H. M. et al. Complexes of Crown Ethers with Uronium Salts: Preparation and Crystal Structure of 18-Crown-6 Uronium Nitrate (1:1) and Benzo-27-Crown-9 Uronium Perchlorate (1:1). *Angew. Chemie Int. Ed. English* **1982**, *21*, 1100–1107.
- (24) Morishima, F., Kusaka, R., Inokuchi, Y., Haino, T. & Ebata, T. Cage effects on conformational preference and photophysics in the host–guest complex of benzenediols with 18-Crown-6. *Phys. Chem. Chem. Phys.* **2016**, *18*, 8027–8038.
- (25) Li, J., Yim, D., Jang, W. D. & Yoon, J. Recent progress in the design and applications of fluorescence probes containing crown ethers. *Chem. Soc. Rev.* **2017**, *46*, 2437–2458.
- (26) Danil de Namor, A. F., Ng, J. C. Y., Llosa Tanco, M. A. & Salomon, M. Thermodynamics of Lithium–Crown Ether (12-crown-4 and 1-Benzyl-1-aza-12-crown-4) Interactions in Acetonitrile and Propylene Carbonate. The Anion Effect on the Coordination Process. *J. Phys. Chem.* **1996**, *100*, 14485–14491.

- (27) Al-Kahtani, A. A., Al-Jallal, N. A. & El-Azhary, A. A. Conformational and vibrational analysis of 18-crown-6-alkali metal cation complexes. *Spectrochim. Acta - Part A Mol. Biomol. Spectrosc.* **2014**, *132*, 70–83.
- (28) Inokuchi, Y. et al. Formation of host-guest complexes on gold surface investigated by surface-enhanced IR absorption spectroscopy. *Chem. Phys. Lett.* **2014**, *592*, 90–95.
- (29) Inokuchi, Y. et al. New insights into metal ion–crown ether complexes revealed by SEIRA spectroscopy. *New J. Chem.* **2015**, *39*, 8673–8680.
- (30) Mathew, A. & Pradeep, T. Noble Metal Clusters: Applications in Energy, Environment, and Biology. Part. Part. Syst. Charact. **2014**, *31*, 1017–1053.
- (31) Liu, Y., Ai, K., Cheng, X., Huo, L. & Lu, L. Gold-Nanocluster-Based Fluorescent Sensors for Highly Sensitive and Selective Detection of Cyanide in Water. *Adv. Funct. Mater.* **2010**, *20*, 951–956.
- (32) Huang, C.-C., Yang, Z., Lee, K.-H. & Chang, H.-T. Synthesis of Highly Fluorescent Gold Nanoparticles for Sensing Mercury (II). *Angew. Chemie Int. Ed.* **2007**, *46*, 6824–6828.
- (33) Durgadas, C. V., Sharma, C. P. & Sreenivasan, K. Fluorescent gold clusters as nanosensors for copper ions in live cells. *Analyst* **2011**, *136*, 933–940.
- (34) Le Guével, X. et al. Formation of Fluorescent Metal (Au, Ag) Nanoclusters Capped in Bovine Serum Albumin Followed by Fluorescence and Spectroscopy. *J. Phys. Chem. C* **2011**, *115*, 10955–10963.
- (35) Lin, Y. & Tseng, W. Ultrasensitive Sensing of Hg^{2+} and CH_3Hg^+ Based on the Fluorescence Quenching of Lysozyme Type VI-Stabilized Gold Nanoclusters. *Anal. Chem.* **2010**, *82*, 9194–9200.
- (36) Xie, J., Zheng, Y. & Ying, J. Y. Highly selective and ultrasensitive detection of Hg^{2+} based on fluorescence quenching of Au nanoclusters by Hg^{2+} – Au^+ interactions. *Chem. Commun.* **2010**, *46*, 961–963.

- (37) George, A., Shibu, E. S., Maliyekkal, S. M., Bootharaju, M. S. & Pradeep, T. Luminescent, Freestanding Composite Films of Au₁₅ for Specific Metal Ion Sensing. *ACS Appl. Mater. Interfaces* **2012**, *4*, 639–644.
- (38) Dainese, T. et al. Au₂₅(SEt)₁₈, a nearly naked thiolate-protected Au₂₅ cluster: Structural analysis by single crystal X-ray crystallography and electron nuclear double resonance. *ACS Nano* **2014**, *8*, 3904–3912.
- (39) Lu, Y., Jiang, Y., Gao, X. & Chen, W. Charge state-dependent catalytic activity of [Au₂₅(SC₁₂H₂₅)₁₈] nanoclusters for the two-electron reduction of dioxygen to hydrogen peroxide. *Chem. Commun.* **2014**, *50*, 8464–8467.
- (40) Zhu, M.; Eckenhoff, W. T.; Pintauer, T.; Jin, R. Conversion of Anionic [Au₂₅(SCH₂CH₂Ph)₁₈]⁻ Cluster to Charge Neutral Cluster via Air Oxidation. *J. Phys. Chem. C* **2008**, *112* (37), 14221–14224.
- (41) E. Brun, K.-F. Zhang, L. Guénée and J. Lacour, *Org. Biomol. Chem.*, **2020**, *18*, 250-254.
- (42) Homberg, A.; Poggiali, D.; Vishe, M.; Besnard, C.; Guénée, L.; Lacour, J. One-Step Synthesis of Diaza Macrocycles by Rh(II)-Catalyzed [3 + 6 + 3 + 6] Condensations of Morpholines and α -Diazo- β -Ketoesters. *Org. Lett.* **2019**, *21* (3), 687–691.
- (43) Poggiali, D.; Homberg, A.; Lathion, T.; Piguet, C.; Lacour, J. Kinetics of Rh(II)-Catalyzed α -Diazo- β -Ketoester Decomposition and Application to the [3+6+3+6] Synthesis of Macrocycles on a Large Scale and at Low Catalyst Loadings. *ACS Catal.* **2016**, *6* (8), 4877–4881.
- (44) Vishe, M.; Hrdina, R.; Guénée, L.; Besnard, C.; Lacour, J. One-Pot Multi-Component Synthesis and Solid State Structures of Functionally Rich Polyether Macrocycles. *Adv. Synth. Catal.* **2013**, *355* (16), 3161–3169.
- (45) Zeghida, W.; Besnard, C.; Lacour, J. Rhodium(II)-Catalyzed One-Pot Four-Component Synthesis of Functionalized Polyether Macrocycles at High Concentration. *Angew. Chemie - Int. Ed.* **2010**, *49* (40), 7253–7256.

- (46) Vishe, M.; Hrdina, R.; Poblador-Bahamonde, A. I.; Besnard, C.; Guénée, L.; Bürgi, T.; Lacour, J. Remote Stereoselective Deconjugation of α,β -Unsaturated Esters by Simple Amidation Reactions. *Chem. Sci.* **2015**, *6* (8), 4923–4928.
- (47) Jarolímová, Z.; Vishe, M.; Lacour, J.; Bakker, E. Potassium Ion-Selective Fluorescent and PH Independent Nanosensors Based on Functionalized Polyether Macrocycles. *Chem. Sci.* **2016**, *7* (1), 525–533.
- (48) Sinn, S.; Biedermann, F.; Vishe, M.; Aliprandi, A.; Besnard, C.; Lacour, J.; De Cola, L. A Ratiometric Luminescent Switch Based on Platinum Complexes Tethered to a Crown-Ether Scaffold. *ChemPhysChem* **2016**, *17* (12), 1829–1834.
- (49) Ray, S. K.; Homberg, A.; Vishe, M.; Besnard, C.; Lacour, J. Efficient Synthesis of Ditopic Polyamide Receptors for Cooperative Ion Pair Recognition in Solution and Solid States. *Chem. - A Eur. J.* **2018**, *24* (12), 2944–2951.
- (50) Vishe, M.; Lathion, T.; Pascal, S.; Yushchenko, O.; Homberg, A.; Brun, E.; Vauthey, E.; Piguet, C.; Lacour, J. Excimer-Based On-Off Bis(Pyreneamide) Macrocyclic Chemosensors. *Helv. Chim. Acta* **2018**, *101* (1), e1700265.
- (51) Homberg, A.; Brun, E.; Zinna, F.; Pascal, S.; Górecki, M.; Monnier, L.; Besnard, C.; Pescitelli, G.; Di Bari, L.; Lacour, J. Combined Reversible Switching of ECD and Quenching of CPL with Chiral Fluorescent Macrocycles. *Chem. Sci.* **2018**, *9* (35), 7043–7052.
- (52) Homberg, A.; Hrdina, R.; Vishe, M.; Guénée, L.; Lacour, J. Stereoselective Deconjugation of Macrocyclic α,β -Unsaturated Esters by Sequential Amidation and Olefin Transposition: Application to Enantioselective Phase-Transfer Catalysis. *Org. Biomol. Chem.* **2019**, *17* (28), 6905–6910.
- (53) Zinna, F.; Voci, S.; Arrico, L.; Brun, E.; Homberg, A.; Bouffier, L.; Funaioli, T.; Lacour, J.; Sojic, N.; Di Bari, L. Circularly-Polarized Electrochemiluminescence from a Chiral Bispyrene Organic Macrocycle. *Angew. Chemie - Int. Ed.* **2019**, *58* (21), 6952–6956.

- (54) Aster, A.; Licari, G.; Zinna, F.; Brun, E.; Kumpulainen, T.; Tajkhorshid, E.; Lacour, J.; Vauthey, E. Tuning Symmetry Breaking Charge Separation in Perylene Bichromophores by Conformational Control. *Chem. Sci.* **2019**, *10* (45), 10629–10639.
- (55) Völker, B., Wölzl, F., Bürgi, T. & Lingenfelter, D. Dye bonding to TiO₂: In situ attenuated total reflection infrared spectroscopy study, simulations, and correlation with dye-sensitized solar cell characteristics. *Langmuir* **2012**, *28*, 11354–11363.
- (56) Dennington, R., Keith, T. A. & Millam, J. M. GaussView {V}ersion {6}. (**2016**).
- (57) Hamdiani, S., Savalas, L. R. T., Purwoko, A. A. & Hadisaputra, S. Theoretical study on the binding selectivity of 18-membered azacrown ethers with alkaline earth metal species. *Acta Chim. Asiana* **2018**, *1*, 17.
- (58) Suárez, S.; Mamula, O.; Scopelliti, R.; Donnio, B.; Guillon, D.; Terazzi, E.; Piguet, C.; Bünzli, J. C. G. Lanthanide Luminescent Mesomorphic Complexes with Macrocycles Derived from Diaza-18-Crown-6. *New J. Chem.* **2005**, *29* (10), 1323–1334.
- (59) Knoppe, S. & Bürgi, T. The fate of Au₂₅(SR)₁₈ clusters upon ligand exchange with binaphthyl-dithiol: Interstaple binding vs. decomposition. *Phys. Chem. Chem. Phys.* **2013**, *15*, 15816–15820.
- (60) Molina, B. et al. Structures and chiroptical properties of the BINAS-monosubstituted Au₃₈(SCH₃)₂₄ cluster. *Nanoscale* **2013**, *5*, 10956.

Supporting Information

Table S1 Calculated masses for each exchange product in the mass spectrum.

Au ₂₅ (2-PET) _{18-2x} (t-CE) _x		
Number of exchange	Formula	Theoretical masses/ Da
X=1	Au ₂₅ (2-PET) ₁₆ (t-CE)	7983
X=2	Au ₂₅ (2-PET) ₁₄ (t-CE) ₂	8575
X=3	Au ₂₅ (2-PET) ₁₂ (t-CE) ₃	9166
X=4	Au ₂₅ (2-PET) ₁₀ (t-CE) ₄	9758

$$\bar{x} = \frac{\sum I_x * X}{\sum I_x}$$

where \bar{x} is an average exchange, I_x is an intensity of the peak and X is an exchange number.

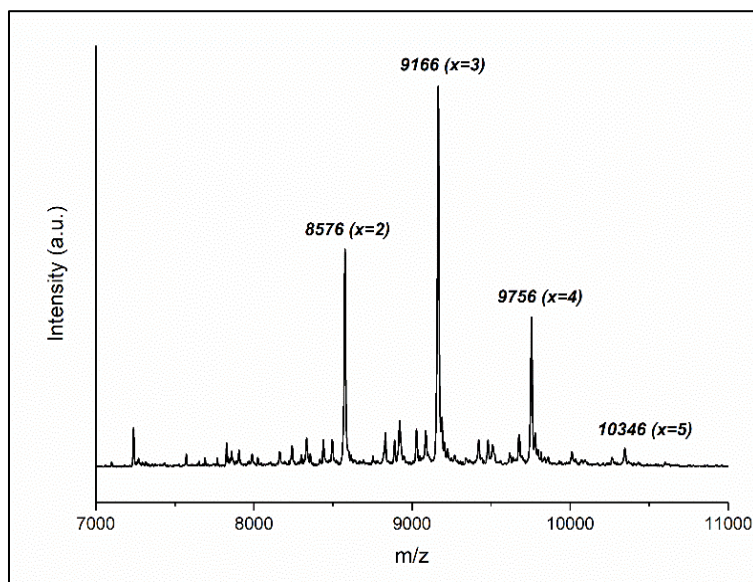


Fig. S1 MALDI mass spectrum of the 1:10 cluster/ligand exchange sample containing maximum up to 5 exchange species.

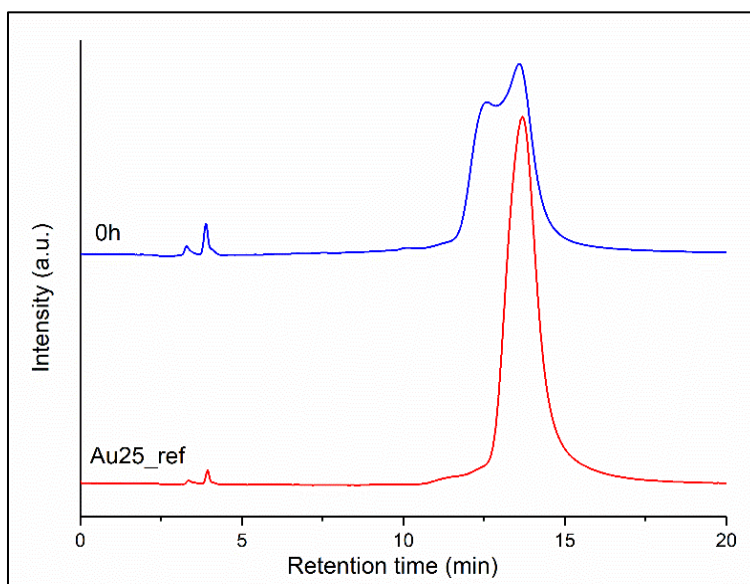


Fig. S2 *In situ* HPLC studies of the ligand exchange reaction. 1:10 cluster/(*t*-CE) ratio was used for *in situ* reaction monitoring.

B. EXPERIMENTAL PART

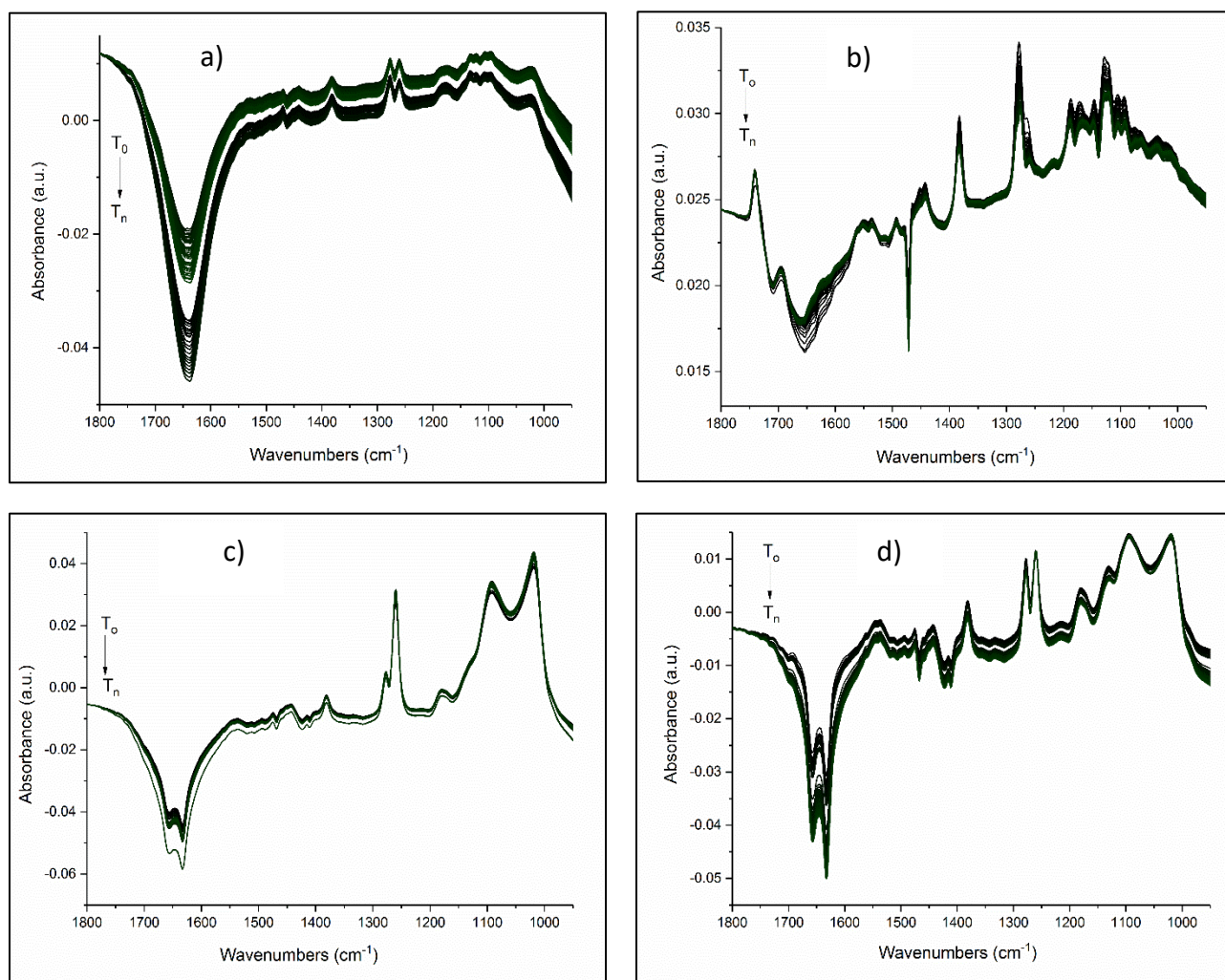


Fig. S3 *In situ* ATR-FTIR spectra of Mⁿ⁺-cluster complexes after flushing water for 1h for a) K⁺, b) Ba²⁺, c) Eu³⁺ and d) Gd³⁺.

B. EXPERIMENTAL PART

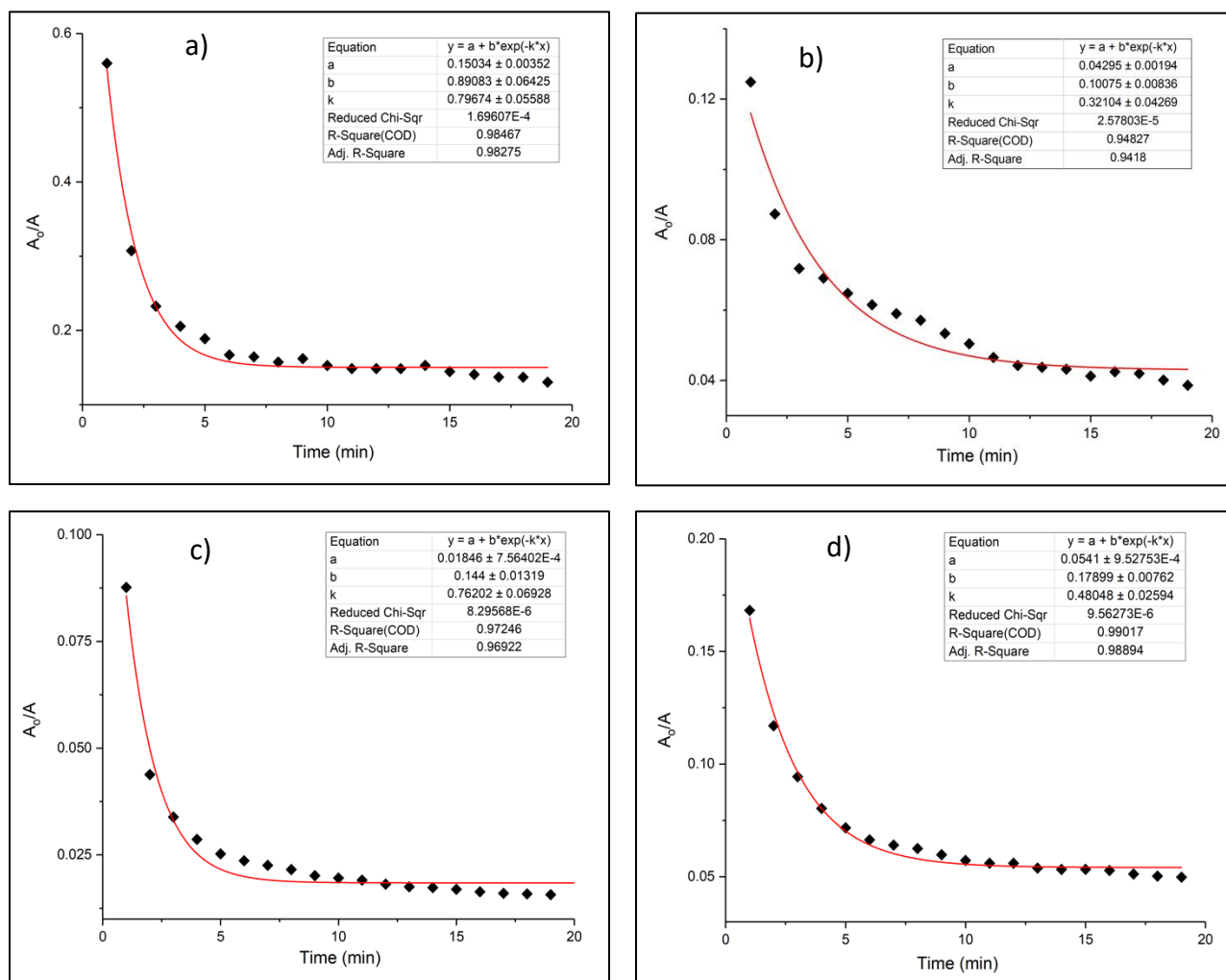


Fig. S4 Kinetic fits for a) K^+ , b) Ba^{2+} , c) Eu^{3+} and d) Gd^{3+} after complex formation. The dots are the values from FTIR experiment, the traces are the corresponding fits.

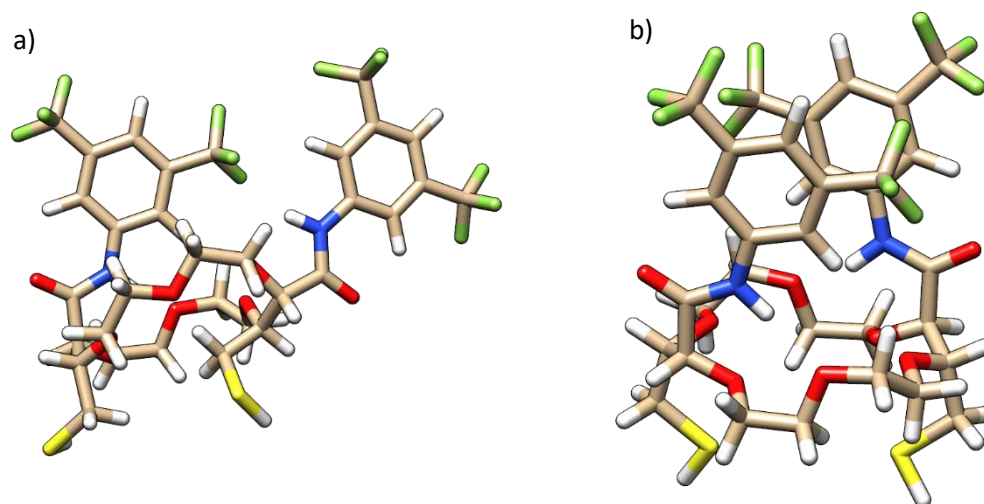


Fig. S5 Optimized a) *t*-CE1 and b) *t*-CE2 geometries of free ligand with *t*-CE1 as the most stable and energetically favorable conformation.

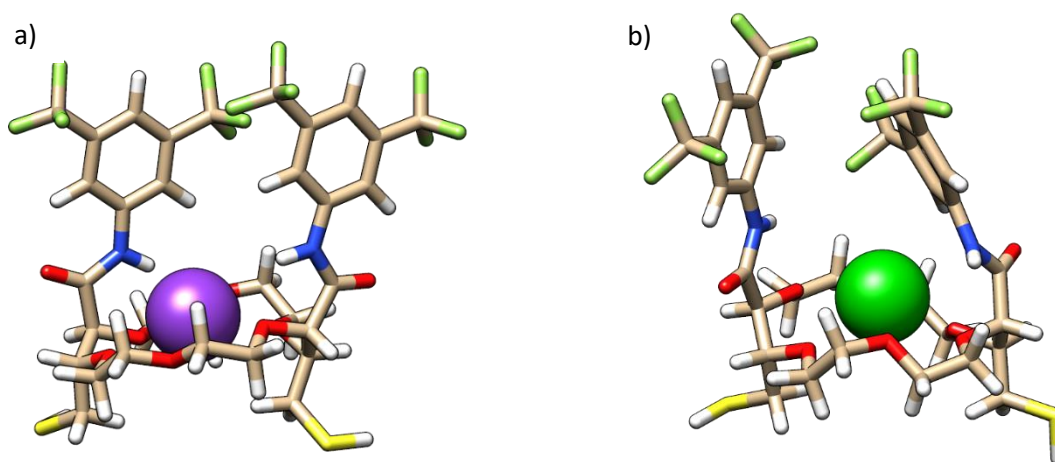


Fig. S6 Conformational changes upon complex formation of *t*-CE1 with a) K⁺ and b) Ba²⁺ based on DFT calculations.

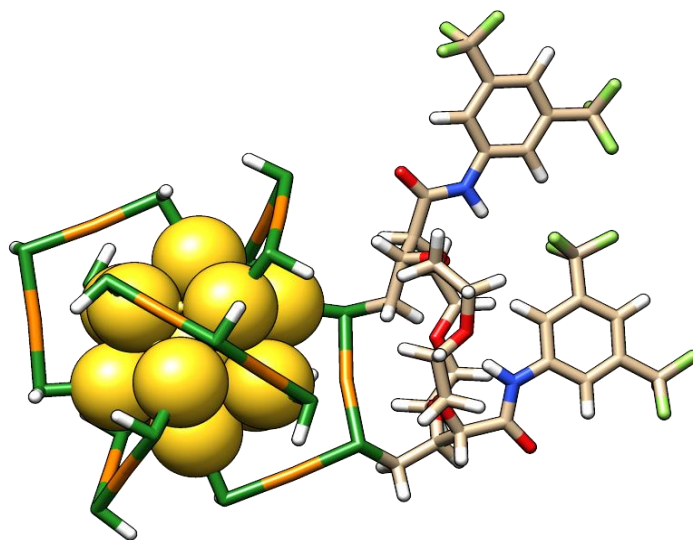


Fig. S7 Intrastaple binding site of the *t*-CE ligand on the cluster surface based on DFT calculations.

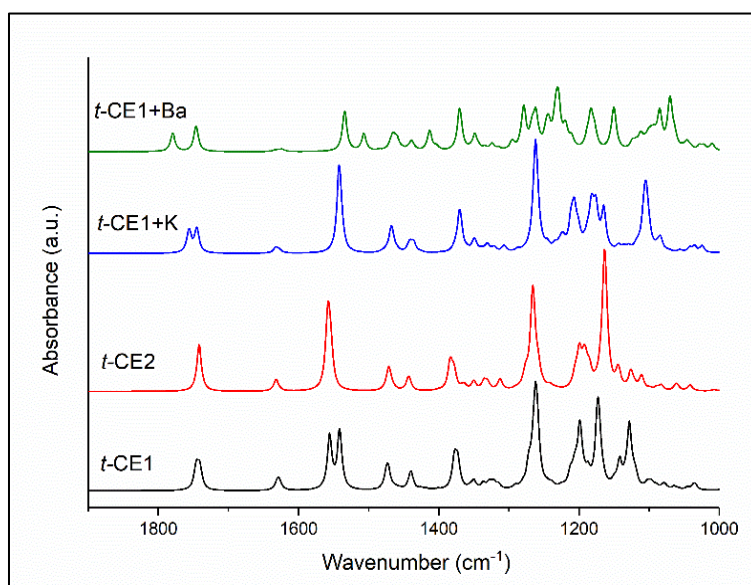


Fig. S8 Calculated IR spectra and corresponding changes upon complexation with free ligand.

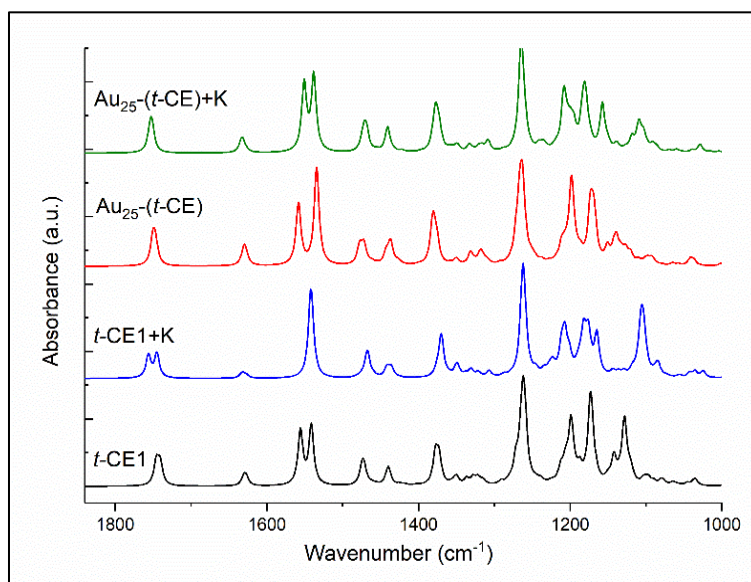


Fig. S9 Calculated IR spectra and corresponding changes upon K⁺-cluster complexation.

5.3. Induced chirality and cooperativity in post-functionalized Au₂₅ cluster

Considerable effort has been devoted to exploring the host-guest interactions based on molecular recognition events at the nanoscale. Gold nanoparticles' (AuNPs) based chemical sensors have already been designed and widely applied in modern nanotechnology. The recent progress in synthesizing crown-based supramolecular host molecules will aid enormously in the design of highly sensitive and selective sensors. However, the investigation of the binding properties of atomically precise clusters is still at its infancy. Previously, we have demonstrated the capability of post-functionalized Au₂₅ cluster to bind multivalent metal cations in aqueous solutions. Moreover, here, we went further to investigate the cooperative binding behavior of enantiopure crown-functionalized Au₂₅ cluster with chiral 3,3-dimethyl-2-butylamine. NMR titration experiments were performed to follow the binding of the amine to the crown cavity. Data fitting with a nonlinear regression algorithm was applied to derive the binding affinities and the cooperativity coefficients for the interaction. The highest Hill's coefficient ($n_H=2$) was obtained when the average number of crown ligand per cluster was $\bar{x}=2.2$. However, the further increase of the ligand had a negative effect on n_H likely due to steric hindrance. On the other hand, higher affinities (micromolar) were reached with the increase of \bar{x} . Thus, by changing the number of the crown ether ligand on the cluster surface, the allosteric effect from positive to negative and the binding affinities can be switched in a controlled manner.

1. Introduction

Molecular recognition processes¹ cover the subset of important molecular transformation in biological systems, i.e. the recognition of proper substrates by enzymes,^{2,3} the transmission of cellular signals,^{4,5} the recognition of one cell by another,^{6,7} the control of transcription, translation and the fidelity of DNA replication.⁸⁻¹² These events involve the binding of a small molecule to a macromolecule to form non-covalent supramolecular complexes. In biochemistry the ligand is an organic molecule that binds to a macromolecule known as a receptor. In common supramolecular terminology, the ligand is called guest which binds to a complementary host molecule. One of the most effortlessly and commercially available host molecule is a class of cyclic organic molecules with several repeating units known as crown ethers. After their discovery by Pederson in 1967 at du Pond,¹³ crown ethers attracted an immense attention owing their outstanding binding properties. Since then, over the decades, a massive progress in the field of supramolecular chemistry to selectively bind metal cations¹⁴⁻²² and organic molecules^{23,24} through non-covalent bonding was achieved by tuning the size of macrocycle²⁵⁻²⁷ (12-crown-4, 15-crown-5, 18-crown-6, cryptands) as well as the type of heteroatom²⁸⁻³⁴ (aza- and thio-crown ethers) constituting the crown cage. Moreover, the complexation with the crown cage can alter certain unique properties that will make them excellent candidates in sensing,²⁵ metal extraction,²⁷ drug formulation and delivery.^{27,35}

From a standpoint of their applications, kinetic and thermodynamic studies of the host-guest interactions are prerequisite for self-organization and self-assembly at the molecular level. A complete understanding of the interaction requires the analyses of binding strength of the guest to a host under equilibrium conditions.³⁶ At this point, the trade-off between affinity and specificity are considered in molecular recognition events. High-affinity interactions arise from strong intermolecular attractions between host and guest whereas the specificity is defined by the capability of the host to bind certain guests in a specific way. A simple way to quantitatively characterize the guest's affinity is to measure the binding constant (K_d dissociation or K_a association constant) at the equilibrium. The value of K_d is equal in magnitude to the

concentration of free ligand at which half of the host molecules are bound to the ligand. Knowing the value of K_d , the binding free energy can be easily calculated using the following equation:

$$\Delta G_{bind}^0 = RT \ln K_d$$

where ΔG_{bind}^0 is the binding free energy, K_d is the dissociation constant.

Normally, the value of K_d refers to as the affinity of an interaction. The most common approach for quantifying supramolecular interactions is a titration of the guest into a solution of host and recording the corresponding electrochemical, optical or chemical changes via NMR,^{37–40} UV-vis³² and fluorescence spectroscopy.^{29–32} NMR is an informative technique and is extensively used for direct measurement of K_d because of proton signals' sensitivity to conformational changes when the complexation takes place. ¹H NMR titration experiments present no challenge in their basic form and involve the measurement of the chemical shift of the “labelled” proton after each titration step and presenting the result as a function of the ligand concentration. The shape of the titration curve known as a binding isotherm, can pinpoint the nature of the host-guest interaction. When the host binds to one guest (1:1 interaction model), then the titration curve is called hyperbolic binding isotherm. In this case the binding events are independent and the host's response to the increase of the guest's concentration is evolving gradually (binding of O₂ to myoglobin⁴¹). Such a graded response is insensitive to small changes in concentration. In contrast, most biological processes are ultrasensitive and even negligible change in the reaction conditions can drastically influence on the titration curve's shape (binding of O₂ to hemoglobin⁴²). When the ultrasensitive response to the environmental changes is due to the binding of the ligand molecules, then the term “allosteric cooperativity” is generally introduced.^{43,44} Cooperative effect due to multiple binding sites with different affinities is evidenced by the deviations from the classical hyperbolic curve shape. The sigmoidal shape of binding isotherm is a blind evidence of allostery. Moreover, when the binding of the first ligand molecule to the host reinforces the binding affinities for the other ligands to bind easily, then the phenomenon is called positive cooperativity. If the binding of one ligand makes more difficult to the other ones to bind, then the negative cooperativity is observed. The straightforward fitting of titration curve can derive a parameter describing the cooperativity. The cooperativity index or Hill's coefficient

$n_H=1$ for a non-cooperative system.⁴⁵ Systems exhibiting positive or negative cooperativity will have a $n_H>1$ and $n_H<1$ value, respectively. The examples of both positive^{46–52} and negative^{53–59} cooperative binding in biological and supramolecular systems are quite abundant. The host-guest interactions by the participation of gold nanoparticles (AuNPs) functionalized with various biomolecules or bioconjugates, and their applications in biomedicine are also well studied.^{60–66} Metal nanoclusters (NCs) with formula $Au_n(SR)_m$ (less than 2 nm in size) become a supreme class of nanomaterials possessing unique size-dependent optical properties.^{67,68} In the ultra-small size regime, the quantum confinement effect in these nanomaterials leads to discrete electronic levels. The total control over the size and the structure in NCs is a key factor to assess their remarkable applications in energy, environment and biology.⁶⁹ However, the studies on binding properties of atomically precise clusters within the concept of molecular recognition is scarcely investigated.

In chapter 5.2 we have demonstrated the binding properties of crown ether-functionalized Au_{25} cluster to trap multivalent metal cations. An *in situ* ATR-FTIR studies on the solid films of cluster deposited on Ge crystals showed a red shift of C-O vibrational stretching modes due to the trapping of the ions in the crown ether.

Herein, we presented the binding properties of crown ether-functionalized Au_{25} (enantiopure cluster) and chiral amines. 1H NMR titration experiments with a large range of guest concentrations and trial experiments were required to optimize and design the best experimental conditions. The subsequent fitting of the titration curve was done using a nonlinear regression algorithm. In this work considerable effort has been devoted to the understanding of the binding affinities of post-functionalized Au_{25} cluster and the influence of the extent of ligand exchange on cooperativity. The main idea was to shed some light on molecular recognition events involving metal nanoclusters.

2. Experimental section

2.1. Materials. Hydrogen tetrachloroaurate (III) tridhydrate (ACS, Alfa Aesar, 99.99%), tetraoctylammonium bromide (Sigma-Aldrich, 98%), 2-phenylethanethiol (Sigma-Aldrich-Fluka,

99+%), sodium borohydrate (Aldrich, $\geq 96\%$), toluene (Fisher, 99.9%), ethanol (Sigma-Aldrich, > 99.8%), methanol (Fisher, 99.9%), dichloromethane (Merck, 99.7+%), enantiopure {N2,N11-bis(3,5-bis(trifluoromethyl)phenyl)-3,12-bis(mercaptomethyl)-1,4,7,10,13,16-hexaoxacyclooctadecane-2,11-dicarboxamide} ligand (dithiolated **18C6** crown, abbreviated *R/S*-CE), 3,3-dimethyl-2-butylamine (Sigma-Aldrich, 97%).

2.2. Synthesis of Au₂₅(2-PET)₁₈ and ligand exchange reaction with *R/S*-CE ligand. Au₂₅(2-PET)₁₈ cluster was synthesized based on reported protocols.^{70,71} Briefly, 1g of HAuCl₄*3H₂O mixed with tetraoctylammonium bromide (abbreviated TOAB) was dissolved in THF and stirred for 15 min. Then 10 mL of 2-PET ligand was added until the solution gradually changed color from red to yellow and eventually turned colorless. At this point, 900 mg NaBH₄ dissolved in 50 mL ice-cold water was added at once and the reaction mixture was allowed to stir for 3 h. Furthermore, the reaction solution was filtered with paper to remove the insoluble Au(I)-SR complexes. The filtered solution was evaporated, and the crude sample was washed with Milli-Q water and MeOH several times to remove unreacted precursors. The purified sample was dried in a vacuum rotary evaporator at room temperature. Note that during this synthesis mainly negatively charged cluster was obtained as evidenced by UV-vis spectra and later oxidized by silica-gel column chromatography under aerobic conditions.

The synthesis of the dithiolated **18C6** crown ligand was done as reported in the reference.⁷² Note that for the ligand exchange reactions only the enantiomeric forms of the ligand named as *R*-CE and *S*-CE were used. The enantiomers of the ligand were separated on a CHIRALPAK® IG semipreparative HPLC column using CHCl₃ as a mobile phase. The flow rate was set 3.0 mL/min at 20 °C. 100 μ L (1 mg/mL) of sample dissolved in DCM was injected directly into the column. Ligand exchange reaction between neutral Au₂₅(2-PET)₁₈ and dithiolated 18C6 crown ligand was carried out under mild conditions (1:2 cluster/ligand molar ratios, room temperature, DCM solution, 16 h) as described in chapter 5.2.

2.3. Protonation of the chiral amines. The choice of guest amine molecule for host-guest interactions is somewhat arbitrary. Herein, chiral 3,3-dimethyl-2-butylamine was chosen. For protonation, 1 equivalent of HCl in Et₂O was added to the amine in DCM (0.1M) and stirred for 1

h at room temperature. Afterwards, the solvents were evaporated in rotavapor and the white powder was freeze dried and kept at 4 °C in a fridge. In the following the protonated *R/S* enantiomers of the amine were named as Ram and Sam.

2.4. Characterization methods. UV-vis spectra were recorded on the Varian Cary 50 spectrophotometer, using a quartz cuvette of 1 cm path length. Spectra were measured in DCM. MALDI-TOF mass analysis was performed on an AXIMA-CFR+ MALDI-TOF-MS (Shimadzu, Duisburg, Germany) mass spectrometer equipped with a nitrogen laser in positive mode. [3-(4-tert-butylphenyl)-2-methyl-2-propenylidene]malononitrile (DCTB) was used as a matrix. A volume of 6 µl of the analyte/matrix mixture was applied to the target and air-dried.

CD spectra were recorded on a JASCO J-815 CD-spectrometer using a quartz cuvette of 2 mm path length. The spectra were recorded in diluted solutions of DCM and the signal of the solvent was subtracted. For each spectrum, three scans at a scanning speed of 100 nm/min at a data pitch of 0.1 nm were averaged. The spectra were recorded at 20 °C; for temperature control, a JASCO PFD-350S Peltier element was used.

NMR spectra were recorded on Bruker Avance 400 MHz spectrometer. ¹H NMR chemical shifts are given in ppm relative to SiMe₄, with the solvent resonance used as an internal reference. NMR-titration reaction was performed in a screw-cup NMR tube in which enantiopure cluster was titrated with the chiral amine. Both samples were dissolved in DCM-*d*₂. Proton spectra were acquired every 10 min for 7 h 30 minutes.

2.5. Fitting programs. The binding isotherms were fitted using non-linear regression algorithms in several software packages such as GraphPad Prism7, OriginPro 2017 and CurveExpert professional 2.6.5. Therefore, several fitting models were used to compare the precision and accuracy of the fitting results (**Table S1**). Herein, all the figures presented below, are obtained from GraphPad Prism 7 software package.

3. Results and discussion

The same ligand exchange reaction conditions were applied as previously reported (chapter 5.2). Briefly, 1:2 cluster: ligand molar ratios were used for the exchange reaction. The dithiolated **18C6**

crown ligand has three stereoisomers (C_2 -*cis*, C_1 and C_2 -*trans* isomers) and only the last isomer results in dithiol exchange. Note that in this work only enantiopure samples were considered for the ligand exchange reaction. The exchanged product was easily separated in size exclusion chromatography column (SEC Bio-Beads™ S-X1 Support gel) into distinguishable fractions. Moreover, the first fraction of mainly 2-4 exchanged species has a reddish color, whereas the second one (1-2 exchange species) is red-greenish. The last fraction is pure Au₂₅. First two fractions were mixed and analyzed by UV-vis and MALDI. Based on the m/z pattern of the ionized species (**Table S2**), the average exchange number of the *R/S*-CE ligand per cluster (\bar{x}) was calculated and further used for titration experiment. Note, that the \bar{x} can be changed by simply modifying the molar ratio between the cluster and ligand during the synthesis. For clarity, the exchanged enantiopure samples (despite of \bar{x}) were called *R*-Au₂₅CE and *S*-Au₂₅CE. ¹H NMR spectra of free *R/S*-CE and the enantiopure cluster were recorded prior to titration experiments to check the purity of the samples and they were used as references for further comparison (**Fig. S1**). The reference ¹H NMR spectrum of protonated amine is presented in **Fig. S2**.

Preliminary UV-vis analyses show no visual optical changes on the spectra after adding the amine to the sample. Although, MALDI mass spectra does not directly indicate the presence of the bonded amine, the relative intensity of the peaks belonging to the exchanged species changed in the presence of the amine in the mixture. Moreover, the intensity and the distribution of the peaks in *R*-Au₂₅CE and *S*-Au₂₅CE become like the reference cluster spectrum after SEC purification. However, except for the relative intensity change, the \bar{x} does not change in the presence of the amine (**Fig. S3 and Fig. S4**).

Au₂₅ cluster protected with PET ligand is achiral, however after post-functionalization with enantiopure dithiolated **18C6** ligand induced chirality in the exchanged cluster is expected. CD measurements were performed to record the spectra for both enantiomers of the cluster as well as after adding chiral protonated amine. In **Fig. 1** it is shown the corresponding CD spectra of the free *R/S*-CE ligand and post-functionalized cluster. Indeed, the ligand exchange reaction induces chirality in the cluster, i.e. both enantiomers are perfect mirror images of each other. CD signals of the amine are in UV region and since the PET ligand itself has strong absorption in that region of the spectrum, it was impossible to observe the CD signals of the amine. Moreover, the chiral

fingerprints of the cluster around 400 nm remain unchanged upon amine addition. It needs to be emphasized, that the chiroptical feature at 400 nm originates from the Au₁₃ core.⁷³ Hence, the adsorption of the chiral ligand distorted the structure and induced chirality in the core. Thus, the overall chirality comes not only from the ligand but also from the core due to its distortion.

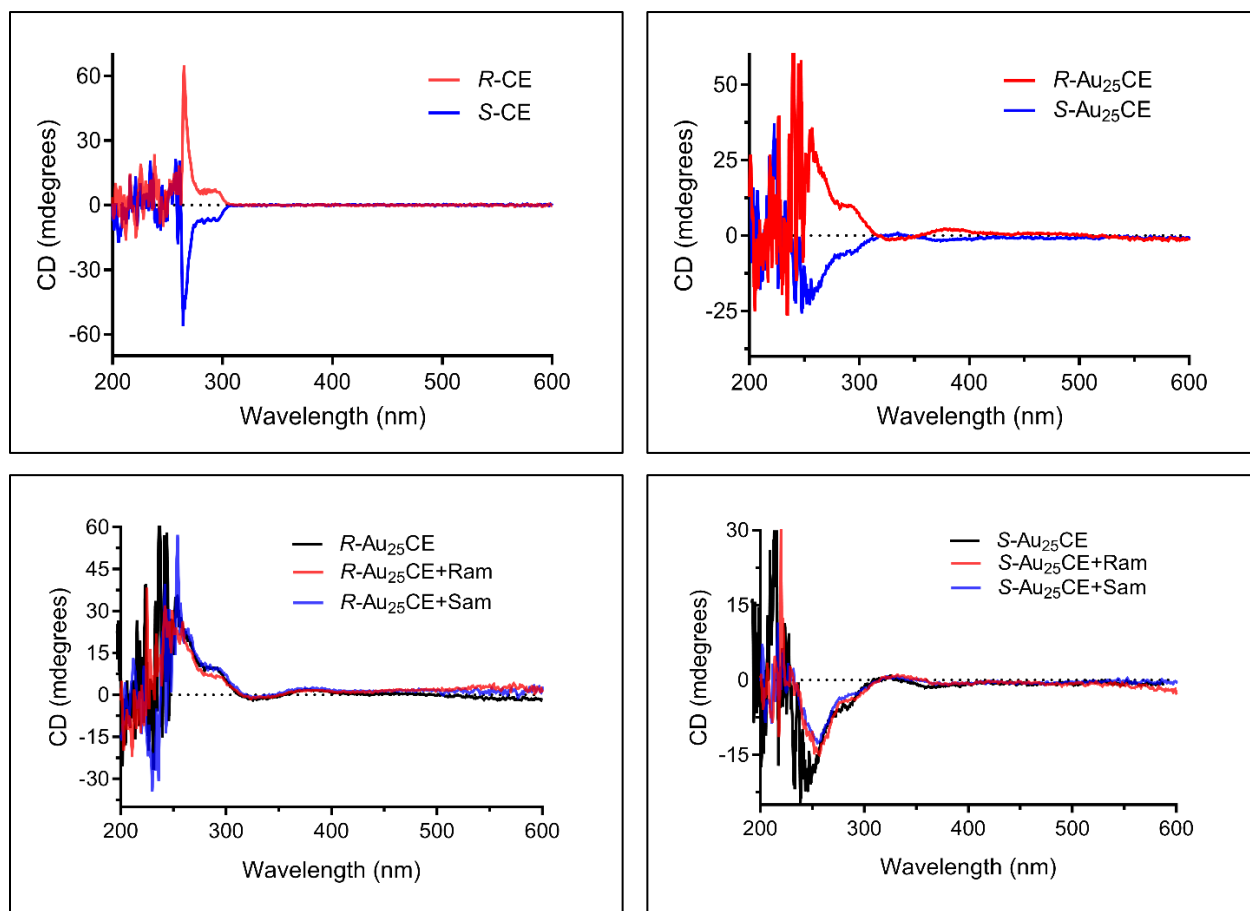


Fig. 1 CD spectra of the (a) *R/S*-CE, (b) *R/S*-Au₂₅CE, (c) *R*-Au₂₅CE and (d) *S*-Au₂₅CE after adding amine Ram/Sam. The spectra were recorded in DCM and the background was subtracted afterwards.

3. NMR titration

Several NMR titration experiments were performed to examine the binding of the protonated chiral amine to post-functionalized chiral Au₂₅. The titration experiments were carried out in DCM-*d*₂ at 298K for almost 8 h by adding a very small amount of guest (0.015 eq per mole of *R/S*-

Au₂₅CE) in each titration step. To ensure that the host concentration stays constant during the experiment (no dilution effect), an NMR tube and a vial with the same concentration of host solution were prepared. Furthermore, the host solution in NMR tube as a titrand was titrated with a guest containing in the vial (titrant).

R-Au₂₅CE and *S*-Au₂₅CE were titrated with both *R/S*-amine (*R/R*, *R/S*, *S/R* and *S/S*, where the first letter stands for the cluster and the second one for the amine accordingly) and the obtained chemical shifts in ¹H NMR were plotted as a function of the guest concentration in logarithmic scale (Log [Guest]). Note, that in the first set of experiments the average number of CE per cluster was 1.8 ($\bar{x}=1.8$, **Fig. 2**). The binding isotherms for each system shows obvious discrepancy from the classical one-site binding hyperbole. In fact, the curve shape indicates the competitive nature of the host-guest interaction. By comparing the binding isotherms for all systems, it is obvious to see that there is a difference in the binding abilities not only between different enantiomers of cluster, but also whether one enantiomer of the cluster binds to the *R* or *S* amine. Moreover, for the systems *R/S* and *S/R* the same binding behavior was expected. To our surprise, they are not identical and there are major differences in cooperativity index and especially in the binding affinity. This matter is not well understood for the moment. As we have shown previously, there are always cations trapped inside the cage. The observed K_d represents not the actual binding constant but more like the “replacement constant” with upcoming *Ram/Sam* during titration. However, the sigmoidal shape of all curves indicates an allosteric (cooperative binding) nature. Upon reaching 2 eq of guest, the sigmoidal binding isotherms reached a plateau, indicating that the equilibrium state is retained in solution. The binding isotherm for *R/R* looks more sigmoidal compared to *R/S*. Therefore, for the *R/R* the Hill’s coefficient ($n_H=1.517$) is expected to be higher than *R/S* ($n_H=1.313$). Even though the dissociation constant for *R/R* ($K_d=8.587 \cdot 10^{-5}$) is calculated to be smaller than that of *R/S* ($K_d=3.574 \cdot 10^{-5}$), both systems show micromolar affinity towards the ligand binding (**Table S3**).

Similar features were seen in the case of *S/R* and *S/S* systems. Herein, the *S/R* shows more cooperative behavior ($n_H=1.855$) and consequently smaller ligand affinity ($K_d=1.742 \cdot 10^{-4}$, millimolar affinity). In contrary, when the cluster is titrated with *S*-amine, smaller value for Hill’s

B. EXPERIMENTAL PART

coefficient was observed ($n_H=1.3$), resulting to a much stronger binding probability ($K_d=9.941 \cdot 10^{-6}$, micromolar affinity).

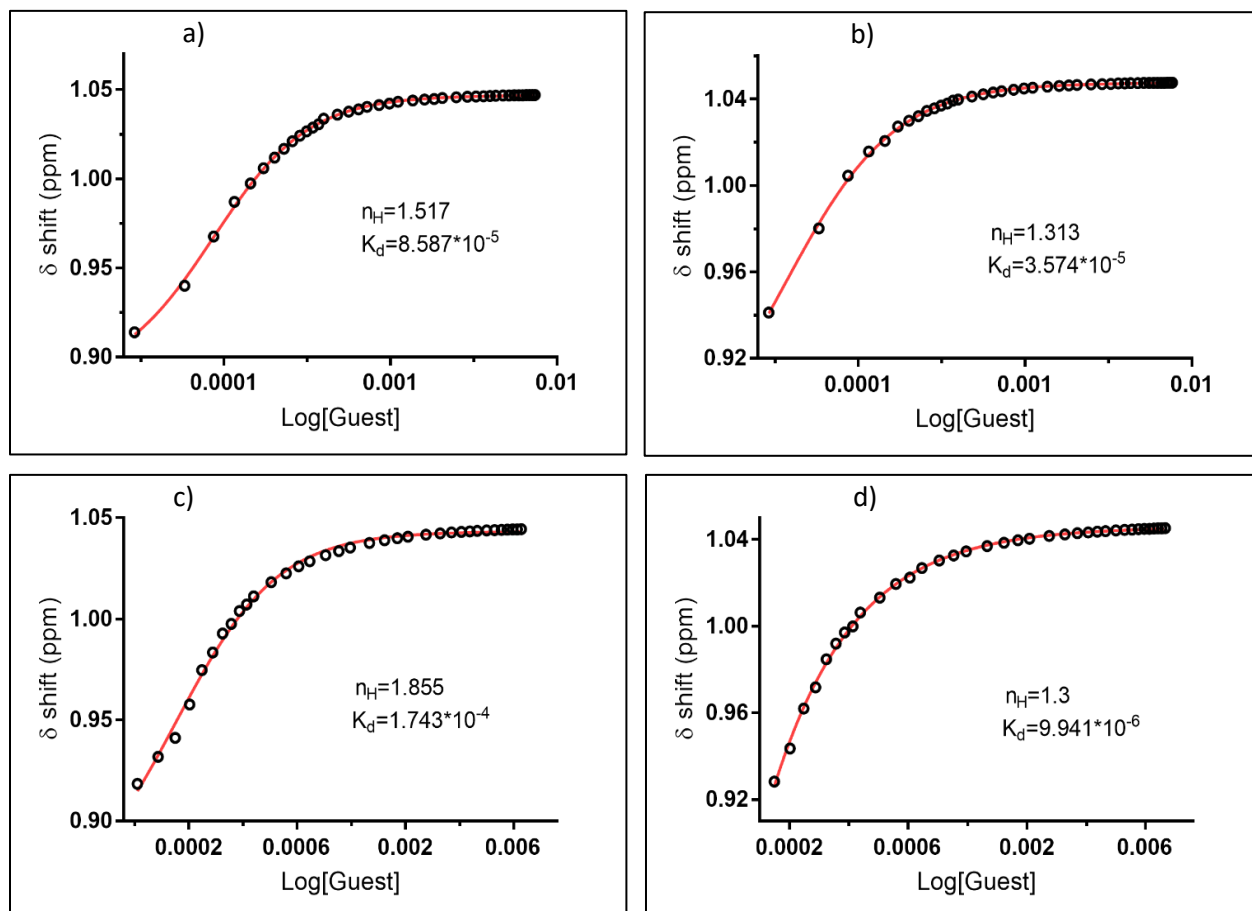


Fig. 2 Binding isotherms of the systems a) *R/R*, b) *R/S*, c) *S/R* and d) *S/S* with $\bar{x}=1.8$. 4 equivalents of the guest in DCM-*d*2 was prepared and added to titrand in small quantities (1-10 μ L). 1.9 mM host and 16 mM guest concentration were used for titration.

The binding differences among enantiomers of the cluster and the ligand itself can be explained by considering the conformational changes occurring upon ligand complexation. Perhaps, the *R/S*-CE being quite bulky, on the cluster surface adopts certain conformations which in one case has more accessibility for the guest depending of course on the absolute configuration of the binding amine. Moreover, the protecting PET-ligand shell as well could have an influence on the overall conformational changes while ligand traps inside the **18C6** macrocycle.

Looking more closely to the NMR shifts one could expect that during titration, the free ligand signal will gradually disappear, and the bound signal will appear. This is the case when the exchange rate is significantly slower than the difference in chemical shifts of free and bound guest. In contrast, when the exchange is fast on the chemical shift timescale, then the signals are an average of the bound and unbound state and they will move gradually away from their initial position. The higher the binding affinity of a guest, the larger is the proportion of bound molecules in solution and thus, the downfield shift of proton signal is more pronounced. This behavior is in line with our experimental results.

To study the influence of the CE number on the cluster surface on cooperativity, other experiments were also carried out, particularly $\bar{x}=2.2$, $\bar{x}=2.6$, $\bar{x}=3$ and $\bar{x}=3.4$. First, the same reaction conditions were applied for the synthesis of the *R/S*-Au₂₅CE using higher amounts of the free CE upon ligand exchange reaction. Second, after SEC separation the first fraction was collected and freeze dried while the second one (mostly, 1-2 exchange) was used as a starting material for the second exchange step. Afterwards, the exchanged product from this synthesis step was mixed with the previous one and further used for titration. MALDI analyses show an average of $\bar{x}=2.2$ for both *R*-Au₂₅CE and *S*-Au₂₅CE. The titration procedure was performed using in total 4 eq of *R/S* amine (**Fig. 3**). As expected, the increase of CE number on the cluster surface increased the number of possible binding sites and thus, enhanced the cooperativity. In general, the higher the cooperative index the smaller the K_d is expected. Note, that the binding isotherms for all the systems except for *S/R*, have sigmoidal curvatures with higher Hill's slopes. In *R/R* and *R/S* systems the differences in binding abilities are negligible whereas in the case of *S/R* and *S/S* the variation in dissociation constant as well as the cooperativity index is higher. The noticeable differences observed in *S/R* system can be again explained by the conformational changes. It is not excluded that at $\bar{x}=2.2$ *R/R*, *R/S* and *S/S* show no specificity towards *R/S*-amine while in *S/R* the *R*-amine binds much stronger which further makes the adjacent binding site less competent. However, the above systems show millimolar binding affinity.

The ligand exchange reaction with higher average exchanged numbers ($\bar{x}>2.2$) were also performed to investigate the effect of the ligand on the binding affinities. To our surprise, the

B. EXPERIMENTAL PART

further increase of the CE ($\bar{x}=2.6$, $\bar{x}=3$ and $\bar{x}=3.4$) (Fig. S5-S7) affects the allosteric competition during host-guest interaction.

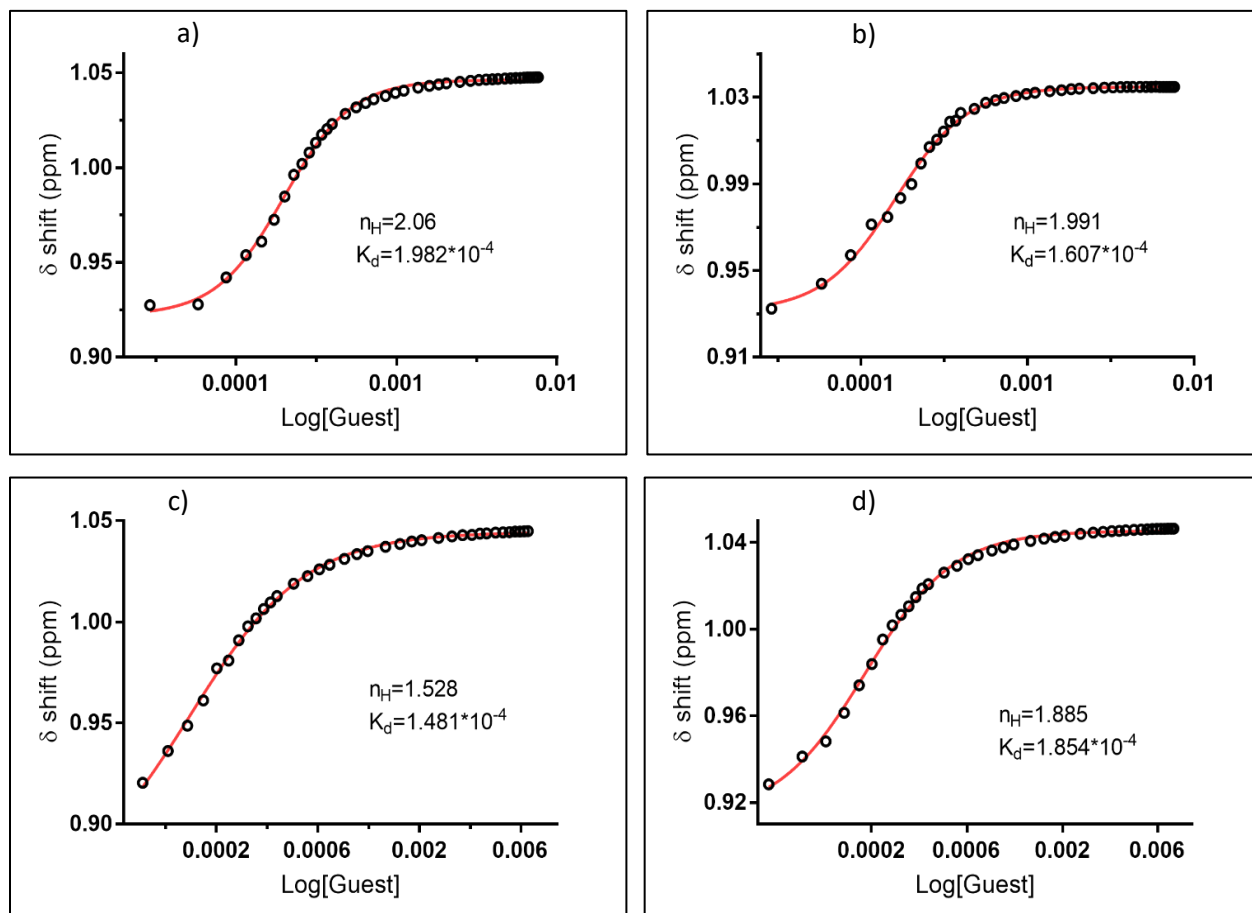


Fig. 3 Binding isotherms of the systems a) R/R , b) R/S , c) S/R and d) S/S with $\bar{x}=2.2$. 4 equivalents of the guest in DCM- d_2 was prepared and added to titrand in small quantities (1-10 μL). 1.9 mM host and 16 mM guest concentration were used for titration.

Despite of the interaction nature between different enantiomers, systems with $\bar{x}=2.6$ and $\bar{x}=3$ exchanged species show smaller Hill's coefficients and hence, very strong binding affinities (micromolar affinity). Moreover, at $\bar{x}=3.4$ the system behaves drastically different and, in some cases, shows no cooperativity. The binding curves resemble classical non-cooperative hyperboles. Perhaps, the more exchanged sample becomes more bulky and rigid, the conformational changes restrict the binding of the other guest molecules. Consequently, if the amine binds, the changes upon complexation make the overall structure less accessible for the

next amine to bind. Thus, by changing the number of exchanged *R/S*-CE ligand on the cluster surface, the allosteric properties can be switched from cooperativity (micromolar affinity) to complete non-cooperativity (millimolar affinity).

It is of interest to perform ^1H NMR titration experiments with enantiopure *R/S*-CE ligand to compare the binding constants and analyze the effect of the cluster on the interaction flexibility. Initially, it was assumed that free CE-amine interactions would be similar to 1:1 complex formation mechanism with no cooperative properties. However, to our surprise, the fitting curves look sigmoidal with $n_{\text{H}} > 1$ cooperativity (**Fig. S8**). This means that there are at least two competitive binding sites. From a detailed structural analysis of CE, two possible binding mechanisms resulting in “sandwich structure” can be determined: a), i.e. two amine molecules bind from up and down sides of the **18C6** cage, i.e. 1:2 sandwiches⁷⁴ and b) one amine molecule binds directly to two host molecules, i.e. 2:1 structure.²⁰ To facilitate better understanding of the origin and possible binding mechanism additional experiments with commercial **18C6** ligand and Job’s analysis⁷⁵ were carried out too (**Fig. S9, Table S4**). Job’s plots confirm that 2:1 binding is retained in solution upon complex formation. This interaction could be facilitated by the competition of two crown ether cages that are brought close enough proximity to hold one guest molecule. Interestingly, the titration of the host with Ram resulted in positive cooperativity ($n_{\text{H}}=1.6$) whereas Sam showed negative allosteric effect ($n_{\text{H}}=0.86$). Since the host itself is not chiral, then chiral discrimination must be ruled out and in this case the origin of such phenomenon is not yet understood. Moreover, improving the structure by functionalization (in case of *R/S*-CE ligand), the differences arise not only from binding different enantiomers of the guest, but also the additional conformational changes caused by the crown moiety’s armchairs. On the other hand, the Job’s plots become very irregular and complicated (not shown). However, for higher-order complexations, including 2:1 stoichiometry, the analyses of the curves need to be done with more sophisticated mathematical models and with great caution. Since, the titration of the guest with ligand alone is quite complicated in nature, then the host-guest interactions with clusters become even more difficult to interpret in terms of stoichiometry and cooperativity. Moreover, considering the fact that *R/S*-Au₂₅CE is not homogeneous and consists

of several exchanged ligands on a cluster surface, the overall situation becomes extremely complicated.

We went on to investigate the possible enantio-discrimination using racemic guest solutions. The host solution of *R/S*-Au₂₅CE ($\bar{x}=3.4$) was titrated with *rac*-amine and the binding constants were summarized in **Table S5**. The chemical shifts of the three methyl groups for both enantiomers and a racemic form at earlier stages of interaction (after adding 0.06 eq of guest) were plotted together to make the comparison more visual (**Fig. 4**).

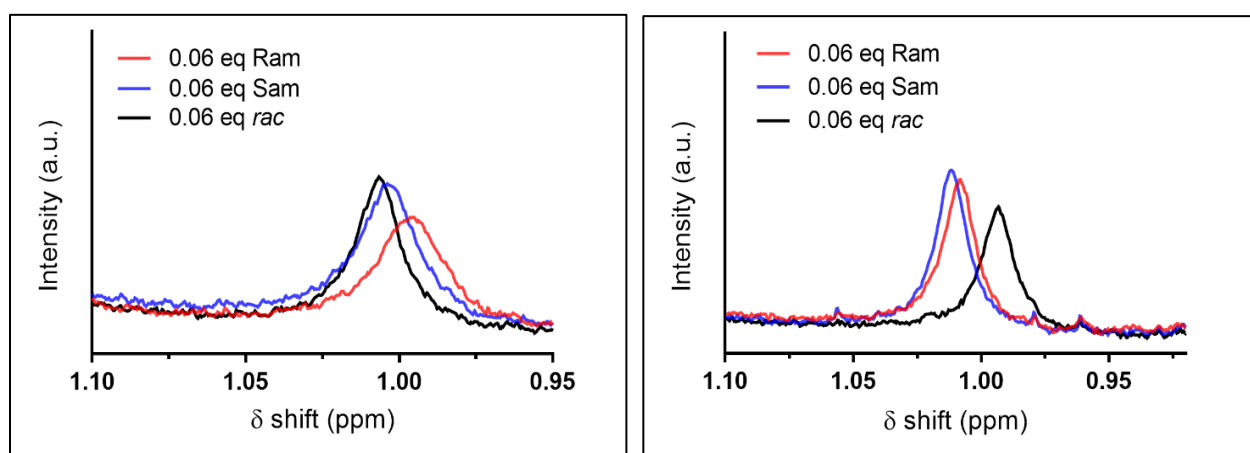


Fig. 4 a) *R*-Au₂₅CE+0.06 eq of protonated enantiopure/*rac*-amine and b) *S*-Au₂₅CE+0.06 eq of protonated enantiopure/*rac*-amine. $\bar{x}=3.4$ was kept constant in all studied cases.

$\delta=0.99$ ppm was observed in the case of *R/R*. The same equivalents of guest made the proton signal more deshielded in the *R/S* system ($\delta=1$ ppm). The racemic mixture of the guest solution not only does not separate the enantiomers due to differences in the binding abilities, but also gave the most downfield shifts. By definition, the racemic form contains equally both enantiomers and the peak supposed to be positioned in between two enantiomers. The mismatch between the obtained results has already been seen in biological systems.⁷⁶ It was explained by the change in solubility when both enantiomers are present in the racemic form. The slight variation of the solubility affects also its binding affinity to the host molecule. Consequently, this has a significant effect on the diagnostic resonances assignable to the three methyl groups. In case of *S*-Au₂₅CE, the proton signal is more shielded for the racemic mixture ($\delta=0.99$ ppm) and more downfielded

while titrated with Sam ($\delta=1.01$ ppm). And again, the only plausible explanation will be the variations in solubility. The latter was not easily observable by bare eye.

4. Conclusions

In summary, we have shown the effect of the exchanged ligand on Au₂₅ cluster's chirality and binding affinity. The ligand exchange reaction with enantiopure *R/S*-CE induced chirality in the cluster giving rise to strong optical fingerprints in CD. ¹H NMR titration experiments have shown the binding of the chiral amine into the crown moieties based on the chemical shifts of the three methyl groups of the guest. The fitting of the data by using non-linear regression algorithm, derived the characteristic binding constants. It has been shown that the increase of the crown ligand on the surface of the cluster decreases the allosteric effect in terms of Hill's coefficient but that makes the guest molecule bind much stronger.

References

- (1) Ariga, K.; Ito, H.; Hill, J. P.; Tsukube, H. Molecular Recognition: From Solution Science to Nano/Materials Technology. *Chem. Soc. Rev.* **2012**, *41* (17), 5800.
- (2) Tomlinson, C. G.; Atack, J. M.; Chapados, B.; Tainer, J. A.; Grasby, J. A. Substrate Recognition and Catalysis by Flap Endonucleases and Related Enzymes. *Biochem. Soc. Trans.* **2010**, *38* (2), 433–437.
- (3) SONKARIA, S.; BOUCHER, G.; FLÓREZ-ÁLVAREZ, J.; SAID, B.; HUSSAIN, S.; OSTLER, E. L.; GUL, S.; THOMAS, E. W.; RESMINI, M.; GALLACHER, G.; et al. Evidence for 'Lock and Key' Character in an Anti-Phosphonate Hydrolytic Antibody Catalytic Site Augmented by Non-Reaction Centre Recognition: Variation in Substrate Selectivity between an Anti-Phosphonate Antibody, an Anti-Phosphate Antibody and Two Hydro. *Biochem. J.* **2004**, *381* (1), 125–130.

- (4) Carnegie, G. K.; Smith, F. D.; McConnachie, G.; Langeberg, L. K.; Scott, J. D. AKAP-Lbc Nucleates a Protein Kinase D Activation Scaffold. *Mol. Cell* **2004**, *15* (6), 889–899.
- (5) Moscat, J.; Diaz-Meco, M. T.; Albert, A.; Campuzano, S. Cell Signaling and Function Organized by PB1 Domain Interactions. *Mol. Cell* **2006**, *23* (5), 631–640.
- (6) Miki, Y.; Oguri, E.; Hirano, K.; Beppu, M. Macrophage Recognition of Cells with Elevated Calcium Is Mediated by Carbohydrate Chains of CD43. *Cell Struct. Funct.* **2013**, *38* (1), 43–54.
- (7) Wang, S.; Wen, Y.; Wang, Y.; Ma, Y.; Liu, Z. Pattern Recognition of Cells via Multiplexed Imaging with Monosaccharide-Imprinted Quantum Dots. *Anal. Chem.* **2017**, *89* (10), 5646–5652.
- (8) Xu, L.; Wang, W.; Wu, J.; Shin, J. H.; Wang, P.; Unarta, I. C.; Chong, J.; Wang, Y.; Wang, D. Mechanism of DNA Alkylation-Induced Transcriptional Stalling, Lesion Bypass, and Mutagenesis. *Proc. Natl. Acad. Sci.* **2017**, *114* (34), E7082–E7091.
- (9) Perales, C. Enhancement of DNA, cDNA Synthesis and Fidelity at High Temperatures by a Dimeric Single-Stranded DNA-Binding Protein. *Nucleic Acids Res.* **2003**, *31* (22), 6473–6480.
- (10) Kellinger, M. W.; Park, G. Y.; Chong, J.; Lippard, S. J.; Wang, D. Effect of a Monofunctional Phenanthriplatin-DNA Adduct on RNA Polymerase II Transcriptional Fidelity and Translesion Synthesis. *J. Am. Chem. Soc.* **2013**, *135* (35), 13054–13061.
- (11) Hassan, A. E. A.; Sheng, J.; Zhang, W.; Huang, Z. High Fidelity of Base Pairing by 2-Selenothymidine in DNA. *J. Am. Chem. Soc.* **2010**, *132* (7), 2120–2121.
- (12) Su, M.-T.; Liu, I.-H.; Wu, C.-W.; Chang, S.-M.; Tsai, C.-H.; Yang, P.-W.; Chuang, Y.-C.; Lee, C.-P.; Chen, M.-R. Uracil DNA Glycosylase BKRF3 Contributes to Epstein-Barr Virus DNA Replication through Physical Interactions with Proteins in Viral DNA Replication Complex. *J. Virol.* **2014**, *88* (16), 8883–8899.
- (13) Pedersen, C. J. Cyclic Polyethers and Their Complexes with Metal Salts. *J. Am. Chem. Soc.* **1967**, *89* (26), 7017–7036.

- (14) Inokuchi, Y.; Ebata, T.; Ikeda, T.; Haino, T.; Kimura, T.; Guo, H.; Furutani, Y. New Insights into Metal Ion–Crown Ether Complexes Revealed by SEIRA Spectroscopy. *New J. Chem.* **2015**, *39* (11), 8673–8680.
- (15) Inokuchi, Y.; Mizuuchi, T.; Ebata, T.; Ikeda, T.; Haino, T.; Kimura, T.; Guo, H.; Furutani, Y. Formation of Host–Guest Complexes on Gold Surface Investigated by Surface-Enhanced IR Absorption Spectroscopy. *Chem. Phys. Lett.* **2014**, *592*, 90–95.
- (16) Al-Kahtani, A. A.; Al-Jallal, N. A.; El-Azhary, A. A. Conformational and Vibrational Analysis of 18-Crown-6–Alkali Metal Cation Complexes. *Spectrochim. Acta Part A Mol. Biomol. Spectrosc.* **2014**, *132* (9661), 70–83.
- (17) Cielen, E.; Tahri, A.; Ver Heyen, K.; Hoornaert, G. J.; De Schryver, F. C.; Boens, N. Synthesis and Spectroscopic Characterisation of Fluorescent Indicators for Na⁺ and K⁺. *J. Chem. Soc. Perkin Trans. 2* **1998**, *2* (7), 1573–1580.
- (18) Danil de Namor, A. F.; Ng, J. C. Y.; Llosa Tanco, M. A.; Salomon, M. Thermodynamics of Lithium–Crown Ether (12-Crown-4 and 1-Benzyl-1-Aza-12-Crown-4) Interactions in Acetonitrile and Propylene Carbonate. The Anion Effect on the Coordination Process. *J. Phys. Chem.* **1996**, *100* (34), 14485–14491.
- (19) Oukhatar, F.; Meudal, H.; Landon, C.; Logothetis, N. K.; Platas-Iglesias, C.; Angelovski, G.; Tóth, É. Macrocyclic Gd³⁺ Complexes with Pendant Crown Ethers Designed for Binding Zwitterionic Neurotransmitters. *Chem. - A Eur. J.* **2015**, *21* (31), 11226–11237.
- (20) Yu, H.-R.; Hu, J.-Q.; Lu, X.-H.; Ju, X.-J.; Liu, Z.; Xie, R.; Wang, W.; Chu, L.-Y. Insights into the Effects of 2:1 “Sandwich-Type” Crown-Ether/Metal-Ion Complexes in Responsive Host–Guest Systems. *J. Phys. Chem. B* **2015**, *119* (4), 1696–1705.
- (21) Pauric, A. D.; Jin, S.; Fuller, T. J.; Balogh, M. P.; Halalay, I. C.; Goward, G. R. NMR Determination of the Relative Binding Affinity of Crown Ethers for Manganese Cations in Aprotic Nonaqueous Lithium Electrolyte Solutions. *J. Phys. Chem. C* **2016**, *120* (7), 3677–3683.

- (22) Junker, A. K. R.; Tropiano, M.; Faulkner, S.; Sørensen, T. J. Kinetically Inert Lanthanide Complexes as Reporter Groups for Binding of Potassium by 18-Crown-6. *Inorg. Chem.* **2016**, *55* (23), 12299–12308.
- (23) Morishima, F.; Kusaka, R.; Inokuchi, Y.; Haino, T.; Ebata, T. Cage Effects on Conformational Preference and Photophysics in the Host–Guest Complex of Benzenediols with 18-Crown-6. *Phys. Chem. Chem. Phys.* **2016**, *18* (11), 8027–8038.
- (24) Hu, W.-B.; Hu, W.-J.; Liu, Y. A.; Li, J.-S.; Jiang, B.; Wen, K. Negative Cooperativity in the Binding of Imidazolium and Viologen Ions to a Pillar[5]Arene-Crown Ether Fused Host. *Org. Lett.* **2015**, *17* (12), 2940–2943.
- (25) Li, J.; Yim, D.; Jang, W.-D.; Yoon, J. Recent Progress in the Design and Applications of Fluorescence Probes Containing Crown Ethers. *Chem. Soc. Rev.* **2017**, *46* (9), 2437–2458.
- (26) Miller, A. J. M. Controlling Ligand Binding for Tunable and Switchable Catalysis: Cation-Modulated Hemilability in Pincer-Crown Ether Ligands. *Dalt. Trans.* **2017**, *46* (36), 11987–12000.
- (27) Kolesnichenko, I. V.; Anslyn, E. V. Practical Applications of Supramolecular Chemistry. *Chem. Soc. Rev.* **2017**, *46* (9), 2385–2390.
- (28) Stein, B. W.; Cary, S. K.; Berg, J. M.; Birnbaum, E. R.; Kozimor, S. A.; Mocko, V.; Scott, B. L. A Series of F-Element Chelators; Diaza Crown Ethers Functionalized with Catecholate Binding Substituents. *J. Organomet. Chem.* **2018**, *857*, 170–179.
- (29) Späth, A.; Koch, C.; König, B. Luminescent Hybrids Combining a Metal Complex and a Crown Ether - Receptors for Peptidic Ammonium Phosphates. *Eur. J. Inorg. Chem.* **2010**, *2010* (19), 2926–2935.
- (30) Gruber, B.; Stadlbauer, S.; Späth, A.; Weiss, S.; Kalinina, M.; König, B. Modular Chemosensors from Self-Assembled Vesicle Membranes with Amphiphilic Binding Sites and Reporter Dyes. *Angew. Chemie Int. Ed.* **2010**, *49* (39), 7125–7128.

- (31) Späth, A.; König, B. Binding of a Hemoregulatory Tetrapeptide by a Bis-Guanidinium Crown Ether. *Tetrahedron* **2010**, *66* (32), 6019–6025.
- (32) Späth, A.; König, B. Ditopic Crown Ether–Guanidinium Ion Receptors for the Molecular Recognition of Amino Acids and Small Peptides. *Tetrahedron* **2010**, *66* (10), 1859–1873.
- (33) Späth, A.; Rummel, E. M.; König, B. Luminescent Lariat Aza-Crown Ether. *Molbank* **2010**, *2010* (1), 1–3.
- (34) Hu, S.-X.; Liu, J.-J.; Gibson, J. K.; Li, J. Periodic Trends in Actinyl Thio-Crown Ether Complexes. *Inorg. Chem.* **2018**, *57* (5), 2899–2907.
- (35) Kralj, M.; Tušek-Božić, L.; Frkanec, L. Biomedical Potentials of Crown Ethers: Prospective Antitumor Agents. *ChemMedChem* **2008**, *3* (10), 1478–1492.
- (36) Kuriyan; Konforti; Wemmer. Molecular Recognition: The Thermodynamics of Binding. *Mol. Life* **2009**, 1–58.
- (37) Kadam, S. A.; Haav, K.; Toom, L.; Haljasorg, T.; Leito, I. NMR Method for Simultaneous Host–Guest Binding Constant Measurement. *J. Org. Chem.* **2014**, *79* (6), 2501–2513.
- (38) Lowe, A. J.; Pfeffer, F. M.; Thordarson, P. Determining Binding Constants from ¹H NMR Titration Data Using Global and Local Methods: A Case Study Using [n]Polynorbornane-Based Anion Hosts. *Supramol. Chem.* **2012**, *24* (8), 585–594.
- (39) Fielding, L.; Rutherford, S.; Fletcher, D. Determination of Protein-Ligand Binding Affinity by NMR: Observations from Serum Albumin Model Systems. *Magn. Reson. Chem.* **2005**, *43* (6), 463–470.
- (40) Williamson, M. P. Using Chemical Shift Perturbation to Characterise Ligand Binding. *Prog. Nucl. Magn. Reson. Spectrosc.* **2013**, *73*, 1–16.
- (41) Loiselle, D. S. The Effect of Myoglobin-Facilitated Oxygen Transport on the Basal Metabolism of Papillary Muscle. *Biophys. J.* **1987**, *51* (6), 905–913.

- (42) Sick, H.; Gersonde, K. Continuous Gas-Depletion Technique for Measuring O₂-Dissociation Curves of High-Affinity Hemoglobins. *Anal. Biochem.* **1985**, *146* (1), 277–280.
- (43) Hunter, C. A.; Anderson, H. L. What Is Cooperativity? *Angew. Chemie Int. Ed.* **2009**, *48* (41), 7488–7499.
- (44) Stefan, M. I.; Le Novère, N. Cooperative Binding. *PLoS Comput. Biol.* **2013**, *9* (6), e1003106.
- (45) Hill A.V. The Possible Effects of the Aggregation of the Molecules of Haemoglobin on Its dissociation Curves. *The Journal of Physiology.* **1910**, pp iv–vii.
- (46) Ermakova, E.; Miller, M. C.; Nesmelova, I. V.; López-Merino, L.; Berbís, M. A.; Nesmelov, Y.; Tkachev, Y. V.; Lagartera, L.; Daragan, V. A.; André, S.; et al. Lactose Binding to Human Galectin-7 (P53-Induced Gene 1) Induces Long-Range Effects through the Protein Resulting in Increased Dimer Stability and Evidence for Positive Cooperativity. *Glycobiology* **2013**, *23* (5), 508–523.
- (47) Acosta, H.; Cáceres, A.; González-Marcano, E.; Quiñones, W.; Avilán, L.; Dubourdiou, M.; Concepción, J. L. Hysteresis and Positive Cooperativity as Possible Regulatory Mechanisms of *Trypanosoma Cruzi* Hexokinase Activity. *Mol. Biochem. Parasitol.* **2014**, *198* (2), 82–91.
- (48) Bury, D.; Dahmane, I.; Derouaux, A.; Dumbre, S.; Herdewijn, P.; Matagne, A.; Breukink, E.; Mueller-Seitz, E.; Petz, M.; Terrak, M. Positive Cooperativity between Acceptor and Donor Sites of the Peptidoglycan Glycosyltransferase. *Biochem. Pharmacol.* **2015**, *93* (2), 141–150.
- (49) London Singh, R. K. Applicability of Positive Cooperativity Model of Enzyme Catalysis on Surfactant-Mediated Reaction of Pararosaniline Hydrochloride Carbocation with Hydroxide Ion. *J. Dispers. Sci. Technol.* **2016**, *37* (2), 239–244.
- (50) Wychowski, A.; Bompard, C.; Grimaud, F.; Potocki-Véronèse, G.; D’Hulst, C.; Wattebled, F.; Roussel, X. Biochemical Characterization of *Arabidopsis Thaliana* Starch Branching Enzyme 2.2 Reveals an Enzymatic Positive Cooperativity. *Biochimie* **2017**, *140*, 146–158.

- (51) Rovira, X.; Malhaire, F.; Scholler, P.; Rodrigo, J.; Gonzalez-Bulnes, P.; Llebaria, A.; Pin, J.-P.; Giraldo, J.; Goudet, C. Overlapping Binding Sites Drive Allosteric Agonism and Positive Cooperativity in Type 4 Metabotropic Glutamate Receptors. *FASEB J.* **2015**, *29* (1), 116–130.
- (52) Ma, Y.-L.; Ke, H.; Valkonen, A.; Rissanen, K.; Jiang, W. Achieving Strong Positive Cooperativity through Activating Weak Non-Covalent Interactions. *Angew. Chemie Int. Ed.* **2018**, *57* (3), 709–713.
- (53) Patra, D.; Mishra, P.; Vijayan, M.; Surolia, A. Negative Cooperativity and High Affinity in Chitooligosaccharide Binding by a Mycobacterium Smegmatis Protein Containing LysM and Lectin Domains. *Biochemistry* **2016**, *55* (1), 49–61.
- (54) Ha, S. H.; Ferrell, J. E. Thresholds and Ultrasensitivity from Negative Cooperativity. *Science* **2016**, *352* (6288), 990–993.
- (55) Joseph, E.; Le, C. Q.; Nguyen, T.; Oyugi, M.; Hossain, M. S.; Foss, F. W.; Johnson-Winters, K. Evidence of Negative Cooperativity and Half-Site Reactivity within an F420-Dependent Enzyme: Kinetic Analysis of F420 H₂:NADP + Oxidoreductase. *Biochemistry* **2016**, *55* (7), 1082–1090.
- (56) Bocedi, A.; Fabrini, R.; Lo Bello, M.; Caccuri, A. M.; Federici, G.; Mannervik, B.; Cornish-Bowden, A.; Ricci, G. Evolution of Negative Cooperativity in Glutathione Transferase Enabled Preservation of Enzyme Function. *J. Biol. Chem.* **2016**, *291* (52), 26739–26749.
- (57) Rossi, D.; Barbosa, N. M.; Galvão, F. C.; Boldrin, P. E. G.; Hershey, J. W. B.; Zanelli, C. F.; Fraser, C. S.; Valentini, S. R. Evidence for a Negative Cooperativity between EIF5A and EEF2 on Binding to the Ribosome. *PLoS One* **2016**, *11* (4), e0154205.
- (58) Marcella, A. M.; Culbertson, S. J.; Shogren-Knaak, M. A.; Barb, A. W. Structure, High Affinity, and Negative Cooperativity of the Escherichia Coli Holo-(Acyl Carrier Protein):Holo-(Acyl Carrier Protein) Synthase Complex. *J. Mol. Biol.* **2017**, *429* (23), 3763–3775.
- (59) Filimonov, I. S.; Berzova, A. P.; Barkhatov, V. I.; Krivoshey, A. V.; Trushkin, N. A.; Vrzheschch, P. V. Negative Cooperativity in the Interaction of Prostaglandin H Synthase-1 with the

Competitive Inhibitor Naproxen Can Be Described as the Interaction of a Non-Competitive Inhibitor with Heterogeneous Enzyme Preparation. *Biochem.* **2018**, *83* (2), 119–128.

(60) Imahori, H.; Fujimoto, A.; Kang, S.; Hotta, H.; Yoshida, K.; Umeyama, T.; Matano, Y.; Isoda, S.; Isosomppi, M.; Tkachenko, N. V.; et al. Host–Guest Interactions in the Supramolecular Incorporation of Fullerenes into Tailored Holes on Porphyrin-Modified Gold Nanoparticles in Molecular Photovoltaics. *Chem. - A Eur. J.* **2005**, *11* (24), 7265–7275.

(61) Zeng, Q.; Marthi, R.; McNally, A.; Dickinson, C.; Keyes, T. E.; Forster, R. J. Host–Guest Directed Assembly of Gold Nanoparticle Arrays. *Langmuir* **2010**, *26* (2), 1325–1333.

(62) Yesilbag Tonga, G.; Mizuhara, T.; Saha, K.; Jiang, Z.; Hou, S.; Das, R.; Rotello, V. M. Binding Studies of Cucurbit[7]Uril with Gold Nanoparticles Bearing Different Surface Functionalities. *Tetrahedron Lett.* **2015**, *56* (23), 3653–3657.

(63) Chen, W.-H.; Lei, Q.; Luo, G.-F.; Jia, H.-Z.; Hong, S.; Liu, Y.-X.; Cheng, Y.-J.; Zhang, X.-Z. Rational Design of Multifunctional Gold Nanoparticles via Host–Guest Interaction for Cancer-Targeted Therapy. *ACS Appl. Mater. Interfaces* **2015**, *7* (31), 17171–17180.

(64) Wang, Y.; Zeiri, O.; Raula, M.; Le Ouay, B.; Stellacci, F.; Weinstock, I. A. Host–Guest Chemistry with Water-Soluble Gold Nanoparticle Supraspheres. *Nat. Nanotechnol.* **2017**, *12* (2), 170–176.

(65) Du, J.; Zhang, P.; Zhao, X.; Wang, Y. An Easy Gene Assembling Strategy for Light-Promoted Transfection by Combining Host–Guest Interaction of Cucurbit[7]Uril and Gold Nanoparticles. *Sci. Rep.* **2017**, *7* (1), 6064.

(66) Mosquera, J.; Henriksen-Lacey, M.; García, I.; Martínez-Calvo, M.; Rodríguez, J.; Mascareñas, J. L.; Liz-Marzán, L. M. Cellular Uptake of Gold Nanoparticles Triggered by Host–Guest Interactions. *J. Am. Chem. Soc.* **2018**, *140* (13), 4469–4472.

(67) Jin, R.; Zeng, C.; Zhou, M.; Chen, Y. Atomically Precise Colloidal Metal Nanoclusters and Nanoparticles: Fundamentals and Opportunities. *Chem. Rev.* **2016**, *116* (18), 10346–10413.

- (68) Chakraborty, I.; Pradeep, T. Atomically Precise Clusters of Noble Metals: Emerging Link between Atoms and Nanoparticles. *Chem. Rev.* **2017**, *117* (12), 8208–8271.
- (69) Mathew, A.; Pradeep, T. Noble Metal Clusters: Applications in Energy, Environment, and Biology. *Part. Part. Syst. Charact.* **2014**, *31* (10), 1017–1053.
- (70) Dainese, T.; Antonello, S.; Gascón, J. A.; Pan, F.; Perera, N. V.; Ruzzi, M.; Venzo, A.; Zoleo, A.; Rissanen, K.; Maran, F. Au₂₅(SEt)₁₈, a Nearly Naked Thiolate-Protected Au₂₅ Cluster: Structural Analysis by Single Crystal X-Ray Crystallography and Electron Nuclear Double Resonance. *ACS Nano* **2014**, *8* (4), 3904–3912.
- (71) Lu, Y.; Jiang, Y.; Gao, X.; Chen, W. Charge State-Dependent Catalytic Activity of [Au₂₅(SC₁₂H₂₅)₁₈] Nanoclusters for the Two-Electron Reduction of Dioxygen to Hydrogen Peroxide. *Chem. Commun.* **2014**, *50* (62), 8464–8467.
- (72) E. Brun, K.-F. Zhang, L. Guénée and J. Lacour, *Org. Biomol. Chem.*, 2019, DOI: 10.1039/c1039ob02375e. (Accepted)
- (73) Noguez, C.; Sánchez-Castillo, A.; Hidalgo, F. Role of Morphology in the Enhanced Optical Activity of Ligand-Protected Metal Nanoparticles. *J. Phys. Chem. Lett.* 2011, *2* (9), 1038–1044.
- (74) Lowe, A. J.; Pfeffer, F. M. Binding of the Terephthalate Dianion by Di- Tri- and Tetrathiourea Functionalised Fused [3] and [5]Polynorbornane Based Hosts. *Org. Biomol. Chem.* **2009**, *7* (20), 4233.
- (75) Renny, J. S.; Tomasevich, L. L.; Tallmadge, E. H.; Collum, D. B. Method of Continuous Variations: Applications of Job Plots to the Study of Molecular Associations in Organometallic Chemistry. *Angew. Chemie Int. Ed.* **2013**, *52* (46), 11998–12013.
- (76) Kel, O.; Fürstenberg, A.; Mehanna, N.; Nicolas, C.; Laleu, B.; Hammarson, M.; Albinsson, B.; Lacour, J.; Vauthey, E. Chiral Selectivity in the Binding of [4]Helicene Derivatives to Double-Stranded DNA. *Chem. - A Eur. J.* **2013**, *19* (22), 7173–7180.

Supporting information

Table S1 The comparison between different fitting programs.

GraphPad Prism 7	OriginPro 2017	CurveExpert Professional 2.6.5
Fitting model		
[Agonist] vs response (variable slope, four parameters)	Hill1	Dose-Response -Hill
$y = \text{Bottom} + \frac{(\text{Top} - \text{Bottom})x^{\text{Hillslope}}}{EC_{50}^{\text{Hillslope}} + x^{\text{Hillslope}}}$ EC ₅₀ - dissociation const	$y = \text{Start} + \frac{(\text{End} - \text{Start})x^n}{\kappa^n + x^n}$ k- dissociation const n- Hill's slope	$y = \alpha + \frac{\theta x^\eta}{\kappa^\eta + x^\eta}$ k- dissociation const η- Hill's slope

Table S2 The number of exchanged species and their corresponding m/z.

Exchange species	Exchange number	Theoretical m/z (Da)
Au ₂₅ (2-PET) ₁₈	x=0	7391
Au ₂₅ (2-PET) ₁₆ (R/S-CE)	x=1	7983
Au ₂₅ (2-PET) ₁₄ (R/S-CE) ₂	x=2	8575
Au ₂₅ (2-PET) ₁₂ (R/S-CE) ₃	x=3	9166
Au ₂₅ (2-PET) ₁₀ (R/S-CE) ₄	x=4	9758

$$\bar{x} = \frac{\sum I_x * X}{\sum I_x}$$

where \bar{x} is an average exchange, I_x is an intensity of the peak and x is an exchange number.

B. EXPERIMENTAL PART

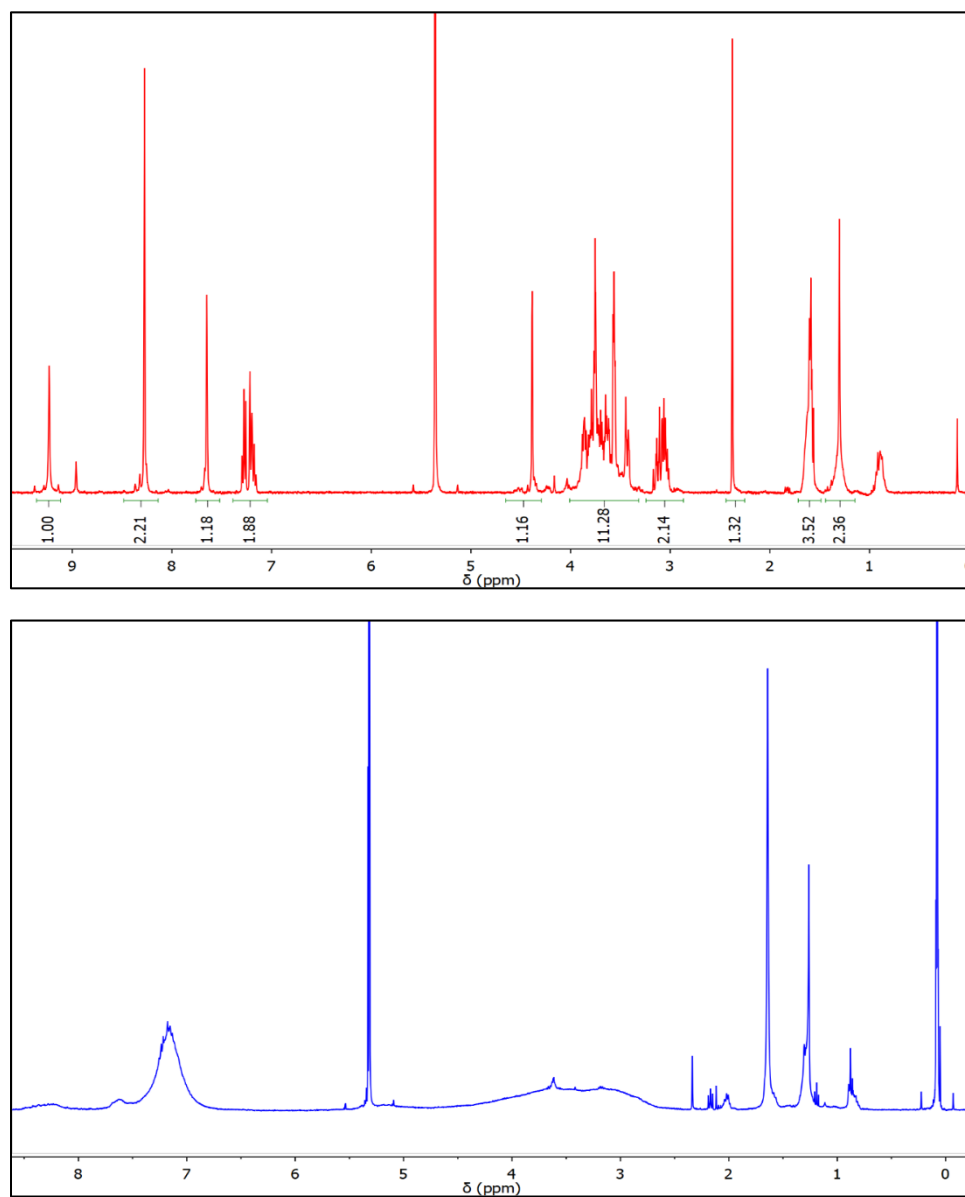


Fig. S1 $^1\text{H-NMR}$ of the free CE ligand (top panel) and Au_{25}CE (bottom panel) in $\text{DCM-}d_2$ at 298K.

B. EXPERIMENTAL PART

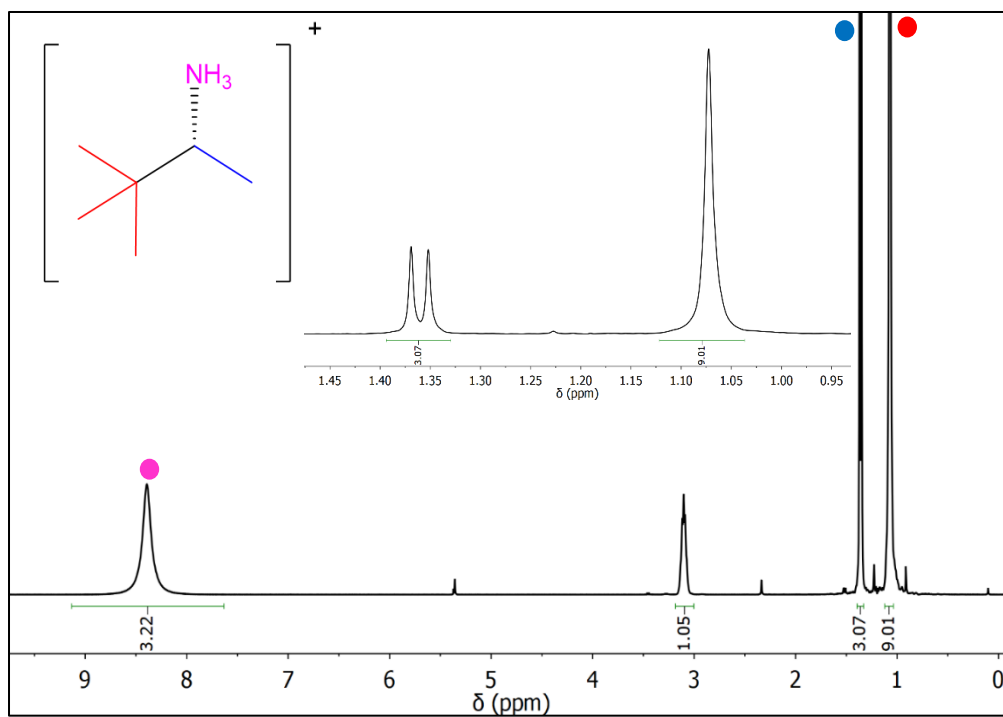


Fig. S2 $^1\text{H-NMR}$ of the protonated amine in DCM-d_2 at 298K.

B. EXPERIMENTAL PART

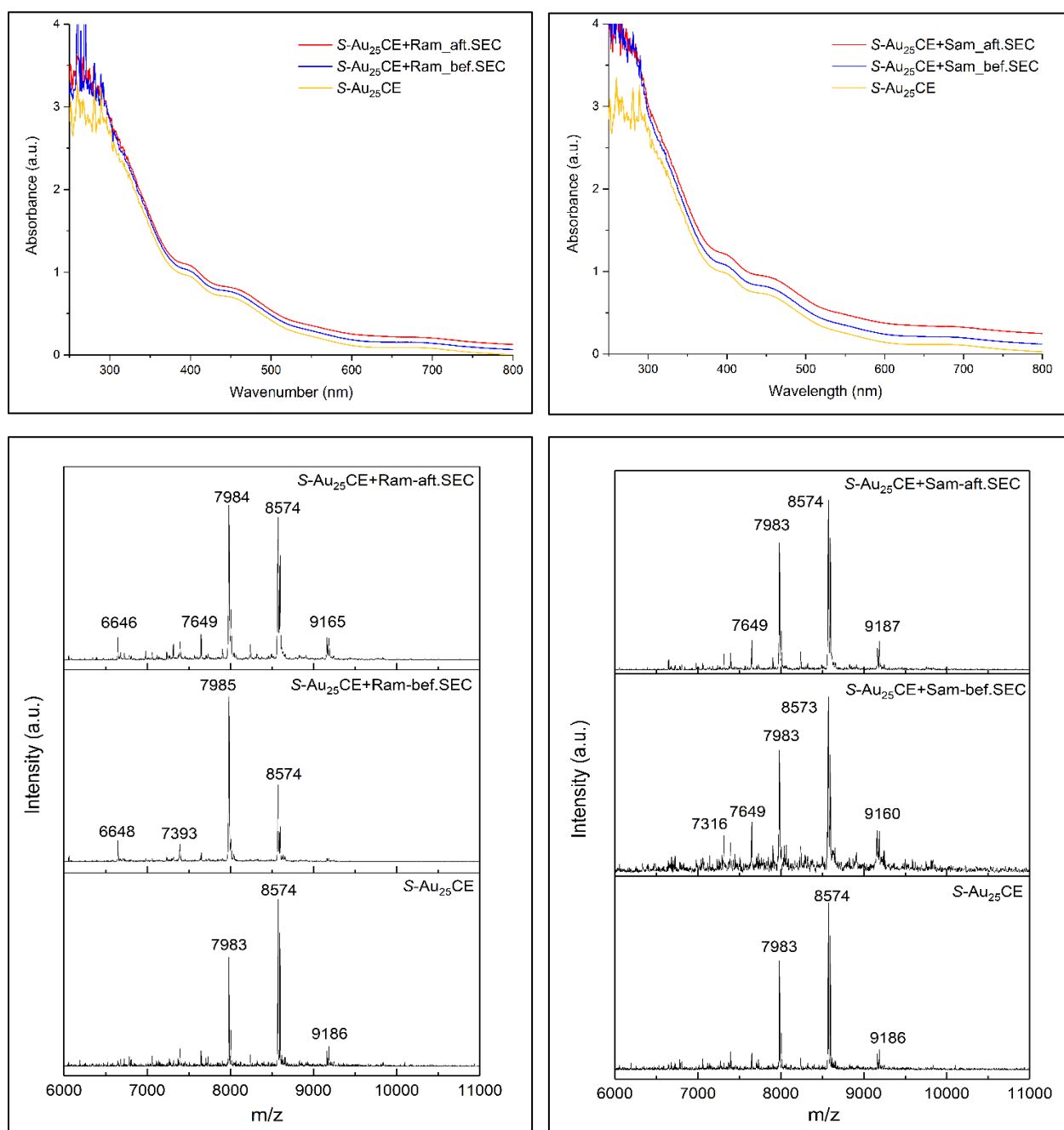


Fig. S3 UV-vis spectra and corresponding MALDI mass analyses of S-Au₂₅CE+Ram/Sam before and after amine purification on SEC.

B. EXPERIMENTAL PART

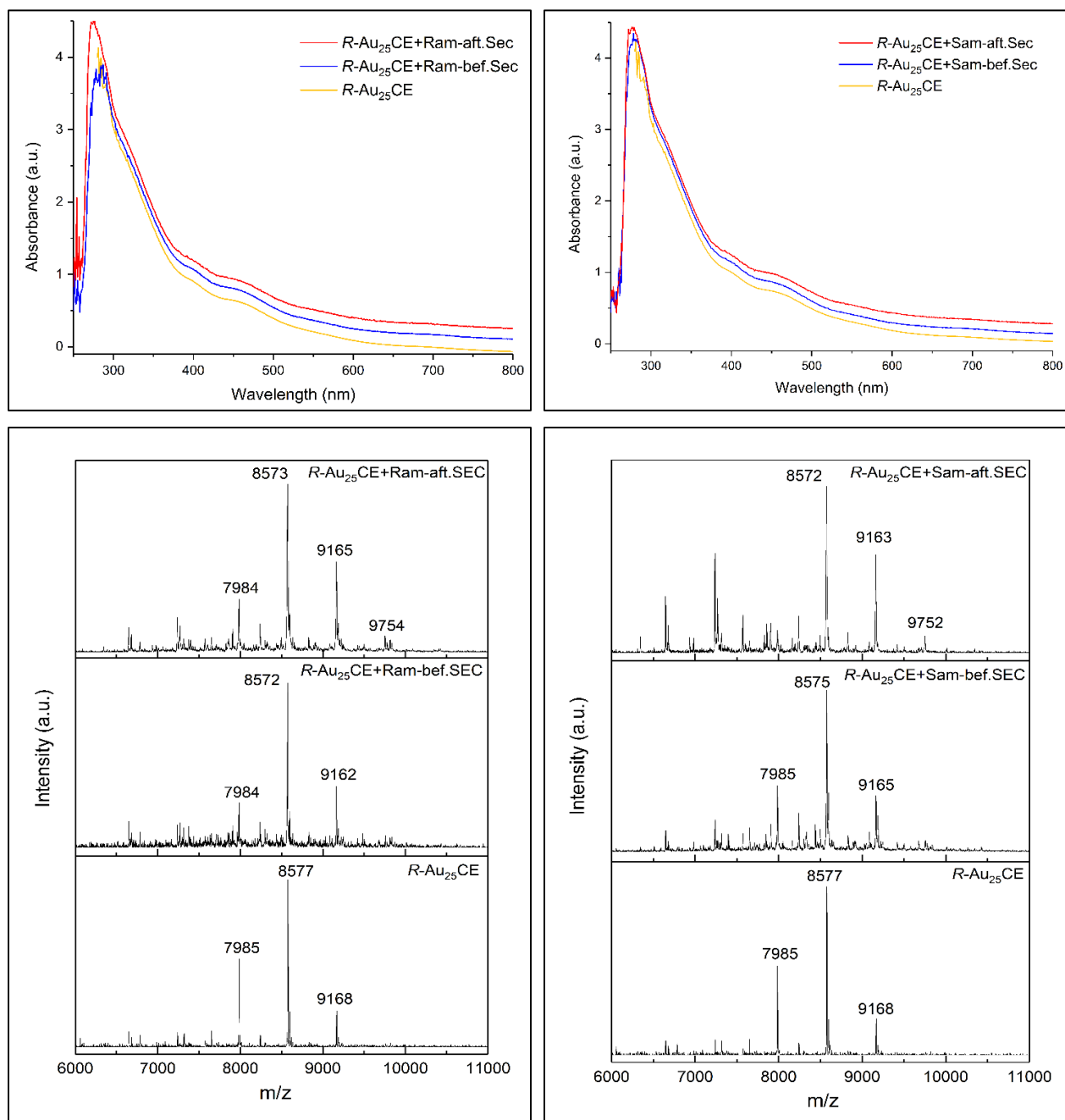


Fig. S4 UV-vis spectra and corresponding MALDI mass analyses of *R*-Au₂₅CE+Ram/Sam before and after amine purification on SEC.

B. EXPERIMENTAL PART

Table S3 The comparison of binding parameters between different enantiomers of cluster and the amine as a function of average exchanged number.

Enantiopure sample	\bar{x}	Prot. Amine	n_H			K_D, M			ΔG^0_{bind} (based on K_d Origin value)
			GraphPad Prism 7	OriginPro 2017	CurveExpert Professional 2.6.5	GraphPad Prism 7	OriginPro 2017	CurveExpert Professional 2.6.5	
R-Au ₂₅ CE	1.8	Ram	1.517	1.516	1.611	8.587*10 ⁻⁵	8.587*10 ⁻⁵	8.5*10 ⁻⁵	-23.2 KJ/mol
R-Au ₂₅ CE	1.8	Sam	1.313	1.313	1.313	3.574*10 ⁻⁵	3.57*10 ⁻⁵	3.57*10 ⁻⁵	-25.35 KJ/mol
S-Au ₂₅ CE	1.8	Ram	1.855	1.854	1.855	1.743*10 ⁻⁴	1.742*10 ⁻⁴	1.74*10 ⁻⁴	-21.4 KJ/mol
S-Au ₂₅ CE	1.8	Sam	1.3	1.255	1.312	9.94*10 ⁻⁶	4.73*10 ⁻⁶	1.49*10 ⁻⁵	-30.4 KJ/mol
R-Au ₂₅ CE	2.2	Ram	2.06	2.06	2.06	1.982*10 ⁻⁴	1.982*10 ⁻⁴	1.982*10 ⁻⁴	-21.1 KJ/mol
R-Au ₂₅ CE	2.2	Sam	1.991	2	1.99	1.607*10 ⁻⁴	1.73*10 ⁻⁴	1.607*10 ⁻⁴	-21.4 KJ/mol
S-Au ₂₅ CE	2.2	Ram	1.528	1.528	1.528	1.481*10 ⁻⁴	1.481*10 ⁻⁴	1.481*10 ⁻⁴	-21.8 KJ/mol
S-Au ₂₅ CE	2.2	Sam	1.885	1.885	1.885	1.854*10 ⁻⁴	1.853*10 ⁻⁴	1.853*10 ⁻⁴	-21.3 KJ/mol
R-Au ₂₅ CE	2.5	Ram	1.051	1.053	1.061	7.455*10 ⁻⁷	9.052*10 ⁻⁷	8.86*10 ⁻⁷	-34.5 KJ/mol
R-Au ₂₅ CE	2.5	Sam	1.113	1.107	1.105	6.372*10 ⁻⁶	5.43*10 ⁻⁶	4.9*10 ⁻⁶	-30 KJ/mol
S-Au ₂₅ CE	2.6	Ram	1.321	1.32	1.321	3*10 ⁻⁵	3*10 ⁻⁵	3*10 ⁻⁵	-25.8 KJ/mol
S-Au ₂₅ CE	2.6	Sam	1.751	1.764	1.751	8.586*10 ⁻⁵	8.877*10 ⁻⁵	8.585*10 ⁻⁵	-23.1 KJ/mol
R-Au ₂₅ CE	3	Ram	1.266	1.269	1.29	1.826*10 ⁻⁷	1.649*10 ⁻⁶	9.52*10 ⁻⁶	-33 KJ/mol
R-Au ₂₅ CE	3	Sam	1.241	1.246	1.263	7.589*10 ⁻⁷	2.29*10 ⁻⁶	2.807*10 ⁻⁷	-32.2 KJ/mol
S-Au ₂₅ CE	3	Ram	1.382	1.382	1.364	5.638*10 ⁻⁵	5.639*10 ⁻⁵	5.305*10 ⁻⁵	-24.2KJ/mol
S-Au ₂₅ CE	3	Sam	1.132	1.132	1.132	4.849*10 ⁻⁵	4.852*10 ⁻⁵	4.85*10 ⁻⁵	-24.6KJ/mol

B. EXPERIMENTAL PART

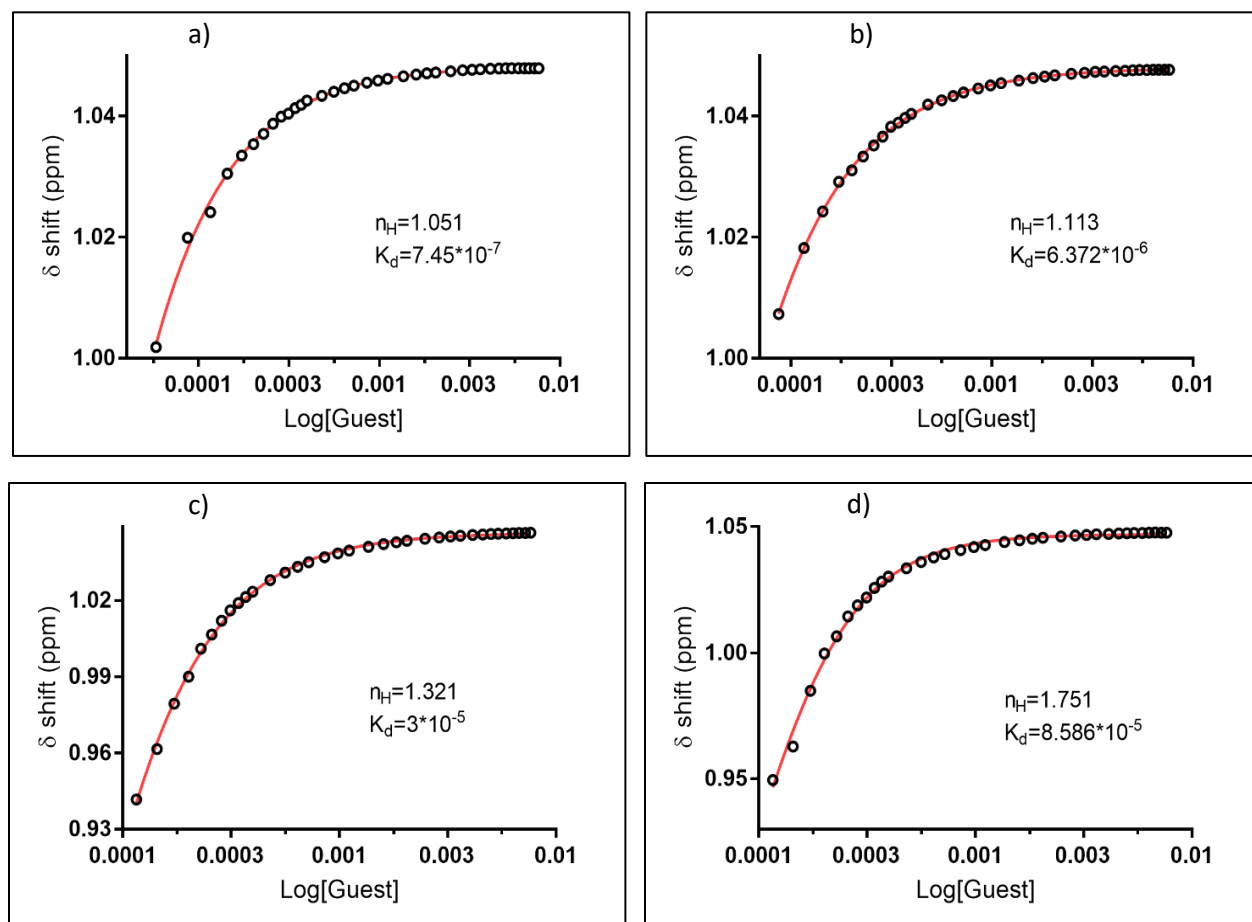


Fig. S5 Binding isotherms of the systems a) R/R and b) R/S with $\bar{x}=2.5$, c) S/R and d) S/S with $\bar{x}=2.6$. 4 equivalents of the guest in DCM-*d*₂ was prepared and added to titrand in small quantities (1-10 μ L). 1.9 mM host and 16 mM guest concentration were used for titration.

B. EXPERIMENTAL PART

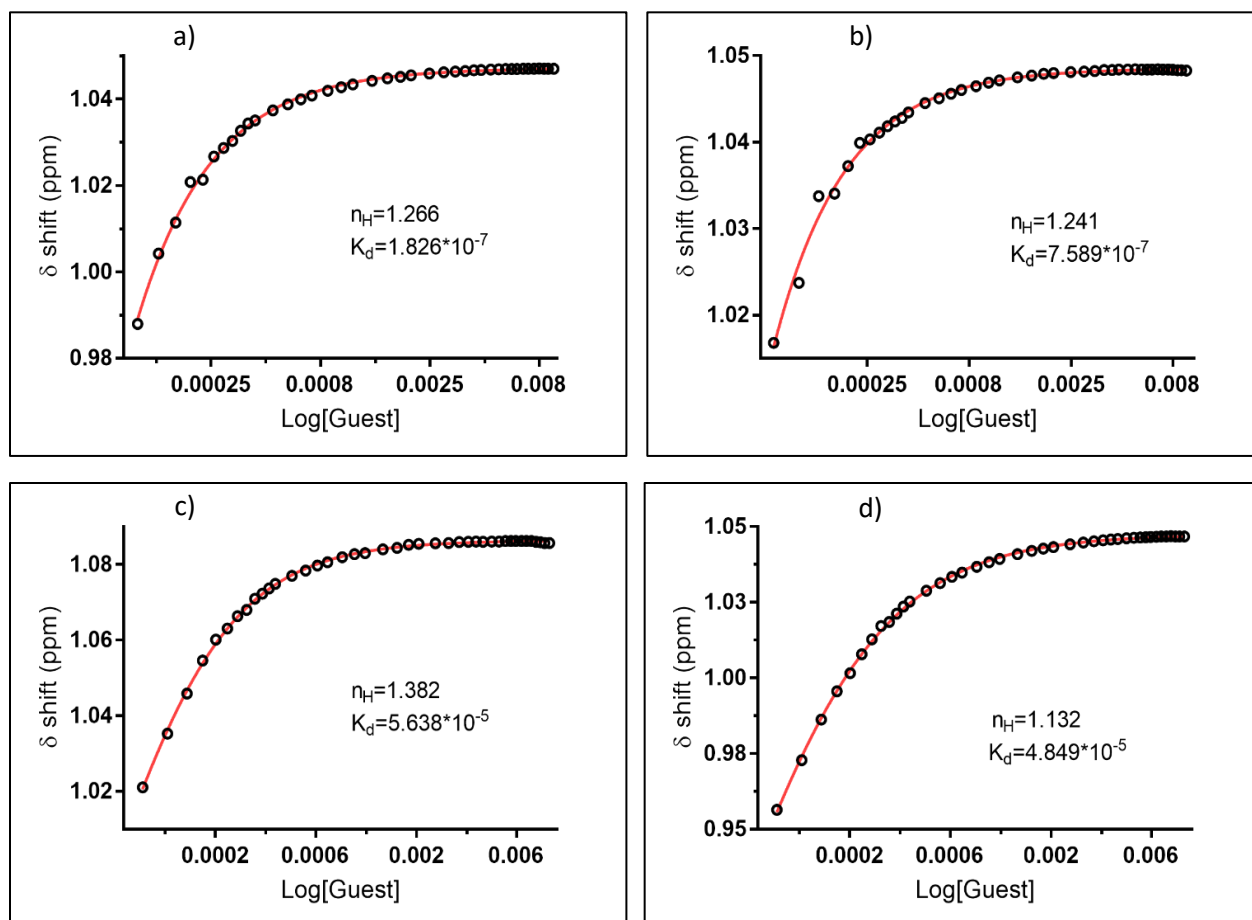


Fig. S6 Binding isotherms of the systems a) R/R, b) R/S, c) S/R and d) S/S with $\bar{x}=3$. 4 equivalents of the guest in DCM-*d*2 was prepared and added to titrand in small quantities (1-10 μ L). 2.67 mM host and 19 mM guest concentration were used for titration.

B. EXPERIMENTAL PART

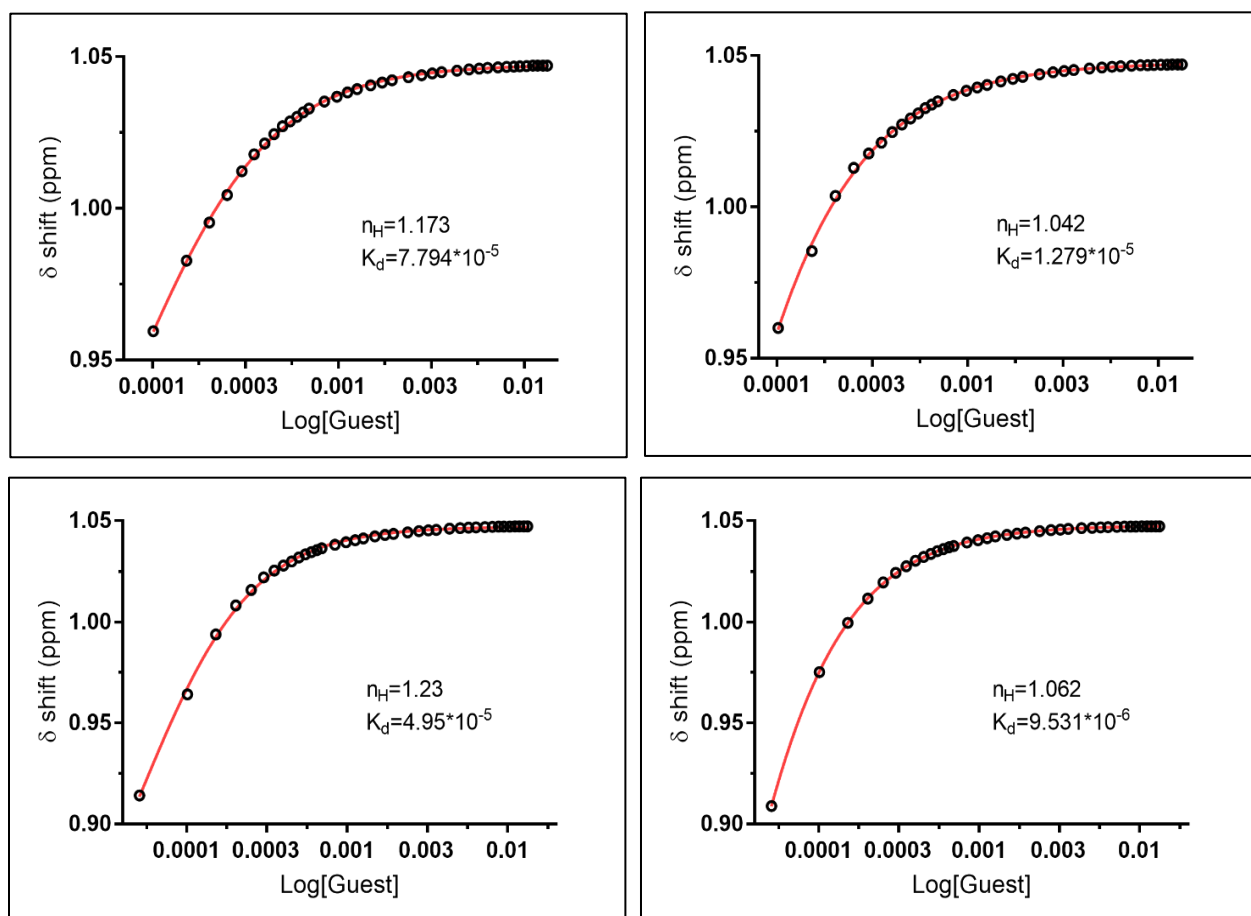


Fig. S7 Binding isotherms of the systems a) R/R , b) R/S , c) S/R and d) S/S with $\bar{x}=3.4$. 4 equivalents of the guest in DCM- d_2 was prepared and added to titrand in small quantities (1-10 μ L). 3.35 mM host and 28 mM guest concentration were used for titration.

B. EXPERIMENTAL PART

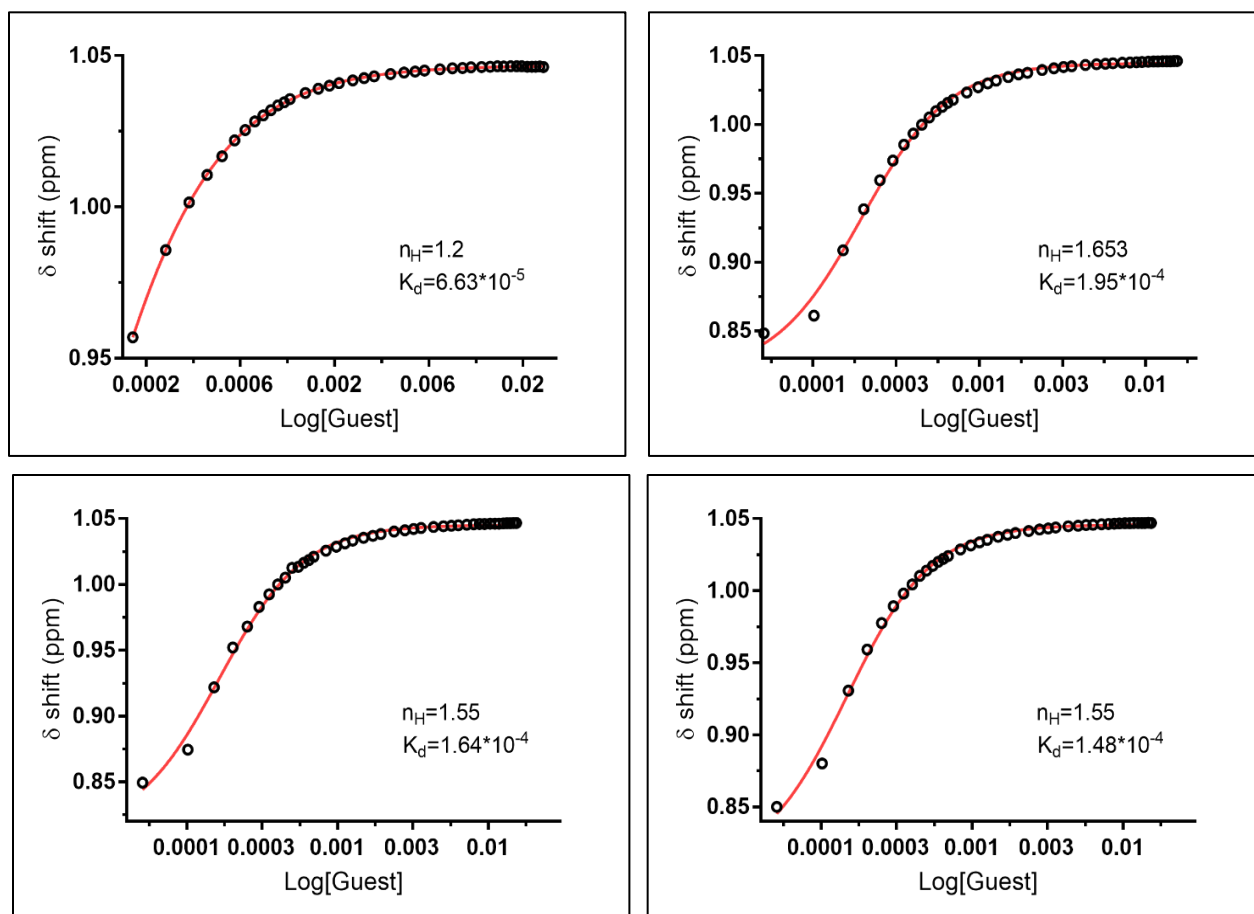


Fig. S8 Binding isotherms of the systems a) R -CE+Ram, b) R -CE+Sam, c) S -CE+Ram and d) S -CE+Sam.

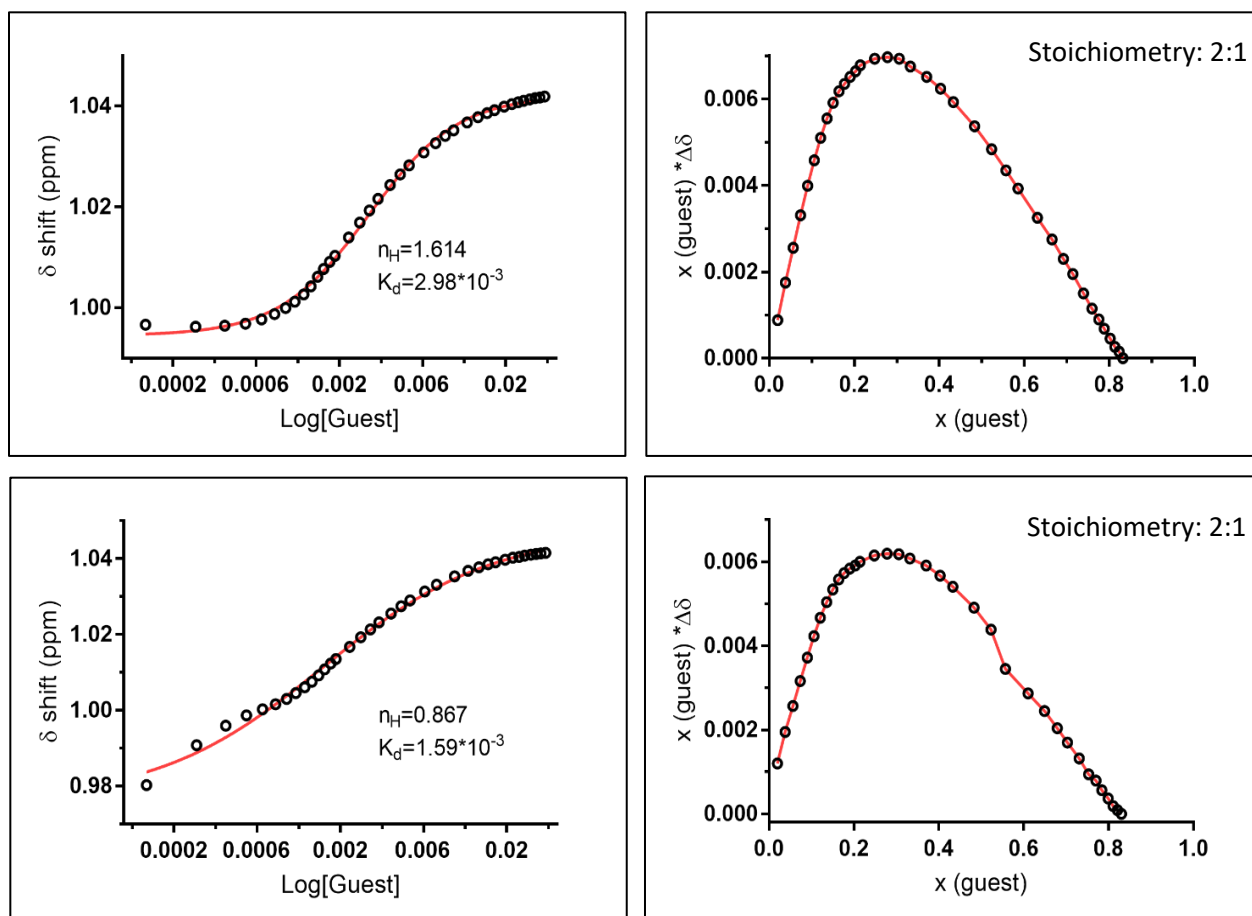


Fig. S9 Binding isotherms of the systems a) *com.18C6+Ram*, b) Job's plot of *com.18C6+Ram*, c) *com.18C6+Sam* and d) Job's plot of *com.18C6+Sam*.

B. EXPERIMENTAL PART

Table S4 The comparison of binding parameters between different enantiomers of ligand and commercial 18C6.

Enantiopure sample	Prot. Amine	n_H			K_D , M			ΔG^0_{bind} (based on K_d Origin value)
		GraphPad Prism 7	OriginPro 2017	CurveExpert Professional 2.6.5	GraphPad Prism 7	OriginPro 2017	CurveExpert Professional 2.6.5	
R-CE	Ram	1.2	1.2	1.2	$6.63 \cdot 10^{-5}$	$6.62 \cdot 10^{-5}$	$6.63 \cdot 10^{-5}$	-24KJ/mol
R-CE	Sam	1.65	1.65	1.65	$1.95 \cdot 10^{-4}$	$1.95 \cdot 10^{-4}$	$1.95 \cdot 10^{-4}$	-21.2KJ/mol
S-CE	Ram	1.55	1.55	1.55	$1.64 \cdot 10^{-4}$	$1.64 \cdot 10^{-4}$	$1.64 \cdot 10^{-4}$	-21.6KJ/mol
S-CE	Sam	1.55	1.55	1.55	$1.48 \cdot 10^{-4}$	$1.48 \cdot 10^{-4}$	$1.48 \cdot 10^{-4}$	-21.8KJ/mol
comm-18C6	Ram	1.614	1.614	1.614	$2.986 \cdot 10^{-3}$	$2.99 \cdot 10^{-3}$	$2.986 \cdot 10^{-3}$	-14.4KJ/mol
comm-18C6	Sam	0.867			$1.59 \cdot 10^{-3}$			

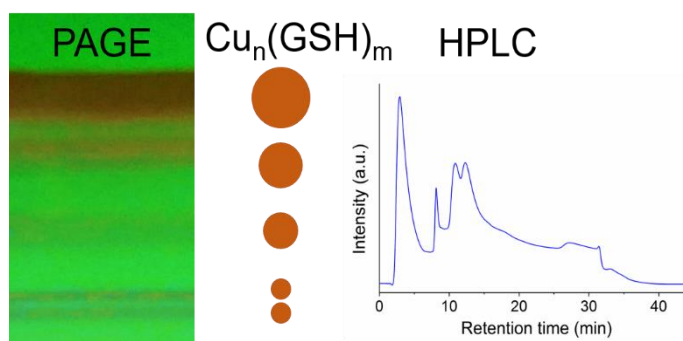
Table S5 The comparison of binding parameters between different enantiomers of cluster and the amine.

Enantiopure sample	$\bar{\chi}$	Prot. Amine	n_H	K_D , M	ΔG^0_{bind} (based on K_d Origin value)
			GraphPad Prism 7	GraphPad Prism 7	
R-Au ₂₅ CE	3.4	Ram	1.173	$7.794 \cdot 10^{-5}$	-23.4 KJ/mol
R-Au ₂₅ CE	3.4	Sam	1.042	$1.279 \cdot 10^{-5}$	-27.9 KJ/mol
R-Au ₂₅ CE	3.4	rac-Am	1.399	$6.501 \cdot 10^{-5}$	-23.8 KJ/mol
S-Au ₂₅ CE	3.4	Ram	1.23	$4.95 \cdot 10^{-5}$	-24.5 KJ/mol
S-Au ₂₅ CE	3.4	Sam	1.062	$9.531 \cdot 10^{-6}$	-28.6 KJ/mol
S-Au ₂₅ CE	3.4	rac-Am	1.249	$4.22 \cdot 10^{-5}$	-24.9 KJ/mol

6. Synthesis of ligand-protected CuNCs

6.1. Facile synthesis, size-separation, characterization, and antimicrobial properties of thiolated copper clusters

Metal nanomaterials have attracted extensive attention in biological labeling and imaging due to their controllable physical and chemical properties. Recently, a lot of effort has been devoted to preparing various ultra-small and functional copper



nanoclusters (CuNCs) with different emissions from blue to red, soluble both in organic and aqueous phases. Herein, a novel one-step synthetic method is proposed for the preparation of stable water-soluble glutathione-capped (GSH-capped) CuNCs. The resulting nanoclusters have a good dispersibility and stability in aqueous media. The stability was examined by several test experiments. The mass detection in ESI-HRMS mode allowed ionization of several doubly charged species with formula Cu_5L_6 , Cu_6L_6 , Cu_7L_6 , Cu_8L_6 and Cu_9L_6 ($\text{L}=\text{C}_{10}\text{H}_{16}\text{N}_3\text{O}_6\text{S}$). The use of advanced separation techniques including liquid chromatography (HPLC), gel electrophoresis (PAGE) and capillary electrophoresis (CE) allowed the separation of several clusters, some of which are larger than $\text{Au}_{25}(\text{GS})_{18}$, as shown by PAGE. To the best of our knowledge, this is the first report on successful size-separation of CuNCs. Moreover, the synthesized CuNCs show a dose-dependent antimicrobial effect. At lower cluster concentration the growth of bacteria is partially reduced. However, at higher concentrations, the bacterial growth is completely restricted.

This chapter is copied from my own paper: ACS Appl. Nano Mater. 2018, 1, 8, 4258-4267

1. Introduction

Metal nanoclusters have attracted considerable attention due to their tunable optical and electronic properties that differ substantially from those of the corresponding atoms and bulk materials. Thus, they provide an immense potential as unique functional building blocks in a wide range of applications such as optoelectronic devices, biosensors, nanoelectronics, medicine and novel catalysts.¹⁻⁷ Metal nanoparticles with dimensions comparable to the Fermi wavelength of an electron exhibit strong quantum confinement. With decreasing size, the continuous electronic bands break down into discrete energy levels, and therefore plasmon bands due to the collective oscillation of free electrons in the nanostructure are no longer observed. Nevertheless, they can still interact with the electromagnetic radiation through electronic transitions between their discrete energy levels, giving rise to rich absorption spectra and fluorescence emission.

The synthesis and characterization of thiol-protected gold clusters with the formula $Au_n(RS)_m$ have been extensively studied and established over the past few years.^{8,9} The rapid progress in synthetic routes of atomically precise and “magic” number clusters made assessment of their remarkable properties and applications possible. Moreover, the size-separation of these clusters was successfully achieved using several chromatographic techniques.^{10,11} Despite extensive research progress in the field of gold and silver nanoclusters,^{12,13} studies focusing on the synthesis and optical properties of other nanoclusters such as copper are still scarce primarily because of the difficulty in preparing stable, well-defined, and small particles.

Recently, research activity has been reported on the synthesis and applications of copper nanoclusters (CuNCs) using RNA, DNA^{14,15} and its oligonucleotides, polymers,¹⁶⁻²⁰ proteins (BSA, HSA),²¹⁻²³ peptides (GSH),²⁴⁻³¹ amino acids (Cys), dendrimers and thiols³²⁻³⁸ as templates to control nucleation and growth of clusters. Depending on the nature and the size of the NCs and the protective ligand shell, as well as preparation protocol,^{21,23} photoluminescence of CuNCs can be tuned from near-infrared (NIR) to ultraviolet (UV). However, to date, there is no report on the separation of the different sizes of copper clusters.

Development of a simple and facile strategy for the synthesis of water-soluble and stable NCs is highly valuable but challenging. The stability of NCs plays a key role to assess their applications.

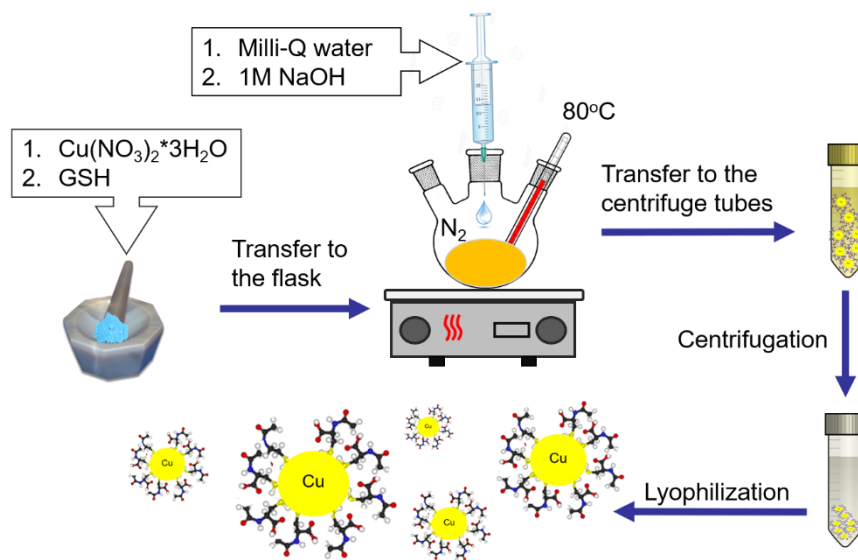
Herein, we propose a simple and green route to synthesize glutathione-capped (GSH-capped) copper clusters. GSH, a natural tripeptide, works as a scaffold to prevent NCs from aggregation. In addition to the thiol group, with its high affinity towards Cu, the additional carboxyl and amino functional groups of GSH (-COOH, -NH₂) improve the solubility of CuNCs in aqueous solution. Furthermore, size-separation of the prepared CuNCs was successfully achieved using several advanced separation techniques including chromatography (HPLC), electrophoresis (PAGE), and capillary electrophoresis (CE-UV).

2. Experimental

2.1. Materials. The following chemicals were used as received: copper nitrate (II) trihydrate (Acros Organic, 99%, for analysis), *L*-glutathione reduced (Carl Roth AG, ≥98%), methanol and isopropanol both HPLC grade (Fisher, 99.9%), acrylamide (Acros Organic, >99%, electrophoresis grade), *N,N'*-methylenebisacrylamide (Bis, Acros Organic, >99%, electrophoresis grade), ammonium persulfate (APS, Acros Organic, 98%, extra pure), *N,N,N',N'*-tetramethylethylenediamine (TEMED, 99.5%, Acros Organic), concentrated (10X) premixed tris(hydroxymethyl-aminomethane) (Tris, Acros Organic, 99.8%, ACS reagent)/glycine (Acros Organic, >99%, for analysis) buffer (250 mM Tris, 1920 mM glycine), 0.5 M Tris-HCl buffer pH 6.8 and 1.5 M Tris-HCl buffer pH 8.8 were purchased from Biorad, sodium chloride (Sigma Aldrich, >99.5%, for analysis). Water was purified with a Milli-Q system (≥18 MΩ cm).

2.2. Preparation of GSH-stabilized CuNCs. In a typical experiment, 76.3 mg of GSH and 30 mg of Cu(NO₃)₂·3H₂O were taken in an agate mortar and ground well for 5 min. The homogeneous powder was dispersed in 10 mL of Milli-Q water, and the formed hydrogel was heated up to 80 °C for 10 min. Then 1 M NaOH was added dropwise until a transparent and clear orange-red solution formed (**Scheme 1**). Apart from the first step, all the others were carried out under nitrogen flow. After cooling to room temperature, the as-prepared clusters were precipitated by H₂O\IPA\MeOH 3.5:2.5:1 mixture by centrifugation (Sigma 3-18K, 11400 RPM, 14239 RCF, 4 °C). This purification process was repeated several times to remove all unreacted precursors and

salts. The purified sample was then freeze-dried with a lyophilizer and kept in the fridge for further use.



Scheme 1 Schematic Representation of the Synthesis of CuNCs.

2.3. Characterization methods. UV-vis spectra were recorded on the Varian Cary 50 spectrophotometer, using a quartz cuvette of 1 cm path length. Spectra were measured in Milli-Q water.

Infrared spectra were measured on a Bruker Vertex 80 V FTIR instrument. Briefly, the cluster was dropped on a Ge crystal and allowed to dry in air. Temperature-dependent FTIR experiments on solid samples were performed with a Biorad Excalibur Instrument equipped with a Specac Golden Gate heatable ATR setup. IR spectra were recorded with a spectral resolution of 1 cm^{-1} , in the range of $600 - 4000\text{ cm}^{-1}$. Temperature range was $30-280^\circ\text{C}$ by increasing in steps of 10°C .

The CM200 transmission electron microscope (TEM), operated at 200 kV, was used for microstructure investigations. TEM samples were prepared by deposition of a drop of sample on a TEM grid with carbon film. The high-resolution TEM (HRTEM) micrographs were acquired to analyze nanoclusters morphology and investigate their size distribution.

The powder diagram of the sample was measured using X-ray $\text{Cu K}\alpha$ radiation on a supernova diffractometer at room temperature. The sample was crushed and put on a Kapton mitogen

cryoloop using a bit of fumbling oil. A ϕ scan of 300° was collected, consisting of 30 images with exposure time 2×25 s. All the images were processed together to obtain the final diffraction pattern.

High-resolution mass spectrometry analysis was performed in positive electrospray ionization mode on a QSTAR Pulsar instrument (Sciex, Concord, ON). The mass spectrum was acquired for 15 minutes by syringe infusion in individual spectra accumulation mode to be able to detect copper nanoclusters over the m/z 100-7000 range. Source voltage and temperature were decreased to prevent CuNCs in-source fragmentation.

For the determination of the apparent size in dynamic light scattering, a ZetaNano ZS (Malvern) device equipped with a He/Ne laser and an avalanche photodiode as a detector was employed at 173° scattering angle. The hydrodynamic diameters were determined using the cumulant method to fit the correlation function which was accumulated for 30 s. The aqueous solution of the sample with a concentration of 1 mg/mL and quartz plastic cuvettes of 1 cm path length were used for the measurements. The same instrument was also employed for electrophoretic measurements, after 120 s of equilibration of the samples at room temperature by using plastic capillary cells (Malvern). The mobility of each sample was measured five times and averaged. The ζ -potential (or z-potential) was calculated from the electrophoretic mobilities (u) with the Smoluchowski's model:³⁹

$$\zeta = \frac{u\eta}{\epsilon_0\epsilon}$$

Here, ϵ_0 is the dielectric permittivity of the vacuum, η is the dynamic viscosity and ϵ is the dielectric constant. The values of the two latter parameters in water at the temperature applied are 8.9×10^{-4} Pa s and 78.5, respectively.

X-ray photoelectron spectroscopy (XPS) analysis was performed on a PHI Quantum 2000 spectrometer with Al K α (1486.6 eV) excitation. The binding energies of Cu 2p, N 1s, O 1s, C 1s and S 2p were recorded and calibrated with C 1s at 284.8 eV.

Thermogravimetric analysis data were measured using a NETZSCH STA449 F3 instrument. The measurements were performed under nitrogen inert atmosphere with a purge rate of 20

mL/min. The sample (about 4.5 mg) was loaded in Al₂O₃ crucibles with a lid to prevent exposure to atmosphere while mounting. The experiments were carried out with a heating rate of 10 °C/min. All measurements were performed in the temperature range 25-600 °C. An experiment has been done using an empty Al₂O₃ crucible as a reference to normalize the data.

The fluorescence spectra were recorded at room temperature on a Fluorolog 3 (Horiba) spectrometer using a 10 x 10 mm quartz cuvette. Oxygen was removed by bubbling nitrogen.

The separation of water-soluble CuNCs has been realized according to their size and charge by high-density polyacrylamide gel electrophoresis (PAGE). It was performed with a Biorad protean II XI system. The best separations were achieved under constant voltage (150 V) with gels at $T=50\%$ and $C=7\%$, where T is the mass-volume percentage of monomer including cross-linker, N,N' -methylene-bis-acrylamide (Bis), and C is the proportion of cross-linker as a percentage of total monomer. The gel was buffered at pH=8.8 in a Tris-HCl solution. The migration buffer consisted of 10x concentrated glycine (1920 mM) and Tris (250 mM) in 80:20 water/methanol. The purified clusters were dissolved in a 5% glycerol solution in Milli-Q water to a concentration of 4 mg/mL. The electrophoretic separation was performed for 6h.

Ion exchange chromatographic HPLC separation of the glutathione-capped copper nanoclusters (CuNCs) was successfully achieved on a JASCO 20XX HPLC system equipped with Proswift®WAX-1S monolith column (4.6 x 50 mm PK/SS) using 10 mM Tris/1 M NaCl in 10 mM Tris buffer in gradient mode at the flow rate of 0.3 mL/min. The analytes were detected with a JASCO 2077 plus UV detector operated at 250 nm.

Capillary electrophoresis with UV-vis detection (CE-UV) has turned out to be a powerful method for the investigation of the CuNCs. CE-UV was performed using an Agilent HP 30CE (Agilent Technologies, Waldbronn, Germany) with fused silica (FS) capillary (Analytik AG, Böckten, Switzerland). The separation was successfully performed in both acidic and basic conditions using 50 mM pH 2.5 phosphate (pK_a 2.12) and 50 mM, pH 9.3 borate (pK_a 9.24) back ground electrolytes (BGEs), respectively, as well as volatile and MS compatible 50 mM pH 9 ammonia (pK_a 9.17) BGE. A 1000 ppm CuNCs+2% v/v acetone was injected into the FS capillary ($L_{tot}= 64.5$ cm, $L_{eff}= 56$ cm) at 25 °C under 30 kV (in positive mode). The sample was detected at 230 nm.

2.4. Quantum yield (QY) measurements. The QY of the as-prepared CuNCs was obtained using Rhodamine 6G in ethanol (literature QY 94% at 488 nm excitation wavelength).⁴⁰ The same excitation wavelength and bandwidth are applied to the sample and the reference. QY was determined according to:

$$QY = \frac{I}{I_R} \times \frac{A_R}{A} \times \frac{\eta^2}{\eta_R^2} \times QY_R$$

where QY is the quantum yield of the sample, I is the integral area under the fluorescence spectrum, η is the refractive index of the solvent used, and A is the absorbance at the excitation wavelength. The subscript R represents the reference. To minimize the reabsorption effects, absorbance was kept at ca. 0.1 at the excitation wavelength of 488 nm.

2.5. Antimicrobial properties. 2.5.1. Organism Preparation. *Escherichia coli*, strain DH5 α , was grown overnight from a single isolated colony in Luria-Bertani (LB) broth at 37 °C. For an assessment of antibacterial activity of CuNCs, the fresh culture of DH5 α was grown from overnight culture until optical density at 600 nm (OD_{600}) reached 0.4.

2.5.2. Bacterial Susceptibility to CuNCs Measured by Colony-Forming Unit (CFU) Assay. For a test of the susceptibility of *E. coli*, DH5 α , to different concentrations of CuNCs, Luria agar plates from a solution of agar were prepared. A 100 μ l sample of a freshly grown DH5 α cultured in LB ($OD_{600} \sim 0.4$) was plated uniformly on a nutrient agar plate with appropriate dilution to get a single colony.⁴¹ Prior to the spreading of the bacterial solutions, the agar plates were uniformly covered with different amounts of CuNCs (100, 200, 400, 500, and 750 μ g). After spreading bacteria, the plates were incubated further at 37 °C overnight. The numbers of resultant colonies were counted after 16-18 h of incubation. CuNCs-free plates, incubated under the same conditions, were used as controls. Before the experiments were started, the stock solution of CuNCs was sterilized with UV radiation overnight.

2.5.3. Bacterial Growth Kinetics in the Presence of CuNCs. For an examination of the bacterial growth kinetics in the presence of CuNCs, *E. coli*, DH5 α , cells were grown in LB supplemented

with different (250, 500 750 $\mu\text{g/ml}$) doses of CuNCs, at 37 °C with continuous shaking on an orbital shaker platform at 180 rpm.⁴² CuNCs-free broth was used as a control. Growth of organisms was observed by measuring OD at 600 nm for various time intervals for 7 h. The OD values were then converted into fold growth by dividing the OD₆₀₀ for the different time points by the initial OD₆₀₀ for the respective set of data.

GraphPad Prism 7 software was used for graphical representation and statistical analysis of data and also to calculate IC₅₀ value of CuNCs for *E. coli*, DH5 α .

3. Results and discussion

3.1. Characterization of CuNCs. The following hypothesis was put forward concerning a possible mechanism for cluster formation:²⁹ A metal-ligand chelate is formed between Cu²⁺ ions and GSH by electrostatic interaction between the metal ion and both thiol and carboxylate groups of GSH. GSH plays a dual role as a stabilizing agent and a reductant. Further addition of 1 M NaOH enhances the reducing capability of the -SH group (pK_a 9.65), hereby reducing the copper ions to atoms that then form clusters. Various parameters, such as metal/ligand ratio, temperature, reaction duration, atmosphere, as well as the type of precursor, were varied to optimize the synthetic conditions. The 1:2 Cu²⁺/ligand molar ratio was found to be the best condition for the synthesis of stable CuNCs. Lower concentrations of thiol ligand are inadequate for protecting the cluster, and on the other hand, higher concentrations of GSH might have led to the further etching of the cluster. Therefore, small and unstable clusters can be formed during the reduction process. Note, that neither strong nor mild reducing agents (NaBH₄, N₂H₄, NH₂OH, ascorbic acid) were used during the synthesis. The half-cell potential of the glutathione/glutathione disulfide redox system E^o_{GSSG/GSH} is -0.262 ± 0.001 V,⁴³ and thus it is sufficient for reducing Cu²⁺ to metallic copper (E^o_{Cu²⁺/Cu⁰} = +0.34 V, E^o_{Cu⁺/Cu⁰} = +0.52 V, E^o_{Cu²⁺/Cu⁺} = +0.16 V) and form clusters. However, the situation is more complex than that. It has been shown^{27, 30, 44–46} that in peptides SH functional group plays a significant role for the formation of relatively stable supramolecular metallogels or Cu (I) coordination polymers favored by the soft acid-soft base interaction.^{44,47} In aqueous solution with high pH values (using 1M NaOH during synthesis process) the -COOH groups are deprotonated whereas -NH₂ is protonated giving rise

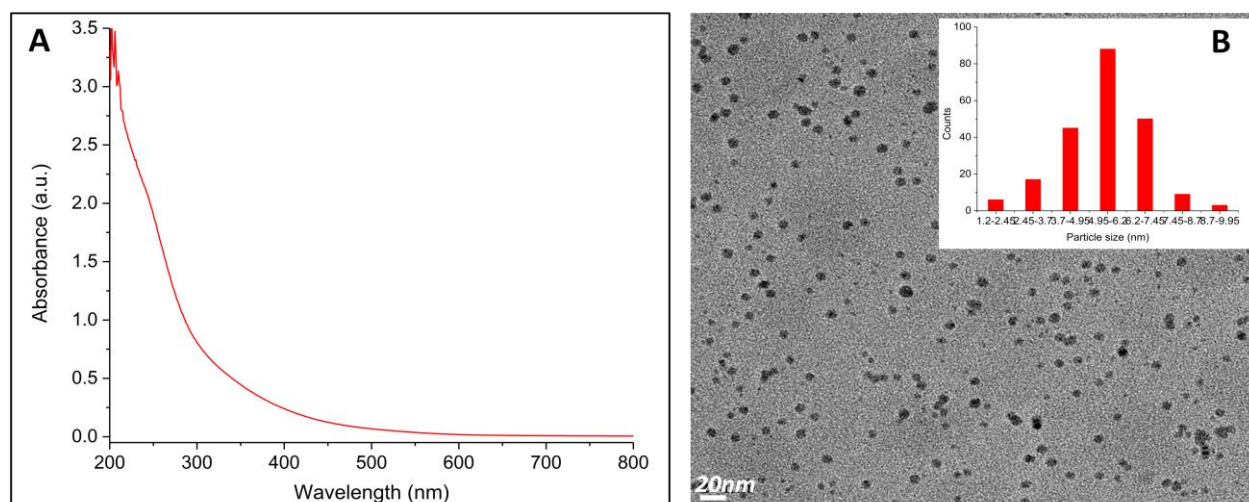


Fig. 1 (A) UV-vis spectrum of crude CuNCs. (B) HRTEM micrograph (inset: size distribution) of CuNCs.

to zwitterionic interactions. At this point, under basic conditions, Cu^+ -SG coordination polymers form a Cu^+ -S(G)- intermediate complex due to the $\text{Cu}^+\dots\text{Cu}^+$ cuprophilic interaction.⁴⁸ Furthermore, the excess of GSH works as an efficient reducing agent to further etch Cu^+ in the Cu^+ -SG coordination polymers and the intermediate complexes, which promotes the formation of isolated CuNCs species.

The absorption spectrum of the clusters lacks clear features (**Fig. 1A**) in the visible spectral range. The absence of a plasmon resonance indicates that the size of the formed clusters is small. For particles of about 3 nm diameter and larger a surface plasmon resonance is expected.⁴⁹⁻⁵¹ The spectrum thus looks remarkably different from Cu nanoparticles with the characteristic surface plasmon resonance around 570 nm. For well-defined (monodisperse) clusters one would expect features due to the quasicontinuous electronic band structure and quantum confinement effects of CuNCs. The absence of such a structure in the spectrum indicates a mixture of different cluster sizes (see below), although the shoulder at 230-260 nm in the spectrum is reminiscent of such spectral features.

The high-resolution transmission electron microscopy (HRTEM) image shows well-dispersed spherical Cu nanoparticles with an average size (diameter) of 5.5 nm (**Fig. 1B**). Note that the imaging of small clusters is very challenging, and they tend to agglomerate during the drying process. On the other hand, under the intense electron beam, metal core fusion may occur

because of electron-beam-induced heating and breaking of metal-sulfur bonds. Hence, the average size from HRTEM is much bigger than the actual size. This is furthermore supported by the absence of diffraction in XRD analysis (**Fig. S1**). The XRD diffractogram of bulk Cu was superimposed with the experimental diffractogram of CuNCs to make the comparison more visible (**Fig. S1**). Notably, the 2θ values at 42.93, 50 and 73.12 corresponding to the Cu(111), Cu(200), and Cu(220) planes are no longer distinguishable in the cluster sample. Hence, the broadening and overlapping of these characteristic lattice planes in the CuNC sample are a direct indication of very small sizes.

The mean hydrodynamic diameter of the clusters in water is in the range 2.3-2.8 nm (**Fig. S2**). The polydispersity index (PI) of the sample is significantly low (less than 0.3), which implies the absence of aggregates. Moreover, considering the size of GSH, about 8 Å, as estimated from the crystal structure (distance between S of Cys and O of Glu), this shows that the metal core of the clusters is very small. This estimation additionally excludes the formation of aggregates and suggests having rather isolated small clusters. The negative charge of the clusters is shown by the electrophoretic measurement. The average z-potential of the dissolved clusters in aqueous solution gives a value of -12 mV.

X-ray photoelectron spectroscopy (XPS) analysis of CuNCs reveals signals of C, O, N, S and Cu, as expected (**Fig. 2A**). The binding energies for Cu $2p_{3/2}$ and Cu $2p_{1/2}$ were located at 932.4 eV and 952.4 eV, which are characteristic peaks for Cu⁰ or Cu⁺. Note that the binding energy difference of the $2p_{3/2}$ level for the two oxidation states of Cu differs by only 0.1 eV. The lack of a satellite peak at 942 eV indicates the absence of Cu²⁺ in the cluster. Hence, in general, the oxidation state of Cu in the CuNCs is 0 and/or +1. The XPS spectra of other elements (S 2p, C 1s, N 1s and O 1s) are shown in **Fig. S3**.

The infrared spectra of GSH⁵² and CuNCs are shown in **Fig. 2B**. The absence of the S-H stretching vibrational mode in the CuNCs spectrum at 2559 cm⁻¹ suggests the cleavage of the S-H bond and binding of the GSH molecules onto the surface of CuNCs through Cu-S bonding.

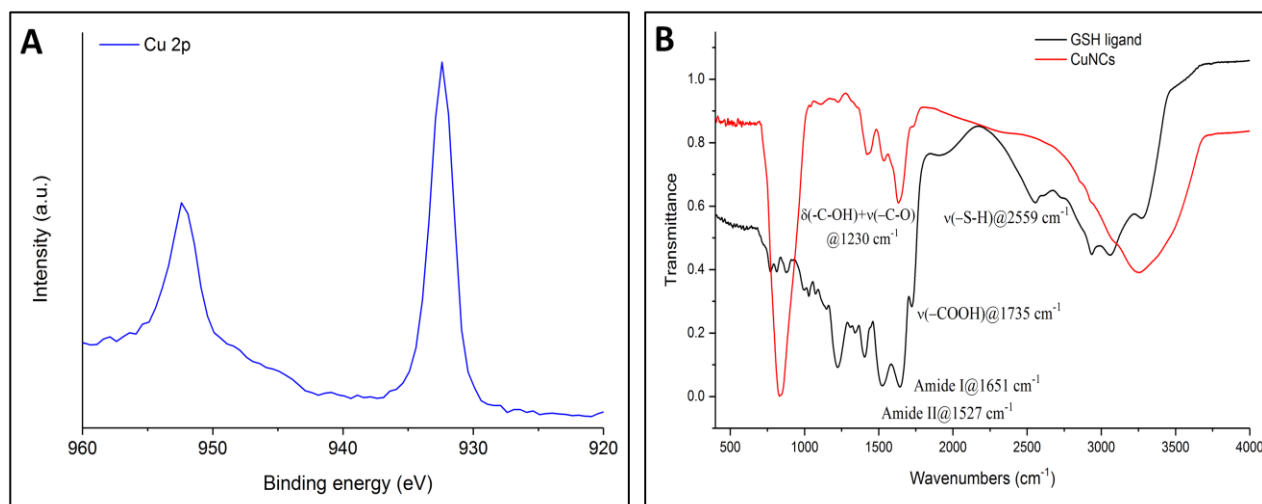


Fig. 2 (A) XPS spectrum of Cu 2p in CuNCs. (B) FTIR spectra of free GSH ligand and CuNCs. Both samples were measured as solid in ATR mode.

In aqueous solution CuNCs exhibit red fluorescence (λ_{\max} = 588 nm, Stokes shift 100 nm, **Fig. S4**) with a quantum yield of 1.3×10^{-4} . The obtained value is much smaller than previously reported ones in literature.^{24–26} Recently, aggregation-induced emission (AIE) was observed in some fluorescent copper nanomaterials.^{44, 53–55} In the aggregates of CuNCs, a long fluorescence lifetime and enhanced emission efficiency are due to the restriction of intramolecular motions that block the nonradiative paths and activate radiative decay. However, the molecular motions of the dispersed sample in aqueous solution are not restricted and give rise to the nonradiative deactivation. As a result, the dispersed CuNCs exhibit lower quantum yields (as we have shown). The narrow excitation spectrum and low quantum yield are quite similar to what is reported in the literature for several CuNCs.^{24–26} Furthermore, the stability of these small clusters is a key issue. Therefore, several experiments were carried out to examine stability under different conditions. In **Fig. S5 and S6** the temperature-dependent FTIR and time-dependent UV-vis spectra are shown. Obviously, no major changes appear on the absorption spectra over the course of 8 days under ambient conditions. Note that TD-UV-vis analysis was performed on the same sample by keeping it in solution without drying or changing its concentration.

Moreover, the cluster shows significant stability against heating up to 190 °C (**Fig. S7**). The mass loss made evident in the TG curve can be assigned to the water contamination which was later proven by the presence of the stretching vibration modes at 3000-4000 cm^{-1} in TD-FTIR spectra (**Fig. S5**). On the contrary, in CuNCs, the characteristic vibrations of $-\text{COOH}$ at 1735 cm^{-1} and $-\text{NH}_2$ at 1527-1651 cm^{-1} remain unchanged up to 190 °C. At higher heating temperatures these vibration modes diminish, and thus, the decomposition of the cluster takes place. From the TG curve the weight percentage of GSH ligand and GSH : Cu ratio were estimated to be 41% and 1:7 respectively. Note that for copper – thiolate polymers a 1:1 ratio is expected. The stepwise decomposition pattern of the TGA curve has been observed for other metal clusters too.⁵⁵⁻⁵⁷ Moreover, the decomposition of the GSH ligand itself completes in 3 steps from 200 to 900 °C whereas in case of Ag@GS cluster the decomposition completes at moderate temperatures (600 °C) by keeping its stepwise mass loss features.⁵⁷ Hence, for GSH-protected clusters the stepwise TGA profiles are expected.

The mass spectrum of the as-prepared crude sample was acquired in positive mode (no signals were observed in negative mode) from m/z 100 to 7000. However, over m/z 1500 no significant signals were observed. The mass spectrum shows singly charged ion clusters in the range m/z 100-900 and doubly charged patterns above m/z 900 (**Fig. 3**).

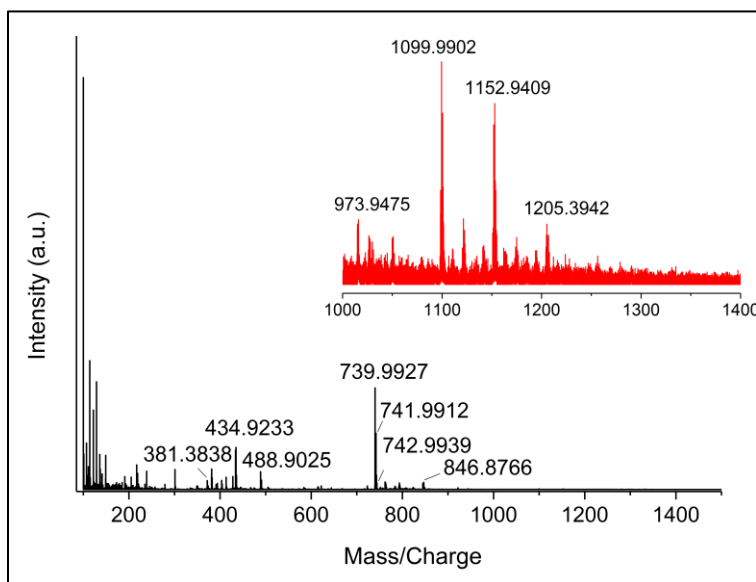


Fig. 3 ESI-HRMS mass spectrum of crude CuNCs.

Note that the low mass range (below m/z 900) is complicated by fragmentation of the sample itself, hereby the isotopic pattern fitting for this region was omitted. For higher mass ranges, the calculated isotopic patterns with H^+ and/or Na^+ adducts match well with experimental mass spectra for the following species: $Cu_9L_6H_2^{+2}$, $Cu_8L_6H_2^{+2}$, $Cu_8L_6Na_2^{+2}$, $Cu_7L_6H_2^{+2}$, $Cu_7L_6Na_2^{+2}$, $Cu_7L_6Na^{+2}$, $Cu_6L_6NaH_2^{+2}$, $Cu_6L_6H_2^{+2}$, and $Cu_5L_6Na_2^{+2}$ (**Fig. S8**). Herein, the GSH/Cu ratio is ca. 1:1 in contrast to the value obtained from TG analysis. Surprisingly, all obtained clusters share the same number of protective ligands (L) and only the number of copper atoms is varied. The discrepancy between TG analysis and ESI concerning the copper:GSH ratio is likely due to the fact that in TG the entire sample is considered whereas in ESI only the small clusters and/or polymers are detected. Despite our effort, no signal from larger CuNCs could be detected in ESI despite their presence in the crude sample, according to PAGE (see the following).

However, it has been shown, that copper (I) can form compounds with different nuclearity, known as clusters with diverse chelating ligands.^{37,58-61} For example, the single crystal structure of pentanuclear Cu (I) clusters is comprised of a Cu_4S_4 core as a crown moiety which traps a copper ion in the center via Cu-S coordination and cuprophilic interaction. On the other hand, in the synthesized rare octanuclear copper (I) cluster four Cu atoms form a square plane whereas the remaining four atoms form trigonal prisms known as a Gyrobifastigium. Moreover, X-ray structure of hexanuclear Cu_6L_6 cluster also has been reported.³⁶ On the basis of what has been already reported for small copper clusters, we assume that the ionized species from the ESI mass spectrum are either a new type of small Cu clusters or fragments of Cu (I) polymers. However, the fact of having relatively big clusters in addition to the small clusters/polymers has been confirmed by PAGE separation of the crude CuNCs using water-soluble AuNCs as molecular weight marker (see the following).

3.2. Size-Separation of CuNCs. Size-separation and further characterization of atomically precise copper clusters open new possibilities in the field of materials sciences and their remarkable applications in biomedicine and catalysis. Several advanced separation techniques (PAGE, CE-UV, HPLC) are particularly appropriate for the size-separation of water-soluble nanoclusters.

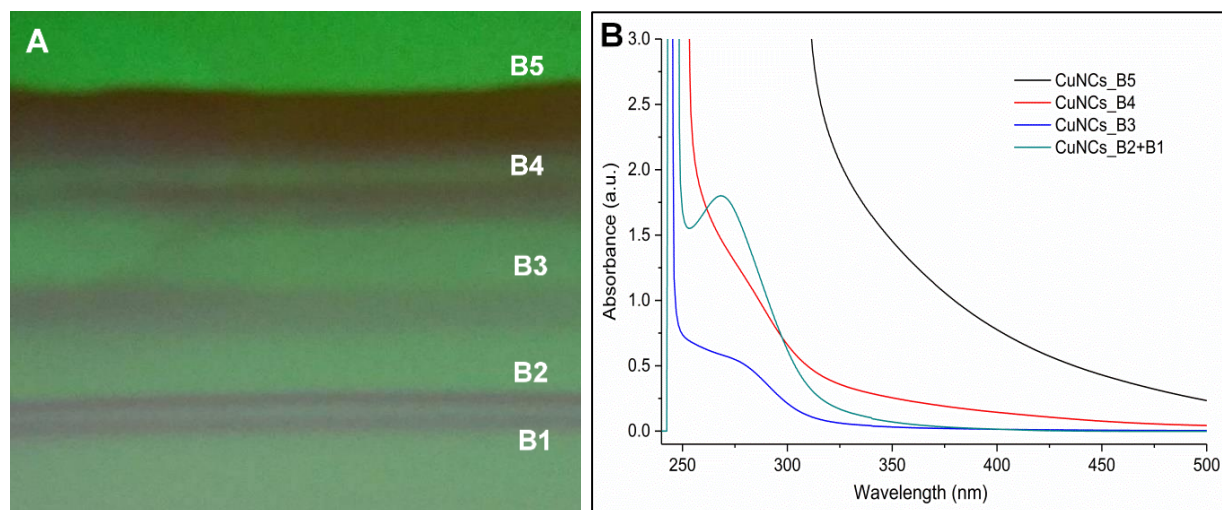


Fig. 4 (A) PAGE separation and (B) corresponding UV-vis spectra of bands of CuNCs measured inside the gel.

Glutathione-protected copper clusters are charged and can therefore be separated according to their size and charge by PAGE and CE.

PAGE of CuNCs leads to the separation of five distinguished bands labeled as B1-B5 (**Fig. 4A**). The bands corresponding to the smallest clusters (B1 and B2) emit red fluorescence under UV excitation but are invisible to the bare eye. These two bands are very close to each other and sometimes remain unseparated as one single band. Thus, they were cut and analyzed as a single band. B3 and B4 bands are more prominent, and it is possible to see them by bare eye. In UV-vis spectra (**Fig. 4B**), the B1 and B2 mixture has an absorption peak centered at 260 nm, while the absorption maximum of B3 has shifted toward higher wavelengths (275 nm). Upon an increase in the size of the cluster (B4), the UV absorption feature around 270 nm tends to decrease. Moreover, the B5 band has no obvious absorption fingerprints like other bands, and the UV-vis is quite the same as the one for the crude sample. From UV-vis spectra, the high energy absorption at ca. 260-275 nm can be assigned as an intraligand (IL) $n(S) \rightarrow \pi^*$ transition.^{59, 61, 62} Additionally, CuNCs show moderate absorption in 300-500 nm and strong absorption below 260 nm. This transition arises from ligand-to-metal charge transfer (LMCT).⁶⁰⁻⁶²

Parts of the gel containing each separated fraction were cut out and placed in Milli-Q water overnight. Unfortunately, the suspended samples get oxidized and changed color gradually from

B. EXPERIMENTAL PART

yellow to greenish (Cu-GSH complexes) and finally blue (Cu⁺²). Note that the stepwise oxidation process was not observed in the crude (unseparated) mixture of CuNCs. The stability of the crude sample additionally was confirmed by running PAGE separation after one year. In fact, the same bands were observed. Additional PAGE separation was run to approximately estimate the size of the species in each band by comparison with well-known and characterized gold Au₂₅ clusters protected with 18 GSH ligands (10433 Da) (**Fig. S9**).⁶³ Obviously, the first band of CuNCs (B1+B2) which is invisible under normal light but detectable under UV irradiation, migrates faster than AuNCs. We assume that this band with lower molecular mass is characteristic for the small clusters or Cu(I) polymers. Hence, in the ESI mass spectrum, the obtained Cu₉L₆, Cu₈L₆, Cu₇L₆, Cu₆L₆ and Cu₅L₆ species are associated with the first band in the gel. In contrast, the last two bands migrate much slower than AuNCs which indicates bigger clusters. Hence, the results from PAGE separation using AuNCs as a molecular weight marker and the GSH/Cu ratios obtained from both TG analyses indicate that the crude sample contains not only small clusters/polymers but also relatively big and well-defined clusters. Unfortunately, ESI and cold-ESI analyses were not successful for detecting higher *m/z* peaks.

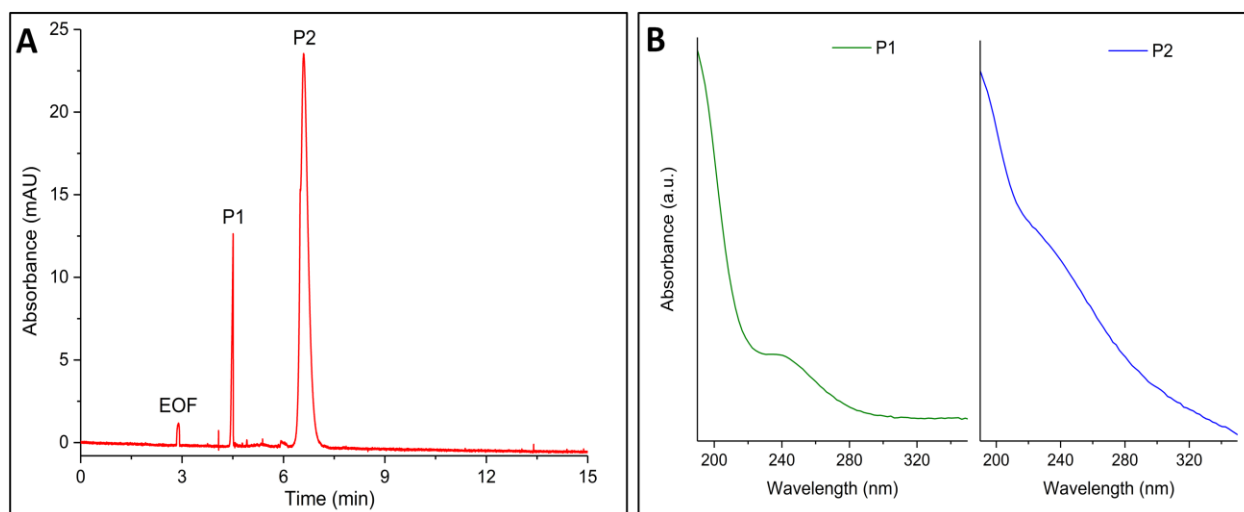


Fig. 5 (A) CE separation and (B) corresponding UV-vis of CuNCs.

Capillary electrophoresis (CE) was also used to separate different fractions. Reducing the loaded amount of samples up to 1000 ppm in CE technique, using 50 mM, pH 9.3 borate buffer (pK_a 9.24) as a back ground electrolyte (basic conditioning, **Table S1**), gives the separation of mainly two

species at 4.7 (P1) and 6.8 (P2) min, respectively, with characteristic UV absorption features (**Fig. 5A,B**). Note that at alkaline pH the electro-osmotic flow (EOF) is sufficiently strong and makes the simultaneous separation of cations, anions, and neutral species in a single analysis possible. Consequently, the observed migration order is cations, neutrals (associated with EOF) and anion species.⁶⁴ Hence, in the case of CuNCs (**Fig. 5A**), CE separation results in negatively charged clusters. Moreover, according to the electropherogram, the first peak presents a symmetric shape whereas the second one is asymmetric with a larger peak width which suggests that several species are contributing to it. Apart from two intense peaks, some minor peaks were also observed. The UV-vis spectrum of the first peak from CE separation has resemblance with both B1+B2 and B3 in PAGE (**Fig. 5B**). Similarly, the second peak could be related to B4. It is difficult to compare other peaks since their intensity in CE was near the limit of detection. It should be noted that the overall analyte stability could be an issue when certain pH media and high tensions are applied.

Four main peaks at 2.9, 8.1, 10.8, and 12.2 min retention times were eluted by using HPLC technique in a gradient mode (**Fig. 6, Table S2**). The UV-vis spectra of the separated peaks measured *in situ* show similar optical features as seen before in PAGE/CE separations. The purification of collected fractions was completed by dialysis in a bag with MWCO 1000 Da.

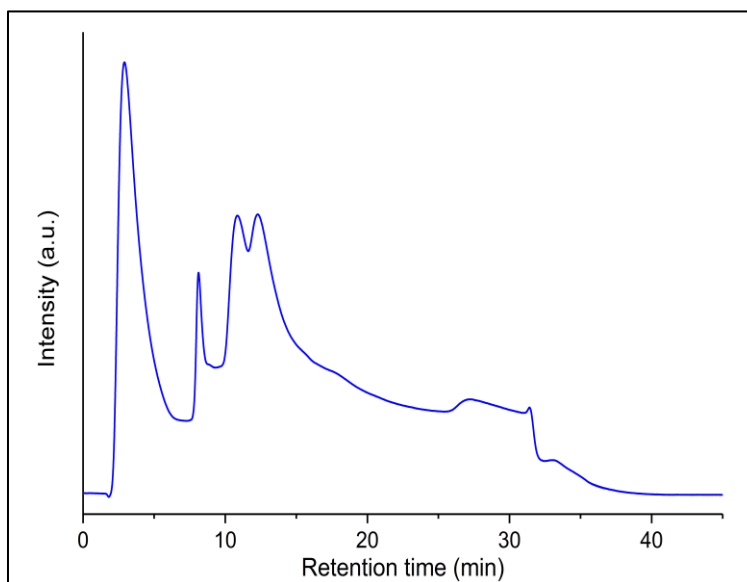


Fig. 6 HPLC separation of CuNCs.

Note that the dialysis was an essential step in the purification process to remove all the salts from the mobile phase. The water was changed every 10 h over the course of 4 days. However, as described above for PAGE, the separated species were no longer stable and get oxidized.

Possibly, in the crude sample, a reductant is created through the decomposition of an unstable species, which stabilizes the other species by preventing them from oxidizing. Hence, after separation, in the absence of such a reductant, the clusters species become unstable. It should be noted that the interaction mechanism of the cluster with the gel (PAGE), BGE (CE-UV) and with the stationary phase (HPLC) is different, and the number of separated bands can vary. In general, the experimental data obtained from several advanced separation techniques combined with spectroscopic studies are in good agreement and confirm the separation of several cluster sizes from the crude mixture.

3.3. Antibacterial Properties of CuNCs. 3.3.1. Colony-Forming Unit (CFU) Assay of CuNCs. The antimicrobial activity of CuNCs was tested by CFU assay. A bar diagram in **Fig. 7** represents the dose-dependent response of nanoclusters on growth of *E. coli* strain DH5 α . Nanocluster-free growth of bacteria is represented as “0” and treated as the control set. The increase in the number (100, 200, 400, 500, 750 μg) of nanoclusters results in low CFU/ml (9.15×10^9 , 6.7×10^9 , 4.15×10^9 , 3.57×10^9 , 3.15×10^9 , respectively) counts compared to control bacteria (12.35×10^9).

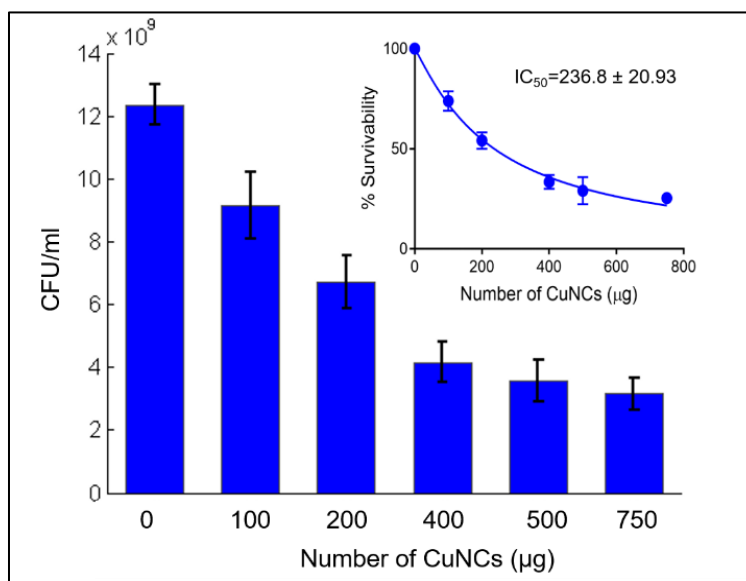


Fig. 7 Antimicrobial activity of CuNCs (inset: IC_{50} value).

The IC₅₀ value of CuNCs was calculated as 236.8 ± 20.93 by converting the bacterial concentration in CFU/ml into percentage and is shown in the inset of **Fig. 7**.

3.3.2. Growth Kinetics of Bacterial Cells Treated with CuNCs. Three different concentrations (250, 500, 750 µg/ml) of CuNCs were chosen on the basis of the IC₅₀ value determined from the CFU assay. The effect of bacterial *E. coli*, DH5α, growth in absence (represented as control) and presence of different doses of nanoclusters is represented in **Fig. 8**. The growth kinetics of DH5α cells treated with CuNCs indicates that nanoclusters could inhibit the growth and reproduction of the bacterial cells. The plot of bacterial fold growth (see the Characterization Methods section) versus time clearly shows the reduction in bacterial growth in presence of CuNCs. In the left panel of **Fig. 8**, the control set shows a typical growth pattern of bacteria including lag phase (which last for ~3 h) where the bacterial cells adjust themselves to the new environment, and log phase where the bacterial cells grow exponentially.

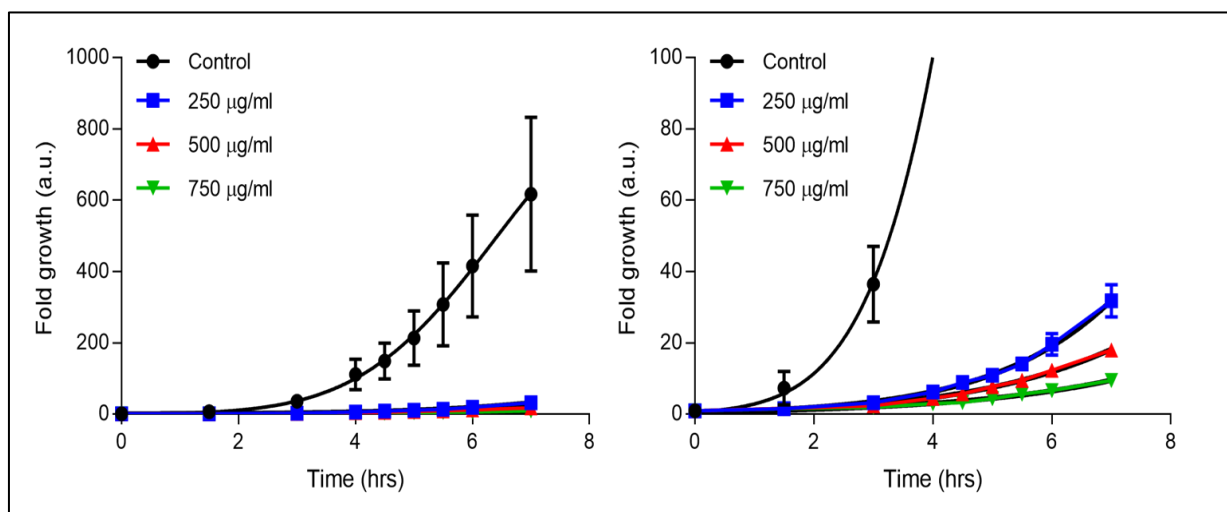


Fig. 8 The fold growth of *E. coli*, DH5α at different concentrations of CuNCs.

However, in the presence of CuNCs the lag phase of bacterial cells is increased (~4 h), and the log phase of *E. coli* is strongly inhibited. At a concentration of 250 µg/ml of nanoclusters, there is slight growth of bacterial cell with increased lag phase time. At higher concentrations (500 and 750 µg/ml) both lag phase and log phase are affected which clearly shows the bactericidal nature

of CuNCs. Hence, CuNCs at low concentration shows bacteriostatic effect, and with an increase in nanocluster concentration there is a transition of bacteriostatic to bactericidal nature of nanocluster toward *E. coli*, DH5 α , cells.

4. Conclusions

In summary, we successfully synthesized small GSH-protected CuNCs. The crude mixture shows high stability in solution under different conditions such as ambient exposure to light and heating up to 200 °C. The FTIR investigation shows cleavage of the S-H bond by the absence of the stretching vibration of the thiol group at 2560 cm⁻¹ which indicates the formation of the metal-sulfur bond. Moreover, the XPS analysis reveals the coexistence of C, O, N, S and Cu elements in CuNCs. The lack of a satellite peak at 942 eV indicates the absence of Cu²⁺ in the cluster. Hence, in general, the oxidation state of copper in the CuNCs can be assigned to be 0 and/or +1. ESI-HRMS spectra of the crude sample compared with theoretical isotopic patterns reveal several ionized species with potentially six GSH ligands (L) surrounding five to nine Cu atoms (Cu₉L₆, Cu₈L₆, Cu₇L₆, Cu₆L₆ and Cu₅L₆). Several clusters were successfully separated in PAGE, HPLC and CE-UV. Comparison with a well-defined Au₂₅(GS)₁₈ cluster in PAGE shows that several copper clusters are larger than Au₂₅. Once separated the purified clusters oxidize within hours, whereas they are stable in the crude mixture.

Future research should be directed toward finding better ligands with different coordination possibilities to avoid the oxidation of the separated clusters. A preliminary assay of antimicrobial nature of CuNCs against *E. coli*, DH5 α , cells was tested by both a colony-forming unit assay and growth kinetic of bacteria in the presence of CuNCs. Both experiments suggest a dose-dependent antimicrobial effect. At a lower concentration of nanoclusters, the growth of bacteria is reduced but when the concentration of nanoclusters is increased, growth of the bacteria is strongly restricted.

References

- (1) Hu, D.; Sheng, Z.; Fang, S.; Wang, Y.; Gao, D.; Zhang, P.; Gong, P.; Ma, Y.; Cai, L. Folate Receptor-Targeting Gold Nanoclusters as Fluorescence Enzyme Mimetic Nanoprobes for Tumor Molecular Colocalization Diagnosis. *Theranostics* **2014**, *4*, 142–153.
- (2) Stampelcoskie, K. G.; Kamat, P. V. Size-Dependent Excited State Behavior of Glutathione-Capped Gold Clusters and Their Light Harvesting Capacity. *J. Am. Chem. Soc.* **2014**, *136*, 11093–11099.
- (3) Ghosh, R.; Goswami, U.; Ghosh, S. S.; Paul, A.; Chattopadhyay, A. Synergistic Anticancer Activity of Fluorescent Copper Nanoclusters and Cisplatin Delivered through a Hydrogel Nanocarrier. *ACS Appl. Mater. Interfaces* **2015**, *7*, 209–222.
- (4) Ghosh, S.; Anand, U.; Mukherjee, S. Luminescent Silver Nanoclusters Acting as Label Free Photo Switch in Metal Ion Sensing. *Anal. Chem.* **2014**, *86*, 3188–3194.
- (5) Selvaprakash, K.; Chen, Y. C. Using Protein-Encapsulated Gold Nanoclusters as Photoluminescent Sensing Probes for Biomolecules. *Biosens. Bioelectron.* **2014**, *61*, 88–94.
- (6) Hyotanishi, M.; Isomura, Y.; Yamamoto, H.; Kawasaki, H.; Obora, Y. Surfactant-Free Synthesis of Palladium Nanoclusters for Their Use in Catalytic Cross-Coupling Reactions. *Chem. Commun. (Cambridge, U. K.)* **2011**, *47*, 5750–5752.
- (7) Zhang, B.; Kaziz, S.; Li, H.; Hevia, M. G.; Wodka, D.; Mazet, C.; Bürgi, T.; Barrabes, N. Modulation of Active Sites in Supported $\text{Au}_{38}(\text{SC}_2\text{H}_4\text{Ph})_{24}$ Cluster Catalysts: Effect of Atmosphere and Support Material. *J. Phys. Chem. C* **2015**, *119*, 11193–11199.
- (8) Jin, R.; Zeng, C.; Zhou, M.; Chen, Y. Atomically Precise Colloidal Metal Nanoclusters and Nanoparticles: Fundamentals and Opportunities. *Chem. Rev.* **2016**, *116*, 10346–10413.
- (9) Chakraborty, I.; Pradeep, T. Atomically Precise Clusters of Noble Metals: Emerging Link between Atoms and Nanoparticles. *Chem. Rev.* **2017**, *117*, 8208–8271.

- (10) Knoppe, S.; Boudon, J.; Dolamic, I.; Dass, A.; Bürgi, T. Size Exclusion Chromatography for Semipreparative Scale Separation of Au₃₈(SR)₂₄ and Au₄₀(SR)₂₄ and Larger Clusters. *Anal. Chem.* **2011**, *83*, 5056–5061.
- (11) Ghosh, A.; Hassinen, J.; Pulkkinen, P.; Tenhu, H.; Ras, R. H. A.; Pradeep, T. Simple and Efficient Separation of Atomically Precise Noble Metal Clusters. *Anal. Chem.* **2014**, *86*, 12185–12190.
- (12) Dichiarante, V.; Tirotta, I.; Catalano, L.; Terraneo, G.; Raffaini, G.; Chierotti, M. R.; Gobetto, R.; Baldelli Bombelli, F.; Metrangolo, P. Super fluorinated and NIR-Luminescent Gold Nanoclusters. *Chem. Commun.* **2017**, *53*, 621–624.
- (13) Díez, I.; Ras, R. H. a. Fluorescent Silver Nanoclusters. *Nanoscale* **2011**, *3*, 1963.
- (14) Rotaru, A.; Dutta, S.; Jentsch, E.; Gothelf, K.; Mokhir, A. Selective dsDNA-Templated Formation of Copper Nanoparticles in Solution. *Angew. Chem., Int. Ed.* **2010**, *49*, 5665–5667.
- (15) Jia, X.; Li, J.; Han, L.; Ren, J.; Yang, X.; Wang, E. DNA-Hosted Copper Nanoclusters for Fluorescent Identification of Single Nucleotide Polymorphisms. *ACS Nano* **2012**, *6*, 3311–3317.
- (16) Ling, Y.; Zhang, N.; Qu, F.; Wen, T.; Gao, Z. F.; Li, N. B.; Luo, H. Q. Fluorescent Detection of Hydrogen Peroxide and Glucose with Polyethyleneimine-Templated Cu Nanoclusters. *Spectrochim. Acta, Part A* **2014**, *118*, 315–320.
- (17) Ling, Y.; Li, J. X.; Qu, F.; Li, N. B.; Luo, H. Q. Rapid Fluorescence Assay for Sudan Dyes Using Polyethyleneimine-Coated Copper Nanoclusters. *Microchim. Acta* **2014**, *181*, 1069–1075.
- (18) Fernandez-Ujados, M.; Trapiella-Alfonso, L.; Costa-Fernández, J. M.; Pereiro, R.; Sanz-Medel, A. One-Step Aqueous Synthesis of Fluorescent Copper Nanoclusters by Direct Metal Reduction. *Nanotechnology* **2013**, *24*, 495601.
- (19) Chen, P.-C.; Li, Y.-C.; Ma, J.-Y.; Huang, J.-Y.; Chen, C.-F.; Chang, H.-T. Size-Tunable Copper Nanocluster Aggregates and Their Application in Hydrogen Sulfide Sensing on Paper-Based Devices. *Sci. Rep.* **2016**, *6*, 24882.

- (20) Ling, Y.; Wu, J. J.; Gao, Z. F.; Li, N. B.; Luo, H. Q. Enhanced Emission of Polyethyleneimine-Coated Copper Nanoclusters and Their Solvent Effect. *J. Phys. Chem. C* **2015**, *119*, 27173–27177.
- (21) Xiaoqing, L.; Ruiyi, L.; Zaijun, L.; Xiulan, S.; Zhouping, W.; Junkang, L. Fast Synthesis of Copper Nanoclusters through the Use of Hydrogen Peroxide Additive and Their Application for the Fluorescence Detection of Hg²⁺ in Water Samples. *New J. Chem.* **2015**, *39*, 5240–5248.
- (22) Ghosh, S.; Das, N. K.; Anand, U.; Mukherjee, S. Photostable Copper Nanoclusters: Compatible Forster Resonance Energy-Transfer Assays and a Nanothermometer. *J. Phys. Chem. Lett.* **2015**, *6*, 1293–1298.
- (23) Wang, C.; Wang, C.; Xu, L.; Cheng, H.; Lin, Q.; Zhang, C. Protein-Directed Synthesis of pH-Responsive Red Fluorescent Copper Nanoclusters and Their Applications in Cellular Imaging and Catalysis. *Nanoscale* **2014**, *6*, 1775–1781.
- (24) Wang, C.; Ling, L.; Yao, Y.; Song, Q. One-Step Synthesis of Fluorescent Smart Thermo-Responsive Copper Clusters: A Potential Nanothermometer in Living Cells. *Nano Res.* **2015**, *8*, 1975–1986.
- (25) Wang, C.; Huang, Y. Green Route to Prepare Biocompatible and Near Infrared Thiolate-Protected Copper Nanoclusters for Cellular Imaging. *Nano* **2013**, *8*, 1350054.
- (26) Wang, C.; Cheng, H.; Sun, Y.; Lin, Q.; Zhang, C. Rapid Sonochemical Synthesis of Luminescent and Paramagnetic Copper Nanoclusters for Bimodal Bioimaging. *ChemNanoMat* **2015**, *1*, 27–31.
- (27) Zhou, T.; Xu, W.; Yao, Q.; Zhao, T.; Chen, X. Highly Fluorescent Copper Nanoclusters as a Probe for the Determination of pH. *Methods Appl. Fluoresc.* **2015**, *3*, 44002.
- (28) Huang, H.; Li, H.; Wang, A.-J.; Zhong, S.-X.; Fang, K.-M.; Feng, J.-J. Green Synthesis of Peptide-Templated Fluorescent Copper Nanoclusters for Temperature Sensing and Cellular Imaging. *Analyst* **2014**, *139*, 6536–6541.

- (29) Das, N. K.; Ghosh, S.; Priya, A.; Datta, S.; Mukherjee, S. Luminescent Copper Nanoclusters as a Specific Cell-Imaging Probe and a Selective Metal Ion Sensor. *J. Phys. Chem. C* **2015**, *119*, 24657–24664.
- (30) Yang, X.; Feng, Y.; Zhu, S.; Luo, Y.; Zhuo, Y.; Dou, Y. One-Step Synthesis and Applications of Fluorescent Cu Nanoclusters Stabilized by L-Cysteine in Aqueous Solution. *Anal. Chim. Acta* **2014**, *847*, 49–54.
- (31) Yuan, X.; Luo, Z.; Zhang, Q.; Zhang, X.; Zheng, Y.; Lee, J. Y.; Xie, J. Synthesis of Highly Fluorescent Metal (Ag, Au, Pt, and Cu) Nanoclusters by Electrostatically Induced Reversible Phase Transfer. *ACS Nano* **2011**, *5*, 8800–8808.
- (32) Li, D.; Chen, Z.; Wan, Z.; Yang, T.; Wang, H.; Mei, X. One-Pot Development of Water-Soluble Copper Nanoclusters with Red Emission and Aggregation Induced Fluorescence Enhancement. *RSC Adv.* **2016**, *6*, 34090–34095.
- (33) Salorinne, K.; Chen, X.; Troff, R. W.; Nissinen, M.; Hakkinen, H. One-Pot Synthesis and Characterization of Subnanometre-Size Benzotriazolate Protected Copper Clusters. *Nanoscale* **2012**, *4*, 4095.
- (34) Ganguly, A.; Chakraborty, I.; Udayabhaskararao, T.; Pradeep, T. A Copper Cluster Protected with Phenylethanethiol. *J. Nanopart. Res.* **2013**, *15*, 1522.
- (35) Wei, W.; Lu, Y.; Chen, W.; Chen, S. One-Pot Synthesis, Photoluminescence, and Electrocatalytic Properties of Subnanometer Sized Copper Clusters. *J. Am. Chem. Soc.* **2011**, *133*, 2060–2063.
- (36) Gao, X.; He, S.; Zhang, C.; Du, C.; Chen, X.; Xing, W.; Chen, S.; Clayborne, A.; Chen, W. Single Crystal Sub-Nanometer Sized $\text{Cu}_6(\text{SR})_6$ Clusters: Structure, Photophysical Properties, and Electrochemical Sensing. *Adv. Sci.* **2016**, *3*, 1600126.
- (37) Nguyen, T.-A. D.; Cook, A. W.; Wu, G.; Hayton, T. W. Subnanometer-Sized Copper Clusters: A Critical Re-Evaluation of the Synthesis and Characterization of $\text{Cu}_8(\text{MPP})_4$ (HMPP = 2-Mercapto-5-N-Propylpyrimidine). *Inorg. Chem.* **2017**, *56*, 8390–8396.

- (38) Zhao, M.; Feng, H.; Zhang, X.; Ao, H.; Qian, Z. Bonding-Induced Emission of Silyl-Protected Copper Nanoclusters for Luminescence Turn-on Detection of Trace Water in Organic Solvents. *Analyst* **2017**, *142*, 4613–4617.
- (39) Rouster, P.; Pavlovic, M.; Szilagyi, I. Destabilization of Titania Nanosheet Suspensions by Inorganic Salts: Hofmeister Series and Schulze-Hardy Rule. *J. Phys. Chem. B* **2017**, *121*, 6749–6758.
- (40) Brouwer, A. M. Standards for Photoluminescence Quantum Yield Measurements in Solution (IUPAC Technical Report). *Pure Appl. Chem.* **2011**, *83*, 2213–2228.
- (41) Roy, S.; Basak, S.; Ray, P.; Dasgupta, A. K. Double Plasmonic Profile of Tryptophan-Silver Nano-Crystals - Temperature Sensing and Laser Induced Antimicrobial Activity. *Photonics Nanostructures - Fundam. Appl.* **2012**, *10*, 506–515.
- (42) Acharya, D.; Singha, K. M.; Pandey, P.; Mohanta, B.; Rajkumari, J.; Singha, L. P. Shape Dependent Physical Mutilation and Lethal Effects of Silver Nanoparticles on Bacteria. *Sci. Rep.* **2018**, *8*, 1–11.
- (43) Millis, K. K.; Weaver, K. H.; Rabenstein, D. L. Oxidation/ reduction Potential of Glutathione. *J. Org. Chem.* **1993**, *58*, 4144– 4146.
- (44) Jia, X.; Yang, X.; Li, J.; Li, D.; Wang, E. Stable Cu Nanoclusters: From an Aggregation-Induced Emission Mechanism to Biosensing and Catalytic Applications. *Chem. Commun.* **2014**, *50*, 237–239.
- (45) Cui, M.; Song, G.; Wang, C.; Song, Q. Synthesis of Cysteine Functionalized Water-Soluble Luminescent Copper Nanoclusters and Their Application to the Determination of chromium (VI). *Microchim. Acta* **2015**, *182*, 1371–1377.
- (46) Wang, C.; Cheng, H.; Huang, Y.; Xu, Z.; Lin, H.; Zhang, C. Facile Sonochemical Synthesis of pH-Responsive Copper Nanoclusters for Selective and Sensitive Detection of Pb²⁺ in Living Cells. *Analyst* **2015**, *140*, 5634–5639.

- (47) Shen, J.-S.; Chen, Y.-L.; Wang, Q.-P.; Yu, T.; Huang, X.-Y.; Yang, Y.; Zhang, H.-W. In Situ Synthesis of Red Emissive Copper Nanoclusters in Supramolecular Hydrogels. *J. Mater. Chem. C* **2013**, *1*, 2092–2096.
- (48) Hermann, H. L.; Boche, G.; Schwerdtfeger, P. Metallophilic Interactions in Closed-Shell copper(I) Compounds—a Theoretical Study. *Chem. - Eur. J.* **2001**, *7*, 5333–5342.
- (49) Vazquez-Vázquez, C.; Barñobre-Lopez, M.; Mitra, A.; López-Quintela, M. A.; Rivas, J. Synthesis of Small Atomic Copper Clusters in Microemulsions. *Langmuir* **2009**, *25*, 8208–8216.
- (50) Pedersen, D. B.; Wang, S. Surface Plasmon Resonance Spectra of 2.8 ± 0.5 nm Diameter Copper Nanoparticles in Both Near and Far Fields. *J. Phys. Chem. C* **2007**, *111*, 17493–17499.
- (51) Chan, G. H.; Zhao, J.; Hicks, E. M.; Schatz, G. C.; Van Duyne, R. P. Plasmonic Properties of Copper Nanoparticles Fabricated by Nanosphere Lithography. *Nano Lett.* **2007**, *7*, 1947–1952.
- (52) Bieri, M.; Bürgi, T. Adsorption Kinetics of L-Glutathione on Gold and Structural Changes during Self-Assembly: An in-situ ATR-IR and QCM Study. *Phys. Chem. Chem. Phys.* **2006**, *8*, 513–520.
- (53) Jia, X.; Li, J.; Wang, E. Cu Nanoclusters with Aggregation Induced Emission Enhancement. *Small* **2013**, *9*, 3873–3879.
- (54) Li, Z.; Guo, S.; Lu, C. A Highly Selective Fluorescent Probe for Sulfide Ions Based on Aggregation of Cu Nanocluster Induced Emission Enhancement. *Analyst* **2015**, *140*, 2719–2725.
- (55) Muller, C. I.; Lambert, C. Electrochemical and Optical Characterization of Triarylamine Functionalized Gold Nanoparticles. *Langmuir* **2011**, *27*, 5029–5039.
- (56) Levi-Kalisman, Y.; Jadzinsky, P. D.; Kalisman, N.; Tsunoyama, H.; Tsukuda, T.; Bushnell, D. A.; Kornberg, R. D. Synthesis and Characterization of $\text{Au}_{102}(\text{P-MBA})_{44}$ Nanoparticles. *J. Am. Chem. Soc.* **2011**, *133*, 2976–2982.
- (57) Farrag, M.; Thamer, M.; Tschurl, M.; Bürgi, T.; Heiz, U. Preparation and Spectroscopic Properties of Monolayer-Protected Silver Nanoclusters. *J. Phys. Chem. C* **2012**, *116*, 8034–8043.

(58) Nguyen, L. M.; Dellinger, M. E.; Lee, J. T.; Quinlan, R. A.; Rheingold, A. L.; Pike, R. D. Convenient Synthesis of Copper (I) Thiolates and Related Compounds. *Inorg. Chim. Acta* **2005**, *358*, 1331–1336.

(59) Yam, V. W. W.; Lam, C. H.; Fung, K. M.; Cheung, K. K. Syntheses, Photophysics, and Photochemistry of Trinuclear copper(I) Thiolate and Hexanuclear copper(I) Selenolate Complexes: X-Ray Crystal Structures of $[\text{Cu}_6(\mu_3\text{-dppm})_4(\mu_3\text{-SePh})_4](\text{BF}_4)_2$ and $[\text{Cu}_6\{\mu\text{-(Ph}_2\text{P)}_2\text{NH}\}_4(\mu_3\text{-SePh})_4](\text{BF}_4)_2$. *Inorg. Chem.* **2001**, *40*, 3435–3442.

(60) Xu, H.; Yip, J. H. K. Novel Luminescent Tetranuclear and Pentanuclear copper(I)-Dithiolates. *Inorg. Chem.* **2003**, *42*, 4492–4494.

(61) Leung, W.-P.; Chan, Y.-C.; Mak, T. C. W. Synthesis and Characterization of an Octanuclear Copper(i) Methanediide Cluster. *Dalt. Trans.* **2013**, *43*, 63–66.

(62) Ford, P. C.; Vogler, A. Photochemical and Photophysical Properties of Tetranuclear and Hexanuclear Clusters of Metals with d10 and s2 Electronic Configurations. *Acc. Chem. Res.* **1993**, *26*, 220–226.

(63) Yuan, X.; Zhang, B.; Luo, Z.; Yao, Q.; Leong, D. T.; Yan, N.; Xie, J. Balancing the Rate of Cluster Growth and Etching for Gram Scale Synthesis of Thiolate-Protected Au₂₅ nanoclusters with Atomic Precision. *Angew. Chem., Int. Ed.* **2014**, *53*, 4623–4627.

(64) Frenz, J.; Hancock, W. S. High Performance Capillary Electrophoresis. *Trends Biotechnol.* **1991**, *9*, 243–250.

Supporting Information

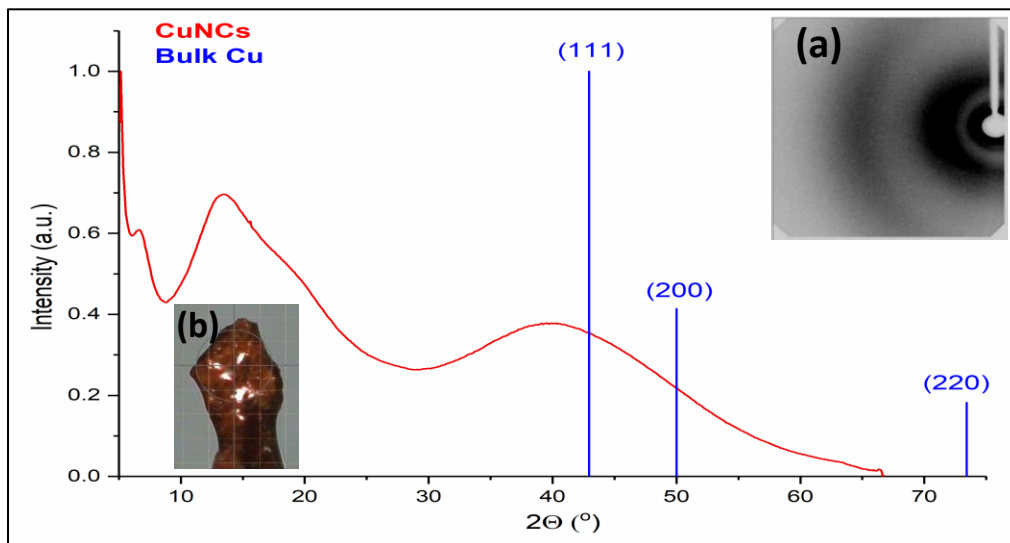


Fig. S1 Powder diagram of the crude CuNCs (normalized to [0,1] of Intensity). The sample was crushed and put on a Kapton mitogen cryoloop using a bit of fumbling oil (insert b). Typical image from the Atlas CCD detector is shown in insert (a).

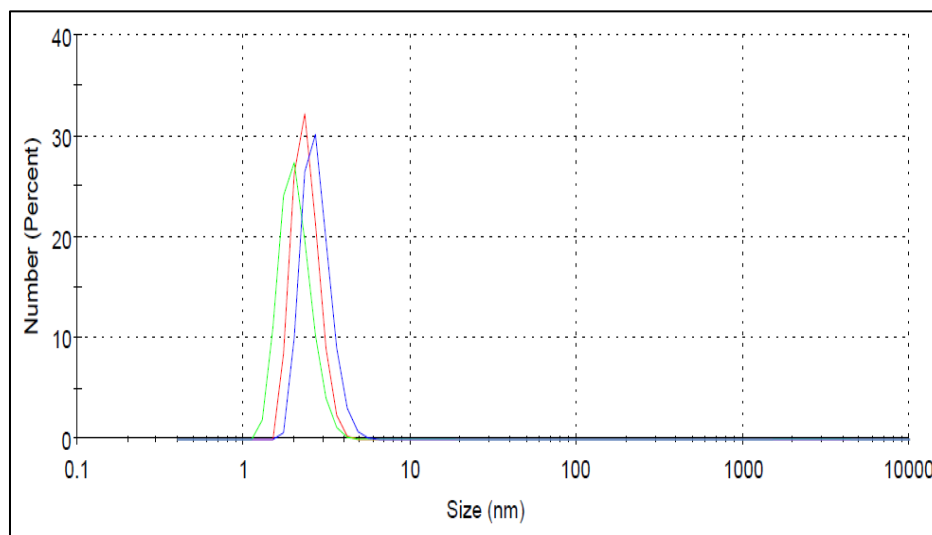


Fig. S2 Size distribution analysis by dynamic light scattering (DLS) (the curves represent three different scans).

B. EXPERIMENTAL PART

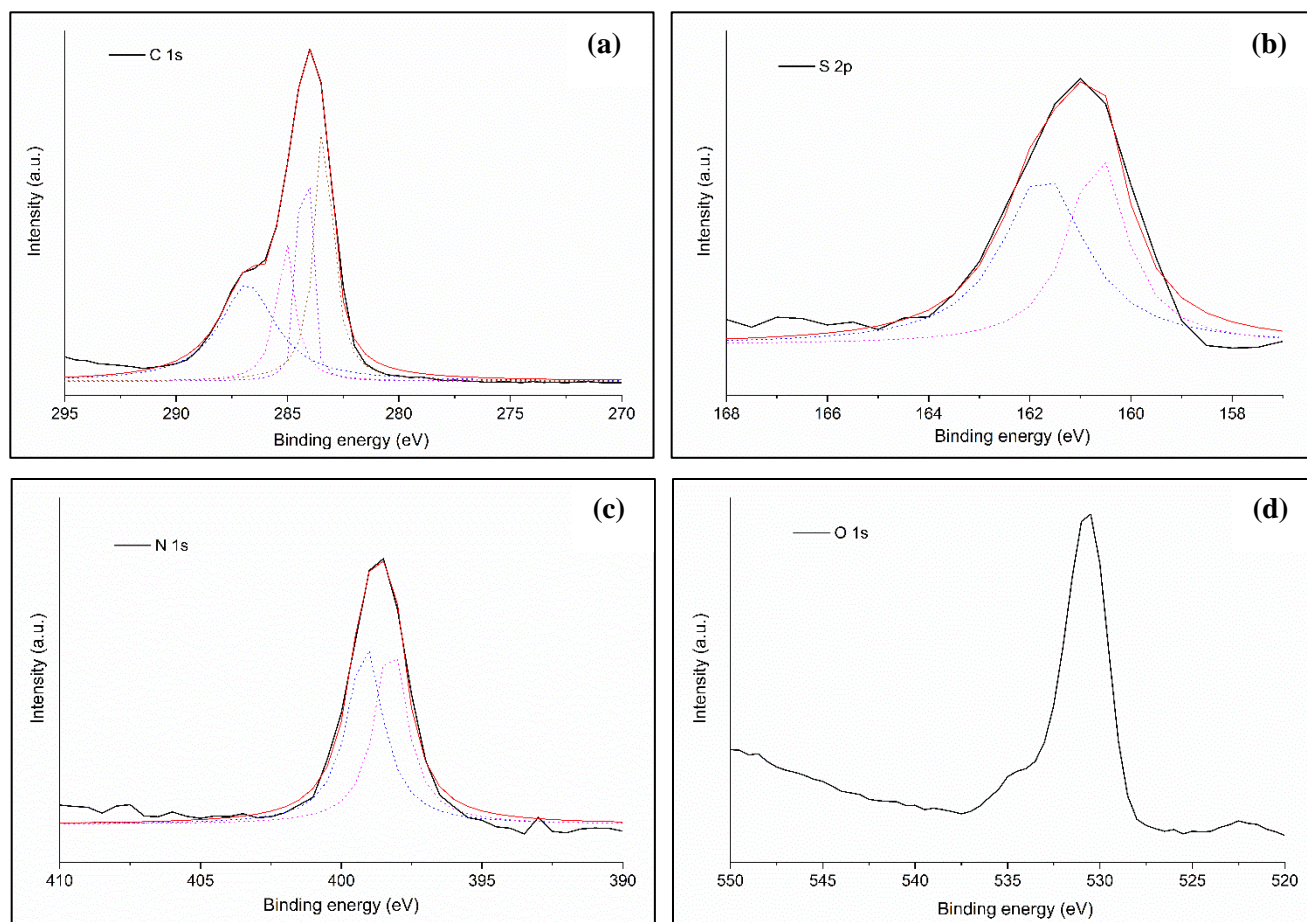


Fig. S3 Typical XPS spectra of (a) C 1s, (b) S 2p, (c) N 1s and (d) O 1s in the crude CuNCs.

B. EXPERIMENTAL PART

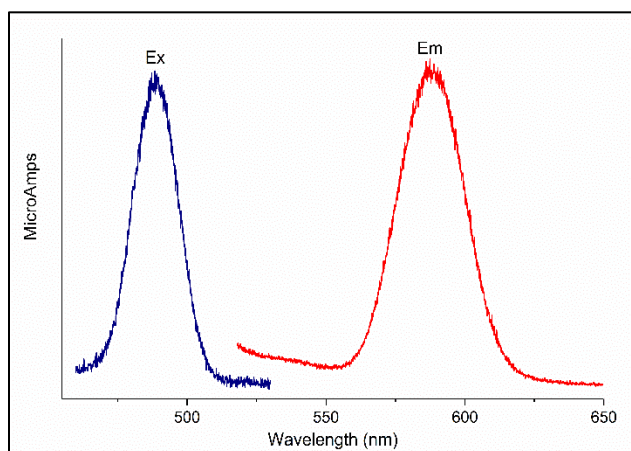


Fig. S4 Excitation (Ex) and emission (Em) spectra of the resultant CuNCs.

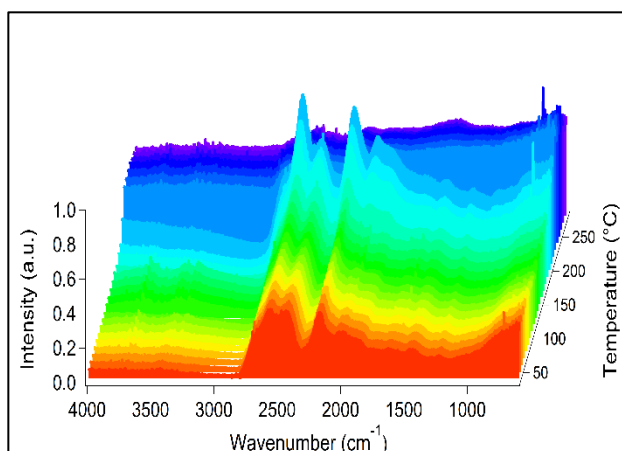


Fig. S5 Temperature dependent FTIR spectra of crude CuNCs.

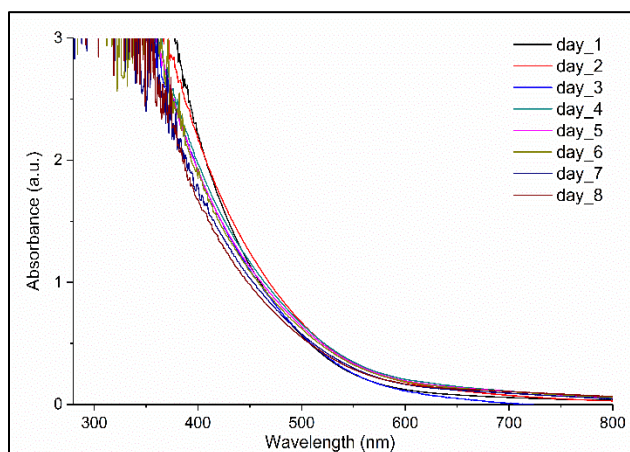


Fig. S6 Time dependent UV-vis spectra of the crude CuNCs.

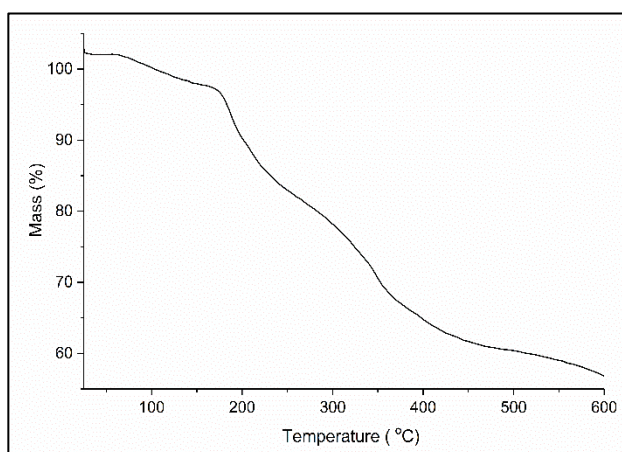


Fig. S7 TGA curve of the crude CuNCs, heating rate of 10 °C/min.

B. EXPERIMENTAL PART

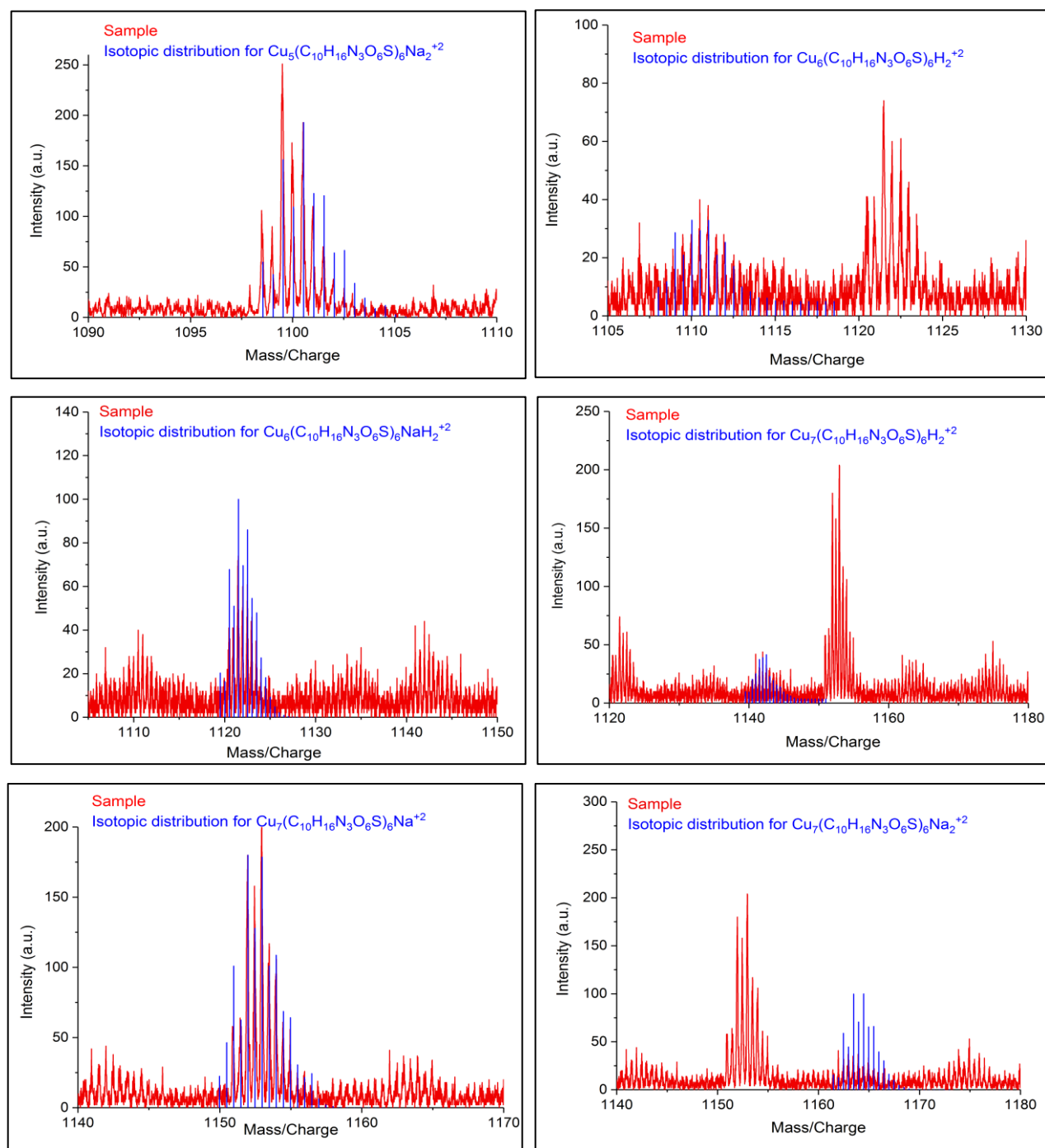


Fig. S8 ESI-HRMS isotopic pattern (blue) fitting with experimental spectra (red) (continued).

B. EXPERIMENTAL PART

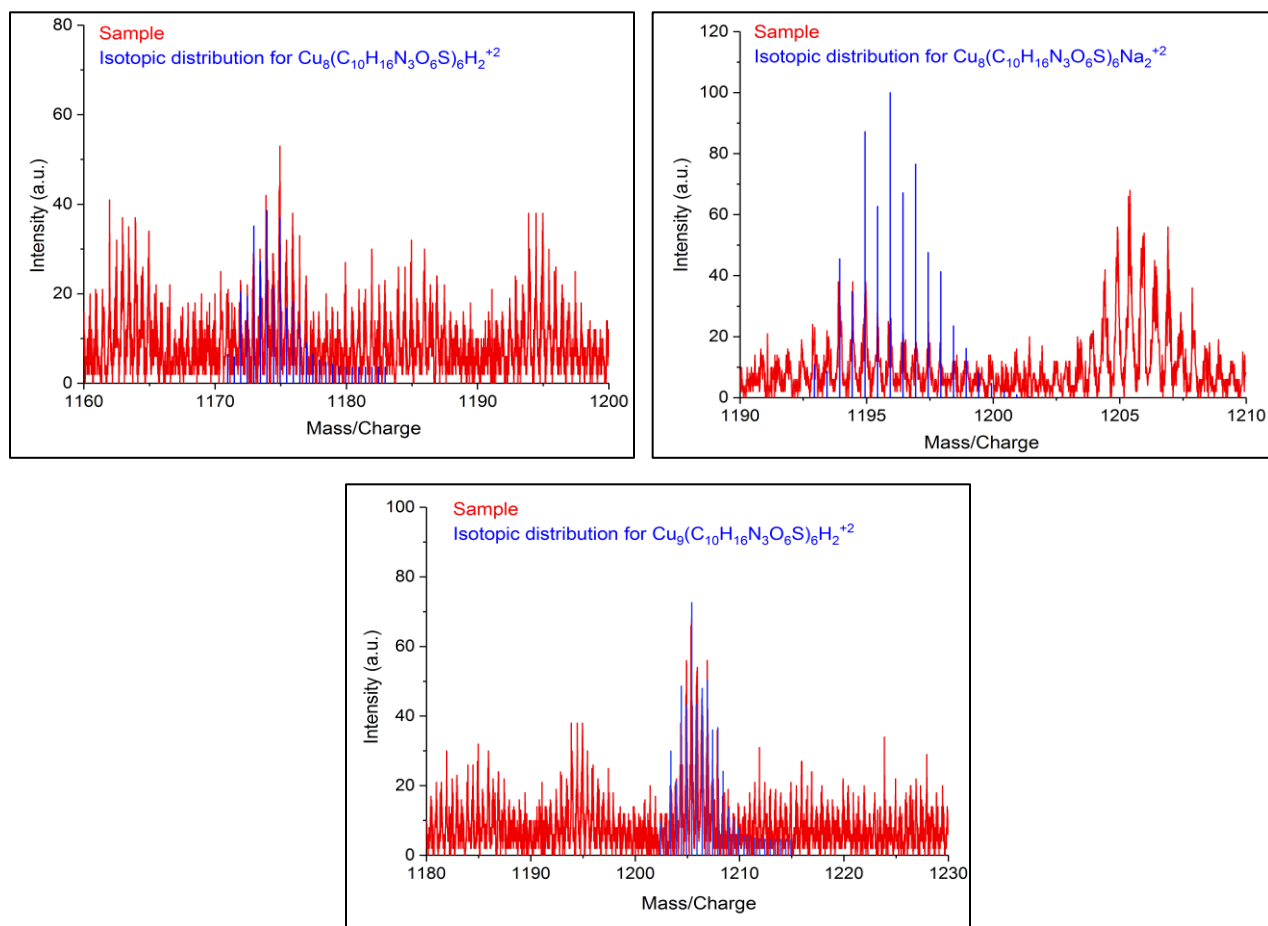


Fig. S8 ESI-HRMS isotopic pattern (blue) fitting with experimental spectra (red).

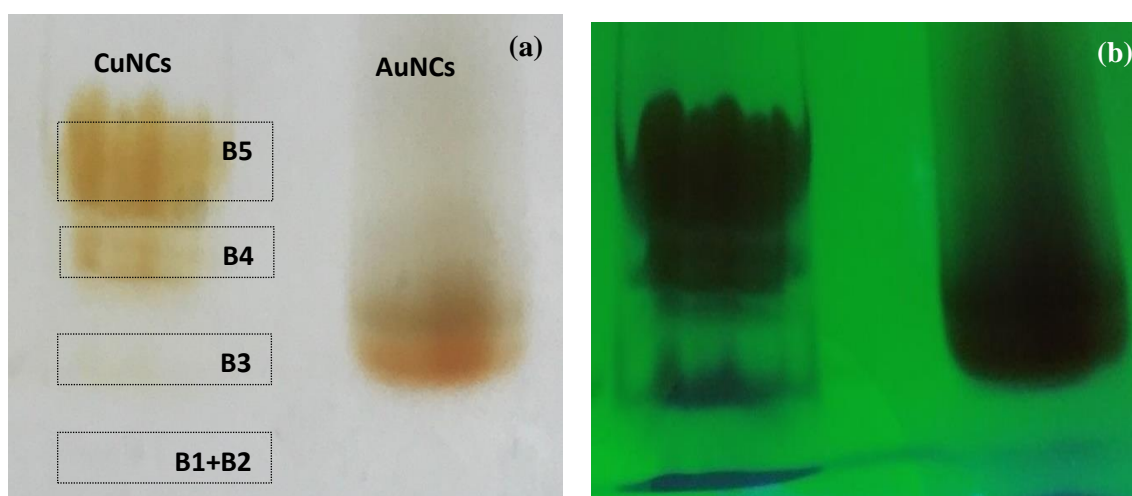


Fig. S9 PAGE separation of CuNCs and AuNCs (both protected with GSH): (a) under normal light and (b) UV-vis irradiation.

B. EXPERIMENTAL PART**Table S1** CE experimental conditions.

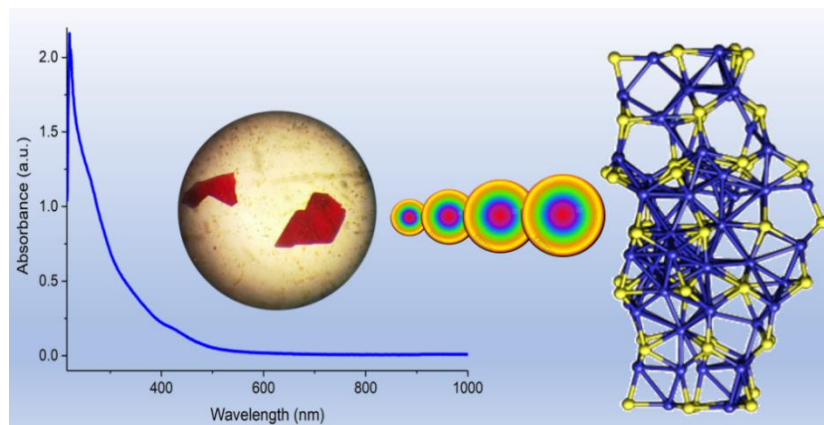
Basic conditioning		
Sequence	Duration	Tension
1bar x 5min MeOH / 1bar x 5min H ₂ O / 1bar x 5min HCl 1M / 1bar x 5min H ₂ O / 1bar x 5min NaOH 1M / 1bar x 5min BGE	30 min	30 kV

Table S2 Gradient mode conditions for HPLC separation.

Retention time (min)	Composition (%)	
	A	B
0.50	100	0.0
1.00	98.0	2.0
1.50	96.0	4.0
2.00	94.0	6.0
2.50	92.0	8.0
3.00	90.0	10.0
3.50	88.0	12.0
4.00	86.0	14.0
4.50	84.0	16.0
5.00	82.0	18.0
5.50	80.0	20.0
6.00	78.0	22.0
6.50	76.0	24.0
7.00	74.0	26.0
7.50	72.0	28.0
8.00	70.0	30.0
8.50	65.0	35.0
9.00	60.0	40.0
9.50	55.0	45.0
10.00	50.0	50.0
26.00	100.0	0.0
40.00	100.0	0.0

6.2. Thiolato protected copper sulfide cluster with the tentative composition $\text{Cu}_{74}\text{S}_{15}(\text{2-PET})_{45}$

Ligand protected copper nanoclusters with precise compositions have attracted considerable attention due to their unique photoluminescent properties. However, the acquisition of structural information,



knowledge of the factors affecting the stability, and high quantum yields are prerequisites for assessing their applications in biomedicine as fluorescent contrast agents, biosensors, and probes for cells. Despite all the effort, only finite examples of single crystal structures of CuNCs are reported. Herein, we report the phosphine-free synthesis and structure determination of 2-PET protected CuNCs. The structure analysis established by single crystal X-ray diffraction reveals the formation of binary $\text{Cu}_{74}\text{S}_{15}(\text{2-PET})_{45}$ sulfide cluster. A similar phenomenon has been observed for several other chalcogenide-bridged copper clusters. The synthesized cluster possesses a rod-like structure, protected with 45 thiol ligands on the surface. Fifteen independent bridged-sulfur atoms couple to the copper atoms inside the core. Calculations for both a neutral and negatively charged cluster showed no major differences in their geometrical structures. Further analysis of frontier MO levels of the closed-shell anion predicts the HOMO-LUMO transition to be intramolecular $L7 \rightarrow L1$ charge transfer, where “ $L7$ and $L1$ ” abbreviations refer to the corresponding sulfur layer in the structure. For the neutral cluster, the calculated spin density is delocalized over the two moieties. On the basis of TDDFT+TB calculations, the onset of the measured absorption spectrum could be satisfactorily reproduced.

This chapter is copied from my own paper: ACS Inorg.Chem. 2020

1. Introduction

Monolayer-protected metal nanoclusters with a size comparable to the Fermi wavelength of conduction electrons have emerged as a new intriguing class of nanomaterials. The ultrasmall size regime introduces quantum confinement effects and thus, size-dependent physical and chemical properties. Furthermore, small clusters are characterized by an energy bandgap. Consequently, metal nanoclusters possessing such size-dependent properties are considered in a variety of potential applications in nanodevices, ultrasensitive and selective biosensors,^{1,2} antibacterial agents,³ as well as promising catalysts.^{4,5} Since the first report of the Brust-Schiffrin two-phase method to synthesize AuNPs,⁶ it was extensively applied for the large-scale preparation of monolayer-protected and atomically precise gold and silver nanoclusters.^{7,8} However, despite extensive research progress in the field of preparing atomically precise and ligand protected Au and Ag nanoclusters, synthesis and investigation of the size-dependent properties of copper nanoclusters are still in their infancy due to their susceptibility to oxidation. Recently, massive progress in the synthetic routes to obtain highly stable and monodisperse clusters with precise composition has successfully been achieved. Moreover, based on the modified Brust-Schiffrin synthetic procedure using various biomolecules as structural templates in biomimetic synthesis and capping ligands,⁹ copper nanoclusters (CuNCs) with the formula of Cu_mL_n were successfully synthesized. In addition, it was shown that the core size of the clusters can be varied by simply changing the amount of the reducing agent used during the synthesis.¹⁰ Furthermore, strong size-dependent photoluminescent properties have been observed among different CuNCs. Using the advanced analytical and spectroscopic characterization tools, the mechanism and the origin of unique photoluminescent and chiroptical properties of CuNCs can be inferred. Although several methods have been extensively applied for the characterization of CuNCs, single crystal diffraction analysis remains the most precise and accurate method for structural investigations. A relatively large number of AuNCs, including $Au_{25}(SR)_{18}$,¹¹ $Au_{38}(SR)_{24}$,¹² $Au_{102}(SR)_{44}$,¹³ $Au_{144}(SR)_{60}$,¹⁴ as well as bimetallic^{15,16} and mixed ligand clusters^{17,18} have been crystallized from organic and aqueous solutions. Icosahedral and cuboctahedral core structures were predominant among gold nanoclusters, indicating that these structural motifs are most

stable. Crystallization of CuNCs, which, on the other hand, are more prone to oxidation, is extremely difficult. However, despite the extensive endeavors, there is only a finite number of reported crystal structures for atomically precise CuNCs.¹⁹ Mostly tertiary phosphine, selenide, and to some extent thiol ligands or a combination of different coordinating ligands simultaneously were used as a protective ligand shell to result in various spherical and polyhedral crystal structures.²⁰ Although they had different ligands and structural skeletons, it is possible to categorize them into similar core structures considered as building blocks. For example, $[\text{Cu}_{13}\{\text{S}_2\text{CN}^n\text{Bu}_2\}_6(\text{acetylide})_4]\text{PF}_6$, $[\text{Cu}_{25}\text{H}_{22}(\text{PPh}_3)_{12}]\text{Cl}$ and $[\text{Cu}_{29}\text{Cl}_4\text{H}_{22}(\text{Ph}_2\text{phen})_{12}]\text{Cl}$ clusters consist of Cu_{13} centered-cuboctahedral and icosahedral cores respectively.^{21–23} $[\text{Cu}_{28}(\text{H})_{15}(\text{S}_2\text{CNR})_{12}]\text{PF}_6$ and $[\text{Cu}_{14}\text{H}_{12}(\text{phen})_6(\text{PPh}_3)_4][\text{Cl}]_2$ consist of tetrahedron Cu_4 core encapsulated inside the copper cage.^{24,25} Other structures having a hexacapped pseudo-rhombohedral Cu_{14} core and a trigonal-bipyramidal $[\text{Cu}_2\text{H}_5]^{3-}$ core within the interior of the structure or unique “atlas-sphere” cluster have been reported.^{20,26–33} The pioneering research in the group of Fenske and others established successful synthetic protocols for the preparation of metal chalcogenide clusters varying by size, composition and structure. Moreover, a massive interest toward the field was in fact due to the availability and possibility of synthesizing atomically precise and chalcogenide-bridged copper clusters with drastically different Cu-S/Te/Se frameworks. For example, Fenske et al. have succeeded in preparation and crystallization of several sulfur-bridged copper clusters including $[\text{Cu}_{12}\text{S}_6(\text{P}^n\text{Pr}_3)_8]$ and $[\text{Cu}_{20}\text{S}_{10}(\text{P}^n\text{Bu}^t\text{Bu}_2)_8]$,³⁴ $[\text{Cu}_{24}\text{S}_{12}(\text{PMeiPr}_2)_{12}]$ and $[\text{Cu}_{50}\text{S}_{25}(\text{PtBu}_2\text{Me})_{16}]$,³⁵ $[\text{Cu}_{52}\text{S}_{12}(\text{SCH}_2\text{C}_6\text{H}_4^t\text{Bu})_{28}(\text{PPh}_3)_8]$ ³⁰ and rather bulky $[\text{Cu}_{136}\text{S}_{56}(\text{SCH}_2\text{C}_4\text{H}_3\text{O})_{24}(\text{dpppt})_{10}]$ ²⁹ clusters. Recently, a series of new copper chalcogenide clusters, e.g. $[\text{Cu}_{12}\text{S}_6(\text{dpppt})_4]$, $[\text{Cu}_{12}\text{Se}_6(\text{dppo})_4]$, $[\text{Cu}_{12}\text{S}_6(\text{dppf})_4]$, $[\text{Cu}_{12}\text{S}_6(\text{PPh}_2\text{Et})_8]$, $[\text{Cu}_{12}\text{S}_6(\text{PEt}_3)_8]$, $[\text{Cu}_{24}\text{S}_{12}(\text{PEt}_2\text{Ph})_{12}]$, $[\text{Cu}_{20}\text{S}_{10}(\text{PPh}_3)_8]$ and $[\text{Cu}_{20}\text{S}_{10}(\text{P}^t\text{Bu}_3)_8]$ have been reported to show bright red photoluminescent properties with high QY.^{36,37} Although we have mentioned several examples of relatively big copper clusters, a number of small clusters have also been reported in the literature.^{38–40} In general, the synthesis of the clusters involves the complexation of phosphine ligand derivatives with copper salts and leads to the formation of reactive species. The latter is further etched to air- and moisture-stable copper clusters in the presence of silylated derivatives of chalcogenides. However, depending on the applied reaction conditions (inert atmosphere,

temperatures below 0 °C or RT, the molar ratio of the starting materials, the reaction duration as well as the nature of the organic solvent), the final products can be drastically varied by their size, composition, and crystal structure.²⁰ In fact, for polyhydrido copper clusters that can be considered as novel hydrogen storage materials, the incorporation of hydrogen atoms inside the metallic framework can be achieved by using sodium borohydride during the initial synthesis procedure.^{26,28} The variations in starting reaction conditions and the equivalent of the reducing agent used directly controls the yield, the structure, and number of incorporated hydrogen atoms inside the ligated cluster.²⁷ To date, in all the reported crystal structures the copper atoms are in mostly a mixed valence state (+1 oxidation state is dominant in the reported structures), and only recently Hayton et al. succeeded in preparing a Cu₂₅ cluster with partial Cu(0) character.²² The structure resembles well that of the magic-size Au₂₅ cluster. Partial Cu(0) character is localized within the Cu₁₃ icosahedral core, which is further protected with phosphine ligands. Recently, Mak et al. prepared a Cu₁₄ cluster from the reduction of copper (II) trifluoroacetate in the presence of 1,2-dithiol-o-carborane ligand. Interestingly, the cluster possesses partial Cu(0) character, and it was the only reported copper cluster that has a completely analogous crystal structure to that of Ag₁₄.⁴¹ Previously, Pradeep et al. have synthesized a Cu₃₈(2-PET)₂₅ cluster.⁴² The composition of the formed cluster has been proposed based on the MALDI mass spectrum and the comparison with the calculated isotopic pattern. No crystal structure has been reported due to the low stability and immediate decomposition of the cluster within a few hours at room temperature.

Considering all the technical and strategic challenges that one can face and our expertise in the field of monolayer-protected metal nanoclusters, we proposed a simple synthetic procedure for preparing copper-sulfur nanoclusters protected with 2-phenylethanethiol ligand (2-PET, shortly). Moreover, the dark reddish brown crystals (crystallized from the saturated solution within 2 weeks) gave diffraction data which were further used for the structure analysis.

Experimental and Computational Details

2.1. Materials. The following chemicals were used as received: copper nitrate (II) trihydrate (Acros Organic, 99%, for analysis), 2-phenylethanethiol (Sigma-Aldrich-Fluka, 99+%), triethylamine (Acros Organic, 99.7%, extra pure) and acetonitrile (Fisher, analytical grade).

2.2. Synthesis of copper clusters. A total of 100 mg of $\text{Cu}(\text{NO}_3)_2 \cdot 3\text{H}_2\text{O}$ (~ 0.42 mmol) were placed in a round-bottom flask connected to a vacuum pump. Then, the flask was filled with N_2 gas, and the following reaction steps were carried out in an inert atmosphere using the Schlenk-line technique. Six milliliters of acetonitrile were added to dissolve the salt. A total of 200 μL (~ 1.5 mmol) of 2-phenylethanethiol (2-PET) was added under vigorous stirring, which resulted in the formation of white-yellowish copper-thiolate supramolecular gel. To promote the complete reduction of copper ions in solution, 200 μL (~ 1.43 mmol) of triethylamine (TEA) as a base was added dropwise until the solution changed color to clear yellowish orange. The reaction mixture was allowed to stir for 3 h. The as-prepared clusters were precipitated in MeOH by centrifugation (Sigma 3-18 K, 11 400 rpm, 14 239 RCF, 4 °C). After precipitation, the crude sample was washed with methanol several times to remove all unreacted precursors and salts. After the purification, the precipitate (53 mg) was then freeze-dried and kept in the fridge for further use.

The crystallization of the sample was done under ambient conditions from the reaction solution before precipitation. The flask with a loosely closed cap was left on the bench, and after about 2 weeks, dark reddish orange crystals were grown from the saturated solution. The crystals were separated by decanting them from the mother liquor. The isolated yield of collected crystals was approximately 34%.

The X-ray powder diffraction pattern of both the yellowish orange precipitate and the isolated crystals is given in **Fig. S1** for comparison. As anticipated, the precipitate is a mixture of different compounds from which reddish orange crystals can be grown.

2.3. Characterization methods. For single crystal analysis, fresh crystals directly from the mother liquor were isolated and were immediately mounted on a kapton loop with protection oil under a cold nitrogen stream. Cell dimensions and intensities were measured at 140 K on an Agilent

Supernova diffractometer with Cu K α ($\lambda = 1.54184\text{\AA}$) radiation equipped with an Atlas CCD camera. The structure was solved by dual space methods (SHELXT),⁴³ and refined using full-matrix least squares in SHELXL,⁴⁴ within the OLEX2 programs.⁴⁵ The ligands were ill-defined so that numerous restraints/constraints were used. Some parts of the core are disordered. More details on the refinement strategy can be found in the **Supporting Information**.

The X-ray powder diffraction pattern was measured in capillary mode using Cu K α 1 radiation on an Empyrean (PANalytical) diffractometer equipped with a focusing X-ray mirror and a PIXcel3D area detector.

Density functional theory (DFT)^{46,47} has been applied for the characterization of the geometry and electronic structure of the $[\text{Cu}_{74}\text{S}_{15}(\text{S}(\text{CH}_2)_2\text{Ph})_{45}]$ cluster. To make the calculations tractable but still meaningful, and also because we are mainly interested in the characterization of the core and its immediate coordination sphere provided by the ligands, we have replaced the $\text{Ph}(\text{CH}_2)_2\text{S}$ -ligands by CH_3S - groups, and only the major component of the disordered part was considered. The calculations have thus been performed on the model system $[\text{Cu}_{74}\text{S}_{15}(\text{SCH}_3)_{45}]$ (**1**). The system is expected to be negatively charged (**1**⁻) because of the lack of almost one Cu(I) ion. No counterion could be identified in the X-ray structure, and 74 copper atoms were identified in the structure. Hence, for our calculations and for the sake of completeness, we considered the model cluster both in its anionic (**1**⁻) and in its radical (**1**[•]) form. The geometries of (**1**⁻) and (**1**[•]) have been optimized with the ADF program package,^{48–50} using the PBE functional⁵¹ combined with Slater-type (STO) basis set from the ADF basis set database.⁵² The Cu atoms were thus described with a TZP basis set of triple- ζ polarized quality and the other atoms by a DZP basis set of double- ζ polarized quality. The atomic core levels were kept frozen up to the 2p level for the Cu atoms, and up to the 1s level for the S and C atoms. The same initial geometry was used for the optimization of the geometries of the anion and the radical: the positions of the heavy atoms in this initial structure correspond to the ones of highest occupancies in the X-ray structure. The calculations were run spin-restricted and spin-unrestricted for (**1**⁻) and (**1**[•]), respectively. Scalar relativistic (SR) effects were included within the zero-order regular approximation (ZORA).^{53,54} Vibrational analyses could not be performed on the optimized geometries because of their prohibitive computational cost. For the electronic excitation calculations, the low-energy part of

the absorption spectrum of the anion has been analyzed by computing with the PBE functional the energies and oscillator strengths of its 50 lowest-lying dipole-allowed electronic excitations within linear response theory in time-dependent DFT (TDDFT) as implemented in ADF.^{55,56} To make the TDDFT calculations tractable, we only included the lowest 400 single-orbital transitions (SOTs). In addition, the 1500 lowest-lying dipole-allowed transitions of the anion have been characterized within the tight-binding approximation to TDDFT (TDDFT-TB).⁵⁷ The TDDFT-TB calculations were based on the results of the PBE ground state calculations. Scalar-relativistic effects were included in all electronic calculations.

The UV-vis spectrum of the dissolved crystal in dichloromethane was recorded on a Varian Cary 5000 spectrophotometer, using a quartz cuvette of 2 mm path length.

The room temperature excitation and luminescence spectra of the single crystals were recorded on a Fluorolog 3-22 (Horiba Jobin Yvon), equipped with a water-cooled photo multiplier tube (PMT). For the quantum yield measurement, an integrated sphere method was used (details are given in the **Supporting Information**). For that, the sample dispersed in methylene chloride was evaporated drop by drop on a Teflon sample holder in order to get a homogenous layer.

NMR spectra were recorded on a Bruker Avance 400 MHz spectrometer. ¹H and ¹³C NMR chemical shifts are given in parts per million relative to SiMe₄, with the solvent (methylene chloride-*d*₂, CD₂Cl₂, δ 5.32) resonance used as an internal reference. Both spectra were measured at 298 K.

The Fourier transform infrared (FT-IR) spectrum was measured on a Bruker Equinox 55 FTIR spectrometer equipped with a narrow-band MTC detector. The FT-IR spectrum was recorded at room temperature with a resolution of 4 cm⁻¹. A cluster solution in methylene chloride was drop cast onto a KBr support, and after solvent evaporation, the IR spectrum was recorded.

Results and Discussion

Single crystal analysis. The copper cluster with a formula of Cu₇₄S₁₅(2-PET)₄₅ was crystalized in the triclinic $P\bar{1}$ space group with two molecules incorporated inside the unit cell (**Table S1**). The derived atomic model of the ligand is rather approximative due to the difficulties in distinguishing

and refining the organic part of some of the ligand molecules. However, most of the ligands could be unambiguously located (**Table S2**). Only the copper and the sulfur atoms are considered for further discussion.

As has been shown for other copper, gold and silver clusters,^{58,59} few sulfur atoms cleaved from the ligand (S-C bond breaking) during the reaction, taking part into the metallic framework. Perhaps, the C-S bond cleavage involves the formation of the phenylethyl radical, which would couple to form 1,4-diphenyl butane. However, the exact mechanism of such reaction has not yet been explored in the literature. In our case, there are 15 of them in the structure. The bridged-sulfur atoms and the sulfur atoms belonging to the ligand differ in the number of bonds they make with the Cu atoms, the latter bonding to less Cu neighbors (**Fig. S2**). This allows for discrimination between them, even when the organic part cannot be modeled with the data at hand.

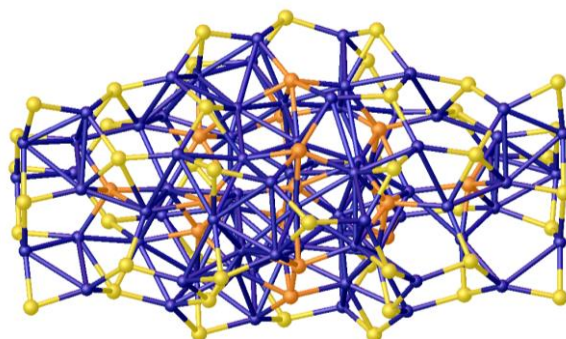


Fig. 1 Core of the cluster. Bridged-sulfur atoms are in orange, and sulfur atoms belonging to ligands are in yellow. The layers are labeled as L1 to L7 from left to right.

The formula for an uncharged complex is $\text{Cu}_{75}\text{S}_{15}(\text{SC}_8)_{45}$ (excluding solvent molecules). Only 74 Cu atoms could be found unambiguously. No counterion could be identified. However, a large hole is present in the crystal, and the electronic density in this hole was artificially removed using the SQUEEZE/BYPASS method,⁶⁰ so we cannot rule out the presence of a counterion in this hole. The presence of copper vacancies inside the lattice planes of some binary Cu(I) selenide are well-known⁶¹ and similar vacancies have also been found in copper and silver sulfide clusters.^{29,62} The

charge of the complex is therefore ambiguous. Bond valence calculations (see **Table S3**) hint at all atoms being Cu(I) so that the charge, if present, should be delocalized over the whole cluster. As it can be seen in **Fig. 1**, the synthesized cluster displays a layered rod-like structure. There are seven sulfur atoms layers, organized in an ABA fashion (see **Fig. 2**). Inside the layers, the S-S bond lengths are within the range 3.5-4.6 Å. The Cu atoms are located within and between the sulfur layers. The positions of the Cu atoms are less well-defined, with structural disorder. Cu-Cu distances range from 2.49 to 4 Å (see **Fig. S3**). Even for the shortest distances, the binding energies are expected to be relatively small^{63,64} so that the interaction with the bridging ligand will determine the geometry. Cu-S coordination is presented in **Fig. S4**. The structure can be spliced up into seven sulfur layers. As can be seen from **Fig. 1**, the cluster is slightly bent and shows near symmetry around layer 4, however, there are some differences in the number of copper atoms in the corresponding layers.

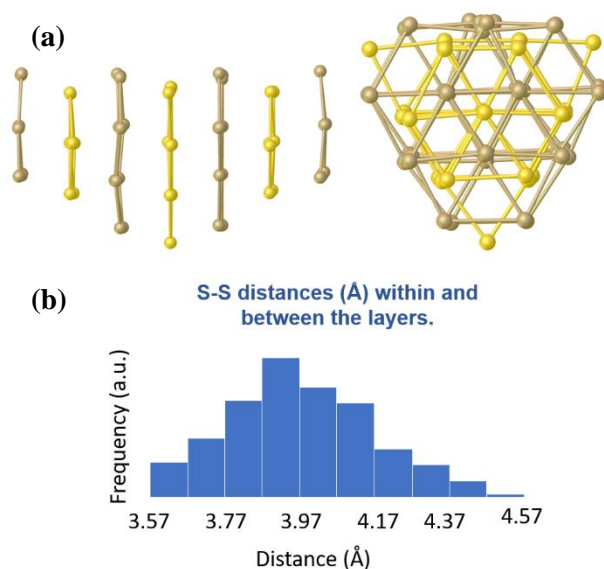


Fig. 2 (a) Side and top view of the layer organization of the sulfur atoms. Two types of layers (A in yellow, B in gold) organize themselves in an ABA pattern. (b) A histogram of the S-S distances is displayed.

On one side (layers 5,6 and 7), the geometry is less well-defined, with a group of four Cu atoms adopting two possible geometrical arrangements. A layer by layer description is given in **Table 1** and in the **Supporting Information (Fig. S5 to S10)**.

Table 1: Repartition of the Cu, free sulfur and ligands in and between the different layers.

	<i>S(ligand)</i>	<i>S(bridged)</i>	<i>Cu atoms</i>
Layer 1	6		3
			6
Layer 2	6	1	0
			10
Layer 3	9	3	3
			13
Layer 4	3	7	6
			12
Layer 5	9	3	2
			9
Layer 6	6	1	1
			6
Layer 7	6		3
Total	45	15	74

All the Cu atoms inside sulfur layers adopt a trigonal planar coordination, surrounded by three sulfur atoms at distances in the range 2.2 to 2.5 Å. The Cu atoms are sitting in the plane formed by the three neighboring sulfur atoms. Cu atoms in between the sulfur layers also preferentially adopt a trigonal planar coordination, but a few of them diverge to an almost tetrahedral coordination or bind to only two sulfur atoms (with further bonding to sulfur and Cu atoms at larger distances).

To sum up, the structure organizes itself in well-defined S layers, with large S-S distances of more than 3.5 Å. The Cu atoms place themselves in between the S atoms, maximizing the numbers of Cu atoms in trigonal planar coordination. This gives rise to different possible arrangements, producing disorder in the Cu atoms and disrupting the symmetry. Moreover a few Cu atoms in the cluster adopt a different coordination, either tetrahedral or linear.

The pioneering work of Prof. Fenske in the field of semiconducting chalcogenide bridged and ligand shielded copper nanoclusters illustrated that the cluster size influences the structure. For the majority of the reported small phosphine-protected copper clusters, a [Cu_{2n}S_n] core can be distinguished.^{34,35} Linear coordination by sulfur atoms and trigonal planar coordination are observed. Larger clusters have more flexibility in their composition, but they tend to keep an

average free chalcogenide/sulfur ratio around 0.5. Our phosphine-free cluster differs, with a much lower free sulfur content. However, its structure is closely related to the observed phosphine-protected copper chalcogenide clusters: the grid formed by the sulfur atoms (**Fig. 1 and Fig. S11**) is a common feature in chalcogenide-metal clusters,^{29,35} and the trigonal planar coordination of the metal is abundantly described.²⁰ Such core constructions and layered structures are not limited to only sulfur containing clusters but are rather common for selenide-bridge copper clusters.

4. DFT calculations: Geometries. The optimized structures of (**1**⁻) and (**1**[•]) are quite similar, and their [Cu₇₄S₁₅(SC)₄₅] skeletons remain close to the one found in the X-ray structure. For better comparison, the histograms of experimental S-S, Cu-S, and Cu-Cu bond lengths were compared with calculated ones for both neutral and charged clusters (**Fig. S12**). As one can see, the difference between measured and calculated data is negligible, and only slight variations in their density probabilities were observed. On the other hand, the absence of major structural/geometrical distortions between neutral and charged states shows that the assumption of a Cu₇₄S₁₅ core is reliable and in agreement with experimental results.

4.1. Electronic structure of (1⁻). To characterize the electronic structure of the closed-shell anion, we propose the analysis of its HOMO-1, HOMO, LUMO and LUMO+1 frontier molecular orbital (MO) levels, as obtained from the calculations with the PBE functional. The frontiers MOs and their energies are given in **Fig. 3**. The HOMO and HOMO-1 are located on the “L7” moiety of the cluster, while the LUMO and LUMO+1 are located on the “L1” moiety (“L7 and L1” abbreviations refer to the corresponding sulfur layer in the structure). The HOMO-LUMO gap amounts to 0.775 eV: it gives an estimate of the energy of the lowest-lying electronic transition, which is expected to mainly be a HOMO-LUMO transition and thus to be an intramolecular “L7” → “L1” charge transfer transition.

Finally, we have calculated the total density of states (TDOS) and the partial (gross population) density of states (PDOS).

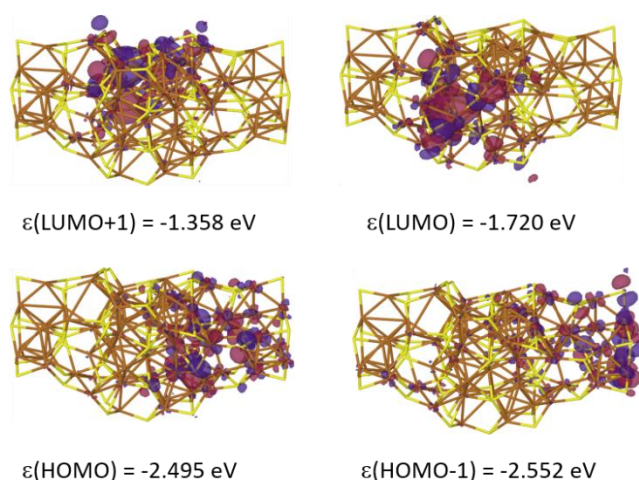


Fig. 3 Frontier MO levels of (**1**[•]) (PBE results).

They are plotted in **Figure S13** for Kohn-Sham orbital energies ϵ in the $[-8.0, -1.0]$ eV energy range: there is a high density of states, as this can be anticipated for such a large system containing 74 d^{10} Cu(I) ions. The highest occupied levels are of mainly Cu(3d) character with substantial contributions from the S(3p) levels for $-4.0 \text{ eV} < \epsilon < \epsilon(\text{HOMO}) = -2.495 \text{ eV}$. The Cu(3d) PDOS is actually peaked around -4.3 eV . The LUMO and LUMO+1 have significant contributions from the atomic Cu(3d), Cu(4s), Cu(4p), S(3p) levels (inset of **Fig. S13**).

4.2. Electronic structure of (1**[•]).** **Fig. 4** shows the calculated spin density of the neutral species: it is delocalized over the two moieties, which suggests that the slight structural change observed upon passing from the anionic to the neutral form is accompanied by a noticeable electronic rearrangement of the frontier MOs.

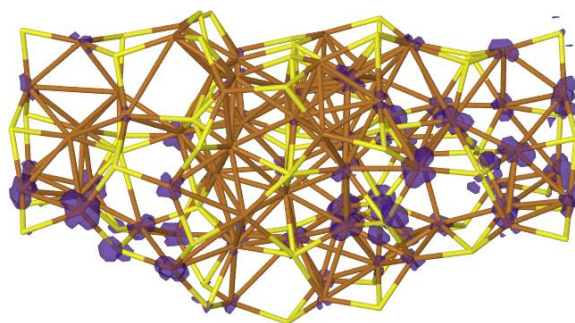


Fig. 4 Calculated spin density of (**1**[•]) (PBE results).

The frontier MO levels of (**1**[•]) are depicted in **Fig. 5**. The comparison of the frontier levels of (**1**[•]) and (**1**⁻) (**Fig. 3**) shows that the energies of the MOs are shifted towards more negative values upon the oxidation and that the spin-up and spin-down HOMOs are now mainly located on the “L1” moiety.

For the spin-up channel, the HOMO-LUMO gap amounts to 0.814 eV; while it amounts to 0.024 eV for the spin-down channel. **Fig. S14** shows for (**1**[•]) the plots of the calculated spin-up and spin-down TDOS and PDOS calculated for $-8.0 \text{ eV} < \epsilon < \epsilon(\text{HOMO}) = -2.2 \text{ eV}$. As observed for the anionic form, the highest-occupied levels originate mainly from the Cu(3d) levels with significant contributions from the S(3p) levels when approaching for $\epsilon > -4.8 \text{ eV}$.

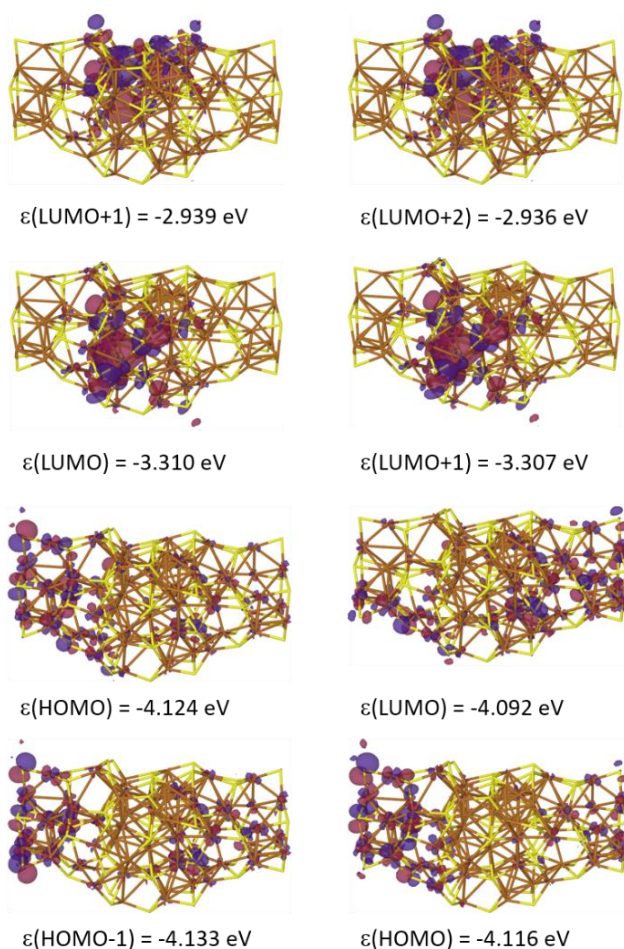


Fig. 5 Frontier MO levels of (**1**[•]) (PBE results). The spin-up and spin-down channels are presented on the left and the right panels of the picture.

Given the high density of frontier occupied levels observed for the anion and radical, their ordering and the shape of the associated MOs are likely to vary with the choice of the exchange-correlation potential and finite basis set. In the present case, for the anion, the use of the PBE GGA and model GRAC exchange-correlation potentials led to similar results. Despite this encouraging agreement, the question of the accuracy of the description achieved for the electronic structures remains open. Investigating further the influence of the chosen theoretical level is however beyond the purpose of the present study, the more so because a possibly definitive description of the electronic structures of the systems would require resorting to the more computationally costly GW method.⁶⁵

4.3. TDDFT calculations. We have characterized within TDDFT the 50 lowest-lying dipole-allowed electronic excitations of the anion. The calculations were done with the PBE functional. The calculated transition energies are in the narrow 0.8-1.4 eV range. The lowest-lying transition is dominated by the HOMO → LUMO transition (90%) and has numerous minor contributions from energetically close HOMO-N → LUMO transitions. The next four transitions are clearly identified as HOMO-N → LUMO (N=1,...,4) transitions. Higher-lying transitions exhibit a significant mixture of MO → MO transitions. The calculations were also supplemented with the results of electronic excitation calculations performed within the tight-binding approximation to TDDFT (TDDFT-TB) as implemented in ADF.⁵⁷ The 1500 lowest-lying dipole-allowed transitions of the anion could thus be characterized. A good agreement is observed between the TDDFT and TDDFT+TB results for the 50 lowest-lying transitions (**Table S4**), which makes us confident about the quality of the TDDFT+TB results. By using the TDDFT+TB results, the onset of the measured absorption spectrum could be satisfactorily reproduced (**Fig. S15**). The simulated and measured absorption spectra were compared by superimposing the $\epsilon=\epsilon(\nu)$ curves (**Fig. S15 inset**).

5. Optical properties. The UV-vis spectrum of the single crystal dissolved in methylene chloride shows distinct electronic transitions at 260, 340 and 420 nm. The lack of a characteristic plasmon band at visible wavelengths indicates that the formed binary cluster has well-defined molecule-like properties and does not support plasmon resonance features at higher wavelengths (**Fig.**

S16). However, starting from 500 nm an increase in absorbance was observed resulting in a small hump. From UV-vis, the high energy absorption at ca. 340 nm can be assigned as an intraligand (IL) $n(S) \rightarrow \pi^*$ transition.^{66–68} Additionally, the transition at 420 nm and strong absorption bellow 260 nm arises from ligand-to-metal charge transfer (LMCT).^{67–69} The calculated molar extinction coefficient at 420 nm is 31 400 L·mol⁻¹·cm⁻¹ (**Figure S16**, right y axis), which is in the range for typical LMCT transitions.

The photoluminescent properties of CuNCs were studied by collecting and accumulating the single crystals inside a capillary tube. The sample was excited at 350 nm and the emission was collected from 380 to 680 nm with an integration time of 1 s (**Fig. S17**). The excitation experiment (for the emission at 500 nm) was carried out in the range of 260–470 nm. For both excitation and emission experiments the slits were kept at 14 nm. The synthesized cluster shows dual fluorescence with emission peaks centered at $\lambda_{em}^1=430$ nm and $\lambda_{em}^2=508$ nm. Large Stokes' shifts (80 nm) were observed between second excitation (350 nm) and first emission (430 nm) peaks. Previously, similar dual-emission was mostly observed in the case of AuNCs^{70,71} and gold(I) complexes,⁷² and occasionally in CuNCs,^{73,74} where the low-energy emission was assigned to a ligand-to-metal charge transfer (LMCT). The high-energy emission was attributed to metal perturbed intraligand phosphorescence. In case of our cluster, the origin of dual emission is not yet understood.

The crystals dissolved in methylene chloride were drop cast inside the Teflon holder and allowed to air-dry. Afterwards, the QY of the homogeneous layer was measured using an integrated sphere method. The details are given in the **Supporting Information**. At room temperature, clusters do not exhibit strong fluorescence, and in fact the measured QY was found to be very small: 5.26×10^{-4} . This number is significantly smaller than the recently reported QY of Cu₁₄ cluster (QY=0.31).⁴¹ However, the number we have obtained is in good agreement with the literature, which states that copper clusters containing less than 13 copper atoms in their compositions are extremely fluorescent, whereas larger copper clusters become poorly emissive.¹⁰ Since our cluster is quite large in size, it is not very surprising to have such a small QY.

Other characterization techniques including NMR spectroscopy (^1H and ^{13}C NMR) as well as FT-IR measurements were also performed in order to analyze the chemical environments and surface properties of the cluster.

The ^1H NMR spectrum of the crystal dissolved in CD_2Cl_2 is shown in **Fig. S18a**. The integral numbers of protons are recalculated manually upon setting the number of phenyl protons to 225 according to the reported formula ($5\text{H} \times 45$ ligand). A broad envelop between 7.7 ppm and 6.2 ppm belongs to the resonances of phenyl protons, whereas the signals in higher field at the range of 4-2.5 ppm give poorly resolved peaks associated with the α - and β - CH_2 groups of the thiol ligand. Note, the positional nomenclature of methylene protons is given with respect to the sulfur atom from the ligand. The integrals of methylene groups in the ^1H NMR spectrum are calculated to be 180, which is in a good agreement with an actual number based on the formula ($4\text{H} \times 45$ ligand). However, since the cluster is very big, it tumbles very slow, and the broadening of the signals causes a significant loss of J-coupling, and thus the assignment of various binding sites or chemical environments of α - and β - CH_2 protons at this point becomes impossible. The ^{13}C NMR spectrum shows weak resonances at 140.82, 129.15, 128.99, 126.92, 40.74 and 27.08 ppm for both aryl and alkyl carbons (**Fig. S18b**). In particular, the chemical shifts at lower field are associated with *i*-C, *o*-C, *m*-C and *p*-C carbon resonances from the aromatic group, whereas the signals at 40.74 and 27.08 ppm are related to β -C and α -C from alkyl chain, respectively.

The FT-IR spectrum of the cluster was measured by drop casting the methylene chloride solution of the dissolved crystal on KBr support. After air drying, a full mid-infrared spectrum was recorded, and shortly afterward the background was subtracted from the sample spectrum (**Fig. S19**). The spectrum shows characteristic vibrational modes of aromatic region and alkane chain. Precisely, the bands above 3000 cm^{-1} (3026 - 3085 cm^{-1}) are stretching vibrations of C-H from the phenyl ring, whereas those between 2850 - 2960 cm^{-1} are characteristic for C-H stretching mode from the alkane chain. The bands between 1410 - 1494 cm^{-1} are ascribed to aromatic C-C stretching vibrations.

6. Conclusions

We have successfully synthesized a new copper nanocluster with a composition of $\text{Cu}_{74}\text{S}_{15}(\text{2-PET})_{45}$. The structure determination by single crystal X-ray crystallography revealed that the sulfur atoms both from the ligand and bridged (sulfide) forms are structured in a layered fashion. The copper atoms bond preferentially in trigonal coordination within and between these layers, giving rise to the rather elongated and bent structure. In total 45 sulfur atoms belonging to the 2-PET ligand are located on the exterior of the cluster, whereas 15 bridged-sulfur atoms construct the skeleton of the cluster with copper atoms. We have shown that the coordination environments of some sulfur and copper atoms gave vacancies similar to what has been previously reported for some Cu_2S sulfide phases. Because of that, we cannot draw a definitive conclusion about the total charge of the cluster. The predicted gas-phase geometries of the model cluster **(1)** in the anionic and neutral forms both satisfactorily agree with the experimental structure, thus suggesting that the structures of the $\text{Cu}_{74}\text{S}_{15}(\text{2-PET})_{45}$ nanocluster in the two redox states are similar. Moreover, based on TDDFT+TB calculations, the measured onset of the absorption spectrum can be satisfactorily reproduced.

References

- (1) Hu, X.; Liu, T.; Zhuang, Y.; Wang, W.; Li, Y.; Fan, W.; Huang, Y. Recent Advances in the Analytical Applications of Copper Nanoclusters. *TrAC - Trends Anal. Chem.* **2016**, *77*, 66–75.
- (2) Guo, Y.; Cao, F.; Lei, X.; Mang, L.; Cheng, S.; Song, J. Fluorescent Copper Nanoparticles: Recent Advances in Synthesis and Applications for Sensing Metal Ions. *Nanoscale* **2016**, *8* (9), 4852–4863.
- (3) Baghdasaryan, A.; Grillo, R.; Roy Bhattacharya, S.; Sharma, M.; Reginato, E.; Theraulaz, H.; Dolamic, I.; Dadras, M.; Rudaz, S.; Varesio, E.; Burgi, T. Facile Synthesis, Size-Separation, Characterization, and Antimicrobial Properties of Thiolated Copper Clusters. *ACS Appl. Nano Mater.* **2018**, *1* (8), 4258–4267.
- (4) Mathew, A.; Pradeep, T. Noble Metal Clusters: Applications in Energy, Environment, and

Biology. *Part. Part. Syst. Charact.* **2014**, *31* (10), 1017–1053.

(5) Sun, C.; Mammen, N.; Kaappa, S.; Yuan, P.; Deng, G.; Zhao, C.; Yan, J.; Malola, S.; Honkala, K.; Häkkinen, H.; et al. Atomically Precise, Thiolated Copper-Hydride Nanoclusters as Single-Site Hydrogenation Catalysts for Ketones in Mild Conditions. *ACS Nano* **2019**, *13* (5), 5975–5986.

(6) Brust, M.; Walker, M.; Bethell, D.; Schiffrin, D. J.; Whyman, R. Synthesis of Thiol-Derivatized Gold Nanoparticles in a Two-Phase Liquid–Liquid System. *J. Chem. Soc., Chem. Commun.* **1994**, No. 7, 801–802.

(7) Jin, R.; Zeng, C.; Zhou, M.; Chen, Y. Atomically Precise Colloidal Metal Nanoclusters and Nanoparticles: Fundamentals and Opportunities. *Chem. Rev.* **2016**, *116* (18), 10346–10413.

(8) Chakraborty, I.; Pradeep, T. Atomically Precise Clusters of Noble Metals: Emerging Link between Atoms and Nanoparticles. *Chem. Rev.* **2017**, *117* (12), 8208–8271.

(9) Wang, Z.; Chen, B.; Rogach, A. L. Synthesis, Optical Properties and Applications of Light-Emitting Copper Nanoclusters. *Nanoscale Horizons*. Royal Society of Chemistry 2017, pp 135–146.

(10) Vázquez-Vázquez, C.; Bañobre-López, M.; Mitra, A.; López-Quintela, M. A.; Rivas, J. Synthesis of Small Atomic Copper Clusters in Microemulsions. *Langmuir* **2009**, *25* (14), 8208–8216.

(11) Zhu, M.; Aikens, C. M.; Hollander, F. J.; Schatz, George C. Correlating the Crystal Structure of A Thiol-Protected Au₂₅ Cluster and Optical Properties. *J. Am. Chem. Soc.* **2008**, *130*, 5883–5885.

(12) Qian, H.; Eckenhoff, W. T.; Zhu, Y.; Pintauer, T.; Jin, R. Total Structure Determination of Thiolate-Protected Au₃₈ Nanoparticles. *J. Am. Chem. Soc.* **2010**, *132* (24), 8280–8281.

(13) Jadzinsky, P. D.; Calero, G.; Ackerson, C. J.; Bushnell, D. A.; Kornberg, R. D. Structure of a Thiol Monolayer-Protected Gold Nanoparticle at 1.1 Å Resolution. *Science* **2007**, *318* (5849), 430–433.

(14) Yan, N.; Xia, N.; Liao, L.; Zhu, M.; Jin, F.; Jin, R.; Wu, Z. Unraveling the Long-Pursued Au₁₄₄ Structure by x-Ray Crystallography. *Sci. Adv.* **2018**, *4* (10), eaat7259.

(15) Wang, S.; Song, Y.; Jin, S.; Liu, X.; Zhang, J.; Pei, Y.; Meng, X.; Chen, M.; Li, P.; Zhu, M. Metal

Exchange Method Using Au₂₅ Nanoclusters as Templates for Alloy Nanoclusters with Atomic Precision. *J. Am. Chem. Soc.* **2015**, *137* (12), 4018–4021.

(16) Chai, J.; Lv, Y.; Yang, S.; Song, Y.; Zan, X.; Li, Q.; Yu, H.; Wu, M.; Zhu, M. X-Ray Crystal Structure and Optical Properties of Au_{38-x}Cu_x(2,4-(CH₃)₂C₆H₃S)₂₄ (x = 0–6) Alloy Nanocluster. *J. Phys. Chem. C* **2017**, *121* (39), 21665–21669.

(17) Nair, L. V.; Hossain, S.; Takagi, S.; Imai, Y.; Hu, G.; Wakayama, S.; Kumar, B.; Kurashige, W.; Jiang, D. E.; Negishi, Y. Hetero-Biicosahedral [Au₂₄Pd(PPh₃)₁₀(SC₂H₄Ph)₅Cl₂]⁺ Nanocluster: Selective Synthesis and Optical and Electrochemical Properties. *Nanoscale* **2018**, *10* (40), 18969–18979.

(18) Yang, H.; Lei, J.; Wu, B.; Wang, Y.; Zhou, M.; Xia, A.; Zheng, L.; Zheng, N. Crystal Structure of a Luminescent Thiolated Ag Nanocluster with an Octahedral Ag₆⁴⁺ Core. *Chem. Commun.* **2013**, *49* (3), 300–302.

(19) Liu, X.; Astruc, D. Atomically Precise Copper Nanoclusters and Their Applications. *Coord. Chem. Rev.* **2018**, *359*, 112–126.

(20) Dehnen, S.; Eichhöfer, A.; Fenske, D. Chalcogen-Bridged Copper Clusters. *Eur. J. Inorg. Chem.* **2002**, *2002* (2), 279.

(21) Chakrahari, K. K.; Liao, J. H.; Kahlal, S.; Liu, Y. C.; Chiang, M. H.; Saillard, J. Y.; Liu, C. W. [Cu₁₃{S₂CNⁿBu₂}₆(Acetylide)₄]⁺: A Two-Electron Superatom. *Angew. Chemie - Int. Ed.* **2016**, *55* (47), 14704–14708.

(22) Nguyen, T. A. D.; Jones, Z. R.; Goldsmith, B. R.; Buratto, W. R.; Wu, G.; Scott, S. L.; Hayton, T. W. A Cu₂₅ Nanocluster with Partial Cu(0) Character. *J. Am. Chem. Soc.* **2015**, *137* (41), 13319–13324.

(23) Nguyen, T. A. D.; Jones, Z. R.; Leto, D. F.; Wu, G.; Scott, S. L.; Hayton, T. W. Ligand-Exchange-Induced Growth of an Atomically Precise Cu₂₉ Nanocluster from a Smaller Cluster. *Chem. Mater.* **2016**, *28* (22), 8385–8390.

(24) Edwards, A. J.; Dhayal, R. S.; Liao, P. K.; Liao, J. H.; Chiang, M. H.; Piltz, R. O.; Kahlal, S.; Saillard, J. Y.; Liu, C. W. Chinese Puzzle Molecule: A 15 hydride, 28 copper Atom Nanoball. *Angew. Chemie - Int. Ed.* **2014**, *53* (28), 7214–7218.

(25) Nguyen, T.-A. D.; Goldsmith, B. R.; Zaman, H. T.; Wu, G.; Peters, B.; Hayton, T. W. Synthesis and Characterization of a Cu₁₄ Hydride Cluster Supported by Neutral Donor Ligands. *Chem. - A Eur. J.* **2015**, *21* (14), 5341–5344.

(26) Dhayal, R. S.; Liao, J.-H.; Lin, Y.-R.; Liao, P.-K.; Kahlal, S.; Saillard, J.-Y.; Liu, C. W. A Nanospheric Polyhydrido Copper Cluster of Elongated Triangular Orthobicupola Array: Liberation of H₂ from Solar Energy. *J. Am. Chem. Soc.* **2013**, *135* (12), 4704–4707.

(27) Dhayal, R. S.; Liao, J. H.; Kahlal, S.; Wang, X.; Liu, Y. C.; Chiang, M. H.; Van Zyl, W. E.; Saillard, J. Y.; Liu, C. W. [Cu₃₂(H)₂₀{S₂P(OiPr)₂}]₁₂: The Largest Number of Hydrides Recorded in a Molecular Nanocluster by Neutron Diffraction. *Chem. - A Eur. J.* **2015**, *21* (23), 8369–8374.

(28) Huertos, M. A.; Cano, I.; Bandeira, N. A. G.; Benet-Buchholz, J.; Bo, C.; Van Leeuwen, P. W. N. M. Phosphinothiolates as Ligands for Polyhydrido Copper Nanoclusters. *Chem. - A Eur. J.* **2014**, *20* (49), 16121–16127.

(29) Fu, M.-L.; Issac, I.; Fenske, D.; Fuhr, O. Metal-Rich Copper Chalcogenide Clusters at the Border Between Molecule and Bulk Phase: The Structures of [Cu₉₃Se₄₂(SeC₆H₄SMe)₉(PPh₃)₁₈], [Cu₉₆Se₄₅(SeC₆H₄SMe)₆(PPh₃)₁₈], and [Cu₁₃₆S₅₆(SCH₂C₄H₃O)₂₄(dpppt)₁₀]. *Angew. Chemie Int. Ed.* **2010**, *49* (38), 6899–6903.

(30) Bestgen, S.; Fuhr, O.; Roesky, P. W.; Fenske, D. Synthesis and Molecular Structure of a Spheroidal Binary Nanoscale Copper Sulfide Cluster. *Dalt. Trans.* **2016**, *45* (38), 14907–14910.

(31) Duan, T.; Zhang, X.-Z.; Zhang, Q. Synthesis and Crystal Structure of a Polynuclear Copper-Selenide Cluster [Cu^I₃₆(Cu^{II}Cl)₂Se₁₃(SePh)₁₂(dppe)₆] · 3EtOH. *Zeitschrift für Naturforsch. B* **2008**, *63* (8), 941–944.

(32) Cook, A. W.; Jones, Z. R.; Wu, G.; Scott, S. L.; Hayton, T. W. An Organometallic Cu₂₀ Nanocluster: Synthesis, Characterization, Immobilization on Silica, and “Click” Chemistry. *J. Am.*

Chem. Soc. **2018**, *140* (1), 394–400.

(33) Cook, A. W.; Jones, Z. R.; Wu, G.; Teat, S. J.; Scott, S. L.; Hayton, T. W. Synthesis and Characterization of “Atlas-Sphere” Copper Nanoclusters: New Insights into the Reaction of Cu²⁺ with Thiols. *Inorg. Chem.* **2019**, *58* (13), 8739–8749.

(34) Dehnen, S.; Fenske, D.; Deveson, A. C. [Cu₁₂S₆(PⁿPr₃)₈] and [Cu₂₀S₁₀(PⁿBu¹Bu₂)₈]: Two Sulfur Bridged Copper Clusters with Cu-S Cluster Cores of Known Compositions but New Structures. *J. Clust. Sci.* **1996**, *7* (3), 351–369.

(35) Dehnen, S.; Fenske, D. [Cu₂₄S₁₂(PMeiPr₂)₁₂], [Cu₂₈S₁₄(P^tBu₂Me)₁₂], [Cu₅₀S₂₅(P^tBu₂Me)₁₆], [Cu₇₀Se₃₅(P^tBu₂Me)₂₁], [Cu₃₁Se₁₅(SeSiMe₃)(P^tBu₂Me)₁₂] and [Cu₄₈Se₂₄(PMe₂Ph)₂₀]: New Sulfur- and Selenium-Bridged Copper Clusters. *Chem. - A Eur. J.* **1996**, *2* (11), 1407–1416.

(36) Eichhöfer, A.; Buth, G.; Lebedkin, S.; Kühn, M.; Weigend, F. Luminescence in Phosphine-Stabilized Copper Chalcogenide Cluster Molecules - A Comparative Study. *Inorg. Chem.* **2015**, *54* (19), 9413–9422.

(37) Yang, X. X.; Issac, I.; Lebedkin, S.; Kühn, M.; Weigend, F.; Fenske, D.; Fuhr, O.; Eichhöfer, A. Red-Luminescent Biphosphine Stabilized “Cu₁₂S₆” Cluster Molecules. *Chem. Commun.* **2014**, *50* (75), 11043–11045.

(38) Dornsiepen, E.; Weigend, F.; Dehnen, S. Transition-Metal-Induced Rearrangement of [(PhSn)₄S₆] Towards Ternary Cu I /Sn/S or Cu II /Sn/S Clusters. *Chem. - A Eur. J.* **2019**, *25* (10), 2486–2490.

(39) Nguyen, T.-A. D.; Cook, A. W.; Wu, G.; Hayton, T. W. Subnanometer-Sized Copper Clusters: A Critical Re-Evaluation of the Synthesis and Characterization of Cu₈(MPP)₄ (HMPP = 2-Mercapto-5-n-Propylpyrimidine). *Inorg. Chem.* **2017**, *56* (14), 8390–8396.

(40) Eichhöfer, A.; Kühn, M.; Lebedkin, S.; Kehry, M.; Kappes, M. M.; Weigend, F. Synthesis and Optical Properties of [Cu₆E₆(SnPh)₂(PPh₂Et)₆] (E = S, Se, Te) Cluster Molecules. *Inorg. Chem.* **2017**, *56* (15), 9330–9336.

(41) Li, Y.; Wang, J.; Luo, P.; Ma, X.; Dong, X.; Wang, Z.; Du, C.; Zang, S.; Mak, T. C. W. Cu 14 Cluster with Partial Cu(0) Character: Difference in Electronic Structure from Isostructural Silver Analog. *Adv. Sci.* **2019**, 1900833 (0), 1900833.

(42) Ganguly, A.; Chakraborty, I.; Udayabhaskararao, T.; Pradeep, T. A Copper Cluster Protected with Phenylethanethiol. *J. Nanoparticle Res.* **2013**, 15 (4), 1522.

(43) Sheldrick, G. M. SHELXT - Integrated Space-Group and Crystal-Structure Determination. *Acta Crystallogr. Sect. A Found. Crystallogr.* **2015**, 71 (1), 3–8.

(44) Sheldrick, G. M. Crystal Structure Refinement with SHELXL. *Acta Crystallogr. Sect. C Struct. Chem.* **2015**, 71 (Md), 3–8.

(45) Dolomanov, O. V.; Bourhis, L. J.; Gildea, R. J.; Howard, J. A. K.; Puschmann, H. OLEX2: A Complete Structure Solution, Refinement and Analysis Program. *J. Appl. Crystallogr.* **2009**, 42 (2), 339–341.

(46) Hohenberg, P.; Kohn, W. Inhomogeneous Electron Gas. *Phys. Rev.* **1964**, 136 (3B), B864–B871.

(47) Kohn, W.; Sham, L. J. Self-Consistent Equations Including Exchange and Correlation Effects. *Phys. Rev.* **1965**, 140 (4A), A1133–A1138.

(48) te Velde, G.; Bickelhaupt, F. M.; Baerends, E. J.; Fonseca Guerra, C.; van Gisbergen, S. J. A.; Snijders, J. G.; Ziegler, T. Chemistry with ADF. *J. Comput. Chem.* **2001**, 22 (9), 931–967.

(49) Fonseca Guerra, C.; Snijders, J. G.; Velde, G.; Baerends, E. J. Towards an Order- N DFT Method. *Theor. Chem. Acc.* **1998**, 99 (6), 391–403.

(50) Baerends, E. J.; Ziegler, T.; Atkins, A. J.; Autschbach, J.; Bashford, D.; Baseggio, O.; Bérces, A.; Bickelhaupt, F. M.; Bo, C.; Boerritger, P. M.; et al. ADF2017, SCM, Theoretical Chemistry, Vrije Universiteit, Amsterdam, The Netherlands, <https://www.scm.com> (last accessed: September 4, 2019).

(51) Perdew, J. P.; Burke, K.; Ernzerhof, M. Generalized Gradient Approximation Made Simple.

Phys. Rev. Lett. **1996**, *77* (18), 3865–3868.

(52) Van Lenthe, E.; Baerends, E. J. Optimized Slater-Type Basis Sets for the Elements 1-118. *J. Comput. Chem.* **2003**, *24* (9), 1142–1156.

(53) Van Lenthe, E. Geometry Optimizations in the Zero Order Regular Approximation for Relativistic Effects. *J. Chem. Phys.* **1999**, *110* (18), 8943–8953.

(54) Van Lenthe, E.; Baerends, E. J.; Snijders, J. G. Relativistic Total Energy Using Regular Approximations. *J. Chem. Phys.* **1994**, *101* (11), 9783–9792.

(55) CASIDA, M. E. Time-Dependent Density Functional Response Theory for Molecules; **1995**; pp 155–192.

(56) van Gisbergen, S. J. A.; Kootstra, F.; Schipper, P. R. T.; Gritsenko, O. V.; Snijders, J. G.; Baerends, E. J. Density-Functional-Theory Response-Property Calculations with Accurate Exchange-Correlation Potentials. *Phys. Rev. A - At. Mol. Opt. Phys.* **1998**, *57* (4), 2556–2571.

(57) Rüger, R.; Van Lenthe, E.; Heine, T.; Visscher, L. Tight-Binding Approximations to Time-Dependent Density Functional Theory - A Fast Approach for the Calculation of Electronically Excited States. *J. Chem. Phys.* **2016**, *144* (18).

(58) Higaki, T.; Liu, C.; Zhou, M.; Luo, T.-Y.; Rosi, N. L.; Jin, R. Tailoring the Structure of 58-Electron Gold Nanoclusters: Au₁₀₃S₂(S-Nap)₄₁ and Its Implications. *J. Am. Chem. Soc.* **2017**, *139* (29), 9994–10001.

(59) Jin, S.; Wang, S.; Song, Y.; Zhou, M.; Zhong, J.; Zhang, J.; Xia, A.; Pei, Y.; Chen, M.; Li, P.; et al. Crystal Structure and Optical Properties of the [Ag₆₂S₁₂(SBu^t)₃₂]²⁺ Nanocluster with a Complete Face-Centered Cubic Kernel. *J. Am. Chem. Soc.* **2014**, *136* (44), 15559–15565.

(60) Spek, A. L. PLATON SQUEEZE: A Tool for the Calculation of the Disordered Solvent Contribution to the Calculated Structure Factors. *Acta Crystallogr. Sect. C Struct. Chem.* **2015**, *71*, 9–18.

(61) Yamamoto, K.; Kashida, S. X-Ray Study of the Cation Distribution in Cu₂Se, Cu_{1.8}Se and Cu_{1.8}S;

Analysis by the Maximum Entropy Method. *Solid State Ionics* **1991**, *48* (3–4), 241–248.

(62) Chitsaz, S.; Fenske, D.; Fuhr, O. Silver Chalcogenide Clusters with Dimethylanilinomercapto Ligands: Syntheses and Crystal Structures of $[\text{Ag}_{65}\text{S}_{13}(\text{SC}_6\text{H}_4\text{NMe}_2)_{39}(\text{dppm})_5]$, $[\text{Ag}_{76}\text{Se}_{13}(\text{SC}_6\text{H}_4\text{NMe}_2)_{50}(\text{PPh}_3)_{6.5}]$, and $[\text{Ag}_{88}\text{Se}_{12}(\text{SC}_6\text{H}_4\text{NMe}_2)_{63}(\text{PPh}_3)_6]$. *Angew. Chemie - Int. Ed.* **2006**, *45* (47), 8055–8059.

(63) Winge, D. R.; Dameron, C. T.; George, G. N.; Pickering, I. J.; Dance, I. G. Cuprous-Thiolate Polymetallic Clusters in Biology. In *Bioinorganic Chemistry of Copper*; Springer Netherlands: Dordrecht, **1993**; pp 110–123.

(64) Mehrotra, P. K.; Hoffmann, R. Cu(I)-Cu(I) Interactions. Bonding Relationships in D10-D10 Systems. *Inorg. Chem.* **1978**, *17* (8), 2187–2189.

(65) Reining, L. The GW Approximation: Content, Successes and Limitations. *Wiley Interdiscip. Rev. Comput. Mol. Sci.* **2018**, *8* (3).

(66) Yam, V. W. W.; Lam, C. H.; Fung, K. M.; Cheung, K. K. Syntheses, Photophysics, and Photochemistry of Trinuclear Copper(I) Thiolate and Hexanuclear Copper(I) Selenolate Complexes: X-Ray Crystal Structures of $[\text{Cu}_6(\mu\text{-dppm})_4(\mu_3\text{-SePh})_4](\text{BF}_4)_2$ and $[\text{Cu}_6\{\mu\text{-}(\text{Ph}_2\text{P})_2\text{NH}\}_4(\mu_3\text{-SePh})_4](\text{BF}_4)_2$. *Inorg. Chem.* **2001**, *40* (14), 3435–3442.

(67) Leung, W.-P.; Chan, Y.-C.; Mak, T. C. W. Synthesis and Characterization of an Octanuclear Copper(i) Methanediide Cluster. *Dalt. Trans.* **2013**, *43* (1), 63–66.

(68) Ford, P. C.; Vogler, A. Photochemical and Photophysical Properties of Tetranuclear and Hexanuclear Clusters of Metals with d10 and s2 Electronic Configurations. *Acc. Chem. Res.* **1993**, *26* (4), 220–226.

(69) Xu, H.; Yip, J. H. K. Novel Luminescent Tetranuclear and Pentanuclear Copper(I)-Dithiolates. *Inorg. Chem.* **2003**, *42* (15), 4492–4494.

(70) Link, S.; Beeby, A.; FitzGerald, S.; El-Sayed, M. A.; Schaaff, T. G.; Whetten, R. L. Visible to Infrared Luminescence from a 28-Atom Gold Cluster. *J. Phys. Chem. B* **2002**, *106* (13), 3410–3415.

(71) Shu, T.; Wang, J.; Lin, X.; Zhou, Z.; Liang, F.; Su, L.; Zhang, X. Dual-Emissive Gold Nanoclusters for Label-Free and Separation-Free Ratiometric Fluorescence Sensing of 4-Nitrophenol Based on the Inner Filter Effect. *J. Mater. Chem. C* **2018**, *6* (18), 5033–5038.

(72) Yam, V. W. W.; Cheng, E. C. C.; Zhou, Z. Y. A Highly Soluble Luminescent Decanuclear Gold(I) Complex with a Propeller-Shaped Structure. *Angew. Chemie - Int. Ed.* **2000**, *39* (9), 1683–1685.

(73) Wei, W.; Lu, Y.; Chen, W.; Chen, S. One-Pot Synthesis, Photoluminescence, and Electrocatalytic Properties of Subnanometer-Sized Copper Clusters. *J. Am. Chem. Soc.* **2011**, *133* (7), 2060–2063.

(74) Yang, J.; Li, Z.; Jia, Q. Design of Dual-Emission Fluorescence Sensor Based on Cu Nanoclusters with Solvent-Dependent Effects: Visual Detection of Water via a Smartphone. *Sensors Actuators B Chem.* **2019**, *297* (July), 126807.

Supporting Information**Experimental Details**

General procedure. All the chemicals were used as received. Standard Schlenk-line technique was used for the synthesis of the cluster. The synthesis of the cluster was carried out under inert atmosphere at room temperature. Briefly, in 100 mg of $\text{Cu}(\text{NO}_3)_2 \cdot 3\text{H}_2\text{O}$ (~0.42 mmol) placed in a round bottom flask connected to vacuum pump, was added 6 mL of acetonitrile to dissolve the salt. Afterwards, 200 μL (~1.5 mmol) of 2-phenylethanethiol (2-PET) were added under vigorous stirring which resulted in the formation of white-yellowish copper-thiolate supramolecular gel. To promote the complete reduction of copper ions in solution, 200 μL (~1.43 mmol) of triethylamine (TEA) as a base were added dropwise until the solution changed the color to clear yellowish orange. The as-prepared clusters were precipitated in MeOH by centrifugation (Sigma 3-18 K, 11 400 rpm, 14 239 RCF, 4 °C). This purification process was repeated several times to remove all unreacted precursors and salts. The purified precipitate (53 mg) was then freeze-dried and kept in the fridge for further use. The crystallization of the sample was followed under ambient conditions. After about two weeks, dark orange-reddish crystals were grown from the saturated solution. The crystals were separated by decanting them from the mother liquor (21.4 mg, 34% yield based on copper salt as a limiting reagent).

Characterization. Anal. Calcd for $\text{C}_{360}\text{Cu}_{74.19}\text{H}_{405}\text{S}_{59.54}$: C, 38.09; H, 3.57. Found: C, 35.39; H, 3.64. Note that the elemental analyses were performed on single crystals and slight variations in the percentage are expected due to the presence of huge amount of solvent molecules co-crystallized with the cluster. ^1H NMR (400 MHz, 298 K, CD_2Cl_2): δ 7.33-7.26 (m, 82H), 7.25-7.15 (m, 143H), 3.04-2.92 (m, 180H). ^{13}C NMR (400 MHz, 298 K, CD_2Cl_2): δ 141 (*i*-C), 129.46 (*o*-C), 129.26 (*m*-C) and 41 (α -C from alkyl chain). FT-IR (KBr support, cm^{-1}): 692 (m), 747 (m), 792 (s), 866 (w), 901 (w), 964 (m), 1024 (s), 1094 (s), 1194 (m), 1259 (s), 1410 (w), 1447 (s), 1494 (s), 1558 (w), 1598 (w), 1631 (w), 1655 (w), 2850 (s), 2921 (s), 2960 (w), 3026 (m), 3059 (w), 3085 (w). UV-Vis (CH_2Cl_2 , 0.03 mM, 298 K, $\text{L}\cdot\text{mol}^{-1}\cdot\text{cm}^{-1}$): 420 ($\epsilon = 31400$).

Quantum yield measurements: Integrated sphere method

An integrating sphere Quanta-phi, Horiba Jobin Yvon was attached to the fluospectrometer via an optical fiber bundle for excitation and emission.

The quantum yield was measured as follows: the emission and absorption of the sample between 300 and 700 nm after excitation at 350 nm is compared with the one of a 0% absorption reference provided by Horiba. When this 0% absorption reference is excited at 350 nm it does not absorb any light. All the light from the source is reflected. On the other hand, residual emission is expected between 380 nm and 700 nm from this reference. The same experimental conditions are kept to record the emission and absorption of the solid sample between 300 and 700 nm after excitation at 350 nm. Since the sample absorbs around 350 nm, the emission between 300 and 370 nm decreases respect to the one measured for the reference. Hence, the difference between the emission of the reference and the emission of the sample at the excitation wavelength is considered as the **number of photons absorbed by the sample**.

On the other hand, the **number of the photons emitted by the sample** is calculated as the emission peak area between 390 nm and 700 nm for the sample minus the emission peak area between 390 nm and 700 nm for the reference. Therefore, the quantum yield is calculated based on equation below:

$$\Phi = \frac{n \text{ photons emitted}}{n \text{ photons absorbed}} = \frac{(Emission \text{ sample} - Emission \text{ blank})_{\lambda=390nm-700nm}}{(Emission \text{ blank} - Emission \text{ sample})_{\lambda=300nm-370nm}}$$

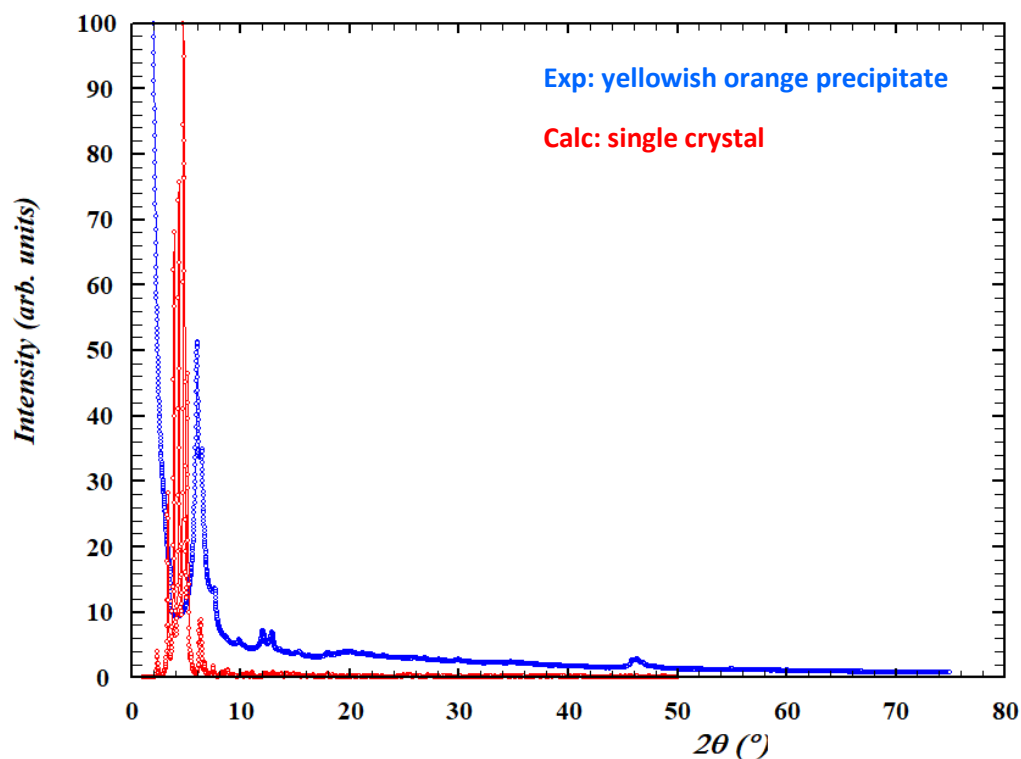


Figure S1. The X-ray powder diffraction pattern of the yellowish orange precipitate (blue curve) superimposed with the calculated X-ray diffraction pattern of a reddish orange crystal (red curve).

X-ray structure determination.

Data were collected on an Agilent Supernova diffractometer equipped with an Atlas detector using Cu K α radiation. Data were integrated in the CrysAlis pro software^[1] and the structure was solved using dual-space methods in SHELXT^[2] and refined in SHELXL^[3] within the OLEX2^[4] program.

Details on the refinement are given in **Table S1**.

The cluster is relatively well-defined, but the ligands show high displacement parameters. Not all of them could be well-determined. The displacement ellipsoids on the carbon atoms of the solvent molecules are extremely large. Hydrogen atoms were not added to the model.

Table S1 Crystal structure refinement details.

Empirical formula	C316 Cu74 N S59.53	
Formula weight	10419.82	
Temperature	140.00(10) K	
Wavelength	1.54184 Å	
Crystal system	Triclinic	
Space group	P-1	
Unit cell dimensions	a = 21.9416(3) Å	$\alpha = 83.3523(13)^\circ$
	b = 28.7216(5) Å	$\beta = 88.2020(11)^\circ$
	c = 37.5021(5) Å	$\gamma = 68.7392(15)^\circ$
Volume	21875.8(6) Å ³	
Z	2	
Density (calculated)	1.582 Mg/m ³	
Absorption coefficient	6.667 mm ⁻¹	
F(000)	10003	
Crystal size	0.399 x 0.334 x 0.117 mm ³	
Theta range for data collection	3.560 to 66.601°.	
Index ranges	-26<=h<=24, -34<=k<=32, -41<=l<=44	
Reflections collected	175660	
Independent reflections	77126 [R(int) = 0.0392]	
Completeness to theta = 66.601°	99.8 %	
Absorption correction	Gaussian	
Max. and min. transmission	0.837 and 0.129	
Refinement method	Full-matrix least-squares on F ²	
Data / restraints / parameters	77126 / 4672 / 4268	
Goodness-of-fit on F ²	1.036	
Final R indices [I>2sigma(I)]	R1 = 0.0758, wR2 = 0.2280	
R indices (all data)	R1 = 0.0953, wR2 = 0.2558	
Extinction coefficient	n/a	
Largest diff. peak and hole	4.253 and -0.908 e.Å ⁻³	

B. EXPERIMENTAL PART

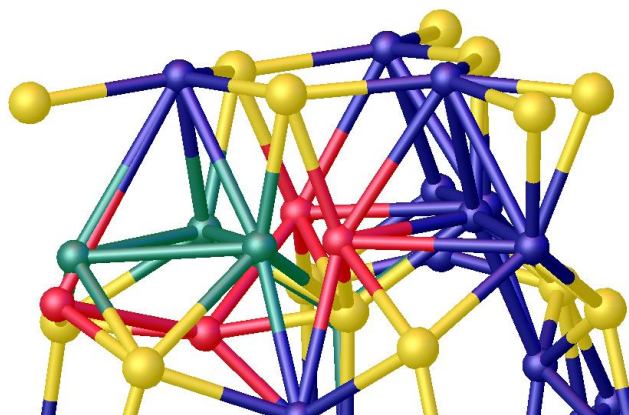
Only one solvent molecule, bound to Cu42 was located. The rest of the solvent was taken care using the squeeze/bypass methods. The formula given in **Table 1** is $\text{Cu}_{74}\text{S}_{59.52}\text{C}_{316}\text{N}_1$. It includes the cluster and one acetonitrile ligand as detailed below:

	Cu	S	C	N
Cu	74			
Free S		15		
Ligands				
Fully determined ligand		38	304	
Partially determined ligand		6.53	10	
<i>S6L</i>		<i>1</i>		
<i>S36L-S37L</i>		<i>2</i>	<i>8</i>	
<i>S41L</i>		<i>1</i>		
<i>S43L-S43M</i>		<i>1</i>	<i>1</i>	
<i>S44L</i>		<i>1</i>	<i>1</i>	
<i>S45L</i>		<i>0.53</i>		
Solvent molecules			2	1
TOTAL Atomic model	74	59.53	316	1

More details on the refinement are included below.

- **Cluster**

The core of the cluster is well-defined with some disorder on some of the copper and sulfur atoms. Especially on one side of the cluster, four of the copper atoms adopt two possible patterns and were refined as two parts, as shown on the figure below, where the copper atoms are depicted in red for one part and in green for the other one.



B. EXPERIMENTAL PART

Apart from the disorder of the group, some copper atoms presented very elongated ellipsoids and were split: (Cu5a Cu5b), (Cu7a Cu7b), (Cu60 Cu61), (Cu69-Cu73),(Cu75 Cu77).

Apart from the 74 Cu atoms which were determined unambiguously, an extra peak was found in an environment compatible with a Cu atom: 2 other Cu atoms at 2.6 and 2.8 Å, and 3 S atoms at 2.3 2.4 and 2.6 Å (this last distance is on the long end). A fully occupied Cu atom was found in an equivalent position. However, this peak, if refined, refined to an occupancy of 0.18. It was therefore not included in the model since other datasets collected on other crystals (but with much lower quality) did not systematically show this peak.

S43 is also disordered over two positions and S45 is also disordered. (This one is only partially occupied in the model).

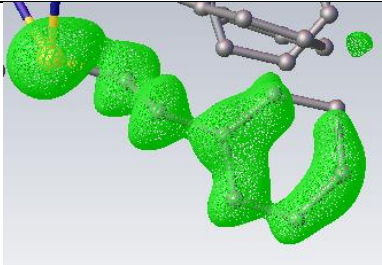
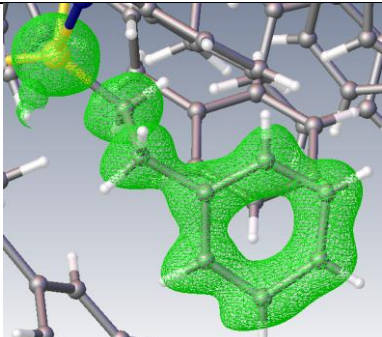
An acetonitrile molecule was also found to bind to Cu42 atoms (Cu-N distance 2.00 Å)

• Ligands

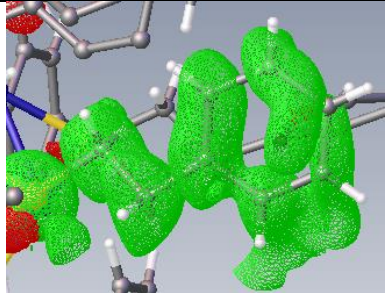
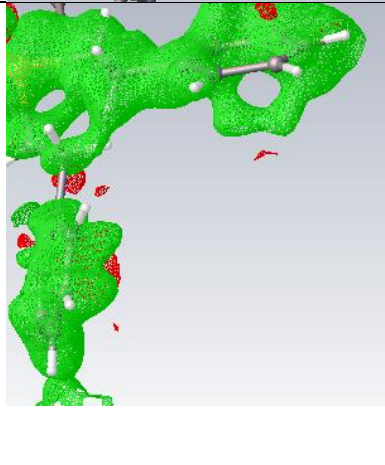
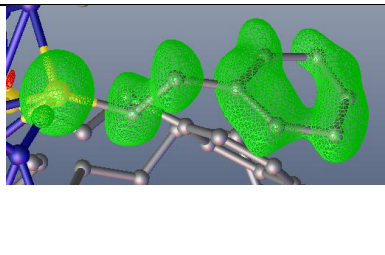
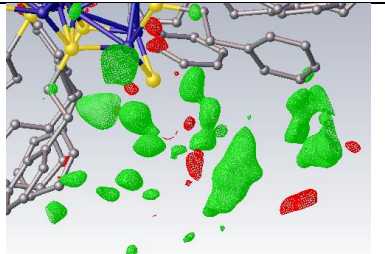
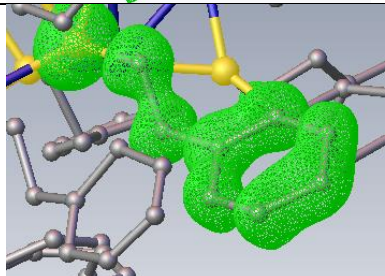
The ligands were not all clearly visible in the difference Fourier maps and strong restraints/constraints were applied, especially on displacement parameters, which otherwise were unreasonably large. In the table below, for each ligand, the strategy taken for the refinement is indicated and, when the ligand could be located, an omit map (different Fourier map with the occupancy of the ligand set to zero) is shown. For non- located ligands, a difference Fourier map (on non-squeezed data) is depicted.

No hydrogen atoms were included in the model.

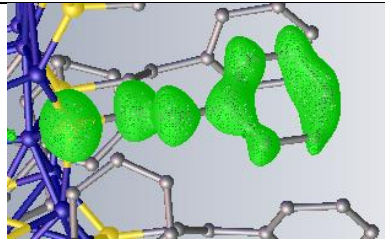
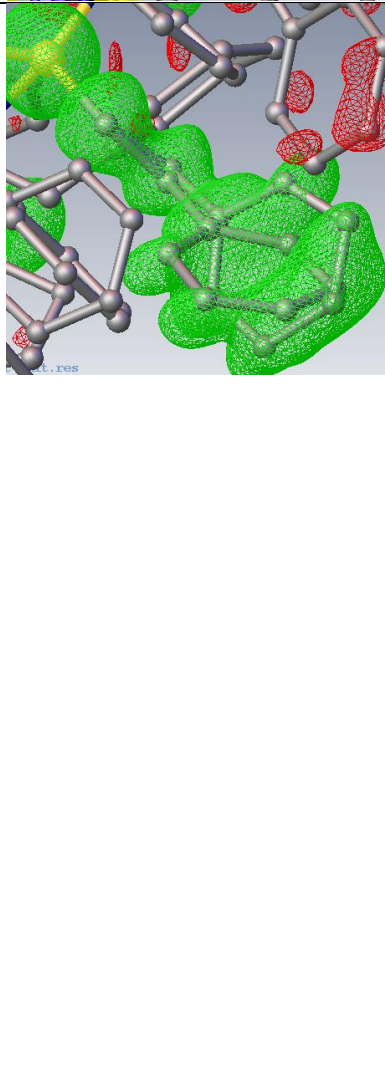
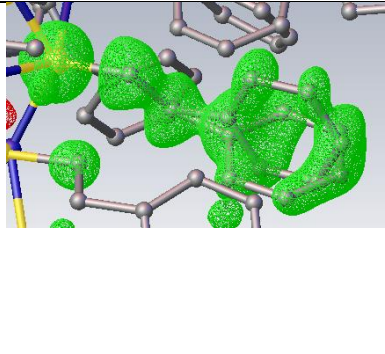
Table S2 Ligand refinement strategy.

Sulfur atom	Details on the refinement	Electron density map (omitting the carbon of the ligand if included in the model)
S1L	Anisotropic Restraints: DFIX 1.39 C3A C8A C8A C7A C7A C6A C5A C6A C5A C4A C4A C3A FLAT C3A C4A C5A C6A C7A C8A SIMU 0.02 0.04 1.7 S1L C1A C2A C3A C8A C7A C6A C5A C4A RIGU S1L C1A C2A C3A C4A C5A C6A C7A C8A	
S2L	Anisotropic Restraints: DFIX 1.39 C12A C11A C13A C12A C14A C13A C15A C14A C16A C15A C16A C11A FLAT C11A C12A C13A C14A C15A C16A RIGU S2L C9A C10A C11A C12A C13A C14A C15A C16A	

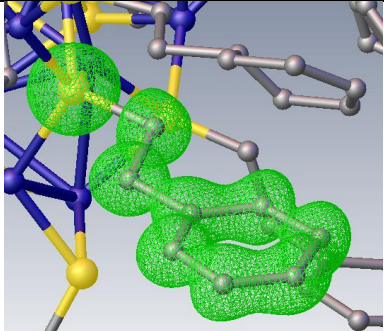
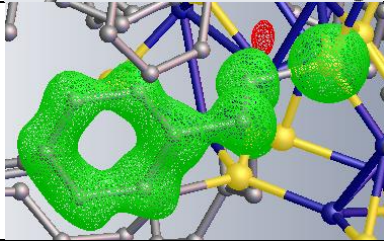
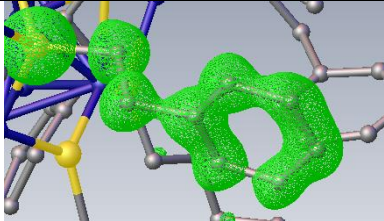
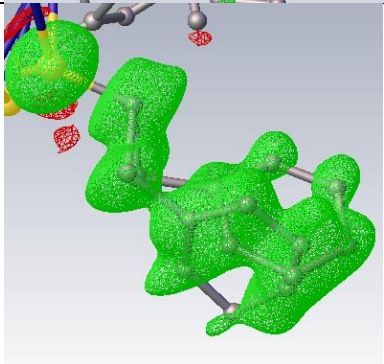
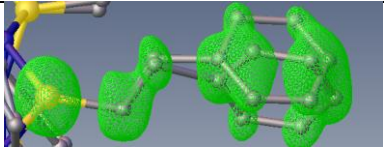
B. EXPERIMENTAL PART

<p>S3L</p>	<p>Anisotropic DFIX 1.52 C18A C17A DFIX 1.5 C19A C18A DANG 2.47 C17A C19A SIMU 0.005 0.02 1.7 C17A C18A C19A C20A C21A C22A > C24A RIGU S3L C17A C18A C19A C20A C21A C22A > C24A</p>	
<p>S4L</p>	<p>2 components Isotropic Rigid bodies for the CH₂-C₆H₅ parts DFIX 1.5 C27B C26B DFIX 1.52 C26B C25B DFIX 1.5 C27A C26A DFIX 1.83 S4L C25A S4L C25B DFIX 1.52 C26A C25A DANG 2.47 C25B C27B DANG 2.47 C25A C27A SIMU 0.02 0.01 2 C25A C25B C26A C26B C27A C27B C28A C28B C29A C29B C30A =</p>	
<p>S5L</p>	<p>DFIX 1.39 C39A C40A C39A C38A C37A C38A C36A C37A C36A C35A C35A C40A FLAT C35A C36A C37A C38A C39A C40A SIMU 0.02 0.04 1.7 C33A C34A C35A C36A C37A C38A C39A C40A RIGU S5L C33A C34A C35A C36A C37A C38A C39A C40A</p>	
<p>S6L</p>	<p>Not located</p> <p>S6L was located and shows quite a large displacement ellipsoid. It could be disordered, hence the difficulty to locate the ligand.</p>	
<p>S7L</p>	<p>RIGU S7L C49A C50A C51A > C55A C56A SIMU 0.02 0.04 1.7 C55A C54A C61A C62A C63A C64A C56A</p>	

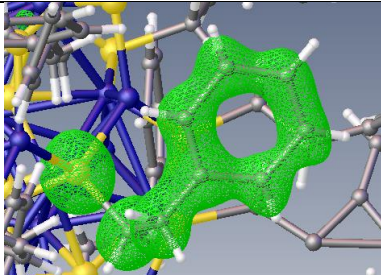
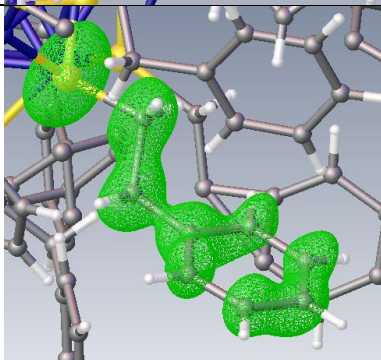
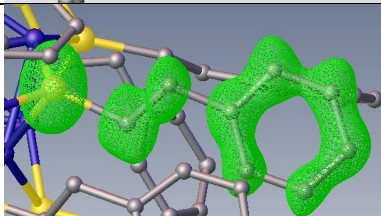
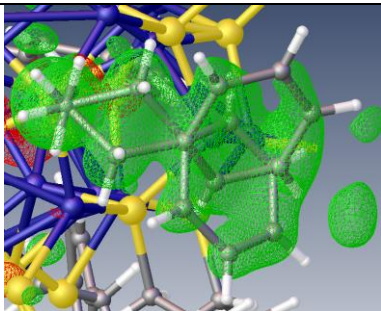
B. EXPERIMENTAL PART

S8L	<p>SIMU 0.005 0.01 1 C57A C58A C59A C60A C61A C62A C63A C64A RIGU 0.001 0.001 S8L C57A C58A C59A C60A C61A C62A C63A C64A</p>	
S9L	<p>2 components, half occupancy</p> <p>DFIX 1.39 C3H C2H C4H C3H C5H C4H C6H C5H C7H C6H C7H C2H DFIX 1.39 C4G C3G C5G C4G C6G C5G C7G C6G C8G C7G C8G C3G DFIX 1.5 C2G C1G C3G C2G DFIX 1.5 C2H C1H C1H C1G SADI C3H C1H C1H C7H SADI C4G C2G C2G C8G DANG 2.5 C1G C3G DANG 2.5 C1G C2H DANG 2.37 C3G C5G DANG 2.37 C4G C6G DANG 2.37 C5G C7G DANG 2.37 C6G C8G DANG 2.37 C7G C3G DANG 2.37 C8G C4G DANG 2.37 C5H C7H DANG 2.37 C6H C2H DANG 2.37 C7H C3H DANG 2.37 C2H C4H DANG 2.37 C3H C5H DANG 2.37 C4H C6H FLAT C2G C3G C8G C7G C6G C5G C4G FLAT C1H C2H C3H C4H C5H C6H C7H SIMU 0.02 0.04 1.7 C1G C2G C1H C2H C7H C6H C5H C7G C8G C6G C4H C3H C5G C4G C3G RIGU C1G C1H C2H C7H C6H C5H C3H C4H RIGU C1G C2G C3G C4G C5G C6G C7G C8G</p>	
S10L	<p>DFIX 1.39 C75A C76A C76A C77A C77A C78A C78A C79A C80A C79A C80A C75A DFIX 1.39 C76B C75B C77B C76B C78B C77B C79B C78B C80B C79B C80B C75B FLAT C75A C76A C77A C78A C79A C80A FLAT C75B C76B C77B C78B C79B C80B SIMU 0.02 0.04 1.7 C20D C73A C74A C75A C75B C76A C76B C77A C77B C78A C78B = C79A C79B C80A C80B RIGU C74A C75A > C78A C79A C80A</p>	

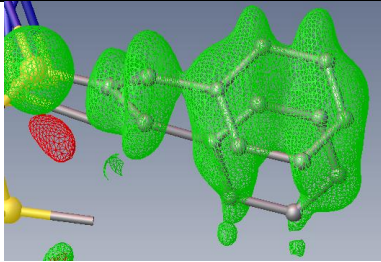
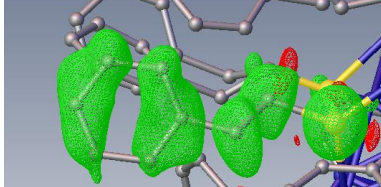
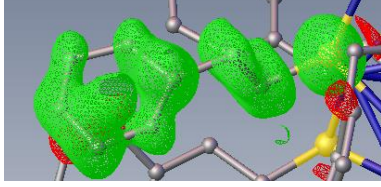
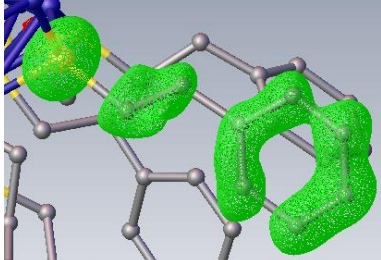
B. EXPERIMENTAL PART

	RIGU C74A C75B C76B C77B C78B > C80B EADP C75B C75A	
S11L	RIGU S11L C81A C82A C83A C84A C85A C86A C87A C88A	
S12L	RIGU S12L C89A C90A > C96A SIMU 0.02 0.04 1.7 C93A C92A C91A C96A C95A C94A C89A C90A S12L	
S13L	RIGU S13L C1C C2C C3C C4C C5C C6C C7C C8C	
S14L	DFIX 1.39 C11C C12C C11C C16C C16C C15C C14C C15C C13C C14C C12C C13C DFIX 1.39 C11D C12D C11D C16D C16D C15D C14D C15D C13D C14D C12D C13D SADI C10C C9C C10D C9C SADI C11C C10C C10D C11D FLAT C11C C12C C13C C14C C15C C16C FLAT C11D C12D C13D C14D C15D C16D DANG 2.37 C11D C15D C12D C14D C15D C13D C16D C12D C11D C13D C16D C14D SIMU 0.04 0.08 1.7 C15D C13C C12C C16D C16C C14C C12D C11C C15C C14D C11D C13D RIGU S14L C9C C10C C11C C12C C13C C14C C15C C16C EADP C10D C10C	
S15L	2 components DFIX 1.39 C20C C19C C24C C19C C24C C23C C23C C22C C22C C21C C21C C20C DFIX 1.39 C19D C24D C24D C23D C23D C22D C22D C21D C20D C21D C20D C19D SADI C18C C19C C18D C19D	

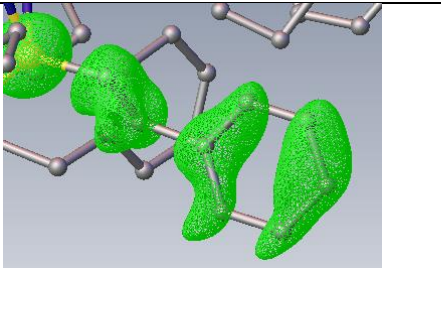
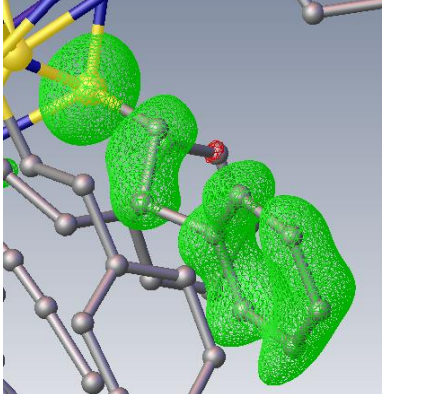
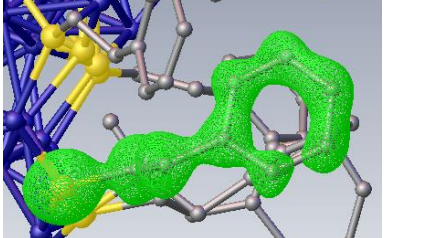
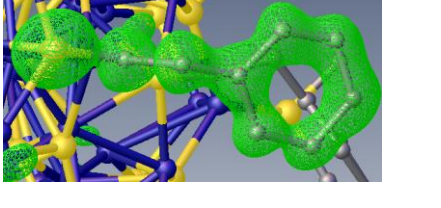
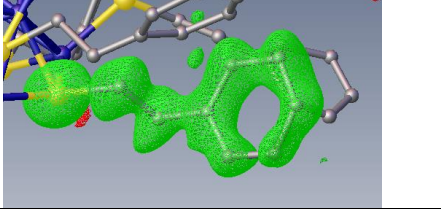
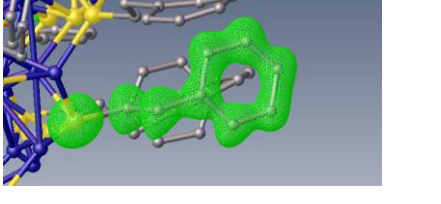
B. EXPERIMENTAL PART

	<p>SADI C17C C18D C17C C18C FLAT C19C C20C C21C C22C C23C C24C FLAT C19D C20D C21D C22D C23D C24D SIMU 0.02 0.04 1.7 C20D C73A C74A C75A C75B C76A C76B C77A C77B C78A C78B C79A C79B C80A C80B RIGU S15L C17C C18C C19C C20C > C24C RIGU S15L C17C C18D C19D C20D C21D C22D C23D C24D EADP C18D C18C</p>	
S16L	<p>SIMU 0.02 0.04 1.7 C25C C26C C27C C32C C31C C30C C29C C28C RIGU S16L C25C C26C C27C C28C C29C C30C C31C C32C</p>	
S17L	<p>DFIX 1.39 C40C C39C C40C C35C C36C C35C C37C C36C C38C C37C C39C C38C FLAT C35C C36C C37C C38C C39C C40C SIMU 0.04 0.08 1.7 C33C C40C C35C C34C C37C C38C C39C C36C RIGU S17L C33C C34C C35C > C39C C40C</p>	
S18L	<p>DFIX 1.53 C42C C41C DFIX 1.39 C44C C43C C45C C44C C47C C46C C46C C45C C48C C47C C48C C43C FLAT C43C C44C C42C C48C C47C C46C C45C RIGU S18L C41C C42C C43C C44C C45C C46C C47C C48C SIMU 0.02 0.04 1.7 C47C C48C C43C C44C C45C C46C C42C C41C</p>	
S19L	<p>2 components</p> <p>DFIX 1.52 C49C C50C C49C C50D DANG 2.47 C49C C51C DANG 2.47 C49C C51D SIMU 0.02 0.04 1.7 C49C C50C C50D C51C C51D C52C C52D C53C C53D C54C C54D = C55C C55D C56C RIGU S19L C49C C50C > C56C RIGU S19L C49C C50D > C56D EADP C56D C51C</p>	

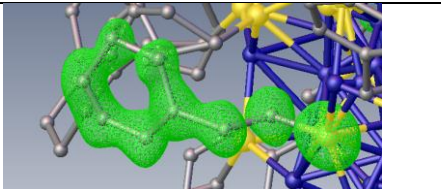
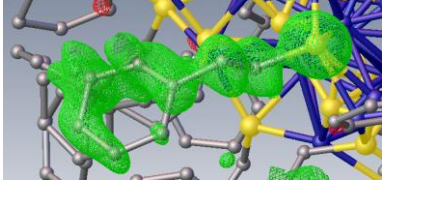
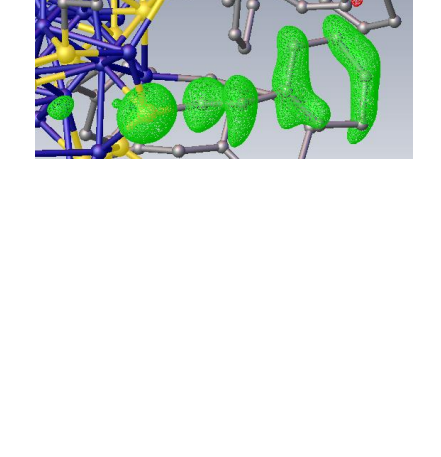
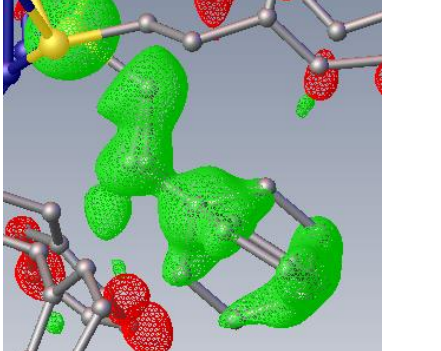
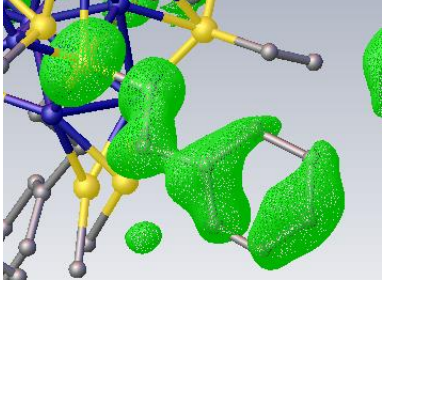
B. EXPERIMENTAL PART

S20L	<p>DFIX 1.49 C57C C58C DFIX 2.55 C59C C57C DFIX 1.39 C62C C61C C62C C63C DFIX 1.39 S20L Cu17 S20L Cu21 S20L Cu33 S20L C57C SIMU 0.02 0.04 1.7 C57C C58C C58D C59C C59D C60C C60D C61C C61D C62C C62D = C63C C63D C64C C64D RIGU C57C C58C C58D C59C > C64C RIGU C57C C58D C59D C60D > C64D RIGU C58C > C64C RIGU S20L C57C C58C > C64C</p>	
S21L	<p>DFIX 1.39 C72C C67C C72C C71C C71C C70C C70C C69C C69C C68C C68C C67C FLAT C66C C67C C72C C71C C70C C69C C68C SIMU 0.02 0.04 1.7 C65C C66C C67C C68C C69C C70C C71C C72C RIGU S21L C65C C66C C67C C68C C69C C70C C71C C72C</p>	
S22L	<p>DFIX 2.5 C73C C75C DFIX 1.52 C74C C73C DFIX 1.39 C80C C75C C80C C79C C79C C78C C78C C77C C77C C76C C76C C75C DANG 2.37 C75C C77C DANG 2.37 C76C C78C DANG 2.37 C77C C79C DANG 2.37 C78C C80C DANG 2.37 C79C C75C DANG 2.37 C80C C76C FLAT C74C C75C C80C C79C C78C C77C C76C SIMU 0.005 0.02 2 C73C C74C C75C C76C C77C C78C C79C C80C RIGU 0.002 0.002 C73C C74C C75C C76C C77C C78C C79C C80C</p>	
S23L	<p>DFIX 1.39 C83C C84C C88C C83C C88C C87C C86C C87C C86C C85C C85C C84C DFIX 1.5 C83C C82C C82C C81C SADI C84C C82C C82C C88C DANG 2.52 C82C C88C FLAT C82C C83C C88C C87C C86C C85C C84C RIGU 0.02 C81C S23L C82C C83C C84C C85C C86C C87C C88C SIMU 0.02 0.04 1.7 C82C C81C C83C C88C C87C C86C C85C C84C</p>	

B. EXPERIMENTAL PART

<p>S24L DFIX 1.39 C95D C94D C94D C93D C96D C93D C96D C92D C92D C91D C95D C91D DFIX 1.5 C91D C90D C90D C89D DANG 2.42 C89D C91D SIMU 0.005 0.01 1 C89D C90D C91D C95D C94D C93D C96D C92D S24L RIGU 0.001 0.001 S24L C89D C90D C91D C92D C96D C93D C94D C95D EADP C96D C92D</p>	
<p>S25L DFIX 1.39 C8E C3E C8E C7E C6E C7E C5E C6E C5E C4E C3E C4E DFIX 1.5 C2E C1E DFIX 1.5 C3E C2E FLAT C3E C4E C5E C6E C7E C8E RIGU S25L C1E C2E C3E C4E C5E C6E C7E C8E</p>	
<p>S26L DFIX 1.39 C12E C11E C16E C11E C16E C15E C15E C14E C14E C13E C13E C12E DFIX 1.5 C11E C10E C9E C10E DANG 2.47 C11E C9E FLAT C11E C12E C13E C14E C15E C16E RIGU C9E C10E C11E C12E C13E C14E C15E C16E</p>	
<p>S27L DFIX 1.39 C21E C21 C22E C21 C23E C22E C24E C23E C24E C20E C21E C20E FLAT C19E C20E C24E C23E C22E C21 C21E SIMU 0.01 0.02 1.7 C18E C19E C20E C21E C22E C23E C24E RIGU 0.02 0.02 C18E C19E C20E C21E C22E C23E C24E</p>	
<p>S28L DFIX 1.39 C32E C27E C28E C27E C29E C28E C30E C29E C31E C30E C32E C31E FLAT C27E C28E C29E C30E C31E C32E SIMU S28L C25E C26E C27E C28E C29E C30E C31E C32E</p>	
<p>S29L DFIX 1.39 C40E C35E C36E C35E C37E C36E C38E C37E C39E C38E C40E C39E FLAT C35E C36E C37E C38E C39E C40E RIGU C33E C34E C35E C36E C37E C38E C39E C40E SIMU 0.02 0.04 1.7 C37E C36E C35E C40E C39E C38E C34E C33E</p>	

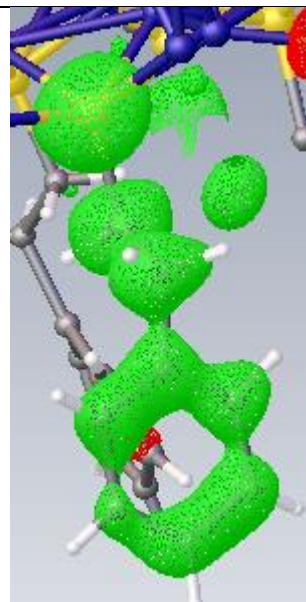
B. EXPERIMENTAL PART

<p>S30L SIMU 0.02 0.04 1.7 C45E C44E C43E C48E C47E C46E C42E C41E RIGU 0.02 0.02 S30L C41E C42E C43E C44E C45E C46E C47E C48E</p>	
<p>S31L DFIX 1.39 C56E C51E C52E C51E C53E C52E C54E C53E C55E C54E C55E C56E FLAT C51E C52E C53E C54E C55E C56E SIMU 0.02 0.04 1.7 C49E C50E C51E C52E C55E C54E C53E C56E RIGU S31L C49E C50E C51E > C54E C55E C56E</p>	
<p>S32L DFIX 1.84 S32L C57E DFIX 1.39 C64E C59E C64E C63E C63E C62E C62E C61E C61E C60E C60E C59E DFIX 1.5 C57E C58E C59E C58E DFIX 2.36 C62E C60E DANG 2.47 C58E C64E DANG 2.47 C58E C60E DANG 2.57 C57E C59E FLAT C59E C60E C61E C62E C63E C64E SIMU 0.02 0.04 1.7 C58E C63E C64E C59E C60E C61E C62E C57E RIGU S32L C57E C58E C59E C60E C61E C62E C63E C64E</p>	
<p>S33L Rigid bodies for the CH₂-C₆H₅ parts SIMU 0.01 0.02 1.7 C65E C66E C66F C67E C67F C68E C68F C69E C69F C70E C70F = C71E C71F C72E C72F RIGU S33L C65E C66E > C72E RIGU S33L C65E C66F > C70F C72F</p>	
<p>S34L DFIX 1.5 C75E C74E C73E C74E DFIX 1.39 C80E C75E C76E C75E C76E C77E C78E C77E C78E C79E C79E C80E DFIX 1.5 C75E C74E DANG 2.41 C77E C79E DANG 2.41 C76E C80E DANG 2.79 C75E C78E FLAT C74E C75E C76E C77E C78E C79E C80E SIMU 0.01 0.02 1.7 C73E C74E C75E C76E C77E C78E C79E C80E RIGU S34L C73E C74E C75E C76E C77E C78E C79E C80E</p>	

B. EXPERIMENTAL PART

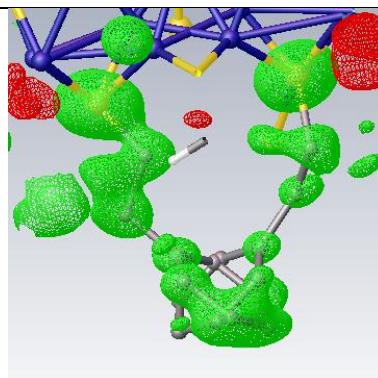
S35L DFIX 1.39 C87E C88E C86E C87E C86E C85E
C84E C85E C83E C84E C83E C88E
DFIX 1.5 C83E C82E C82E C81E
FLAT C83E C84E C85E C86E C87E C88E
SIMU 0.02 0.04 1.7 C81E C82E C83E C84E
C85E C86E C87E C88E
RIGU S35L C81E C82E C83E C84E C85E C86E C87E
C88E

A small extra peak in the difference Fourier map close to the ligand. We could not find a disordered model that make sense to explain this peak.

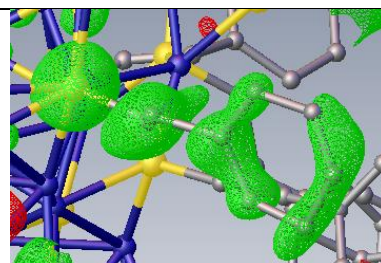


S36L **For S36L and S37I, only half a ligand position was**
S37L **found.** The ligands containing S36L and S37I are
intertwined. The other two half ligand seem to be too
disordered to be found in the difference Fourier map.
The ligands are refined isotropically.

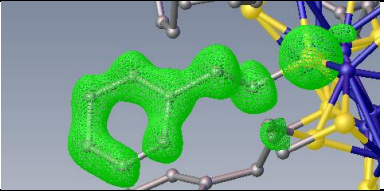
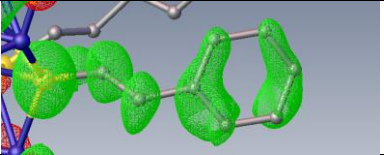
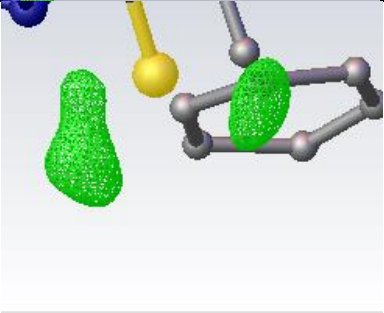
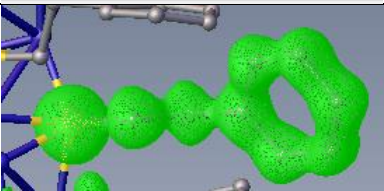
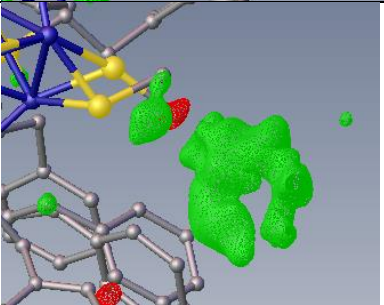
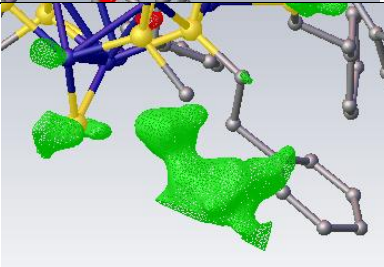
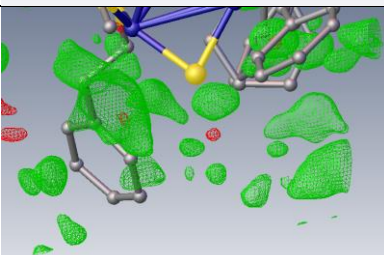
DFIX 1.39 C92E C91E C96E C91E C96E C95E C94E C95E
C93E C94E C92E C93E
DFIX 1.39 C3AA C0BA C3AA C9AA C8AA C9AA C8AA
C7AA C7AA C6AA C0BA C6AA
DFIX 1.5 C90E C89E
DFIX 1.5 C91E C90E
DANG 2.57 C89E C91E
FLAT C91E C92E C93E C94E C95E C96E
FLAT C6AA C7AA C8AA C9AA C3AA C0BA
SIMU 0.01 0.02 1.7 C6AA C7AA C8AA C9AA C3AA
C0BA C91E > C96E



S38L DFIX 1.39 C16G C11G C15G C16G C15G C14G C13G
C14G C13G C12G C12G C11G
DFIX 1.5 C9G C10G C11G C10G
FLAT C11G C12G C13G C14G C15G C16G
SIMU 0.02 0.04 1.7 C9G C10G C11G C12G C13G C16G
C15G C14G
RIGU S38L C9G C10G C11G C12G C13G C14G C15G
C16G



B. EXPERIMENTAL PART

S39L	RIGU C17G C18G C19G C20G C21G C22G C23G C24G	
S40L	RIGU S40L C25G C26G > C32G SIMU 0.02 0.04 1.7 C25G C26G C27G C32G C31G C30G C29G C28G	
S41L	Ligand not located	
S42L	RIGU S42L C41G C42G C43G C44G C45G C46G C47G C48G	
S43L	Ligand not modelled The Fourier difference map shows some remaining electronic density, but the modelling of the ligand was unsatisfactory	
S44L	Ligand not modelled The Fourier difference map shows some remaining electronic density, but the modelling of the ligand was unsatisfactory.	
S45L	Ligand not located	

B. EXPERIMENTAL PART

- SOLVENT

Other solvent molecules could not be localized, and the squeeze/bypass procedure was used to take care of disordered solvent molecules. Two larger holes were found in between the cluster molecules, presumably containing acetonitrile molecules. Other smaller holes were found closer to the disordered ligands. The probe radius was increased to 1.25, which reduced the occurrence of these small holes to 3, with very low residual density.

SQUEEZE RESULTS

position	Volume (Å ³)	Electron count
0.000 0.000 0.000	2099	370
0.878 0.000 0.500	2731	461
0.500 0.500 0.000	108	16
0.954 0.673 0.364	13	0
0.046 0.327 0.636	13	0

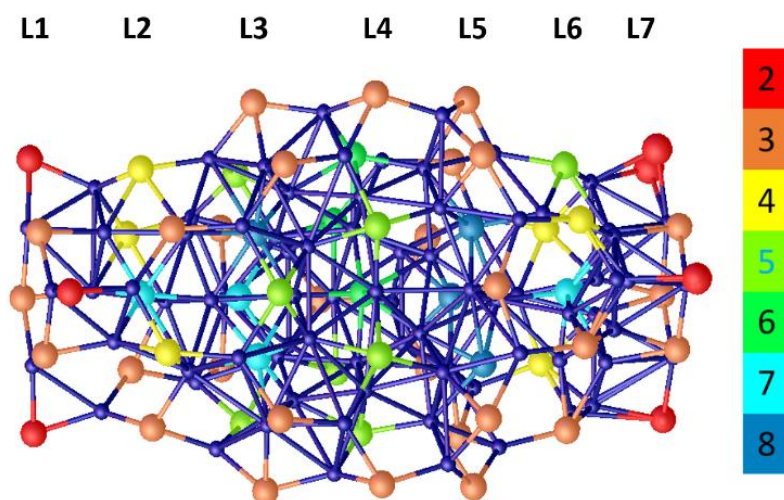


Fig. S2 The sulfur atoms are colour coded according to the number of Copper atoms at less than 3 Å.

Table S3. Cu environment. The occupancy of not fully occupied Cu is given between parenthesis after the atom name. The bond valence sum is calculated only considering the Cu-S bonds (For Cu42, the value

B. EXPERIMENTAL PART

taking also into account the acetonitrile molecule is given in parenthesis). The distortion parameters are calculated as the distance of the Cu from the mean plane formed by the three sulfur atoms bonding to the copper. The absence of this parameter indicates a coordination for the Cu far from planar trigonal. The atoms indicated by a * are low occupancy disordered Cu atoms. The position of the neighboring S atoms may not be adequately determined, as the sulfur atoms were modelled without disorder. The Cu-S distances and hence the valence calculation is therefore not reliable.

Cu atom	calculated bond valence sum	Number of S atom closer to 2.42 Å	Distortion parameter	Number of Cu atoms closer to 2.6
<i>Cu69(0.278)*</i>	1.51	2		1
Cu79	1.03	3	0.09	0
Cu81	1.16	3	0.05	0
Cu59	0.88	2		<u>1</u>
Cu54	0.82	3	0.04	0
<i>Cu70(0.557)</i>	0.96	3	0.07	0
Cu64	1.01	3	-0.30	2
Cu63	1.06	3	0.21	1
<i>Cu5B (0.67)</i>	0.90	2	0.20	1
Cu31	1.00	3	0.03	0
Cu30	1.02	3	0.04	0
Cu33	1.00	3	0.02	0
Cu32	1.01	3	0.03	0
Cu35	1.00	3	0.06	0
Cu34	1.01	3	0.04	0
Cu37	0.77	2		<u>1</u>
Cu36	0.76	2		<u>1</u>
Cu39	0.82	3	0.12	<u>0</u>
Cu38	0.84	3	0.14	1
<i>Cu60 (0.84)</i>	1.14	3	0.01	0
Cu55	1.07	3	<u>0.02</u>	0
Cu73	1.01	3	0.03	0
Cu57	1.11	3	0.12	0
Cu56	1.12	3	0.20	0
Cu19	1.02	3	0.11	0
Cu18	1.07	3	0.07	0
Cu53	0.82	3	0.05	0
Cu52	0.72	2	0.42	0

B. EXPERIMENTAL PART

Cu51	0.72	2	0.40	1
Cu50	0.84	2	-	1
Cu13	1.06	3	0.10	0
Cu12	0.91	3	<u>0.31</u>	2
Cu11	0.91	2	0.58	1
Cu10	0.91	3	0.32	2
Cu17	1.06	3	0.05	0
Cu16	1.02	3	0.50	0
Cu15	1.04	3	0.10	0
Cu14	1.07	3	0.37	0
Cu6	1.05	3	0.04	0
Cu4	0.97	3	0.16	1
Cu3	1.09	3	0.03	0
Cu2	1.12	3	0.00	0
Cu1	1.04	3	0.06	0
Cu1A	1.19	3	0.17	0
Cu65	1.01	3	0.31	2
Cu7A(0.29)	0.93	2	0.15	1
Cu72(0.443)	0.78	1	0.08	2
Cu9	1.09	3	0.03	0
Cu7B(0.71)	0.93	2	0.15	1
Cu75(0.17)*	0.67	1	0.15	2
Cu61(0.16)*	0.76	2	0.83	0
Cu76(0.443)	0.96	2	0.09	2
Cu74(0.557)	0.76	1	0.07	2
Cu8	1.07	3	0.03	0
Cu77(0.83)	1.01	3	0.13	2
Cu26	0.94	2	0.75	0
Cu27	0.93	3	0.05	0
Cu24	0.94	3	0.10	0
Cu25	0.95	3	0.08	0
Cu22	0.88	3	0.03	0
Cu23	0.94	3	0.05	0
Cu20	0.84	3	0.03	0
Cu21	0.86	3	0.01	0
Cu66 (0.443)*	1.22	2		2
Cu71(0.557)	0.80	3	0.04	2
Cu78	0.97	4	0.11	0
Cu5A (0.33)	0.85	2	0.25	1
Cu28	0.92	3	0.05	0
Cu29	0.93	3	0.09	0
Cu44	0.84	3	0.05	2

B. EXPERIMENTAL PART

Cu45	0.84	2	0.03	2
Cu46	1.08	3	0.05	0
Cu47	0.89	3	0.05	0
Cu40	0.79	2		0
Cu41	0.87	3	0.08	2
Cu42	0.73 (0.97)	1	0.57	1
Cu43	1.07	3	0.02	0
Cu62	1.06	3	0.35	1
Cu68(0.443)	1.17	2		0
Cu58	1.12	3	0.09	0
Cu48	0.89	3	0.02	0
Cu49	0.89	2	0.51	2
Cu67(0.557)	1.08	2		3

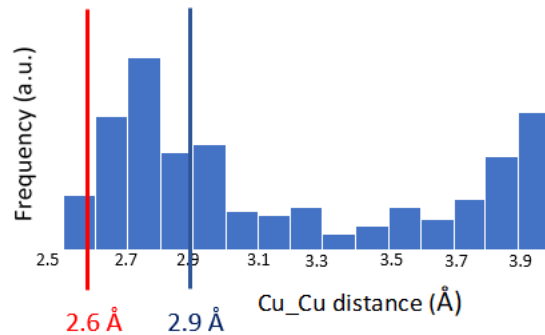
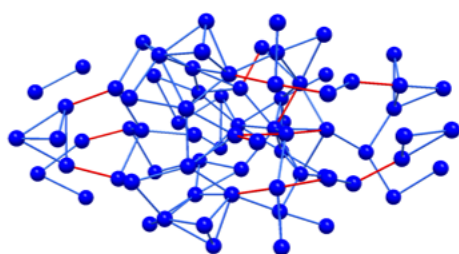


Fig. S3 Cu organization. The histogram of the Cu-Cu distances is shown on the right. On the left, Cu-Cu distances less than 2.6 Å are displayed in red and the ones up to 2.9 Å are displayed in blue.

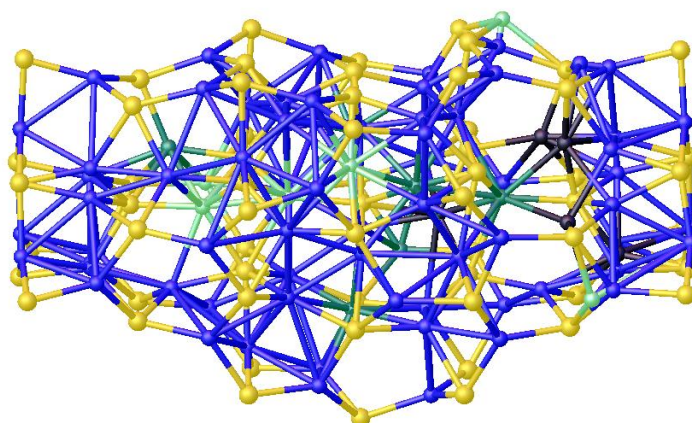


Fig. S4 Cu-S coordination. Cu atoms in the ideal trigonal planar geometry are depicted in blue. Atoms that are distorted from this geometry are depicted in black if they have 2 neighbouring Cu atom closer than 2.6 Å, in dark green if they have one and in light green if they have zeros.



Fig. S5 L1(left) and L7(right) layers. There are 3 copper atoms (in blue) within L1 and L7 with trigonal coordination. Each copper atom is bound to 3 sulfur atoms (in yellow) in the range of 2.22-2.28 Å. In L7 one sulfur atom is disordered (depicted in orange/brown). Hexagonal ring-like geometries are formed with 3 copper atoms bound to 3 sulfur atoms in the same plane, the remaining sulfur atoms occupying apex positions.

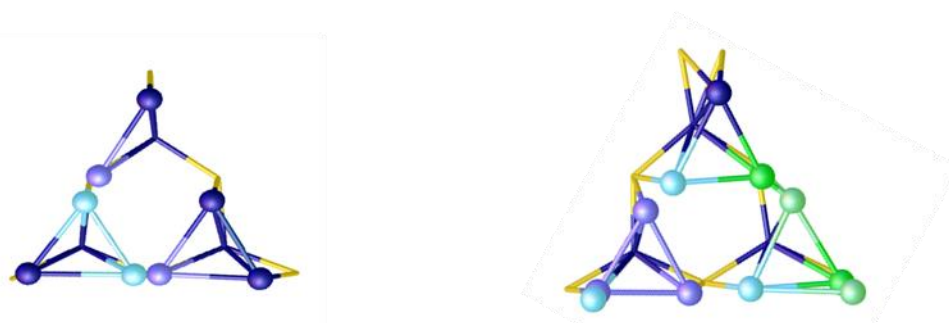


Fig. S6 L1→L2 (left) and L7→L6 (right) interlayers. Layer 1 and 7 are shown in wireframe (S disorder omitted). The Cu atoms between layers 1 and layers 2 and between layer 7 and layer 6 are shown as sphere. Fully occupied atoms are in dark blue. On the left (**L1→L2**), there are two groups of disordered atoms, each with two atoms whose occupancies sum up to 1. The occupancies of these 2 different groups were refined independently and led for each group to one low occupancies atom (around 0.3-0.4) depicted in light blue and the complementary high occupancy atom depicted in violet. On the right (layer 7 to layer 6) there is a group of 6 disordered atoms which were refined in two groups: the one depicted in cyan with occupancy 0.44 and the one in violet with occupancy 0.66. In green are other disordered Cu atoms with a low (lighter green) and high (darker green) occupancy part (around 0.2 against 0.8, the occupancies of each groups of two atoms were refined independently). Six Cu atoms reside between layer 1 and 2 and layer 6 and 7. Disorder strongly affects the position of the Cu atoms, but similar features are observed: three amongst them form a tetrahedra with the Cu atoms of the previous layer (with relatively long Cu-Cu bonds of 2.8 Å) and Cu-Cu dimers also form. These Cu atoms are closer to the S atoms of layer 2 and 6 and are all arranged in a trigonal coordination sometimes slightly distorted with longer Cu-S bonds.

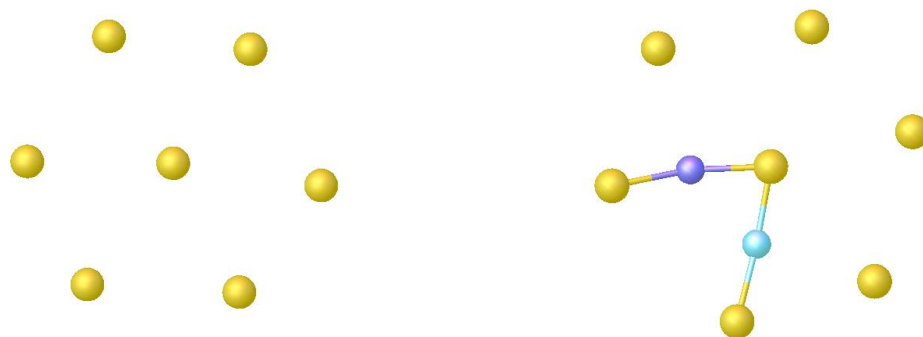


Fig. S7. L2(left) and L6(right) layers. In layer6 (right) the Cu atom depicted in cyan has occupancy around 0.44 and the one in violet 0.66.

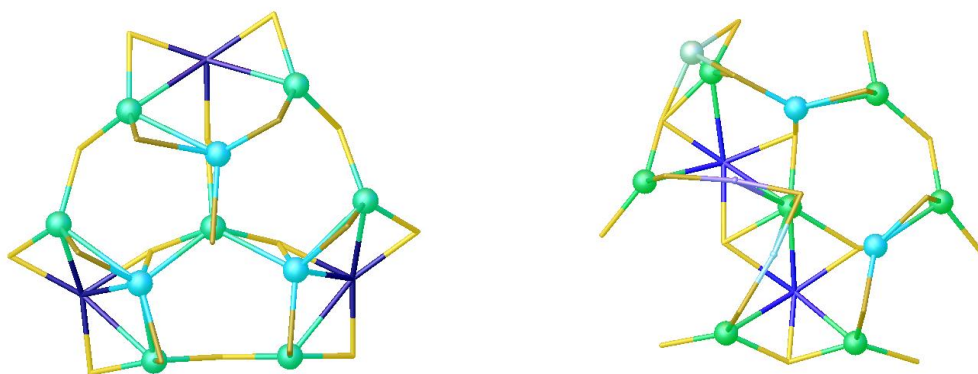


Fig. S8 L2→L3 (left) and L6→L5 (right) interlayers. L2 and L6 are depicted as wireframe in goldish while L3 and L5 are in yellow wireframe (Cu atoms for these layers omitted). There are 10 atoms of Cu between L3 and L4. Three are closer to L2 (cyan). Each of them bond to 3 sulfur atom neighbours in L2 but since they are shifted from this plane, they do not adopt an ideal planar trigonal configuration. The atoms close to L3 (green) are in planar trigonal conformation, each bound to 2 atoms in L3 and one in L2. There are 9 atoms of Cu between L6 and L5. The two ones closer to L6 (cyan) have 3 sulfur neighbours, but only two from L6, they form a third bond with an atom in L5, adopting a slightly distorted geometry from the trigonal planar one. The atoms close to L3 still adopt an almost planar triangular conformation, each atom bounds to 2 atoms in L3 and one in L2, but with much more distortion.

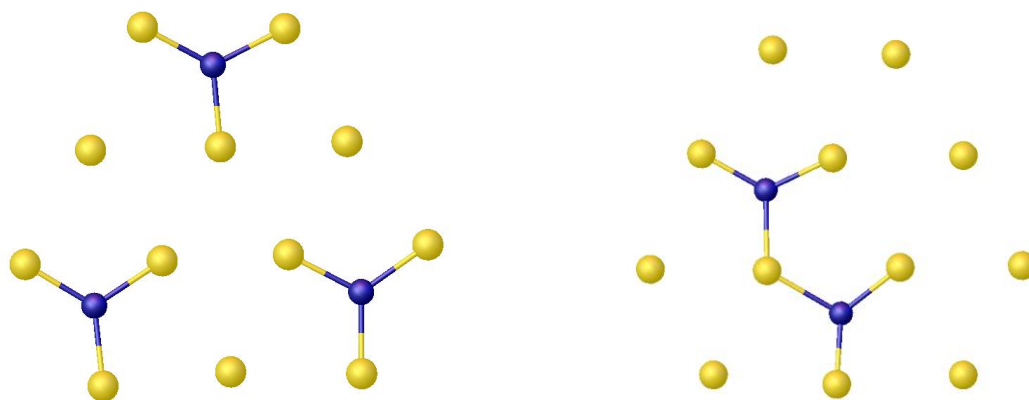


Fig. S9 L3(left) and L5(right) layers. In L3 there are 3 Cu atoms (blue) in perfect trigonal planar coordination (displacement of the Cu atoms from the plane formed by the sulfur atoms is less than 0.03 Å). In L5 there are 2 Cu atoms also in perfect trigonal planar coordination.

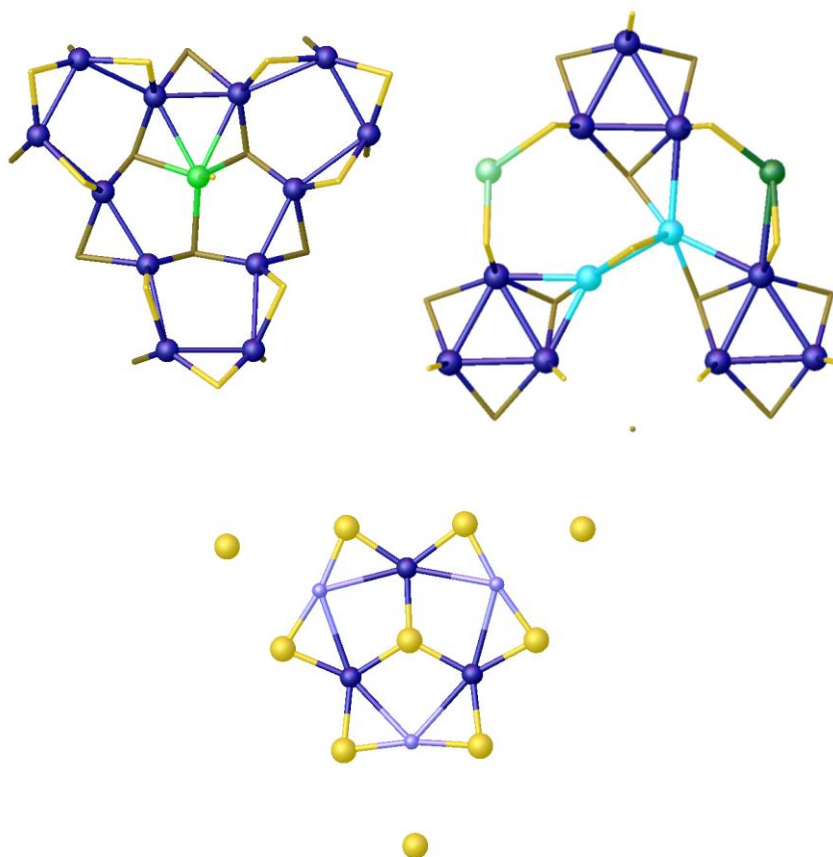


Fig. S10 L3→L4 (top left) and L5→L4 (top right) interlayers, L4 layer (bottom). Layers L3 and L4 and L5 are in wireframe, gold for L3 and L5, yellow for L4. The Cu atoms for these layers are omitted in the top view. Three Cu atoms with perfect trigonal planar coordination (dark blue) are sitting in L4. Three Cu atoms with only 2 short Cu-S bonds are also present. The coordination for these atoms is completed by at least five Cu atoms with for each atom at least some of them presenting shorter distances (between 2.6 and 2.7 Å). For L3→L4 there are 13 Cu atoms. All have trigonal planar coordination, with few distortions, except the central atom (in green) that is almost tetrahedral. L5→L4 slightly differs. In this layer, there are 12 atoms (plus one very low occupancy). Nine of them (in dark blue) form Cu₃ triangles (with Cu-Cu distances in the range 2.7-2.8 Å). Each side of the triangle is capped by a ligand whose sulfur atom belongs to L5. A third sulfur atom belonging to the other layer completes the trigonal planar coordination sphere of the Cu (The Cu atoms being always displaced by less than 0.1 Å from the plane formed by the three triangles). Two extra copper atoms (light blue) adopt an unusual configuration with only two sulfur atoms at very close distances (less than 2.23 Å). Bonds to Cu atoms and for one of them (Cu49) to a further away sulfur (Cu_S=2.63 Å) complete the coordination sphere. Finally, there is one fully occupied atom (dark green) in distorted planar trigonal configuration.

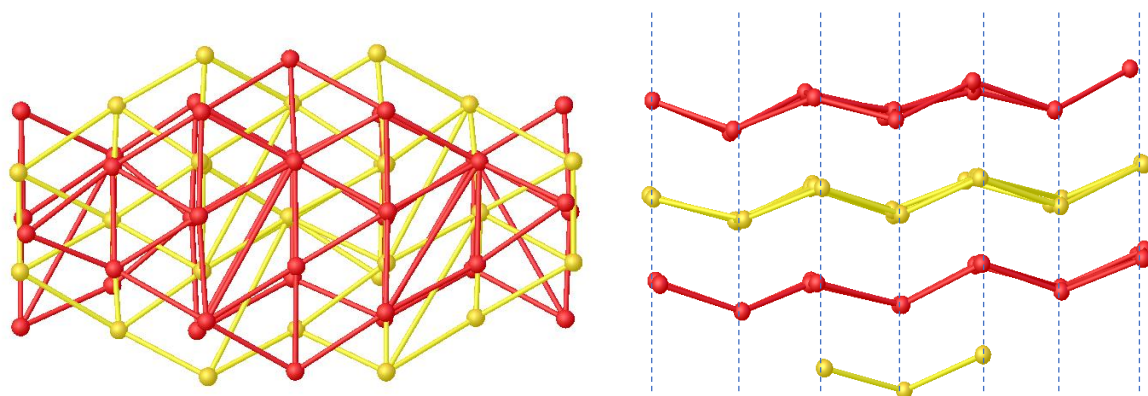


Fig. S11. Alternative grid view of the sulfur atoms. The two figures are different views, rotated by 90 degrees. The S substructure can be decomposed in four layers forming a triangular grid. The layers are arranged in an ABA fashion (A layers in red, B layers in yellow). They are not planar but form a zig-zag arrangement, in contrary to the seven layers already described (and shown as dashed line on the right figure).

B. EXPERIMENTAL PART

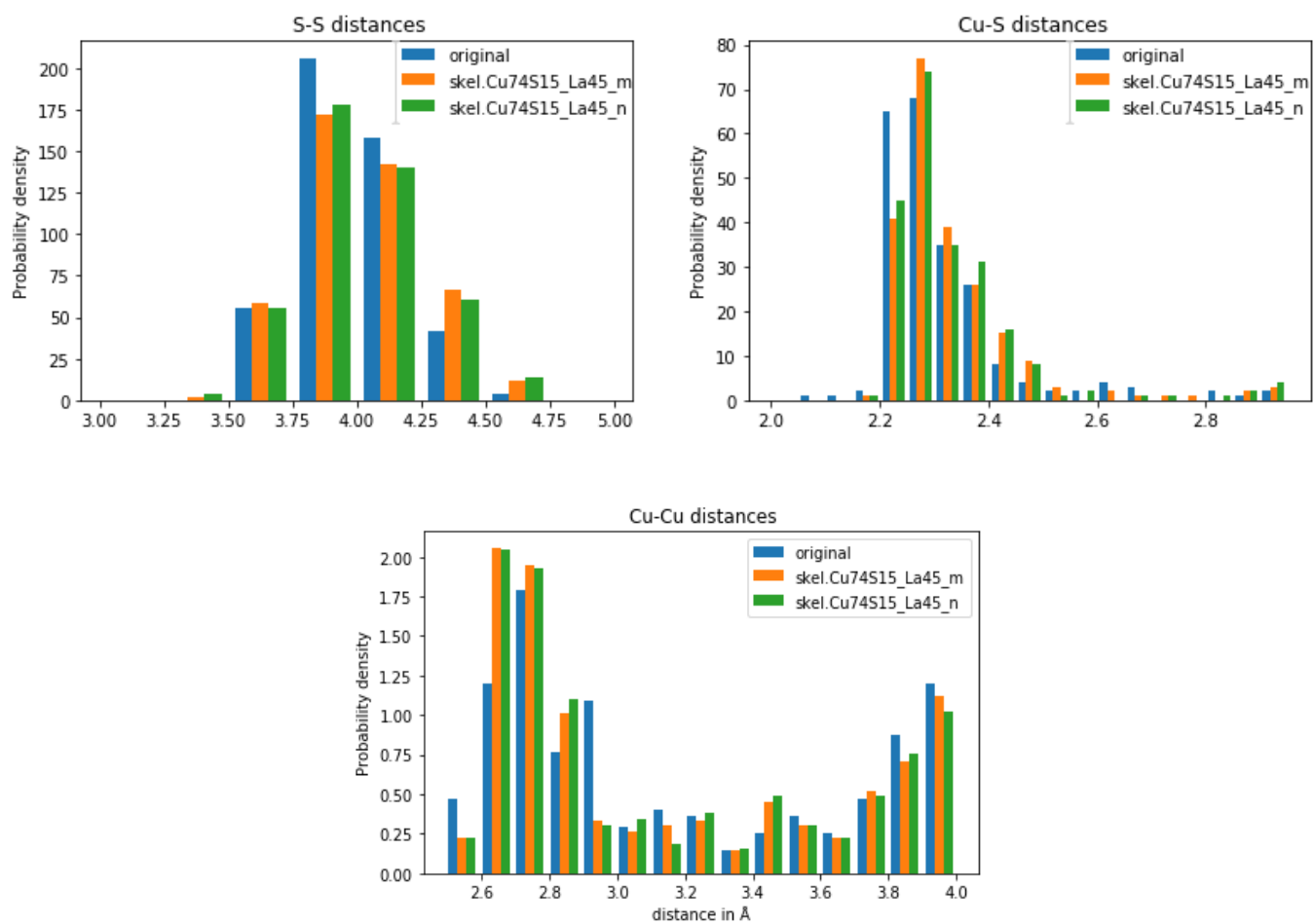


Fig. S12 Histograms of calculated (neutral and charged) and measured S-S, Cu-S and Cu-Cu bond lengths. The label “original” refers to the initial structure derived from single crystal X-ray measurements, whereas “m” and “n” refer to the charged and neutral clusters from DFT calculations.

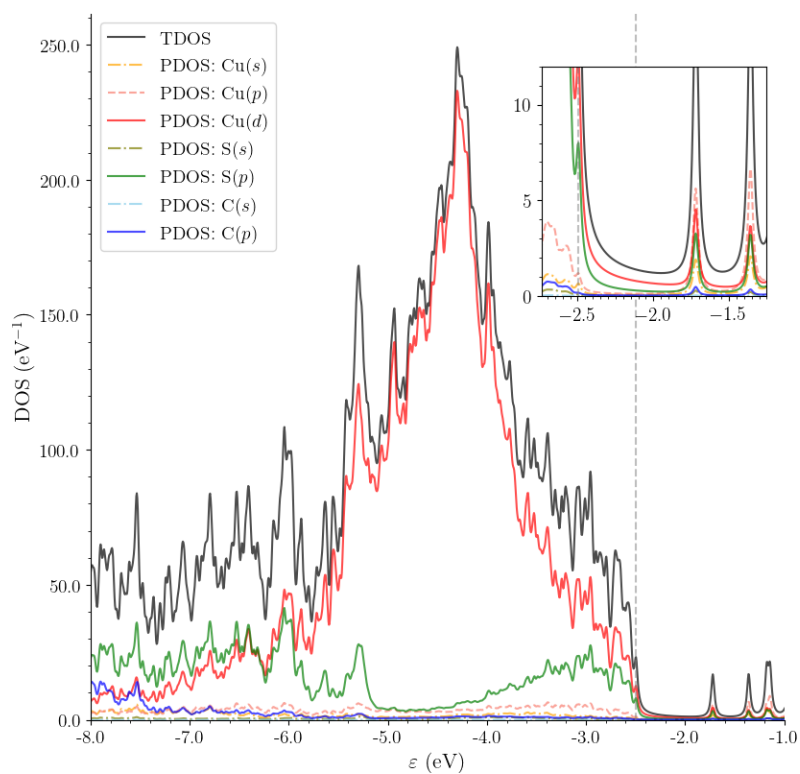


Fig. S13 Calculated total and partial (gross population) density of states of (**1**); the vertical dashed line indicates $\epsilon(\text{HOMO}) = -2.495$ eV (PBE results; δ functions are approximated by Lorentzians having a full-width-at-half-maximum of $2\sigma/\sqrt{\pi}$ with $\sigma = 0.02$ eV).

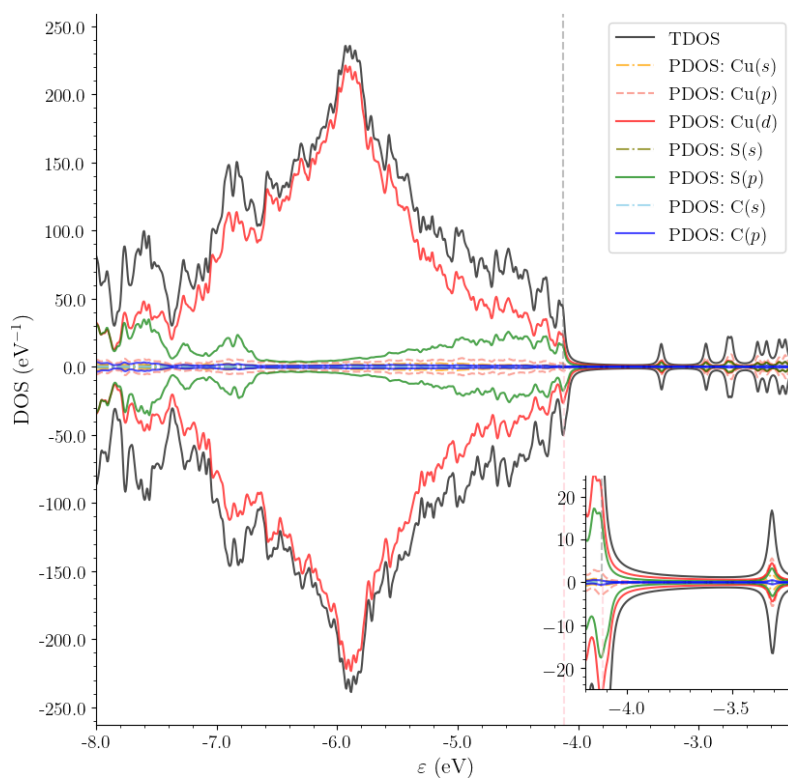


Fig. S14 Calculated total and partial (gross population) density of states of (**1•**) plotted in the upper (resp., lower) part for the spin-up (resp., spin-down) channel; the vertical dashed lines indicate the position of the spin-up (gray line) and spin-down (pink line) HOMOs (PBE results; δ functions are approximated by Lorentzians having a full-width-at-half-maximum of $2\sigma/\sqrt{\pi}$ with $\sigma = 0.02$ eV).

Table S4. Results of the TDDFT and TDDFT+TB electronic excitation calculations for (**1**): energies (E) and oscillator strengths of the 50 lowest-lying dipole-allowed transitions.

TDDFT		TDDFT-TB	
E (eV)	f	E (eV)	f
0.807	5.39E-03	0.785	3.61E-03
0.846	8.69E-04	0.834	3.24E-04
0.889	8.40E-03	0.860	1.69E-03
0.897	5.42E-03	0.875	2.55E-03
0.907	1.42E-03	0.898	8.61E-04
0.935	3.73E-04	0.930	2.87E-04
0.968	8.05E-04	0.944	2.89E-04
0.979	9.22E-04	0.959	1.31E-03
0.990	3.66E-03	0.974	7.49E-04
1.017	3.72E-03	0.990	8.00E-04
1.041	4.87E-03	1.007	9.59E-04
1.060	6.62E-04	1.019	2.72E-03
1.081	2.42E-04	1.064	5.27E-04
1.097	8.19E-04	1.076	2.20E-05
1.101	6.42E-04	1.084	2.49E-04
1.131	1.26E-03	1.114	7.47E-04
1.152	4.08E-03	1.128	4.01E-04
1.159	5.15E-03	1.142	1.50E-03
1.160	3.14E-03	1.145	3.13E-03
1.171	8.62E-04	1.155	7.17E-05
1.192	1.59E-03	1.180	8.60E-04
1.207	1.32E-03	1.188	5.23E-04
1.211	1.17E-03	1.198	7.74E-04
1.238	1.33E-03	1.219	1.51E-03
1.244	8.61E-04	1.224	4.00E-04
1.251	3.96E-03	1.230	1.36E-03
1.254	1.85E-03	1.237	8.84E-04
1.260	6.89E-04	1.240	2.30E-03
1.267	3.59E-03	1.246	6.45E-04
1.271	5.80E-04	1.253	4.65E-03
1.278	9.76E-03	1.261	2.12E-03
1.292	7.28E-03	1.267	2.22E-04
1.296	2.00E-03	1.291	4.37E-04
1.312	1.00E-03	1.292	1.96E-04
1.314	1.89E-04	1.296	1.26E-03
1.318	5.32E-05	1.302	6.49E-04
1.325	3.31E-03	1.303	1.28E-04
1.339	4.99E-03	1.319	6.15E-04
1.347	1.94E-03	1.324	1.15E-03
1.352	3.05E-03	1.325	2.58E-04
1.356	1.55E-04	1.342	1.22E-03
1.368	1.83E-03	1.345	4.09E-03
1.374	2.70E-03	1.353	2.03E-03
1.377	1.17E-03	1.356	8.61E-05
1.383	2.08E-03	1.358	7.42E-04
1.388	3.79E-03	1.360	6.18E-04
1.391	1.13E-03	1.363	3.09E-03
1.392	3.05E-04	1.371	1.64E-04
1.396	5.63E-03	1.376	2.72E-04
1.402	7.37E-03	1.377	4.19E-04

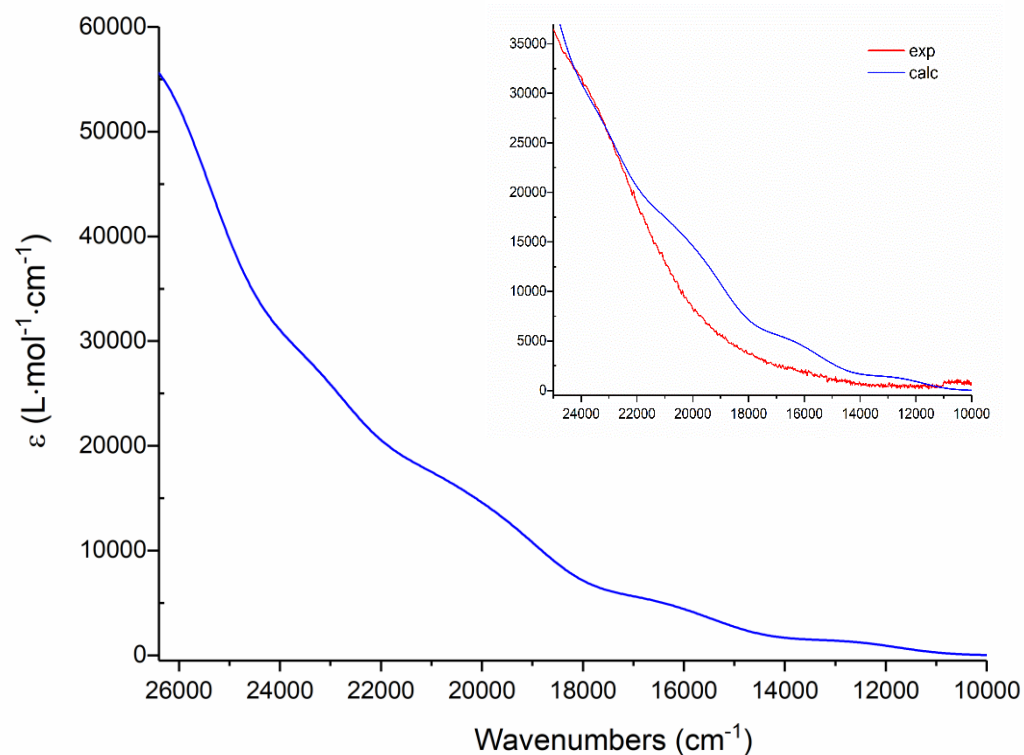


Figure S15. Simulated absorption spectrum of (**1**) obtained by convoluting the calculated oscillator strengths with Gaussians having a full-width at half maximum of 2000 cm^{-1} (TDDFT-TB results for the 1500 lowest-lying dipole-allowed transitions). Note that only the low-energy part of the simulated spectrum is shown. Inset: Comparison between simulated (blue curve) and measured (red curve) absorption spectra by superimposing the $\epsilon=\epsilon(\nu)$ curves. The simulated spectrum is shifted by 5700 cm^{-1} to higher energies to achieve a satisfactory agreement between theory and experiments.

B. EXPERIMENTAL PART

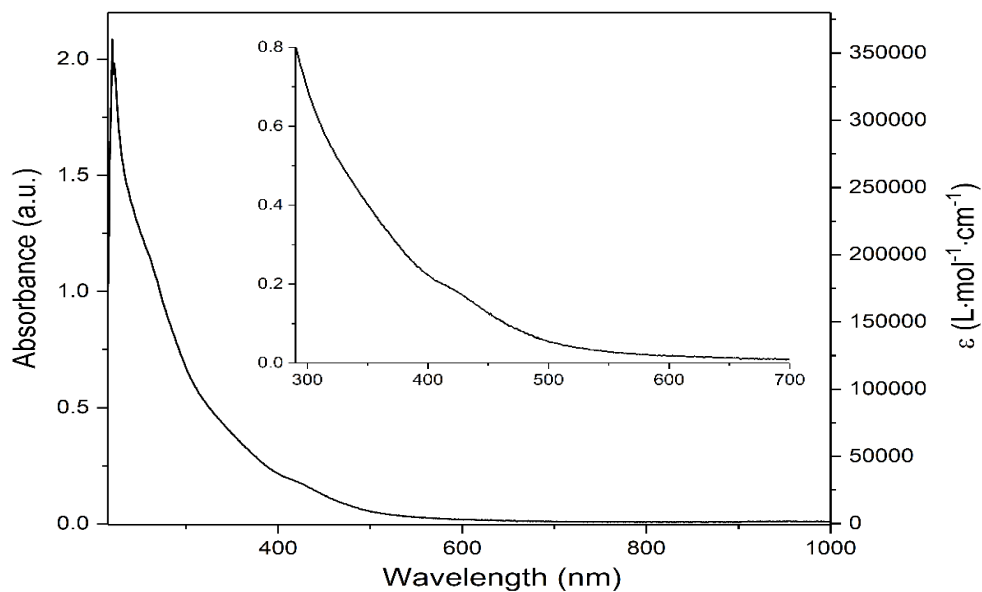


Fig. S16 UV-vis spectrum of a single crystals dissolved in methylene chloride (0.03 mM). The calculated molar extinction coefficients plotted as a function of wavelengths are presented on the right Y axis of the spectrum.

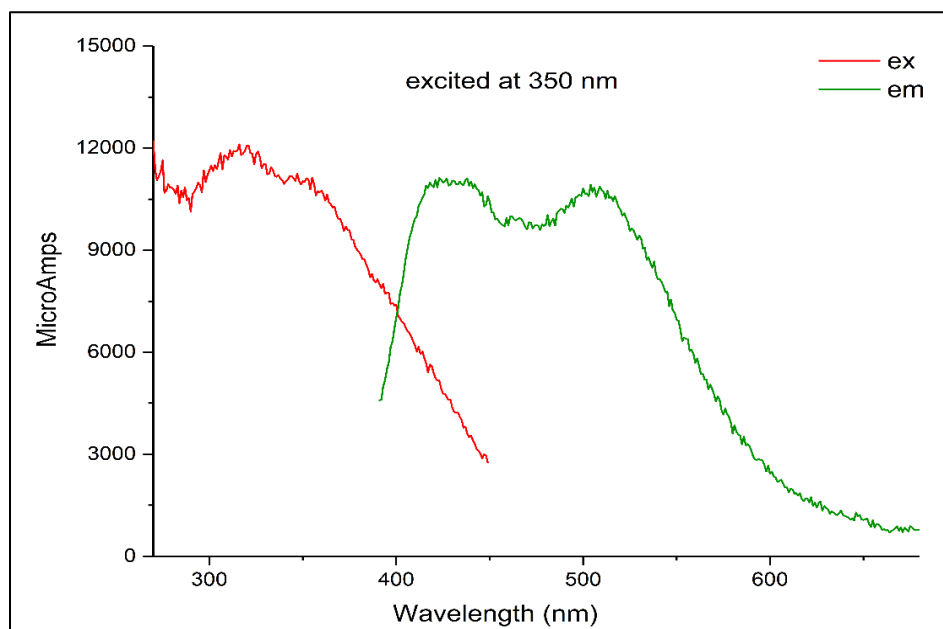


Fig. S17 Excitation and emission spectra of the CuNCs recorded in solid state.

B. EXPERIMENTAL PART

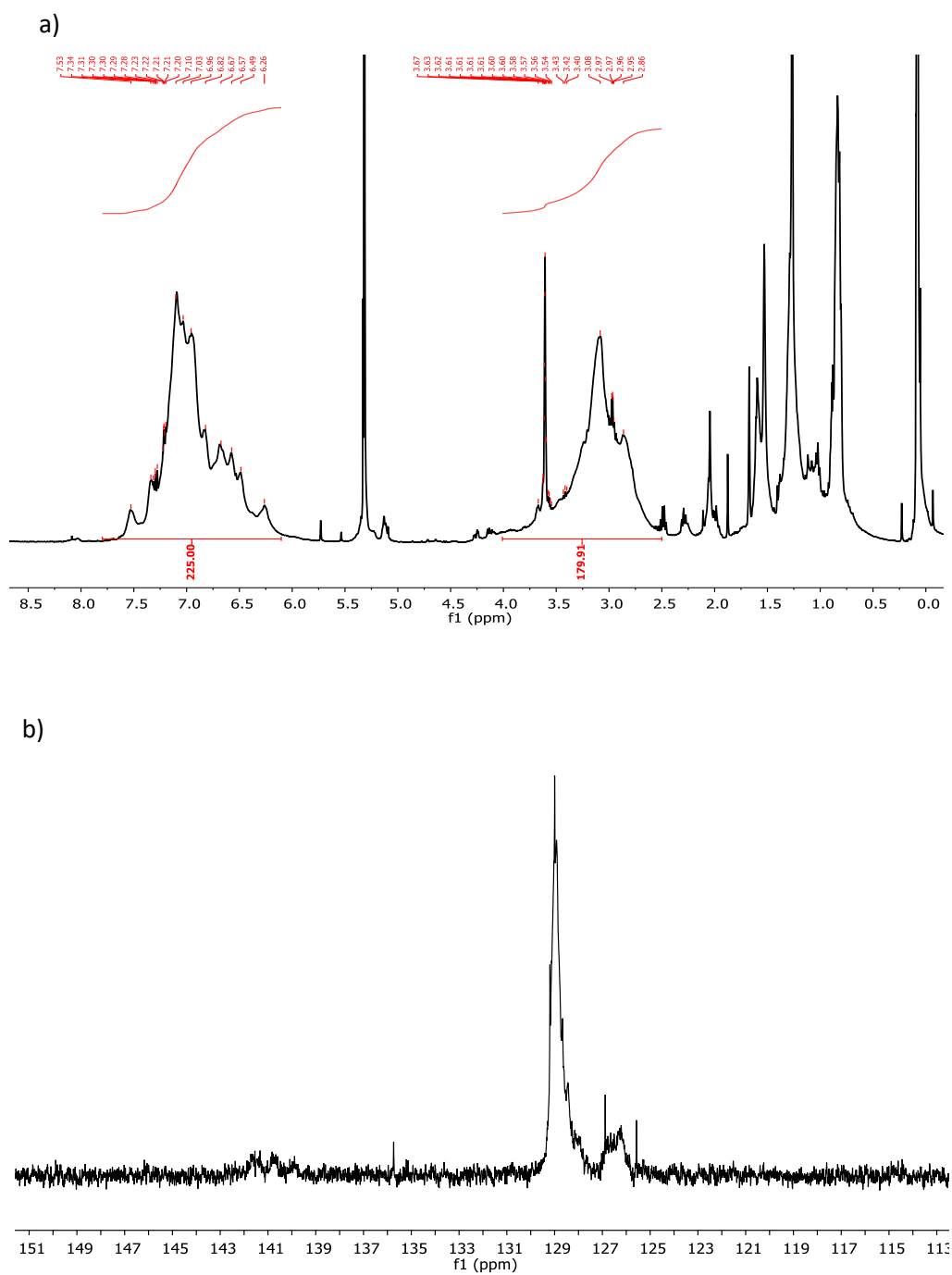


Fig. S18 a) ^1H NMR and b) ^{13}C NMR spectra of the crystal dissolved in CD_2Cl_2 (1.61 mM) at 298 K. For ^{13}C NMR, only the aromatic region is resented.

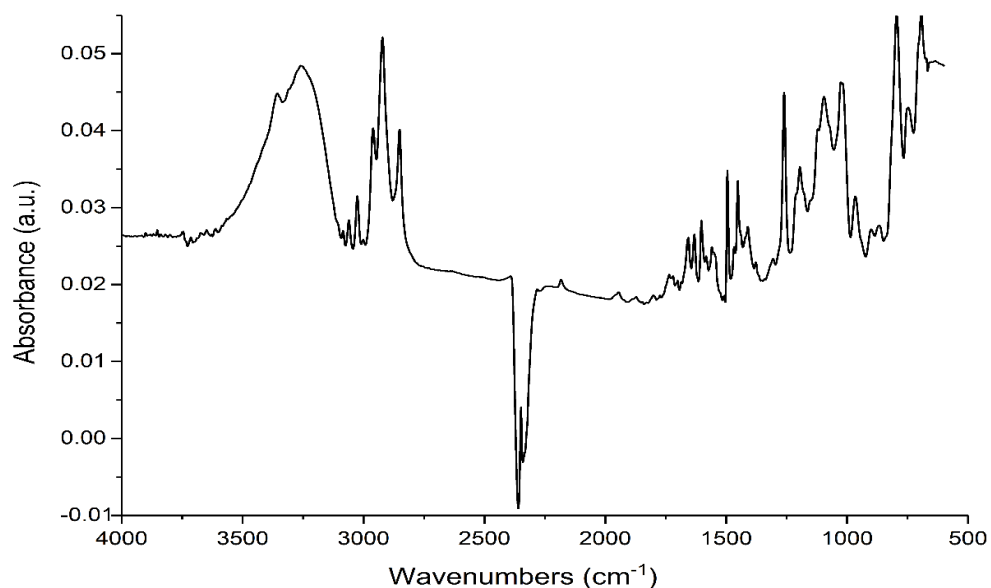


Fig. S19 FT-IR spectrum of the crystal. The crystal was dissolved in methylene chloride and afterwards was drop cast on KBr support. The background was subtracted from the measured sample spectrum. The large and intense bands between 3500-3100 cm^{-1} and 2500-2200 cm^{-1} belong to the stretching vibrational modes of O-H of water and C-O of CO_2 respectively.

References

- (1) *CrysalisPro Software System*, RIGAKU, Agilent Technologies Ltd, Yarnton, Oxfordshire, England, (2014).
- (2) Sheldrick, G. M. SHELXT – Integrated Space-Group and Crystal-Structure Determination. *Acta Crystallogr. Sect. A Found. Adv.* **2015**, *71* (1), 3–8.
- (3) Sheldrick, G. M. Crystal Structure Refinement with SHELXL. *Acta Crystallogr. Sect. C Struct. Chem.* **2015**, *71* (1), 3–8.
- (4) Dolomanov, O. V.; Bourhis, L. J.; Gildea, R. J.; Howard, J. A. K.; Puschmann, H. OLEX2: A Complete Structure Solution, Refinement and Analysis Program. *J. Appl. Crystallogr.* **2009**, *42* (2), 339–341.

General Conclusions

Ligand exchange allows one to tune the chiroptical properties of clusters in addition to introducing new valuable functionalities. It is therefore very important to choose appropriate functional ligands. This post-functionalization strategy has displayed the importance of the precise engineering of the ligand shell in order to alter the size-dependent physical and chemical properties of clusters and introduce new functionalities for various applications.

We have shown that the ligand exchange reaction between intrinsically chiral $\text{Au}_{38}(\text{2-PET})_{24}$ and chiral MT4 ligand can result in the formation of up to ten exchanged species with a composition of $\text{Au}_{38}(\text{2-PET})_{24-x}(\text{MT4})_x$. The adsorption of the helical ligand resulted in obvious changes on the optical spectrum of the cluster. The diminishing of the UV-vis bands intensity and even the red shift of some electronic transitions at higher ligand concentrations indicated the electronic changes upon ligand exchange although the core size of the cluster has been preserved. On the other hand, the adsorption of the MT4 ligand significantly changes the CD line shapes and even causes the inversion of the sign of some peaks.

The ligand exchange reaction between $\text{Au}_{25}(\text{2-PET})_{24}$ cluster and *t*-CE ligand also caused smoothing of the optical fingerprint bands in the UV-vis spectra correlated with the change in solution color as well as changes in NMR signals. Calculations highlighted the most probable and energetically favorable interstaple binding site for the *t*-CE ligand. Moreover, MALDI-TOF mass analysis showed the formation of up to $x=5$ $\text{Au}_{25}(\text{2-PET})_{18-2x}(\textit{t}\text{-CE})_x$ exchange species. The reaction monitoring with HPLC showed immediate changes in the chromatogram after ligand injection, in agreement with NMR, which showed a fast first ligand exchange. The ATR-FTIR studies of ion binding ability of the $\text{Au}_{25}(\text{2-PET})_{18-2x}(\textit{t}\text{-CE})_x$ sample with aqueous solutions of M^{n+} salts (where M^{n+} is K^+ , Ba^{2+} , Gd^{3+} and Eu^{3+}) revealed significant red shifts of C-O stretching vibrations due to an ion encapsulation into a crown cavity. The complexation leads to some conformational changes of the ligand, which is also reflected in the calculated vibrational spectra.

The ligand exchange reaction with enantiopure *R/S*-CE induced chirality in the cluster giving rise strong optical fingerprints in CD. ^1H NMR titration experiments have shown the binding of the

protonated enantiopure chiral amines into the crown moieties based on the ^1H NMR chemical shifts of the “labelled” proton of the guest. The fitting of the data by using non-linear regression algorithm, derived the characteristic binding constants.

Unlike monolayer-protected gold nanoclusters, the field of copper clusters is insufficiently explored mainly due to difficulties in preparing stable and atomically precise CuNCs. However, we successfully synthesized small GSH-protected CuNCs. The crude mixture shows high stability in solution under different conditions such as ambient exposure to light and heating up to 200 °C. ESI-HRMS spectra of the crude sample compared with theoretical isotopic patterns reveal several ionized species with potentially six GSH ligands (L) surrounding five to nine Cu atoms (Cu_9L_6 , Cu_8L_6 , Cu_7L_6 , Cu_6L_6 and Cu_5L_6). Several clusters were successfully separated in PAGE, HPLC and CE-UV. A preliminary assay of antimicrobial nature of CuNCs against *E. coli*, DH5 α , cells was tested by both a colony-forming unit assay and growth kinetics of bacteria in the presence of CuNCs. Both experiments suggest a dose-dependent antimicrobial effect.

We have successfully synthesized a new copper nanocluster with a composition of $\text{Cu}_{74}\text{S}_{15}(\text{2-PET})_{45}$. The structure determination by single crystal X-ray crystallography revealed that the sulfur atoms both from the ligand and bridged (sulfide) forms are structured in a layered fashion. The copper atoms bind preferentially in trigonal coordination within and between these layers, giving rise to the rather elongated and bent structure. In total 45 sulfur atoms belonging to 2-PET ligand are located on the exterior of the cluster whereas 15 bridged-sulfur atoms construct the skeleton of the cluster with copper atoms. The predicted gas-phase geometries of the model cluster in the anionic and neutral forms both satisfactorily agree with the experimental structure, thus suggesting that the structures of the $\text{Cu}_{74}\text{S}_{15}(\text{2-PET})_{45}$ nanocluster in the two redox states are similar. Moreover, based on TDDFT+TB calculations the measured onset of the absorption spectrum can be satisfactorily reproduced.

Abbreviations

APS	Ammonium persulfate
AuNCs	Gold nanoclusters
ATR-FTIR	Attenuated total reflectance Fourier transform infrared spectroscopy
BGE	Background electrolyte
CE	Capillary electrophoresis
CD	Circular dichroism
CuNCs	Copper nanoclusters
DCM	Dichloromethane
DFT	Density functional theory
EOF	Electroosmotic flow
HPLC	High performance liquid chromatography
HOMO	Highest occupied molecular orbital
LMCT	Ligand-to-metal charge transfer
LUMO	Lowest unoccupied molecular orbital
MNCs	Monolayer-protected metal nanoclusters
MALDI	Matrix-assisted laser desorption/ionization
MT4	[4]-helicene-2-thiol
MeOH	Methanol
NMR	Nuclear magnetic resonance
PAGE	Polyacrylamide gel electrophoresis
Ram/Sam	Protonated 3,3-dimethyl-2-butylamine
SEC	Size exclusion chromatography
<i>t</i> -CE	Di-thiolated 18C6
TEA	Triethylamine
THF	Tetrahydrofuran
TOAB	Tetraoctylammonium bromide
2-PET	2-phenylethanethiol

List of publications

- **Baghdasaryan AM**, Hobosyan MA, Khachatryan HL, et al. The role of chemical activation on the combustion and phase formation laws in the Ni-Al-promoter system. *Chem Eng J.* **2012**;188:210-215. doi:10.1016/j.cej.2012.01.137.
- **Baghdasaryan AM**, Niazyan OM, Khachatryan HL, Kharatyan SL. DTA/TG study of tungsten oxide and ammonium tungstate reduction by (Mg+C) combined reducers at non-isothermal conditions. *Int J Refract Met Hard Mater.* **2014**;43:216-221. doi:10.1016/j.ijrmhm.2013.12.003.
- **Baghdasaryan AM**, Niazyan OM, Khachatryan HL, Kharatyan SL. DTA/TGA study of molybdenum oxide reduction by Mg/Zn & Mg/C combined reducers at non-isothermal conditions. *Int J Refract Met Hard Mater.* **2015**;51:315-323. doi:10.1016/j.ijrmhm.2015.04.037.
- **Ani Baghdasaryan**, Thomas Burgi, “Ligand exchange reactions on Au₃₈: selective arrangements of helical dithiolates”, summary of the Master Thesis, Journal CHIMIA, issue 7-8/**2015**, vol 69.
- **Baghdasaryan A**, Grillo R, Roy Bhattacharya S, Sharma M, Reginato E, Theraulaz H, Dolamic I, Dadras M, Rudaz S, Varesio E and Burgi T. Facile Synthesis, Size-Separation, Characterization, and Antimicrobial Properties of Thiolated Copper Clusters. *ACS Appl Nano Mater.* **2018**;1(8):4258-4267. doi:10.1021/acsanm.8b01049.
- **Ani Baghdasaryan**, Céline Besnard, Latevi Max Lawson Daku, Teresa Delgado, and Thomas Burgi, “Thiolato protected copper sulfide cluster with the tentative composition Cu₇₄S₁₅(2-PET)₄₅”.-*Inorg.Chem.* **2020** (accepted).

Curriculum vitae

Personal information

Name: Ani Baghdasaryan
Date of birth: 05.01.1991
Nationality: Armenian
Contact: Phone: +41 22 37 96551, Email: Ani.Baghdasaryan@unige.ch
Website: ORCID: 0000-0003-1324-5683 • ResearcherID: W-5169-2019

Education

April 2015-January 2020: Ph.D. candidate in Chemistry, University of Geneva. PhD supervisor:
Thomas Burgi
2013-2015: MSc in Chemistry, University of Geneva
2008-2012: BSc in Inorganic Chemistry, Yerevan State University

Employment History

04/2015-06/2020: Research Assistant, Department of Physical Chemistry, University of Geneva
12/2010-09/2013: Laboratory Assistant, Institute of Chemical Physics, NAS of Armenia, Armenia
2010-2013: President of Students' Council, Faculty of Chemistry, Yerevan State University
2009-2010: Secretariat of Students' Council, Faculty of Chemistry, Yerevan State University

Institutional Responsibilities

2015-2020: Research and Teaching Assistant, University of Geneva
2010-2013: Laboratory Assistant at the Institute of Chemical Physics, NAS of RA, Armenia
2009-2013: Member of Students' Council, Yerevan State University, Armenia

Approved Research Projects

(i) Group of Professor Thomas Burgi, April 2015 – January 2020, Department of Physical Chemistry, University of Geneva:

- *Post-functionalization of atomically precise AuNCs and their applications in sensing.*
- *Synthesis, characterization and applications of CuNCs.*

(ii) Group of Professor Thomas Burgi, August 2014 – November 2014, Department of Physical Chemistry, University of Geneva:

- *Ligand exchange reactions on Au₃₈: selective arrangements of helical dithiolates.*

(iii) Group of Professor Thomas Burgi, June 2014 – July 2014, Department of Physical Chemistry, University of Geneva:

- *Photocatalysis on Au/SiO₂ nanocomposites.*

(iv) Group of Professor Allan Williams and Dr. Céline Besnard, April 2014 to May 2014, Department of Inorganic and Analytic Chemistry and Laboratory of Crystallography, Department of Quantum Matter Physics, University of Geneva:

- *Crystallography of coordination compounds.*

(v) Group of Professor Hans Hagemann, November 2013 to February 2014, Department of Physical Chemistry, University of Geneva

- *Hydrogen-fluorine exchange in $\text{Ca}(\text{BH}_4)_2\text{-Ca}(\text{BF}_4)_2$.*

(vi) Group of Professor Suren Kharatyan, September 2011 to May 2012, Department of Inorganic Chemistry, Yerevan State University

- *The Mechanism of ammonium paramolybdate reduction by (Mg+C) and (Mg+Zn) mixtures at non-isothermal conditions.*

Teaching Activities

Teaching Assistant for undergraduate students, Department of Physical Chemistry, University of Geneva

Fall semester 2015: Bomb calorimetry.

Spring semesters 2016-2018: Vibrational Circular Dichroism (VCD) of chiral molecules.

Prizes, Awards, Fellowships

2017	Ernst et Lucie Schmidheiny Foundation, University of Geneva: Travel grant
2015	“Platform Chemistry”, Swiss Academy of Science and the Swiss Chemical Society: Travel award
2015	Scientific Committee of the “Journées Andre Collet De La Chiralite_JACC”-Lyon, France: Best poster prize
2013	Calouste Gulbenkian Foundation - Lisbon, Portugal: Travel grant
2013	Faculty of Science, University of Geneva, Switzerland: Werner Stiftung Scholarship
2013	Faculty of Science, University of Geneva, Switzerland: Excellence Master Fellowship
2013	ARPA Institute competition, Second place for “Direct combustion synthesis of biocompatible Ti-foams from oxide precursors” innovation, Yerevan, Armenia
2012	ARPA Institute competition, Second place for “New method for obtaining molybdenum and molybdenum carbide fine-powders” innovation”, Yerevan, Armenia
2011	“Student 2011” and Yerevan State University Student Council Medal, Yerevan, Armenia
2011	Annual Conference of Students Scientific Society: First place for the scientific activity and presentation on the topic “The study of Ni-Al interaction mechanism by the method of differential thermal analysis”, Yerevan, Armenia
2010	CSMS fund: The sixth awardee of the personal stipend after academician A.B. Nalbandyan

Personal Skills

- Specialized in Material Synthesis Processes such as Synthesis, post-functionalization and applications of monolayer protected, atomically precise metal nanoclusters.

- Specialized in Spectroscopic and analytical characterization techniques such as UV-vis spectroscopy, Fluorescence spectroscopy, CD/VCD spectroscopy, ATR-FTIR spectroscopy, NMR spectroscopy, liquid chromatography (HPLC), capillary electrophoresis (CE), polyacrylamide gel electrophoresis (PAGE), ESI and MALDI mass spectrometry, X-ray Diffraction (XRD), DSC/TGA.
- Proficient in Origin Pro, Olex2, Chimera, MestReNova, GraphPad, CurveExpert Professional, MS Office, ChemDraw
- Multilingual, fluent in Armenian, English, Russian, and intermediate level in French